CONJUGATE TRANSFER PROCESSES IN A PILOT-SCALE UNBAFFLED AGITATED VESSEL WITH A PLAIN JACKET

Erik James Bentham

Submitted in accordance with the requirements for the degree of Doctor of Philosophy

The University of Leeds

School of Chemical and Process Engineering

Faculty of Engineering

September 2015

The candidate confirms that the work submitted is his own, except where work which has formed part of jointly authored publications has been included. The contribution of the candidate and the other authors to this work has been explicitly indicated below. The candidate confirms that appropriate credit has been given within the thesis where reference has been made to the work of others.

Chapters 2, 5 and 6 contain work based on jointly authored publications. The co-authors of these publications (Tariq Mahmud and Peter J. Heggs) have provided guidance during the course of the work and scrutinised the results presented in the papers. Some corrections in the manuscripts and checking equations are attributable to these co-authors. These are the some specific words (or order of words) for added clarity, and added parts of some sentences.

Chapter 2 contains some introductory work on heat transfer also present in the following paper:-

BENTHAM, E. J.; HEGGS, P. J.; MAHMUD, T.; 2015b; *Run-around Coils for Energy Efficiency*; Proc. 14th UK Heat Transfer Conference; Heriot-Watt University, Edinburgh.

Chapter 5 contains work based on the following two papers:-

BENTHAM, E. J.; HEGGS, P. J.; MAHMUD, T.; 2013; *Investigation of flow and pressure drop in a plain jacket of a stirred tank reactor*; Proc. 13th UK Heat Transfer Conference; Imperial College London. Paper 148.

BENTHAM, E. J.; HEGGS, P. J.; MAHMUD, T.; 2015a; *Heat Transfer in a Plain Jacket of a Pilot Scale Stirred Tank Reactor*; Proc. CHT-15, 6th International Symposium on Advances in Computational Heat Transfer, May 25-29, 2015, Rutgers University, New Brunswick, NJ, USA; International Centre for Heat and Mass Transfer Digital Library, Begell House.

Chapter 6 contains work based on the following paper:-

MAHMUD, T.; BENTHAM, E. J.; HEGGS, P. J.; 2015; *Modelling the Free-Surface Turbulent Flow and Heat Transfer in an Unbaffled Vessel Agitated by a Pitched Three-Blade Turbine*; Proc. 14th UK Heat Transfer Conference; Heriot-Watt University, Edinburgh.

ACKNOWLEDGEMENTS

Scholarship

The Engineering and Physical Sciences Research Council (EPSRC) has provided funding in the form of both living expenses and tuition fees for the author in this project.

General Acknowledgements

I would like firstly to express my gratitude to my supervisors Dr. Tariq Mahmud and Prof. Peter J. Heggs, for suggesting this project as a further investigation into heat transfer in agitated vessels, to take steps beyond my MEng project (Bentham, 2011). They have both been highly motivational and have provided me with essential information and resources, without which this project would have taken an inordinate amount of time. Prof. Heggs has also supported me charismatically during times of great stress caused by various outside influences.

I would like to thank Dr. Susan Pollard for training in the operation of the large scale equipment (25L and 50L vessels) in the iPRD laboratory in the Chemistry Department at the University of Leeds. I also express my gratitude to Nik Fitch and Scott Shaw for working with me to gain some very useful data from these large scale reactors.

I would also like to thank my examiners, Prof. Frans Muller (internal) and Prof. Graeme White (external). Their suggestions for improvement have helped to enhance the quality of this thesis. Frans also provided useful information on the dimensions of the 25 litre reactor during the development of the thesis.

I would like to thank other authors in the subjects involved or discussed in this thesis. As well as the authors in the list of references, I would like to thank Aray Kairzhanova and Muzammil Ali for previous developments on the models with Prof. Heggs.

I give a big thanks to Alan Burns, who has contributed with the programming and development of the ANSYS CFX software and delivered lectures on CFD and CFX, as well as Jujar Panesar, Segun Ilori, Sandy Black and János Szuhánszki for helping with various challenges with using the CFD programs. Additionally, I thank Prof. Mike Fairweather for delivering my introductory lectures in CFD during my MEng course and Maryam Gharebaghi for initially demonstrating the use of CFD software.

My thanks are also given to the various organisers and mentors on training courses, such as the Speed PhD, time management course, health and safety training, LabVIEW course by National Instruments, and the C++ course by the University of Leeds. These people include Andrew Bowen, Mick China and Natalie Scanlon.

I also thank the staff involved in the graduate office, as well as the IPSE staff, for helping with the formal procedures. These people include Moyra Culbert, Celia Taylor, Simon Welsh, Suzanne Bramwell, James Ford, Prof. Mojtaba Ghadiri, Kirn Jutlla, Sian Owen, Heather Strachan and Prof. Mi Wang.

I thank my family for their support. My father, Keith, originally sparked my interest in this subject and suggested the Chemical Engineering degree was best out of the options I had considered before starting university. My mother, Leila, has always encouraged me on whichever path I've been on. My brothers, Harry, Angus and Magnus, and sisters, Katy, Vikki and Isabella, have supported me when the times were rough, providing advice, consolation and inspiration. My grandparents, James and Dorothy Bentham, and John and Kirsti Miller, have also been supporting me and are very proud that I have reached this far in academia. John Miller, in particular, has been ready to get involved in helping to alleviate various stressful elements if they had gone too far.

I also thank my friends for being there for me and keeping me connected. Honourable mentions include Irina Flyagina, Chelsea Back, Liane El-Masry, Raymond White, Alex Taylor, Daniel Chan, Chelsey Needham, Jack Simpson, Beth Ellison, Sam Kelly, Julieth Figueroa Rosette, Aušra Raulušonytė, Roisin Allana Kiernan and Sarah Taylor. Without people such as these, the world would be a lonely place.

Courses and Training Attended

5th October 2011 – LabVIEW Hands-on Training Course with National Instruments.

6th October 2011 – Welcome to the Faculty of Engineering.

19th October 2011 – Initial training in iPRD large scale glassware, heating water.

24th to 25th October 2011 – Speed PhD.

26th October 2011 – CIEH Safety Training Course.

23rd November 2011 – Further training in iPRD large scale glassware, heating acetone.

14th March 2012 – LabVIEW Intermediate Course.

2nd to 4th April 2012 – C++ Course.

24th April 2012 – Prepare For Your Transfer (Engineering).

25th April 2012 – Search and Save (Engineering).

27th April 2012 – Working With Literature (Engineering).

30th April 2012 – Project Managing your Research Degree.

4th May 2012 – Time Management during your Research Degree.

15th October 2012 – Skill Recognition / Articulation and Finding Jobs Outside Academic Research (Careers Centre).

29th October 2012 – Interview Skills (Careers Centre).

24th July 2013 – Being Enterprising and Innovative in Academia.

22nd October 2013 – The Final Stages of your Research and Thesis Presentation.

29th January 2014 – Scientific Research Philosophy and Methodology: Putting Theory into Practice.

17th March 2015 – Engaging Non-Specialists with your Research.

19th October 2015 – Engineering Training for Postgraduates Engaged in Teaching.

Teaching Activities Conducted

Autumn/Winter 2011, 2012, 2013, 2014 and 2015 – Demonstrating for 2nd year undergraduate modules on the use of Aspen HYSYS and Microsoft Excel for numerical techniques.

Winter/Spring 2012, 2013, 2014, 2015 and 2016 – Demonstrating for MEng / MSc students on the use of ANSYS Workbench (Design Modeler), ANSYS FLUENT and ICEM CFD.

Conferences Attended

30th August to 1st September 2011 – 12th UK Heat Transfer Conference (University of Leeds). Attendee / assistant.

6th November 2012 – iPRD Conference (Weetwood Hotel, Leeds). Presentation and poster.

2nd to 3rd September 2013 – 13th UK Heat Transfer Conference (Imperial College London). Paper and presentation.

2nd December 2013 – Fourth Annual University of Leeds Postgraduate Researcher Conference / Showcase. Attendee.

4th December 2014 – Fifth Annual University of Leeds Postgraduate Researcher Conference / Showcase. Attendee.

25th to 29th May 2013 – International Centre for Heat and Mass Transfer (ICHMT): 6th International Symposium on Advances in Computational Heat Transfer (CHT-15) (Rutgers University, New Brunswick, New Jersey, USA). Paper and presentation.

7th to 8th September 2015 – 14th UK Heat Transfer Conference (University of Edinburgh and Heriot-Watt University, Edinburgh). Paper, poster and presentation.

ABSTRACT

Conjugate flow and heat transfer has been investigated in an unbaffled pilot-scale stirred tank reactor with a plain jacket. The vessel volume was 25 litres with a nominal capacity of 20 litres. Experiments and three-dimensional CFD simulations have been conducted on this vessel. The experiments involved heating, boiling, and cooling of methanol as well as water. The heat transfer medium in the jacket was an oil mixture called 'DW-Therm'. The CFD simulations of some aspects of these experiments have been broken down into jacket-only and process-only simulations, followed by a fully conjugate simulation.

The link between flow patterns, pressure drop and heat transfer in conventional jackets of stirred tank reactors has been analysed. The experiments and CFD simulations have been performed using a range of DW-Therm inlet temperatures. The CFD results were compared with experimental data of temperature measurements and with the use of engineering correlations found in the literature to predict heat transfer coefficients from the experimental data. The simulations produced values of total heat transferred by the jacket within 10% of the experimental results.

The simulations of boiling inside the vessel approximated a constant process temperature which was used to investigate the jacket-only phenomena. The process-only and the conjugate simulations simulated heating of water inside the vessel. Mathematical analysis as well as and industrially and academically used correlations from the literature were used to estimate heat transfer coefficients for boiling and external heat loss. These correlations for overall heat transfer coefficients overlook maldistribution of heat transfer coefficients in jackets that use a liquid heat transfer medium. This is industrially important because it provides new information to consider when maintaining highly temperature-dependent processes, in which adequate heat transfer to or from the process is required. This could be for a variety of reasons, from maintenance of product quality to preventing runaway reactions.

TABLE OF CONTENTS

LIST OF TABLES

LIST OF FIGURES

ABBREVIATIONS AND NOMENCLATURE

Symbol	Meaning	Units
A	Constant used in mathematical analysis	-
A	Area of heat transfer surface	m^2
A'	Area of heat transfer surface per unit length = A/Z	m
$\tilde{A}$	Effective cross sectional area of vessel wall	m^2
A_X	Cross-sectional area	m^2
b	Constant used in mathematical analysis	-
b	Blade width	m
B	Constant used in mathematical analysis	-
B_1	Constant used in vortex depth correlation	-
B	Parameter used in CFD equations (expanded in text)	Pa s^{-1}
c_P	Specific heat capacity at constant pressure	J kg^{-1} K^{-1}
$\tilde{c}_P$	Mean specific heat capacity at constant pressure	J kg^{-1} K^{-1}
C	Constant of integration, or constant used in mathematical analysis	-
C	Heat capacity rate = $\dot{M}c_P$ or $\dot{M}\tilde{c}_P$; subscript is not a number	W K^{-1}
C^*	Ratio of minimum to maximum heat capacity = C_{min}/C_{max}	-
C_n	Constant used in mathematical analysis; subscript is a number	-
$\tilde{C}_P$	Molar heat capacity of the total vessel contents	J mol^{-1} K^{-1}
C_μ	Turbulence constant	-
d	Impeller diameter	m
D	Diameter (in general) or Tank Diameter	m
E	Thermal effectiveness	-
E'	Thermal effectiveness at specified water level	-
f	Is a function of	-
F	Function	-
g	Gravitational field strength	m s^{-2}
h	Specific enthalpy	J kg^{-1}

h_l	Liquid surface height above tank bottom	m
h_l^*	Dimensionless liquid surface height = h_l/d	-
H_l	Initial liquid surface height above tank bottom	m
H_l^*	Dimensionless initial liquid surface height = H_l/d	-
k	Turbulent kinetic energy (in CFD equations)	J kg^{-1}
K	Dimensionless constant used in correlations	-
K_m	Coolant proportionality constant $= \alpha_o A_o'/\left(\dot{M}c_P\right)_m$	m^{-1}
K_n	Arbitrary constant, numbered n	-
K_p	Process proportionality constant$= \alpha_i A_i/(Mc_P)_p$	s^{-1}
K_w	Thermal diffusivity of wall material $= \lambda_w/(\rho c_P)_w$	m^2 s^{-1}
l	Length or distance	m
L	Length or distance	m
$LMTD$	Log Mean Temperature Difference	K
$\dot{m}$	Mass flux = $\dot{M}/A_X$	kg m^{-2} s^{-1}
M	Mass	kg
M_R	Molecular weight	kg kmol^{-1}
$\dot{M}$	Mass rate	kg s^{-1}
n	Integer or Number	-
n	Number	-
N	Number	-
N_A	Number of kilogram-moles of reactant A	kmol
N_{TU}	Number of Transfer Units $= UA/C_{min}$	-
p	Dimensionless constant $= \Delta r/2r$	-
p	Pressure	Pa
P	Function used in mathematical analysis	-
P	Parameter used in CFD equations (expanded in text)	Pa s^{-1}
P_W	Wetted Perimeter	m
$\dot{q}$	Heat flux	W m^{-2}
Q	Function used in mathematical analysis	-
Q	Heat	J
$\dot{Q}$	Rate of heat transfer	W
r	Radius or radial distance	m
R	Universal gas constant	kJ mol^{-1} K^{-1}
R_s	Shear stress	Pa

s	Distance	m
S	Suppression Factor	-
S_{ij}	Strain rate tensor	s^{-1}
S_R	Strain rate	s^{-1}
t	Time	s
T	Temperature	K or °C
T^+	Dimensionless temperature	-
T_p'	Average process temperature at specified water level	K or °C
u^*	Shearing stress velocity $= \sqrt{R_s/\rho}$	m s^{-1}
U	Overall heat transfer coefficient	W m^{-2} K^{-1}
v	Velocity (component)	m s^{-1}
$\bar{v}$	Mean velocity (time averaged velocity)	m s^{-1}
v'	Fluctuating component of velocity $= v - \bar{v}$	m s^{-1}
v_{imp}	Rotational speed of impeller	rev s^{-1}
$\boldsymbol{v}$	Velocity (vector)	m s^{-1}
V	Volume of reaction fluid	m^3
$\dot{V}$	Volumetric flow	m^3 s^{-1}
W	Wall thickness	m
x	Volume fraction	-
x_g	Vapour mass quality	-
X	Mathematical parameter used in a heat transfer correlation	-
X_{tt}	Martinelli parameter	-
y	Substitution variable used in mathematical analysis	-
y^+	Dimensionless distance $= s_y \cdot u^* \cdot \rho/\mu$	-
z	Height of jacket from the base	m
z_{bl}	Height of impeller blade parallel to axis of rotation	m
z_l	Height of liquid surface from the base	m
Z	Total height of jacket from the base	m

Greek	Meaning	Units
α	Individual heat transfer coefficient	W m^{-2} K^{-1}
β	Coefficient of Thermal Expansion	K^{-1} or $°C^{-1}$
β'	Model coefficient (used in CFD models)	-
β_m	Bulk Modulus	Pa
δ_w	Vessel wall thickness	m
Δ	Increment	-
ε	Turbulence dissipation rate	J kg^{-1} s^{-1}
ε_g	Emissivity of glass	-
ϵ	Enhancement Coefficient	-
θ	Normalised temperature	-
ϑ	Angle	rad
λ	Thermal conductivity	W m^{-1} K^{-1}
μ	Dynamic viscosity	kg m^{-1} s^{-1}
μ_e	Effective viscosity	kg m^{-1} s^{-1}
μ_t	Turbulent viscosity	kg m^{-1} s^{-1}
ν	Kinematic viscosity	m^2 s^{-1}
ξ	Dimensionless radial distance = $r/(d/2)$	-
ρ	Density	kg m^{-3}
$\dot{\rho}$	Volumetric mass transfer rate	kg m^{-3} s^{-1}
σ	Stefan-Boltzmann constant	W m^{-2} K^{-4}
σ_k	Constant term in CFD calculations	-
σ_R	Reynolds stress term	N m^{-3}
σ_ω	Constant term in CFD calculations	-
τ	Stress	Pa
τ_s	Shear stress	Pa
φ_{ij}	Pressure-strain tensor	Pa s^{-1}
Φ	Viscous heat generation term	W m^{-3}
χ	Proportionality constant	W K^{-1}
ω	Specific turbulence dissipation rate	s^{-1}
Ω_r	Rotation frequency	rad s^{-1}

Dimensionless numbers

Bo	Boiling number $= \dot{q}/\dot{m}h_{fg}$
Fr	Froude number $= v/\sqrt{gD_H}$
Fr_a	Froude number with agitation $= v_{imp}^2 d/g$
Ga	Galileo number = ${\mathrm{Re}_a}^2/\mathrm{Fr}_a$
Gr	Grashof number $= g\beta\Delta T\rho^2 L^3/\mu^2$
Gz	Graetz number = $\left(D_H/L_j\right)$RePr
Nu	Nusselt number $= \alpha L/\lambda$
Pr	Prandtl number $= c_p\mu/\ \lambda$
Ra	Raleigh number $= \mathrm{Gr}\cdot\mathrm{Pr} = g\beta\tilde{c}_p\Delta T\rho^2 L^3/\mu\lambda$
Re	Reynolds number $= \rho v D_H/\mu$
Re_a	Reynolds number with agitation $= \rho v_{imp} d^2/\mu$
Vi	Viscosity ratio = μ_b/μ_w

Subscript	**Meaning**
0	Initial or where $t = 0$
1	Initial or entry (or first in a series)
2	Final or exit (or second in a series)
∞	Background (referring to radiation)
a	During agitation
ann	Annulus
amb	Ambient
b	Bulk
bl	Blade(s)
$boil$	During boiling
$bulk$	Bulk
c	Critical
c	Cold stream
$calc$	Calculated value
$cond$	Condenser
cur	Curvature

C	Coil
CF	Complementary Function
CFD	Value from CFD simulation
def	Definition
e	Equivalent or effective
$expt$	Value measured or calculated using experimental data
ext	External heat exchanger stream
$evap$	Evaporated
f	Fluid or liquid
fc	Forced convection
fg	Vaporisation
F	Fanning (friction factor)
g	Gas or vapour
h	Hot stream
$huber$	Huber internal
H	Hydraulic
i	Radial distance increment number
i	Inner wall / inner surface
i	Direction 1 (in tensor notation)
ii	Inner surface of the inner wall (jacket-process)
imp	Impeller
int	Internal heat exchanger stream
io	Outer surface of the inner wall (jacket-process)
int	Intermediate heat exchanger stream
j	Height increment number
j	Jacket
j	Direction 2 (in tensor notation)
k	Direction 3 (in tensor notation)
l	Liquid
$loss$	Lost to surroundings
lv	From vapour to liquid
m	Heat transfer medium
max	Maximum
min	Minimum

mod	Modified
M	Moody (friction factor)
n	Time increment number
n	Integer or Number
nb	Nucleate boiling
nc	Natural convection
N	At the maximum time increment number (end)
o	Outer wall / outer surface
oi	Inner surface of the outer wall (jacket-surroundings)
oo	Outer surface of the outer wall (jacket-surroundings)
p	Vessel (process) contents
P	At constant pressure
r	Reduced
r	In the radial direction
s	Surface
set	Set point
SP	Stanton-Pannell (friction factor)
t	Turbulent (or of the turbulence)
T	Total
TU	Transfer units
u	Ullage region
uo	Outer surface of the ullage region
v	Vapour or vapour stream
w	Vessel wall
W	At the maximum wall radius
x	In the x direction
X	Cross sectional
y	In the y direction (usually perpendicular to the wall)
z	In the z direction (usually vertical)
Z	At the maximum jacket height
α	Phase under study (in multi-phase flow models)
ϑ	In the angular direction

Abbreviation	**Meaning**

BEM	Boundary Element Method
BSL	Baseline
CFD	Computational Fluid Dynamics
DNS	Direct Numerical Simulation
EARSM	Explicit Algebraic Reynolds Stress Model
ESDU	Engineering Sciences Data Unit
FDM	Finite Difference Method
FEM	Finite Element Method
GGI	General Grid Interface
HTC	Heat Transfer Coefficient
iPRD	Institute of Process Reasearch and Development
LDA	Laser Doppler Anemometry
LES	Large Eddy Simulation
LRR-IP	Launder, Reece and Rodi Isotropization of Production
LRR-QI	Launder, Reece and Rodi Quasi-Isotropic
LVF	Liquid Volume Fraction
ODE	Ordinary Differential Equation
OHTC	Overall Heat Transfer Coefficient
PDE	Partial Differential Equation
QUICK	Quadratic Upstream Interpolation for Convective Kinematics
RANS	Reynolds Averaged Navier-Stokes
RS	Reynolds Stress
RSM	Reynolds Stress Model
RST	Reynolds Stress Transport
SCAPE	School of Chemical and Process Engineering
SIMPLE	Semi-Implicit Method for Pressure Linked Equations
SSG	Speziale, Sarkar and Gatski
SST	Shear Stress Transport
STR	Stirred Tank Reactor
URL	Uniform Resource Locator (Web Address)
VOF	Volume of Fluid

1 INTRODUCTION

1.1 Background and Motivation for the Research

The ultimate purpose of this thesis is to investigate heat transfer (and hence temperature control) in a stirred tank reactor with a plain jacket. Modelling heat transfer in this type of system to provide a detailed understanding of the process is very important, both for the purpose of ensuring optimum product quality and for helping to reduce incidence of adverse events such as runaway reactions in the chemicals industry.

The current modelling techniques used by industry assume perfect mixing, uniform distribution of flow up the jacket, and a steady state process to which the concept of an 'overall heat transfer coefficient' (OHTC) can be applied. However, these assumptions are far from the truth. In this field, the more information obtained, the better.

This research is novel because previous literature has only touched lightly on heat transfer in plain jackets and the formulae for approximating average wall heat transfer coefficients may vary very significantly depending on which correlations are used. Recent literature on thermal runaway reaction research in vessels, such as that conducted by Rudniak *et al*. (2011), still assumes a constant jacket temperature.

Additionally, the literature contains some articles on heat transfer in unbaffled jacketed stirred vessels with pitched blade turbines (such as Milewska and Molga, 2007), but while these do include modelling exothermic reactions, they do not model a free surface. A free surface should be modelled for increased accuracy, because it affects the shape of the flow volume, changes the surface area for heat transfer and limits the total heat capacity of the contents of the vessel. Literature that does model a free surface, on the other hand, generally does not model heat transfer and uses Rushton turbines or paddle impellers rather than pitched blade turbines (for example, Haque *et al*., 2006). This thesis aims to combine these aspects.

It is fortuitous that the experiments done as part of this investigation have yielded many data about the process temperature and these are similar to the results from computational fluid dynamics (CFD) simulations, which have also yielded many data in particular on the flow patterns of the heat transfer fluid in the jacket under the set conditions that were used in the experiments.

A stirred tank reactor (STR) is a vessel designed to hold liquid chemicals, with a stirrer or agitator to mix the contents. STRs are a robust type of equipment used in many types of unit operation, both in large scale production and in the fine chemicals and pharmaceuticals industries. Processes include mixing, heating, cooling, boiling, performing chemical reactions (endothermic or exothermic), and crystallisation. In combination with a condenser, reflux and distillation operations can also be performed.

Figure 1.1 – 25 litre jacketed stirred tank reactor in iPRD, University of Leeds.

A common way to heat or cool the contents of an STR is to use a so-called ‘jacket’. An STR with a jacket is called a ‘jacketed’ STR. Figure 1.1 is an image of a jacketed STR with a capacity of 25 litres, in the Institute of Process Research and Development (iPRD) located in the School of Chemistry, University of Leeds. It is jointly used in projects by both the iPRD and SCAPE (the School of Chemical and Process Engineering), and has at times been hired for testing by pharmaceutical companies. This is the equipment used in the experimental investigations and approximated using CFD for the purpose of simulation.

A schematic of a jacketed STR is illustrated in figure 1.2. A heat transfer fluid is pumped through the jacket. The inlet temperature of the heat transfer fluid is controlled, usually by a separate heat exchanger or by a heating and/or cooling device such as a Huber heater/chiller (Huber, 2014). If the heat transfer fluid is hotter than the liquid inside the vessel, the STR is being heated. If the heat transfer fluid is colder than the liquid inside the vessel, the STR is being cooled.

The industrial engineer is usually expected to make the following assumptions when using heat transfer correlations: The overall heat transfer coefficient is constant for the process and over the entire surface; the mass rate and inlet temperature of the heat transfer medium is constant; all specific heat capacities are constant; the liquid in the vessel is perfectly mixed (uniform temperature); no phase changes occur, and heat losses are negligible (Green and Perry, 2007).

Correlations for heat transfer in the jacket side, based on experimental work, were developed for laminar flow by Chen *et al*. (1946), and for turbulent flow a correlation found in Perry and Chilton (1973). Bondy and Lippa (1983) and Dream (1999) use these equations as the basis of their correlations.

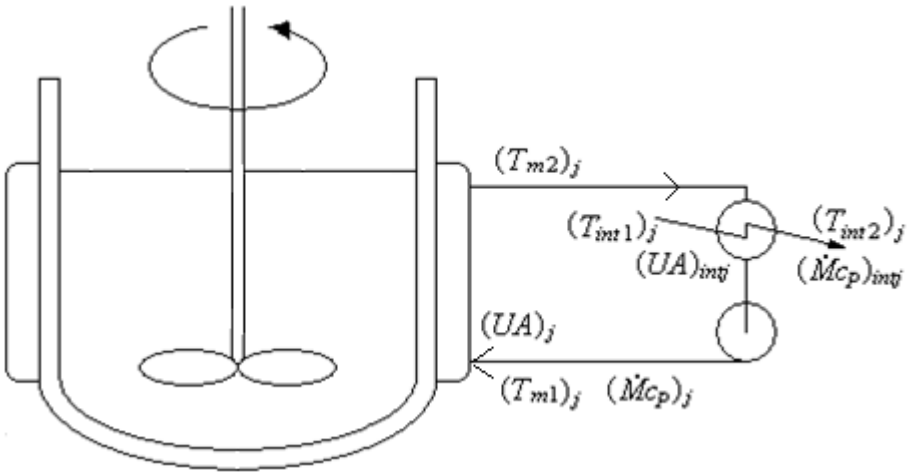

Figure 1.2 – Schematic of a jacketed stirred tank reactor. Based on Heggs and Hills (1994).

One of the underlying reasons this PhD project was started was to help towards preventing runaway reactions. These are behind some of the most major industrial disasters in history. For example, in the Bhopal disaster, a runaway reaction was caused by mischarging of water into a tank of methyl isocyanate, a highly toxic substance. This caused thousands of deaths when the methyl isocyanate escaped as a gas and was blown towards the nearby town. The Seveso disaster was caused by an accidental triggering of a runaway reaction. There have been tens of other incidents less well-known but still

significant. Some of these may have been due to uneven, non-homogeneous temperature profiles in the jacket, hence why much of the literature on jacket temperature profiles has links to investigations into runaway reactions.

In large scale STRs, highly inhomogeneous and transient hydrodynamic conditions prevail, where the mean velocities and turbulence quantities may vary by orders of magnitude inside the vessel, resulting in imperfect mixing and non-uniform temperature distribution. However, experiments in novel chemical reactions from pilot to industrial scale are inherently highly expensive and may carry high risk if unexpected effects occur. Simulation using mathematical models, including computational fluid dynamics (CFD) is therefore more practicable.

Various mathematical models for heat transfer in STRs have been developed in the past. These are based on the perfect mixing assumption, where the chemicals inside the reactor are treated as a homogeneous body of liquid. Lumped parameter models are the most common type of the perfectly mixed model. These use only an overall heat transfer coefficient (OHTC), which is a steady state concept being employed in a transient process. This essentially ignores the heat capacity of the vessel wall. They are divided into models that only account for the thermal inertia of the contents of the vessel (which is also called the 'process'), and models which additionally accommodate the thermal inertia of the vessel itself and the other peripheral equipment. Models using distributed parameters also include conjugate heat transfer between the jacket and process side. These models use individual heat transfer coefficients and the thermal inertia from at least the vessel wall, and produce data on how the wall temperature is expected to change with time.

CFD overcomes the assumption of perfect mixing, which is a major flaw of both the lumped parameter and distributed parameter models. This is because in reality, some areas are mixed better than others, and so the temperature at some positions in the process may be significantly under or over the temperature that would occur in a perfectly mixed system. "Hot spots" at some points may trigger unprecedented temperature spikes, particularly in exothermically reactive systems.

The most basic type of CFD model is the Reynolds averaged Navier-Stokes (RANS) model, which includes k-ε, k-ω and Reynolds Stress models (RSM). However, these are known to be inadequate at providing the detail required in large and complex turbulent systems such as reactors, because they do not model certain flows accurately enough,

including radial jet flows that are present in many reactor mixing systems. Large eddy simulation (LES) is a more reliable method of simulation, but is only recently being used in academia and industry, because of the need for high memory and processing speed required even for today's computers. Direct numerical simulation (DNS) is the most accurate method, as it accounts for all scales of turbulence, but it is computationally extremely costly in terms of time, and only used for problems involving small distances or small Reynolds numbers.

Modelling the bulk behaviour of the type of reactive systems used in industry on a large scale is riddled with complications. Turbulent flow is chaotic, and thus experimental results thus often yield natural variations even under the “same” conditions. Nevertheless, much serious scientific work has been conducted in an attempt to model turbulence using various assumptions and empirically derived correlations. Numerical simulation at smaller scales, moving from RANS to LES to DNS, yields more accurate results simply because more of the system's complexity is taken into account and it more closely resembles reality. This however increases the computational requirements in terms of time, memory and processing speed, and therefore cost. Unless future computers are developed powerful enough to simulate everything within an area on the order of a cubic metre cheaply enough and within a practical amount of time, there will always be a point at which the actual experiment becomes more cost effective than increasing the accuracy of numerical simulations.

The models developed in this thesis will be extremely powerful tools in facilitating the design, operation and safety of stirred tank reactors at all scales, but in particular pilot scale as this investigation focuses on.

1.2 Aims and Objectives Achieved

Figure 1.3 displays a block diagram covering the proposed development of the research studies. The aims and objectives achieved for this particular project are listed below.

1. Conduct experimental work on heating and cooling water and methanol in the pilot-stale stirred tank reactor with a plain jacket.
2. Develop analytical solutions for heating, cooling and boiling the contents of the vessel.
3. Develop a lumped parameter model of the heating and cooling processes involved.
4. Develop a distributed parameter model for the conjugate process.

5. Develop a mathematical model using Bernoulli's equation to describe the pressure drop in the jacket system.
6. Perform steady state non-isothermal CFD simulations of the jacket system to compare with the predictions of the Bernoulli model for pressure drop and the lumped parameter model for heat transfer.
7. Perform steady state isothermal CFD simulations of the process side to establish the two-phase flow properties in the unbaffled reactor.
8. Perform steady state non-isothermal CFD simulations of the process side to establish heat transfer within the vessel.
9. Perform transient non-isothermal CFD simulations of the process side to establish the changes over time.
10. Perform steady state conjugate CFD simulations to combine the effects of the jacket and process sides.

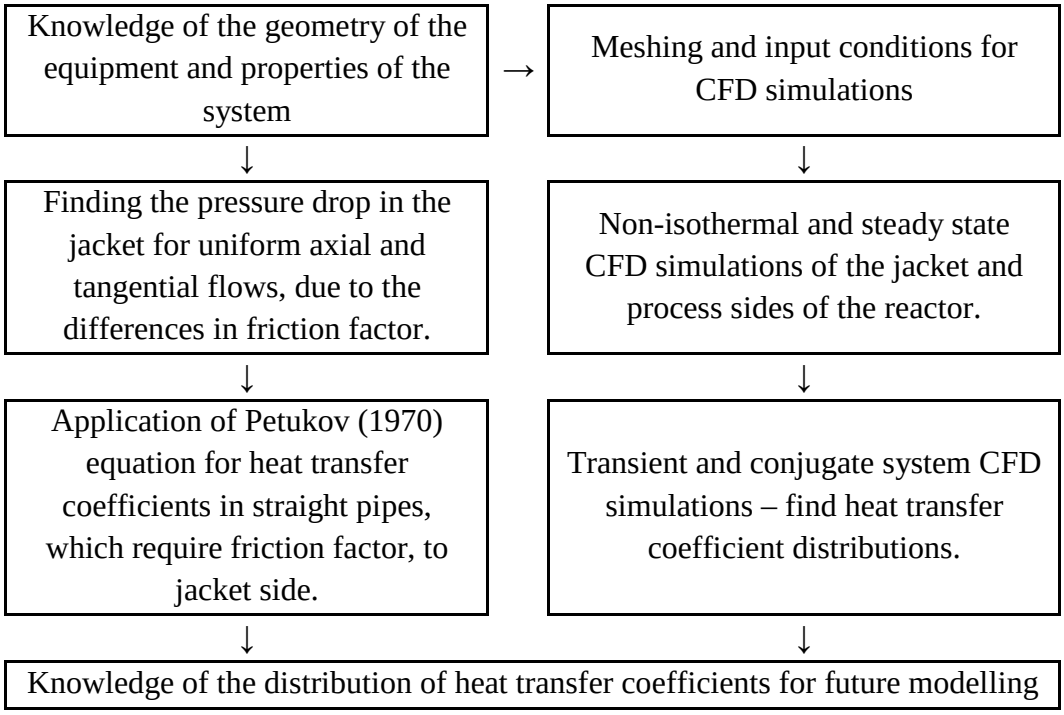

Figure 1.3 – Block diagram illustrating the proposed development of the research studies.

1.3 Structure of the thesis and linkage between chapters

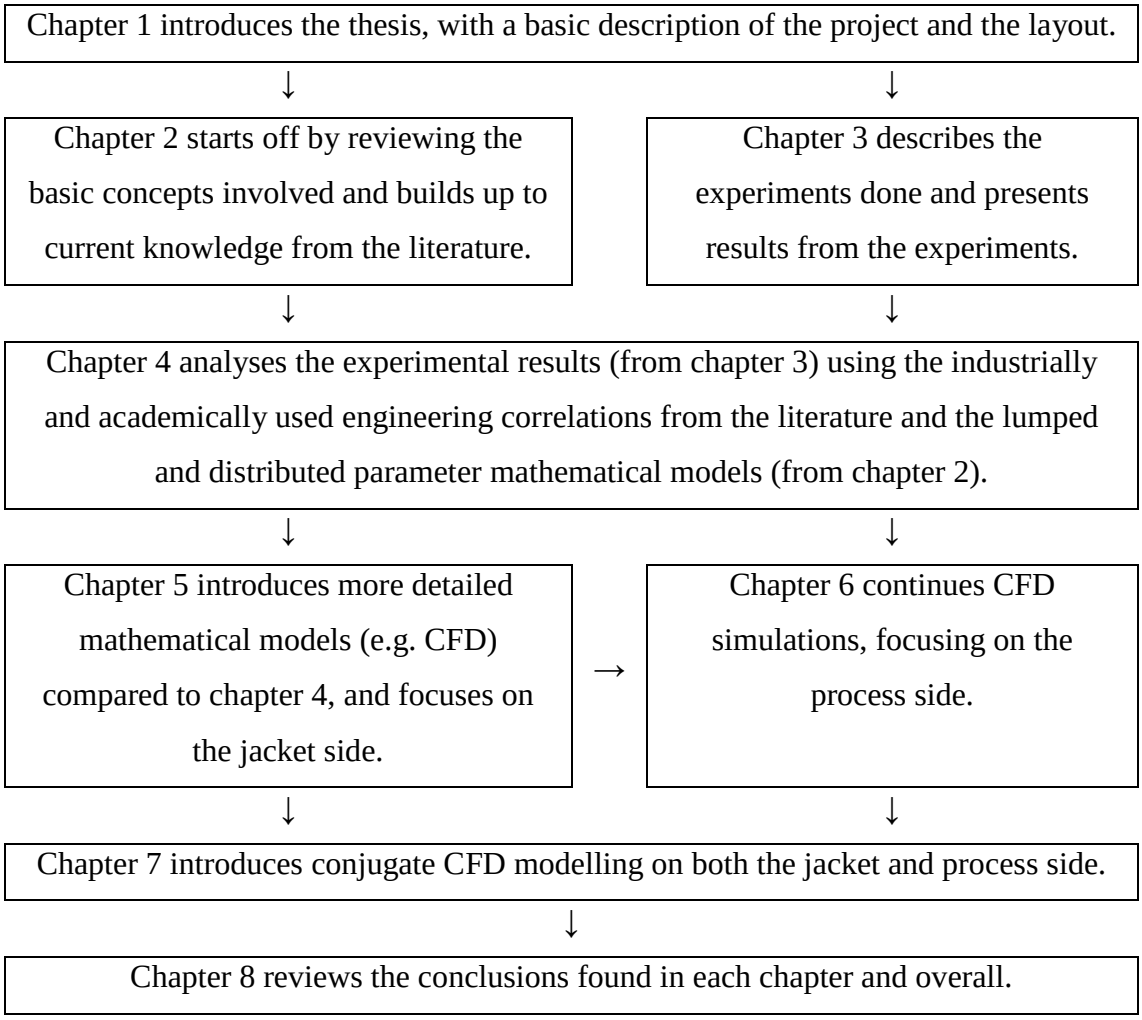

Figure 1.4 – Block diagram illustrating the structure of the thesis and linkage between chapters.

Figure 1.4 displays a block diagram of the linkage between chapters.

Chapter 2 starts off by explaining the basic concepts and assumptions involved in modelling the system. The literature is reviewed and the various analytical and empirical techniques and mathematical models (such as the lumped parameter and distributed parameter models) are introduced and reviewed. Industrially and academically used engineering correlations are described and compared.

Chapter 3 describes the experimental procedure. Details of the equipment, measurements taken and the experimental results are presented here.

Chapter 4 combines chapters 2 and 3, by using the techniques described in chapter 2 to analyse the experiments conducted in chapter 3. Lumped parameter and distributed parameter models are also used to analyse the data obtained.

Chapters 5 and 6 move on from chapter 4 by introducing higher level mathematical models (CFD). Chapter 5 covers modelling of the jacket side, starting with the Bernoulli model and moving on to higher level CFD models. Chapter 6 covers modelling of the process side with CFD, also using some of the results from chapter 5 for jacket side heat transfer.

Chapter 7 combines chapters 5 and 6, by introducing conjugate simulation. That is, both the jacket and process side are modelled together and the interaction between the two is observed.

Chapter 8 then summarises the results of the previous chapters.

2 LITERATURE REVIEW

2.1 Introduction to Past Developments in the Literature

Modelling any process always necessitates a simplification of the real thing. In mathematical modelling, this takes the form of assumptions. Irrelevant assumptions are not required to be stated, as these are likely to be a very large number of real-world influences that may affect the process but, it is hoped, only in a negligible manner. Another type of assumption is a simplification of random effects that would be too complex to model individually. A common example to this effect is the assumption that a volume of liquid is a single entity with specific physical properties, rather than separate molecules interacting. These assumptions are not explicitly stated, but are rather given symbols and numerical values, and related to more basic units such as temperature and pressure, by empirically derived formulae. The field of thermodynamics arises from this type of assumption, as it describes macroscopic effects resulting from statistical mechanics (Gibbs, 1902). It must be noted that random effects and chaotic effects are very different, as random effects tend to become more predictable on a macroscopic scale due to the law of large numbers (Wolfram Mathworld, 2012), whereas chaotic effects become less predictable at larger scales and require more detailed numerical simulation such as CFD.

More relevant assumptions are about phenomena that can have a noticeable effect, but often dramatically increase the complexity of modelling. The steady state concept of an overall heat transfer coefficient (OHTC) is used in the lumped parameter models. The most often-used type of model is the first type of lumped parameter model, which uses linear ordinary differential equations (ODEs) to simulate the temperature and concentration profiles for the process. The outer jacket side and heat loss effects may also be modelled with a separate OHTC, which is one of the developments in chapter 3 of this thesis. The second type of lumped parameter model (Ali, 2009) includes the heat capacity of the vessel equipment, most critically the vessel itself. The assumption of a steady state OHTC is relaxed in the distributed parameter models and replaced with individual film heat transfer coefficients. Both the lumped and distributed parameter models have the assumption of perfect mixing in the vessel, which is relaxed when CFD is used.

The lumped parameter models assume an instantaneous response to temperature change, and can often be modelled either analytically or numerically. On the other hand, the distributed parameter models include transient conduction and take into account the

gradual movement of heat through the wall. Partial differential equations (PDEs) are used and the process response is modelled numerically. The differential equations in the distributed parameter model are non-linear. Numerical methods to solve them may include the boundary element method (BEM), the finite difference method (FDM) and the finite element method (FEM).

Other assumptions may include isothermal flow in the jacket, which is the same as assuming an infinite mass flow of the heat transfer medium. This assumption is relaxed in the CFD models of the jacket.

2.2 Operation of STRs – General Review

2.2.1 Mechanisms of Heat Transfer

All forms of heat transfer are transient processes that transfer energy across space from hotter areas to colder areas, due to the driving force of temperature difference. Heat transfer occurs by three pathways – conduction, convection and radiation.

Heat transfer by conduction occurs when molecules transfer kinetic energy either by direct collisions between other molecules or through intermolecular forces. Conduction occurs much less in fluids than in solids as the intermolecular forces are much weaker. These forces include van der Waals forces, hydrogen bonds, ionic interactions, covalent bonds and metallic bonds. In metallic bonds, more energetic electrons at a hotter area in a metal spread out and share their energy with the other atoms, on average, resulting in the colder atoms becoming hotter.

Heat transfer by convection occurs in fluids and can be divided into forced and free (natural) convection. Free convection occurs due to density differences in the fluid, the most common effect being that hotter fluids are generally less dense and will rise due to buoyancy effects. This is taken into account more in the effects of heat loss on the outside of the reactor. Forced convection is induced by the stirrer to enable heat to mix more readily inside the reactor, and also by the pump used to move the heat transfer medium through the jacket.

Heat transfer by thermal radiation occurs due to electromagnetic waves, and can transfer heat through any medium, but can be limited by opacity and reflectivity. This accounts for some heat losses through the jacket, and is greater at larger scales. Hence, large scale reactors often have insulation against radiative heat transfer (such as reflective surfaces).

2.2.2 Heat Transfer Equipment

Figure 2.1 illustrates the three most common types of heat transfer systems in STRs. Either an external heat exchanger, a coil, a jacket, or a combination of any of these may be used. Within these categories, there are also many types of agitators, jackets and coils.

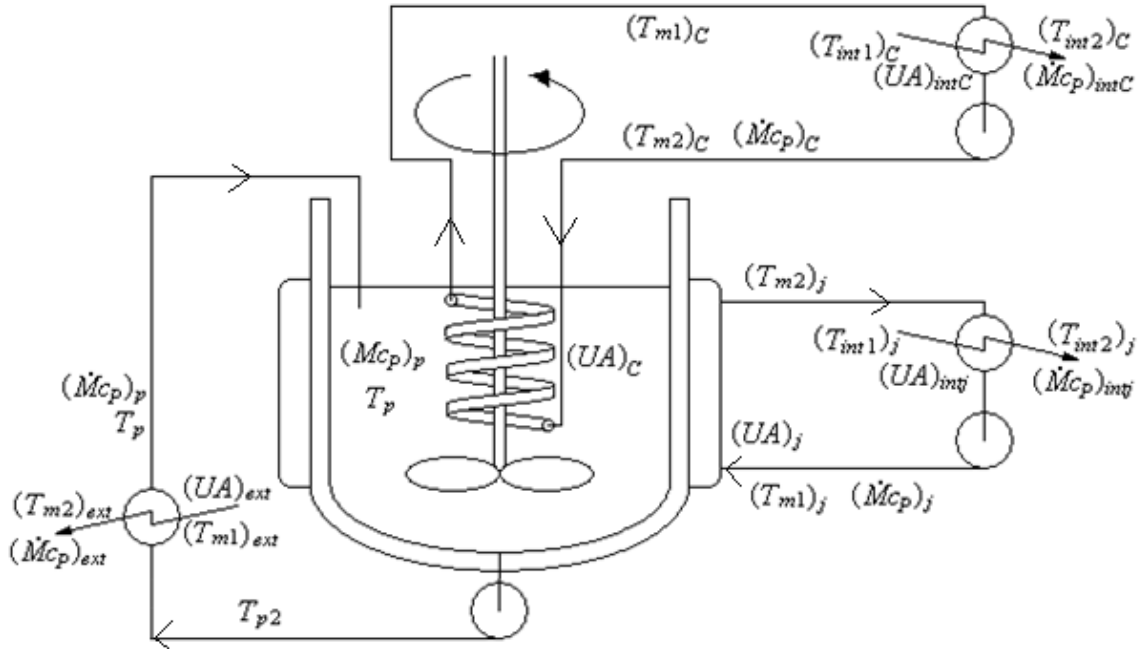

Figure 2.1 – Heating and cooling options for STRs: external heat exchanger, jacket and coil. Based on combined schematics in Heggs and Hills (1994).

When an external heat exchanger is used, the content of the vessel is extracted and pumped through the heat exchanger. The heated or cooled stream is then returned to the bottom of the vessel. This is the most effective option because the heat transfer area and conduction through the walls between the hot stream and the cold stream is often much greater in a heat exchanger as opposed to a coil or jacket. Unfortunately, however, as corrosive or unsuitable substances may be used, the pipework and internal components of the heat exchanger would all have to be lined with corrosion-resistant glass and would therefore be more bulky, fragile and costly. For reasons of both cost and safety, therefore, the jacket is considered the most robust option.

The use of a jacket or internal coil will form a run-around coil system, which is a system that uses a pump-around stream (containing an intermediate heat transfer medium) to carry heat between two separate streams (Bentham *et al*., 2015b). In this case, the heat is transferred from the process contents to an external heat exchanger and into the pump-around stream. The inlet temperature of the jacket or coil then depends on the heat transferred by the external heat exchanger.

Figure 2.2 – Different types of jacket – plain (left), half-pipe (centre), dimple (right).

Figure 2.2 displays some different types of jacket (plain, half-pipe and dimple). These have different flow patterns and calculations to describe their behaviour, for example a half-pipe jacket is essentially an external coil. The dimples in the dimple jacket are for the purposes of increasing turbulence, which enhances heat transfer. Other features include nozzles and vanes inside the jacket to direct the flow. The plain jacket, which is the focus of this investigation, has no such guidance of flow.

2.2.3 Mixing Equipment

Thorough mixing of the vessel contents is highly desirable, with perfect mixing being the ideal due to higher predictability and simplicity of calculations. Agitation can be divided into proximity impellers (where the blades are set up close to the vessel wall) and the more common non-proximity impellers. Examples of proximity impellers are illustrated in figure 2.3. Examples of non-proximity impellers are illustrated in figure 2.4.

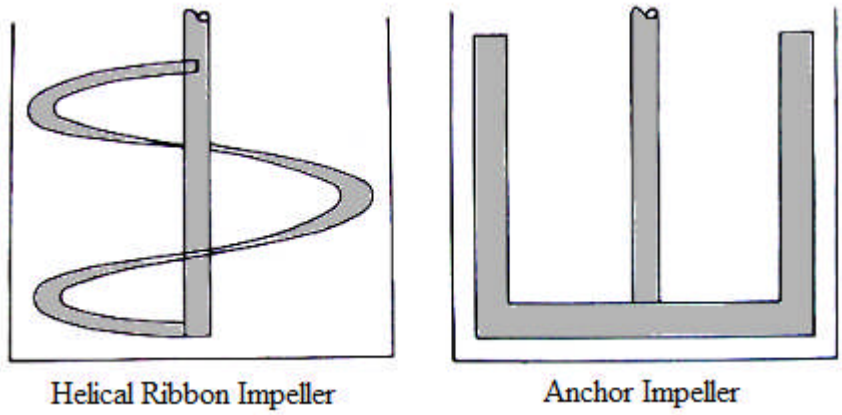

Figure 2.3 – Examples of proximity impellers. Adapted from Penney (1983).

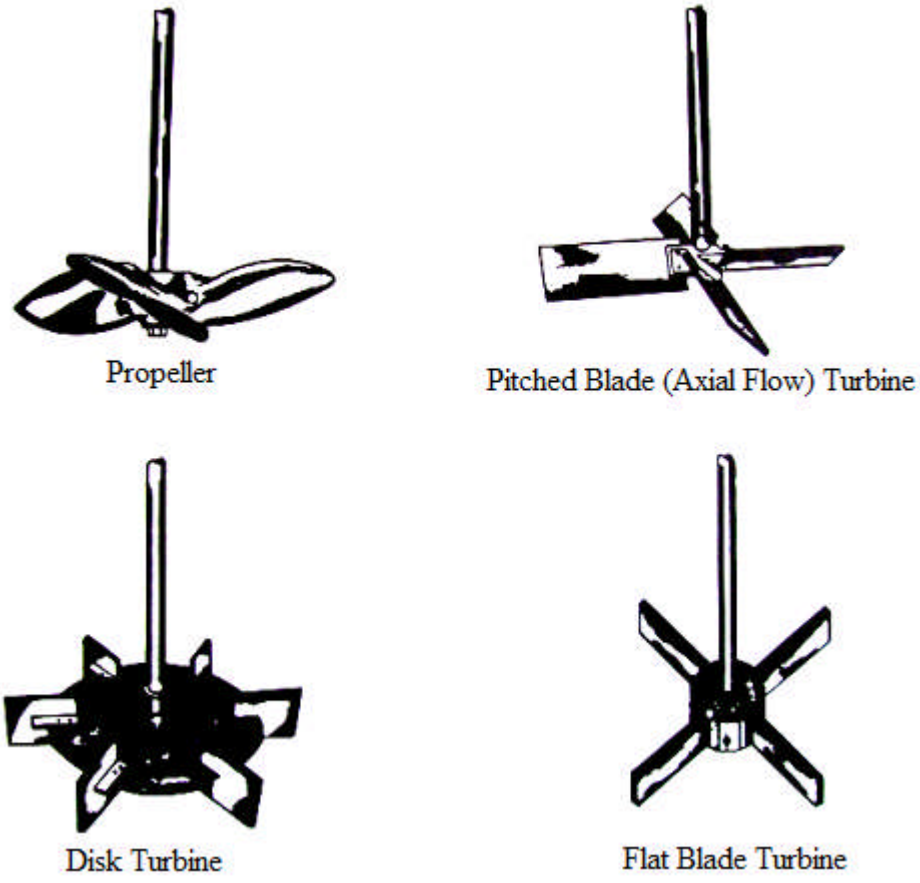

Figure 2.4 – Examples of non-proximity impellers. Adapted From Penney (1983), courtesy of Mixing Equipment Co., Rochester, NY.

2.3 Heat Transfer Calculations

Figure 2.5 illustrates cold and hot streams passing through a simplified heat exchanger, with the temperature of the cold stream increasing from T_{c1} to T_{c2} and that of the hot stream decreasing from T_{h1} to T_{h2}.

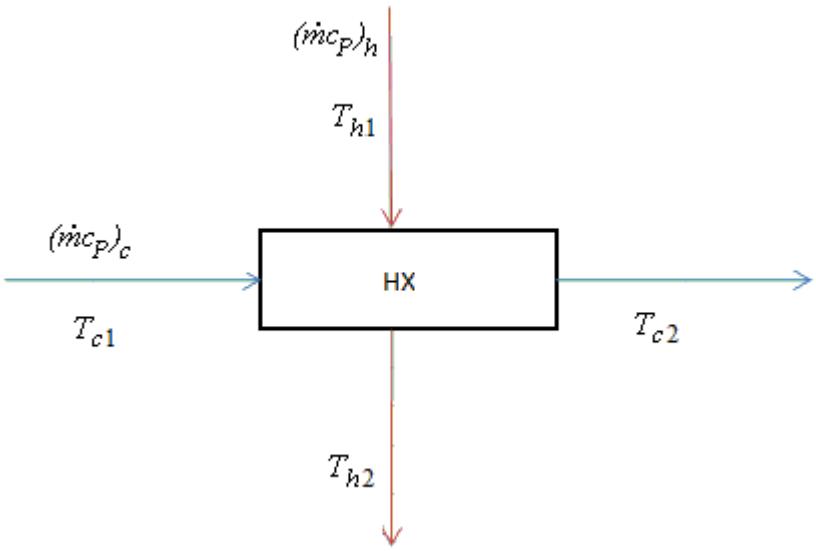

Figure 2.5: Basic representation of a heat exchanger.

2.3.1 Effectiveness-N_{TU} Methodology

The most common and familiar methodology used nowadays in heat transfer calculations is still the *LMTD* (Log Mean Temperature Difference) methodology. However, the *E*-N_{TU} methodology (where *E* is the 'thermal effectiveness' and N_{TU} is the 'number of transfer units') has several useful advantages over the *LMTD* methodology. The effectiveness, for example, can be compared for different heat exchangers or systems as a direct assessment of the efficiency of the system, which is useful for optimisation calculations. This is a result of the dimensionless values used. On top of this, fewer variables are required to specify the system compared to the *LMTD* method, making the *E*-N_{TU} method easier to use. Kays *et al*. (1964, pp 22-24) provides examples of the advantages of the *E*-N_{TU} method, the main arguments being:-

- Effectiveness is a simply defined parameter for overall performance, giving thermodynamic significance, and should stand alone as a dependent variable.
- The *LMTD* rate equation oversimplifies heat transfer design, giving the impression that it is a rate equation only, rather than both a rate equation and an energy balance.
- The *E*-N_{TU} methodology simplifies the algebra used to predict the performance of complicated flow arrangements.
- The *E*-N_{TU} methodology does not require calculation of the log mean temperature difference and often negates the need to perform iterations. It is therefore more straightforward.

If either the N_{TU} or effectiveness are known, graphs can be used which relate effectiveness, N_{TU} and heat capacity rate ratio (C^*). These are available for many different heat exchanger configurations, stream types and flow arrangements (ESDU 98005, 1998). These are sufficiently accurate to visually assess values for design requirements, since the actual values will not be exactly the same as the values predicted.

The basic equations governing the *E*-N_{TU} method are as follows (ESDU 98003, 1998):

$$C \equiv (\dot{m}c_P) \tag{2.1}$$

$$\dot{Q} = C_c(T_{c2} - T_{c1}) = C_h(T_{h1} - T_{h2}) \tag{2.2}$$

Equation (2.3) is derived from the fact that for any single heat exchanger, the stream with the smallest heat capacity rate (C_{min}) will have the largest temperature difference ($[\Delta T]_{max}$) and vice versa.

$$\dot{Q} = C_{min}[(T_{c2} - T_{c1}) \; or \; (T_{h1} - T_{h2})]_{max} = C_{max}[(T_{c2} - T_{c1}) \; or \; (T_{h1} - T_{h2})]_{min} \tag{2.3}$$

Effectiveness is defined from the temperature changes as in equation (2.4).

$$E = \frac{\dot{Q}}{\dot{Q}_{max}} = \frac{[(T_{c2} - T_{c1}) \; or \; (T_{h1} - T_{h2})]_{max}}{T_{h1} - T_{c1}} = \frac{C_{max}}{C_{min}} \frac{[(T_{c2} - T_{c1}) \; or \; (T_{h1} - T_{h2})]_{min}}{T_{h1} - T_{c1}} \tag{2.4}$$

where:-

$$\dot{Q}_{max} = C_{min}(T_{h1} - T_{c1}) \tag{2.5}$$

Ineffectiveness is therefore defined in equation (2.6).

$$1 - E = \frac{T_{h1} - T_{c1} - [(T_{c2} - T_{c1}) \; or \; (T_{h1} - T_{h2})]_{max}}{T_{h1} - T_{c1}} = \frac{[(T_{h2} - T_{c1}) \; or \; (T_{h1} - T_{c2})]_{min}}{T_{h1} - T_{c1}} \tag{2.6}$$

N_{TU} and C^* are defined in equations (2.7) and (2.8) respectively.

$$N_{TU} = \frac{UA}{C_{min}} = \frac{UA'L}{C_{min}} = \frac{UA}{C_{min}} \frac{C_{min}[(T_{c2} - T_{c1}) \; or \; (T_{h1} - T_{h2})]_{max}}{UA\Delta T_m} = \frac{[(T_{c2} - T_{c1}) \; or \; (T_{h1} - T_{h2})]_{max}}{\Delta T_m} \tag{2.7}$$

$$C^* = \frac{C_{min}}{C_{max}} = \frac{[(T_{c2} - T_{c1}) \; or \; (T_{h1} - T_{h2})]_{min}}{[(T_{c2} - T_{c1}) \; or \; (T_{h1} - T_{h2})]_{max}} \tag{2.8}$$

From equations (2.4) and (2.8), effectiveness can also be represented by equation (2.9).

$$E = \frac{1}{C^*} \frac{[(T_{c2} - T_{c1}) \; or \; (T_{h1} - T_{h2})]_{min}}{T_{h1} - T_{c1}} \tag{2.9}$$

Equation (2.5) can be used to find the following:-

$$E = \frac{C_c}{C_{min}} \frac{T_{c2} - T_{c1}}{T_{h1} - T_{c1}} = \frac{C_h}{C_{min}} \frac{T_{h1} - T_{h2}}{T_{h1} - T_{c1}} \tag{2.10}$$

Equation (2.10) can be used to find normalised temperatures (θ) for the outlet of each streams, as in equation (2.11) and (2.12), noting that θ_{c1} and θ_{h1} are defined as 0 and 1 respectively.

$$\theta_{c2} = (T_{c2} - T_{c1})/(T_{h1} - T_{c1}) = E\frac{C_{min}}{C_c} \tag{2.11}$$

$$\begin{aligned}\theta_{h2} &= (T_{h2} - T_{c1})/(T_{h1} - T_{c1}) = (T_{h1} + T_{h2} - T_{h1} - T_{c1})/(T_{h1} - T_{c1}) \\ &= [(T_{h1} - T_{c1}) - (T_{h1} - T_{h2})]/(T_{h1} - T_{c1}) = 1 - E\frac{C_{min}}{C_h}\end{aligned} \tag{2.12}$$

Therefore, from equation (2.11), if C_{min} is equal to C_c then θ_{c2} is equal to the effectiveness. Also, from equation (2.12), if C_{min} is equal to C_h then θ_{h2} is equal to the ineffectiveness.

2.3.2 Individual Heat Transfer Coefficients

Heat passing from the hot stream to the cold stream must travel through several layers of resistance – the two films and fouling layers on each side, and the wall itself, as displayed in figure 2.6.

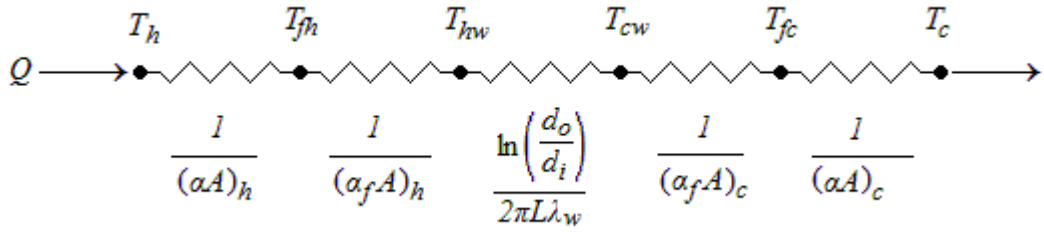

Figure 2.6 – Passage of heat between streams, displaying the layers of resistance.

For any point along the heat exchanger, the governing equation for heat transfer through these layers is as follows:-

$$\begin{aligned}\dot{Q} = UA(T_h - T_c) &= (\alpha A)_h(T_h - T_{fh}) = (\alpha_f A)_h(T_{fh} - T_{hw}) \\ &= \frac{2\pi L\lambda_w}{\ln\left(\frac{d_o}{d_i}\right)}(T_{hw} - T_{cw}) = (\alpha_f A)_c(T_{cw} - T_{fc}) \\ &= (\alpha A)_c(T_{fc} - T_c)\end{aligned} \tag{2.13}$$

For a clean surface and negligible wall resistance, α_f and λ_w tend to infinity, and T_{hw} and T_{cw} are considered equal as T_w. The equation for T_w is then as follows:-

$$T_w = [T_h(\alpha A)_h + T_c(\alpha A)_c]/[(\alpha A)_h + (\alpha A)_c] \tag{2.14}$$

Since U is based on the outside surface, it is also referred to as U_o. The areas of the inside and outside of the wall are A_o and A_i where, assuming a cylinder:-

$$A_o = 2\pi r_o L, \qquad A_i = 2\pi r_i L \tag{2.15}$$

and:-

$$\frac{1}{U_o} = \frac{A_o}{(\alpha A)_h} + \frac{A_o}{\left(\alpha_f A\right)_h} + \frac{A_o}{2\pi\lambda_w L}\ln\left(\frac{d_o}{d_i}\right) + \frac{A_o}{\left(\alpha_f A\right)_c} + \frac{A_o}{(\alpha A)_c} \tag{2.16}$$

2.3.3 Non-Isothermal Cooling Medium in the Jacket

The relevant calculations use a term called the proportionality constant, χ, to describe the heat transfer in different heat exchangers (including jackets) by relating the heat transfer to the temperature difference between the inlets of the hot and cold streams. This is described in Heggs and Hills (1994). Considering a cooling operation in a jacketed stirred tank, the whole "hot stream" is the constant temperature T_p of the process fluid. This is represented in equation (2.17).

$$T_{h1} = T_{h2} = T_p \tag{2.17}$$

The process temperature is constant when a phase change is taking place, with no pressure drop, no sub-cooling and no superheating. The process temperature can also be considered constant when using the assumption of perfect mixing and the consideration of an instant of time. The following conditions therefore apply, reflecting the two-stream heat transfer operation:-

$$T_{c1} = T_{m1} \tag{2.18}$$

$$C_h = \left(\dot{M}c_P\right)_p = Q/(T_{h1} - T_{h2}) = Q/\left(T_p - T_p\right) \Rightarrow \infty \tag{2.19}$$

$$C_c = \left(\dot{M}c_P\right)_m \tag{2.20}$$

The heat transfer rate decreases exponentially as the heat is transferred along the length of the heat exchanger. The overall heat transfer related to the inlet temperatures of the hot and cold streams is therefore expressed as equation (2.21):-

$$\begin{aligned}\dot{Q} &= (T_{h1} - T_{c1})C_c\{1 - exp[-UA/C_c]\} \\ &= \left(T_p - T_{m1}\right)\left(\dot{M}c_P\right)_m\left\{1 - exp\left[(UA)_j/\left(\dot{M}c_P\right)_m\right]\right\}\end{aligned} \tag{2.21}$$

where $(UA)_j$ denotes the UA value for the jacket. The proportionality constant is defined as the following:-

$$\chi = \dot{Q}/(T_{h1} - T_{c1}) = \left(\dot{M}c_P\right)_m\left\{1 - exp\left[-(UA)_j/\left(\dot{M}c_P\right)_m\right]\right\} \tag{2.22}$$

Using the E-N_{TU} methodology:-

$$\dot{Q} = EC_{min}(T_{h1} - T_{c1}) = E\left(\dot{M}c_P\right)_m\left(T_p - T_{m1}\right) \tag{2.23}$$

It can then be seen that the expression for χ is much simpler:-

$$\chi = EC_{min} = E\left(\dot{M}c_P\right)_m \tag{2.24}$$

where:-

$$E = \left\{1 - exp\left[-(UA)_j/\left(\dot{M}c_P\right)_m\right]\right\} \tag{2.25}$$

2.3.4 Correlations for Individual Heat Transfer Coefficients

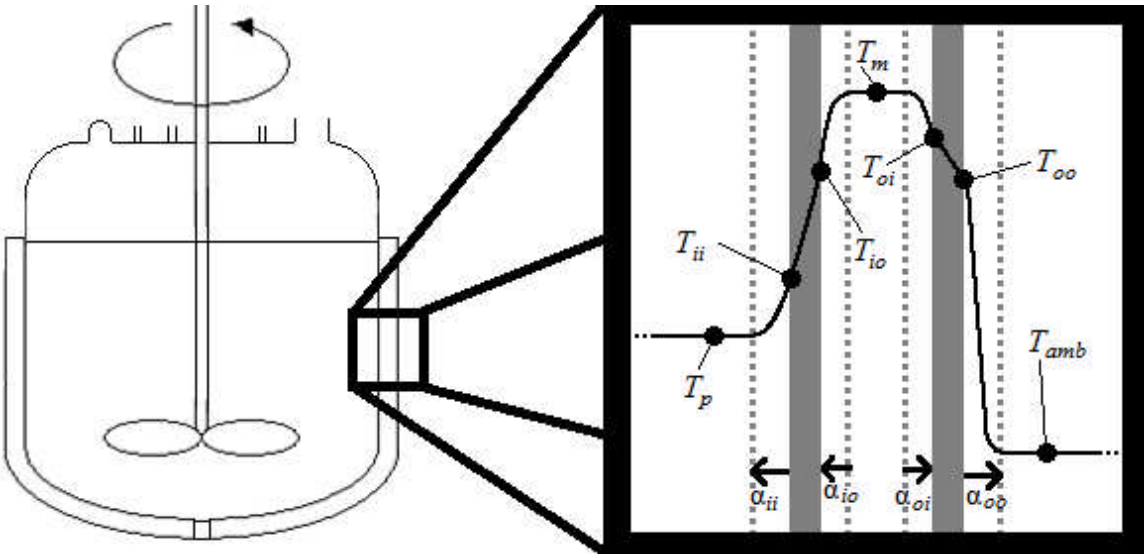

Figure 2.7 – Temperature profile and individual heat transfer coefficients across the jacket walls during heating. In this case $T_p < T_m > T_{amb}$.

Figure 2.7 illustrates the temperature profiles and the nomenclature for the individual heat transfer coefficients across the jacket walls during heating (as in the main experimental analysis, rather than cooling as described in the previous section). If the values of $\dot{Q}$ have been found, the correlations can be used iteratively to find the film heat transfer coefficients α and the corresponding surface temperatures. As an example, the temperatures on either side of the inner wall can be found by equation (2.26).

$$\dot{Q} = A_{iw}\lambda_w\frac{\mathrm{d}T_i}{\mathrm{d}r} = (T_{io} - T_{ii})\frac{2\pi\lambda_w z_w}{\ln(D_{io}/D_{ii})} \tag{2.26}$$

Many so-called “jacket side heat transfer coefficients” include agitator speed and the Reynolds number of the vessel contents. These are therefore referring to the process side

heat transfer coefficient on the inner wall while being heated by a jacket (using the nomenclature of this thesis, this is denoted by the term α_{ii}). The correlations require a Nusselt number (Nu_{ii}), which is provided by correlations in the literature (examples of which are given below). The film heat transfer coefficient on the inner wall (process side) and its relationship to the Nusselt number is given in equation (2.27).

$$\alpha_{ii} = \frac{\dot{Q}}{A_{ii}\left(T_{ii} - T_p\right)} = \mathrm{Nu}_{ii}\frac{\lambda_p}{D_{ii}} \tag{2.27}$$

In the experiments conducted for this thesis, the reactors were clean (that is, there were no fouling coefficients), so there was only one individual heat transfer coefficient for each side of the glass. Hewitt *et al.* (1994, pp. 940) describes the jacket side heat transfer coefficient as being "very dependent on the positions of the inlet and outlet connections" when there is no phase change occurring in the jacket.

As reported by Hewitt *et al.* (1994, pp. 940), for liquid water in a cast iron jacket, a values of α_{ii} from Brown *et al*. (1947) ranged from 631 W m^{-2} K^{-1} to 1170 W m^{-2} K^{-1}. In that investigation, Brown *et al*. (1947) also stated that a 50% increase in agitation speed could cause a 21% increase in heat transfer coefficient, although at the cost of a 200% increase in power for the agitator.

A possible correlation for heating with a jacket while using pitched blade mechanical agitators is given by Penney (1983), as displayed in equation (2.28): This equation was first developed by Brooks and Su (1959) for steam condensing in the jacket (isothermal operation) and later adapted by Nagata *et al*. (1972).

In equation (2.28), the geometrical correction is displayed in square brackets.

$$\mathrm{Nu}_{ii} = 0.54\mathrm{Re}_a^{2/3}\mathrm{Pr}^{1/3}\left(\frac{\mu_b}{\mu_w}\right)^{0.14}\left[\left(\frac{z_{bl}/d}{1/5}\right)^{0.15}\left(\frac{n_{bl}}{6}\right)^{0.15}[\sin(\vartheta_{bl})]^{0.5}\right] \tag{2.28}$$

where the Re and Pr are the Reynolds and Prandtl numbers respectively, μ_b and μ_w are the viscosities in the bulk process and at the inner wall respectively, z_{bl} is the height of the impeller blade parallel to the axis of rotation, d is the impeller diameter, n_{bl} is the number of blades, and ϑ_{bl} is the angle (in radians) between a pitched blade on the impeller and a plane normal to the axis of rotation.

Under the conditions stated in equation (2.29), Nagata *et al*. (1971) instead suggested the correlation in equation (2.30) for the jacket side heat transfer coefficient, for unbaffled reactors with no coils.

$$\mathrm{Re_a} > 100, \qquad 2 < \mathrm{Fr_a} < 2000 \tag{2.29}$$

$$\mathrm{Nu}_{ii} = 0.51\mathrm{Re}_a^{2/3}\mathrm{Pr}^{1/3}\left(\frac{\mu_w}{\mu_b}\right)^{-0.14} \times\left[\left(\frac{d}{D}\right)^{-0.25} v_{imp}^{0.15}[\sin(\vartheta_{bl})]^{0.5}\left(\sum_{\mathrm{i}}\frac{z_{bli}}{\mathrm{i}z_l}\right)^{0.15}\right] \tag{2.30}$$

ESDU 81045 (1981) describes a correlation for concentric flow in annuli. This would approximate the case in the jacket, if the flow was uniformly distributed and rose equally at all sides. The basic correlation is the Petukov (1970) equation, which additionally accounts for friction in the pipes. This is described in ESDU 92003 (1992) with equation (2.31):-

$$\mathrm{Nu}_j = \frac{(f/2)\mathrm{RePr}}{1.07 + 12.7(f/2)^{1/2}(\mathrm{Pr}^{2/3} - 1)} \tag{2.31}$$

where:-

$$f = 1/\{4[1.82\log_{10}(\mathrm{Re}) - 1.64]^2\} \tag{2.32}$$

The Reynolds number range for this correlation is from 4×10^3 to 3×10^6. Thus, it would not be applicable in laminar flow cases such as uniform upwards flow in the jacket.

Bondy and Lippa (1983) suggested a jacket side correlation for laminar flow based on Seider and Tate (1936). This is displayed in equation (2.33).

$$\mathrm{Nu}_j = \alpha_j D_e/\lambda_m = 1.86\left[\mathrm{Re}\cdot\mathrm{Pr}\left(D_e/L_j\right)\right]^{0.33}(\mu/\mu_w)^{0.14} \tag{2.33}$$

where the ‘equivalent diameter’ is:-

$$D_e = (D_{oi}^2 - D_{io}^2)/D_{io} \tag{2.34}$$

For turbulent flow, Bondy and Lippa (1983) suggest a correlation from Perry and Chilton (1973), displayed in equation (2.35).

$$\mathrm{Nu}_j = \alpha_j D_e/\lambda_m = 0.027\mathrm{Re}^{0.8}\mathrm{Pr}^{0.33}(\mu/\mu_w)^{0.14} \tag{2.35}$$

For transitional flow, Bondy and Lippa (1983) provide a graph connecting these two equations.

Kakaç *et al*. (1987) provided tables and graphs, with related equations, to find the Nusselt number and pressure drop in the following conditions, for laminar convective heat transfer in concentric annular ducts:-

For fully developed flow:-

- Constant temperatures at both walls.
- Constant heat fluxes at both walls.
- Constant temperature at one wall, constant heat flux at the other.

For thermally developing flow:-

- Uniform temperatures at both walls, different from entering fluid temperature (fundamental solution of the first kind).
- One wall insulated, one wall at uniform heat flux (fundamental solution of the second kind).
- One wall insulated, one wall at uniform temperature, different from entering fluid temperature (fundamental solution of the third kind).
- One wall at uniform heat flux, one wall at uniform temperature equal to the entering fluid temperature.

However, no data are available for non-uniform heat transfer across any walls.

Dream (1999) listed equations for the jacket and process side heat transfer coefficients under laminar and turbulent flow in the jacket, with different agitator types, and with different jacket types. The preferred equation for laminar flow inside the jacket here is that of Chen *et al*. (1946). This includes the Grashof number (Gr), which is used in calculations of free convection. The equation for turbulent flow is also that from Perry and Chilton (1973). However, while Bondy (1983) suggests for unbaffled jackets to neglect the multiplier $(1 + 3.5\, D_e/D_{ann})$, which, in the literature, is called the "turbulent flow coil correction factor". The equation in Dream (1999) suggests that this term should be *included* for unbaffled jackets. The correlation for turbulent flow in Dream (1999) is as displayed in equation (2.36). However, this can produce values of heat transfer coefficient significantly higher than experimental values due to the inclusion of the term.

$$\mathrm{Nu}_j = \alpha_j D_e/\lambda_m = 0.027\mathrm{Re}^{0.8}\mathrm{Pr}^{0.33}(\mu/\mu_w)^{0.14}(1 + 3.5\, D_e/D_{ann}) \qquad (2.36)$$

where:-

$$D_{ann} = (D_{io} + D_{oi})/2 \tag{2.37}$$

Garvin (1999) provided equations to calculate the corrected Reynolds number and Nusselt numbers in concentric annular ducts. This was adapted from ESDU 78031 (1978). First, instead of the 'equivalent diameter' D_e , the hydraulic diameter D_H is used:-

$$D_H = D_{oi} - D_{io} \tag{2.38}$$

The curvature diameter formula is:-

$$D_{cur} = D_{io}/\cos(\mathrm{a}) \tag{2.39}$$

where:-

$$\mathrm{a} = \tan^{-1}\left(2L_j/\pi\, D_{io}\right) \tag{2.40}$$

For laminar flow, a curvature formula is first worked out:-

$$\mathrm{X} = \mathrm{Re}^{0.5}(D_H \mathrm{Pr}/D_{cur})^{0.25} \tag{2.41}$$

Then the Nusselt numbers are worked out. For $\mathrm{X} > 4.9$:-

$$\begin{aligned}\mathrm{Nu}_j = \alpha_j D_H/\lambda_m \\ = 0.0984\mathrm{X}[1 - (1.48/\mathrm{X}) + (23.2/\mathrm{X}^2) - (120/\mathrm{X}^3) \\ + (212/\mathrm{X}^4)](\mu/\mu_w)^{0.14}\end{aligned} \tag{2.42}$$

and for $\mathrm{X} < 4.9$:-

$$\mathrm{Nu}_j = \alpha_j D_H/\lambda_m = \sqrt[3]{\left(h_{jfc} D_H/k\right)^3 + \left(h_{jnc} D_H/k\right)^3} \tag{2.43}$$

where the forced convection component is:-

$$\alpha_{j,fc} D_H/\lambda_m = 4.86 + \mathrm{Ge} \tag{2.44}$$

and the natural convection component is:-

$$\alpha_{j,nc} D_H/\lambda_m = \pm 0.7287 \phi_{nc}^{0.33}\left[\mathrm{Gr} \cdot \mathrm{Pr}\left(D_H/L_j\right)\right]^m \tag{2.45}$$

Where the entrance correction factor Ge is:-

$$\mathrm{Ge} = 0.09525[\mathrm{Gz}/(1 + 0.0525\mathrm{Gz}^{0.67})](\mu/\mu_w)^{0.14} \tag{2.46}$$

For aiding flow ($T_w > T_m$), the symbol $\pm$ is positive and $m = 0.28$.

For opposing flow ($T_w < T_m$), the symbol $\pm$ is negative and $m = 0.25$.

For turbulent flow, equation (2.47) is used:-

$$\mathrm{Nu}_j = 0.0192\mathrm{Re}^{0.795}\mathrm{Pr}^{0.495}\exp\{-0.0225[\ln(\mathrm{Pr})]^2\}\,\mathrm{Ge}(\mu/\mu_w)^m \times\{1 + 0.059[\mathrm{Re}(D_H/D_{cur})^2]^{0.34}\} \tag{2.47}$$

where for $\mathrm{Re}(D_H/D_{cur})^2 > 4.72$:-

$$\mathrm{Ge} = 1 \tag{2.48}$$

In this case, for aiding flow ($T_w > T_m$), $m = 0.30$.

For opposing flow ($T_w < T_m$), $m = 0.18$.

For $\mathrm{Re}(D_H/D_{cur})^2 < 4.72$:-

$$\mathrm{Ge} = 1 + 5.71\big(D_H/L_j\big)\big[1 - \exp\big(-0.07L_j/D_H\big)\big] \tag{2.49}$$

and $m = 0.18$.

For transitional flow, there is no well-defined method. Garvin (1999) suggests to interpolate between the upper laminar limit and the lower turbulent limit against the logarithm of Re.

Free convection is usually considered negligible in turbulent forced convection flows, but is included in laminar forced convection flows. In the equation in Garvin (1999), described above, for the jacket side heat transfer coefficients (α_{io} and α_{oi}), the laminar flow equation uses Gr as a parameter also. Thus, the coefficient of thermal expansion (β) of the jacket oil is needed. This can be approximately derived from the data of density vs. temperature, as follows:-

$$\beta = \frac{1}{V}\frac{\mathrm{d}V}{\mathrm{d}T} \approx \rho\frac{\frac{1}{\rho(T_2)} - \frac{1}{\rho(T_1)}}{T_2 - T_1} \tag{2.50}$$

The effects of free convection in the jacket can be to either aid or oppose the forced convective flow. Figures 2.8 and 2.9 illustrate some cases.

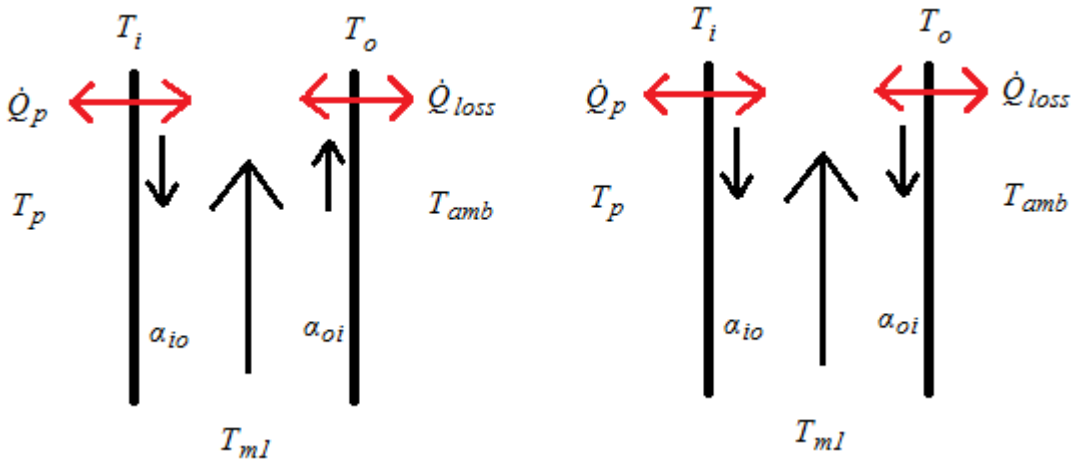

Figure 2.8 – Free convection opposing and aiding flow, during heating of the reactor contents, when $T_p < T_m < T_{amb}$ (left) and when $T_p < T_m > T_{amb}$ (right).

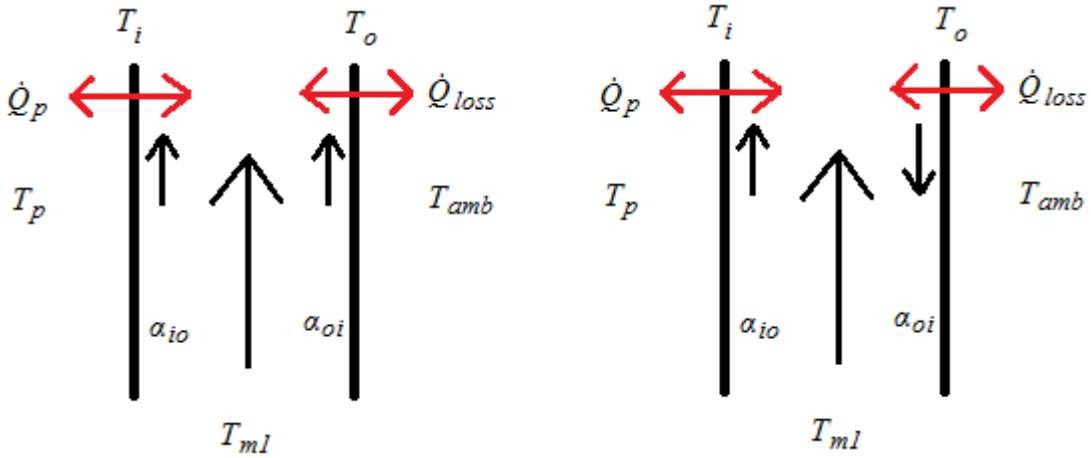

Figure 2.9 – Free convection opposing and aiding flow, during cooling of the reactor contents, when $T_p > T_m < T_{amb}$ (left) and when $T_p > T_m > T_{amb}$ (right).

In figure 2.8, during heating, the flow is opposed by free convection because the inner wall is colder than the heat transfer medium. The medium (flowing upwards) is subsequently denser at the wall, and natural convection produces a force slowing the flow and reducing the heat transfer coefficient (α_{io}).

In figure 2.9, during cooling, the flow is aided on the inside by heat from the process side, increasing α_{io}. Usually the case will be as in the right hand image, but when cooling below the ambient temperature, T_m is the lowest and the flow is aided on both sides as in the left hand image.

As in the left hand images of figures 2.8 and 2.9, the flow on the outside wall may be aided if the outside temperature T_{amb} is higher than the jacket medium temperature, but in most cases the right hand image will be the case, and the colder surroundings will cause opposition to the flow, thus reducing the heat loss coefficient (α_{oo}).

Gnielinski (2009) provided a correlation for turbulent flow in concentric annular ducts:-

$$\mathrm{Nu} = \frac{(f_M/8)\mathrm{Re}\cdot\mathrm{Pr}}{k_1 + 12.7\sqrt{f_M/8}\,(\mathrm{Pr}^{2/3}-1)}\left[1+\left(\frac{D_H}{L_j}\right)^{2/3}\right]F_{ann}K \tag{2.51}$$

where:-

$$k_1 = 1.07 + \frac{900}{\mathrm{Re}} - \frac{0.63}{1+10\mathrm{Pr}} \tag{2.52}$$

and:-

$$f_M = [1.8\log_{10}(\mathrm{Re}^*) - 1.5]^{-2} \tag{2.53}$$

where:-

$$\mathrm{Re}^* = \mathrm{Re}\times\left[\left(1+r^{*2}\right)\ln(r^*) + \left(1-r^{*2}\right)\right]/[(1-r^*)^2\ln(r^*)] \tag{2.54}$$

and:-

$$r^* = r_i/r_o \tag{2.55}$$

For heat transfer at inner wall, and outer wall insulated:-

$$F_{ann} = 0.75{r^*}^{-0.17} \tag{2.56}$$

For heat transfer at outer wall, and inner wall insulated:-

$$F_{ann} = 0.9 - 0.15{r^*}^{-0.6} \tag{2.57}$$

and for a liquid heat transfer medium:-

$$K = \left(\frac{\mathrm{Pr}}{\mathrm{Pr}_w}\right)^{0.11} \tag{2.58}$$

Gnielinski (2009) stated that equation (2.56) represented experimental data of concentric annular ducts to ±5% within the specified conditions. However, no data are available in Gnielinski (2009) for heat transfer at both sides.

Gaddis (2010) describes alternate methods for calculating the jacket side heat transfer coefficient by Lehrer (1970) and Stein and Schmidt (1993). These methods were not mentioned in the papers by Bondy and Lippa (1983), Dream (1999) or Garvin (1999). They are more complex; however, they are still reported to have large errors – up to 50% deviation from experimental values. According to Gaddis (2010), the mean relative error

for the jacket side heat transfer coefficient in jackets with tangential inlet tubes was 26.4% for Stein and Schmidt (1993) and 44.0% for Lehrer (1970).

Although the range of scales and geometries for the investigated reactors is severely limited, Gaddis (2010) provides essential dimensions for the reactors in which these experiments were performed, giving examples of the solution by both Lehrer (1970) and Stein and Schmidt (1993). As a suggestion to mitigate overestimation of the heat transfer coefficient, Gaddis suggests that both methods should be used and that the lower coefficient should be considered.

In a further paper, Lehrer (1971) suggested that plain concentric cylindrical jackets, with a height-to-diameter ratio of approximately unity, could be "equated to a number of equal time-constant backmix vessels in series". A comparison of tangential inlet and radial inlet was made. It was found that in jackets with a radial inlet pipe, there were virtually no "dead zones" (of low flow) in the jacket, but that the heat transfer was nevertheless more effective with a tangential inlet. According to the Scopus database as of September 2015, this paper has not been cited in any subsequent journals or books, at least since 1996. This can be taken as an indicator that the relationship between flow and heat transfer in jackets of reactors has still not been thoroughly investigated in the literature, as of the time of publication of this thesis.

2.3.5 Boiling Heat Transfer

Boiling heat transfer is discussed in general by Hewitt *et al.* (1994). Alane (2007) discussed a calculation for the inside heat transfer coefficient (α_{ii}) during boiling, but used correlations for tubes. As stated by Alane (2007), this method was recommended by Worley *et al*. (1985) and finalised by Gungor and Winterton (1986). Alane's work was on a thermosyphon reboiler and used the Dittus-Boelter correlation for tubes (Dittus and Boelter, 1930). In this case, however, a correlation for an agitated vessel is to be used, such as equation (2.28) or (2.30). Pool boiling with a stirrer, as in the experiments conducted for this thesis, is calculated from two parts – the part due to convection by the agitator (which will be denoted α_a here) and the part due to nucleate boiling (which will be denoted α_{boil}).

The overall expression is given by equation (2.59), where ϵ is the enhancement coefficient due to boiling, S is the suppression factor and x_g is the vapour mass quality. α_a is equivalent to α_{ii} without boiling, as previously described in section 2.3.4.

$$\alpha_{ii} = \epsilon\left(1 - x_g\right)^{0.8}\alpha_a + S\alpha_{boil} \tag{2.59}$$

The enhancement factor ϵ was described in equation (2.60):-

$$\epsilon = 1 + 1.37X_{tt}^{-0.86} + 24000\mathrm{Bo}^{1.16} \tag{2.60}$$

where X_{tt} is the Martinelli parameter:-

$$X_{tt} = \left(\frac{1 - x_g}{x_g}\right)^{0.9}\left(\frac{\rho_g}{\rho_f}\right)^{0.5}\left(\frac{\mu_f}{\mu_g}\right)^{0.1} \tag{2.61}$$

and Bo is the boiling number:-

$$\mathrm{Bo} = \dot{q}/\dot{m}h_{fg} \tag{2.62}$$

and where ρ_g and ρ_f are the vapour and liquid densities respectively, and μ_g and μ_f are the corresponding viscosities, $\dot{q}$ is the heat flux from the jacket, $\dot{m}$ is the mass flux of the agitated liquid (in the direction of flow) and h_{fg} is the latent heat of vaporisation.

As in Alane (2007), the pool boiling coefficient α_{boil} is calculated using the correlation by Cooper (1984), displayed by equation (2.63) where p_r is the reduced pressure and M_R is the molecular weight.

$$\alpha_{boil} = \frac{55p_\mathrm{r}^{0.12}\dot{q}^{0.67}}{[-\log(p_\mathrm{r})]^{0.55}M_R^{0.5}} \tag{2.63}$$

Finally, the suppression factor S is calculated using equation (2.64).

$$S = \left\{1 + 1.15 \times 10^{-6}\epsilon^2\left[\mathrm{Re}_a\left(1 - x_g\right)\right]^{1.17}\right\}^{-1} \tag{2.64}$$

Note that results of all these heat transfer correlations are compared in later chapters once valid results have been obtained to compare them. It turns out in chapter 4, for example, that the description of boiling heat transfer from Alane (2007) here is difficult to assess due to difficulty in identifying the values of vapour mass quality and boiling number, because the cross section of flow in the vessel is difficult to define.

2.4 Modelling Flow in STRs

The flow of fluids in the vessel occurs primarily due to forced convection by the stirrer and partially due to free convection on the outer surface in contact with the wall with the

jacket fluid behind. The vessel used in the experiments conducted for this thesis is unbaffled and thus have a free surface vortex as well as an internal flow pattern that would require CFD modelling to thoroughly investigate.

2.4.1 Vortex Formation

The vessel used in the studies of this thesis was unbaffled, that is, there was nothing intruding into the vessel contents intended to suppress the formation of a vortex. In the experiments, therefore, a significant vortex was present in the reactor.

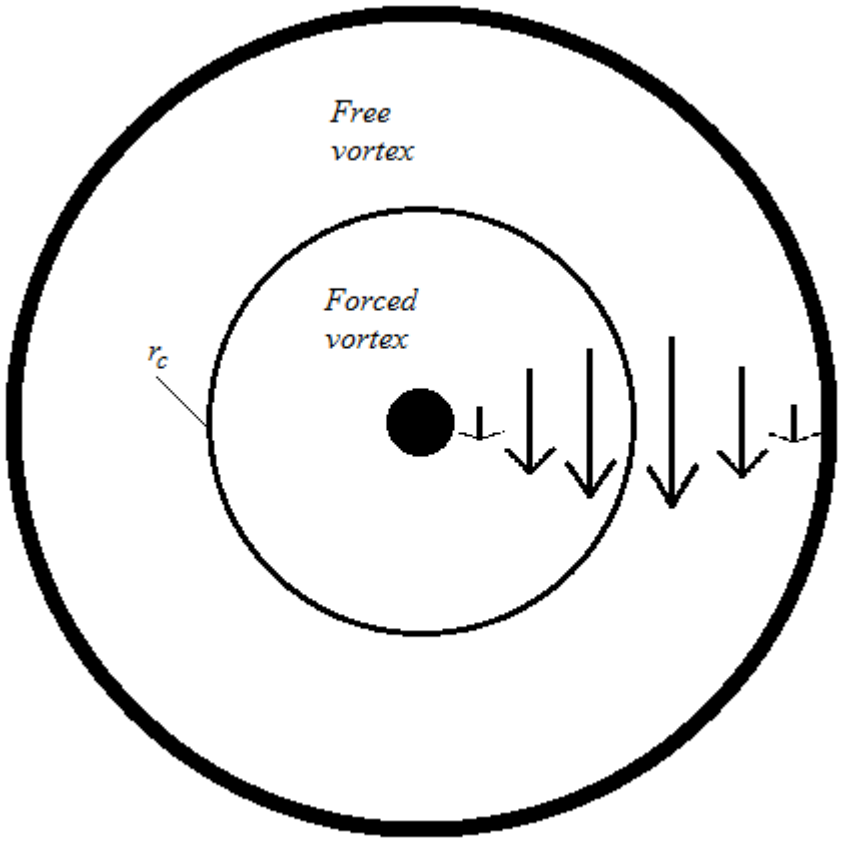

Figure 2.10 – Free and forced vortices, view from above. The arrows denote the relative tangential velocities. The greatest velocity is at the critical radius, r_c.

Brennan (1976) studied vortex models by Nagata *et al*. (1955), Braginskii (1967), and Zlokarnik (1971). These were models in which the flow was separated into an inner forced vortex, which is like a rotating cylinder of liquid, and an outer free vortex. These parts of the vortex are displayed, as seen from above, in figure 2.10. The tangential velocity of a forced vortex increases linearly with increasing radius, and that of a free vortex increases proportionally to the inverse of the radius (slowing down with increasing radius). Brennan found that Nagata's model and Zlokarnik's correlations did not take account of the factors of blade width, liquid depth or impeller diameter satisfactorily, and required further

modification before it could be reliably used. In addition, some parameters had to be empirically found for the geometries initially, such as the critical radius r_c, which is the radius where the transition occurs between the forced vortex and the free vortex. Also, Braginskii's approach required more data on the power output of the impeller.

Brennan (1976) also made further empirical correlations to account for blade width and liquid depth, as well as a means to estimate the critical radius r_c, which was found to be "independent of impeller diameter and blade width". Also, probes and immersed coils had an effect similar to baffles – they "were observed to suppress the vortex". Brennan also found that the impeller depth "had negligible effect" on the vortex geometry, as long as the impeller was fully submerged below the liquid surface. However, this is likely to only be true in cases where the maximum impeller depth is limited by the practical shape of the reactor (that is, if the reactor body was shaped like a long tube with a single impeller at the very bottom, the vortex it creates may not significantly affect the surface).

Vortex depth (h_V) is defined as the distance between the initial liquid height (h_0) and the minimum liquid height (h_{min}) which is at the bottom of the free vortex (at the centre of the vortex, ignoring the impeller shaft), as displayed in figure 2.11.

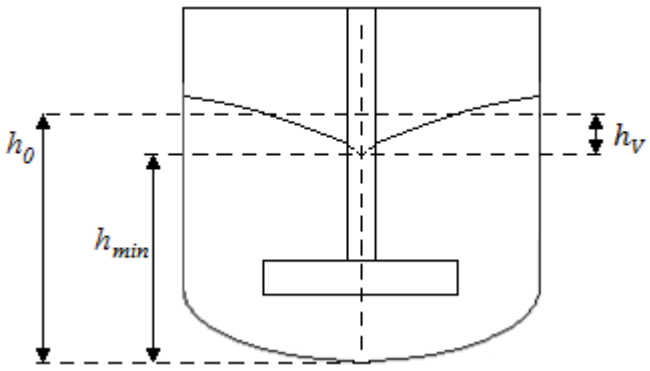

Figure 2.11 – A diagram to illustrate vortex depth, h_V.

Correlations for predicting the vortex depth for various impeller types have been reported by Rieger *et al*. (1979), but the vortex profile as it varies with radius was not described in this paper. Equation (2.65), from Rieger *et al*. (1979), is the most relevant correlation to the work carried out in this thesis, derived from an experimental investigation to provide the vortex depth for a pitched three-blade turbine, for a Galileo number (Ga) between 10^8 and 10^{10}, using an empirically derived constant (B_1) of 0.71 ± 0.03 under these conditions.

$$\frac{h_V}{d} = B_1 \mathrm{Ga}^{0.069} \left(\frac{D}{d}\right)^{-0.38} \mathrm{Fr}^{1.14\mathrm{Ga}^{-0.008}(D/d)^{-0.008}} \tag{2.65}$$

where *D* and *d* are the tank and impeller diameter, respectively, and Fr is the Froude number.

Rieger *et al*. (1979) also produced a formula for the critical vortex depth (h_{Vc}), displayed in equation (2.66), where h_{imp} is the height of the base of the impeller from the bottom of the tank and b is the blade width.

$$\frac{h_{Vc}}{d} = \frac{D}{d} - \frac{h_{imp}}{d} - \frac{b}{d} \tag{2.66}$$

Markopoulos and Kontogeorgaki (1995) discussed the earlier literature, noting that the vortex depth "mainly depends on the impeller type and impeller speed". Some correlations for "vortex depth", from other literature sources (such as Rieger *et al*., 1979) were presented in a table for different agitator types. Several turbines were included (pitched turbines, disc turbines, a propeller, an anchor and a grid agitator) for different ranges of conditions. According to their study, the "vortex factor" (the ratio of the vortex depth to the impeller diameter) became independent of the Reynolds number, when the Reynolds number was more than 10^4. The "vortex depth" parameter is used for the bottom of the forced vortex, neglecting the shaft (that is, it is treated as if the shaft was infinitely thin). Additionally, the formulae for forced and free vortices were separate.

Ciofalo *et al*. (1996) presented a vortex geometry correlation that connects the free and forced vortices (at the critical radius) that was presented in a book by Nagata (1975) and corrected by Smit and Düring (1991). In this correlation, some dimensionless numbers are first defined:-

$$\xi = r/(d/2) \tag{2.67}$$

$$h_l^* = h_l/d \tag{2.68}$$

$$H_l^* = H_l/d \tag{2.69}$$

where r is the radial distance from the central axis of the tank, h_l is the liquid height from the base of the reactor and H_l is the initial liquid height from the base. This assumes a flat-bottomed vessel, which is not the case in this thesis (the reactor investigated in this thesis uses a torispherical base).

The dimensionless liquid height is then defined for below the critical dimensionless radial distance ξ_c (forced vortex) and above it (free vortex), as follows, where:-

$$\text{when} \quad \xi < \xi_c, \qquad h_l^* = (H_l^* - h_1^*) + \left(\frac{\pi^2}{2}\right)\mathrm{Fr}\xi^2 \tag{2.70}$$

$$\text{when} \quad \xi > \xi_c, \qquad h_l^* = (H_l^* + h_2^*) + \left(\frac{\pi^2}{2}\right)\mathrm{Fr}\xi_c^4\left[\frac{1}{\xi_T^2} - \frac{1}{\xi^2}\right] \tag{2.71}$$

where ξ_T is the dimensionless radial distance at the tank wall and:-

$$h_1^* = \pi^2\mathrm{Fr}\left[\xi_c^2 - \frac{\xi_c^4}{\xi_T^2}\left(\frac{3}{4} - \ln\frac{\xi_c}{\xi_T}\right)\right] \tag{2.72}$$

$$h_2^* = \pi^2\mathrm{Fr}\frac{\xi_c^4}{\xi_T^2}\left[\frac{1}{4}\ln\frac{\xi_c}{\xi_T}\right] \tag{2.73}$$

The formula for the dimensionless critical radius ξ_c, reported in Nagata (1975) and experimentally investigated by Yamamoto (referred to in Nagata, 1975) is based on paddle impellers rather than pitched blade impellers and is as follows:-

$$\xi_c = 1.23\left(0.57 + 0.35\frac{d}{D}\right)\left(\frac{b}{D}\right)^{0.036} \times N_{bl}^{0.116}\frac{\mathrm{Re}}{1000 + 1.43\mathrm{Re}} \tag{2.74}$$

where N_{bl} is the number of blades and b is the blade width.

2.4.2 CFD Modelling of Flow

Zwart *et al*. (2003) presented a method for resolving interface volume fractions in CFD models of free-surface flows, “based on a compressive advection scheme for the fluid volume fractions”. This paper analysed 2D flow of water over a bump, with air above. This is also a standard tutorial that can set up in ANSYS CFX. The “interface compression level” in ANSYS CFX is based on this scheme, with maximum interface compression being the default value in the models used. In this scheme, conservation of mass and momentum for both phases in each computational cell in the grid are related by a volume fraction term and the average values are used in the cell. In Zwart *et al.*'s (2003) paper, discrete conservation equations for phasic continuity and velocity are presented as evolutionary equations. Mass flows are discretized in such a way “to avoid pressure-velocity decoupling”, based on the interpolation scheme by Rhie and Chow (1983). “Finite element shape functions are used to evaluate the gradients for pressure and viscous forces” (Zwart *et al.*, 2003). A discrete equation for pressure is also derived. However, in the steady state CFD simulation of the process side of the vessel, conducted in this thesis, the surface geometry was still difficult to define.

Li *et al*., (2004) conducted an investigation of CFD in a vessel stirred with a retreat curve impeller. They found that the results are similar to the use of a Rushton turbine. Also, the Shear Stress Transport (SST) model worked very well to produce results similar to experimental observations using Laser Doppler Anemometry (LDA). The SST model is a mixture of the best qualities of the *k*-ω and *k*-ε models, where the *k*-ε model is used away from the wall and the *k*-ω model is used near the wall. These models are described in detail in chapter 5.

In the paper by Li *et al*. (2004), it was found that the random component of turbulent kinetic energy in the region between the impeller and the vessel wall could not be experimentally resolved sufficiently, because of high velocities in that region driving the tracer particles out, so that a comparison with the CFD results was not possible in this region. In any case, as the paper explains, the SST model severely underestimates the magnitude of the turbulent kinetic energy, because it incorrectly assumes "locally isotropic turbulence". In this case, the use of a six-equation Reynolds Stress model may be more useful.

Javed *et al.* (2006) carried out CFD simulations using the standard *k*–ε turbulence model to predict the flow patterns in the baffled reactor of Distelhoff *et al.* (1997). This gave "reasonably good predictions of the mean axial and radial velocities in the tank, including in the impeller stream" (Javed *et al.*, 2006). Predicted mixing times for a tracer were similar in the simulation and the experiment. However, Javed *et al*. concluded that the *k* values measured in Distelhoff's experiments were significantly higher than in the CFD prediction. Also, due to a lack of experimental data, the accuracy of the simulation above the impeller was limited.

Haque *et al*. (2006) numerically simulated flow and vortex shape in unbaffled vessels with a paddle impeller and Rushton turbine and compared the results to previously published experimental data. They used a volume of fluid (VOF) method and a homogeneous multi-phase flow model to work out the geometry of the gas-liquid interface and compute turbulent flow fields. A Reynolds stress turbulence (RST) model was used, as well as an SST model. While the RST model displayed more prominent eddies caused by the jet-like radial flow from the paddle impeller, it was not clear which was the better predictor overall. The paper discussed the comparison of free-vortex shape, stating that the SST model was closer to the experimental data in the inner region of the vortex and the RST model was closer in the outer region.

Smirnov and Menter (2008) later introduced a curvature correction term for the SST model, based on Spalart and Shaw (1997). Compared to the normal SST model, this provided results much closer to experiments, comparable to the RST model (Smirnov and Menter, 2009).

Mahmud *et al.* (2009) carried out their own experiments to determine the flow and vortex characteristics in an unbaffled vessel with a magnetic stirrer. They used laser Doppler velocimetry to measure the flow field at varying stirrer speeds. They then modelled their experiment with SST and RST models. Again, they found that the SST and RST models were similar, and also that there was reasonably good quantitative agreement between the models and the experimental results.

All the investigations so far described were conducted to compare the vortex geometry using Rushton turbines or paddle impellers and flat-bottomed reactors, so more experimental work is required to investigate more detailed profiles using different impeller types and differently shaped vessels (for example torispherical base and hemispherical base).

Chandra and Singh (2015) investigated Newtonian fluid flow and heat transfer in a flat-bottomed unbaffled vessel equipped with a pitched blade turbine with 6-blades at 45 degrees. The results were compared to an experimental study of this setup in Armenante *et al*. (1997). Chandra and Singh used a tetrahedral mesh and the chosen model was the standard k-ε model with standard wall functions, with a second-order upwind discretisation scheme and semi-implicit method for pressure linked equations (SIMPLE). Good agreement was found with the experimental results. A suggestion for more thorough investigation would be to use other models such as SST and Reynolds Stress models to compare with the k-ε model.

2.5 Modelling Heat Transfer in STRs

2.5.1 Experimental Investigations and Analysis

Heat transfer in stirred tank reactors has been investigated empirically and by mathematical modelling. Calorimetry has been used to obtain experimental data in investigations of heat production with exothermic reactions. Landau (1996) describes this process in detail. Reactors used for calorimetry typically range from 0.1 L to 10 L in capacity, and many have sophisticated temperature control, for example a design consisting of two reservoirs – one hot and one cold – to allow the jacket temperature to

change rapidly in response to a sudden change in process temperature. In an exothermic reaction, the onset of heat production causes the jacket to respond by rapid cooling to attempt to keep the process at the same temperature. The heat balance of the jacket can then be used to assess the heat produced by the reaction. Reaction kinetics can subsequently be derived once the behaviour of the vessel contents is studied in detail.

Snee *et al*. (1993) conducted a study of the reaction between secondary butyl alcohol and propionic anhydride, and the effects of using sulphuric acid (H_2SO_4) as a catalyst to increase the rate of heat production. Over a range of compositions and temperatures, the generation of heat was measured using differential scanning calorimetry (DSC) and adiabatic calorimetry. Also, the reaction's isothermal kinetics were investigated. These were measured using spectrophotometry and compared to similar data which used isothermal reaction calorimetry. Key assumptions used for the kinetics were that the dependences of heat production on temperature and concentration are separable, and that the temperature dependence follows the Arrhenius equation. The separability of temperature and concentration dependence was supported by the experiments at different temperatures resulting in the same observed mechanism. The results agreed that addition of H_2SO_4 as a catalyst caused larger exotherms overall. Without the catalyst, the initial rate of conversion only decreased with time. In the presence of H_2SO_4, the conversion rate started off lower, but increased with time, until the conversion approached unity and thus forced the rate to decrease. The DSC data were much less reliable than the adiabatic calorimetry, despite corrections made for the thermal lag and heating of the equipment. Also, some corrections to the kinetics were able to be made by Saw (2003).

Investigating a last-resort safety measure, Gustin *et al*. (1993) reported on vent sizing for the runaway reaction between phenol and formaldehyde. This reaction has been used in the chemical industry to produce formo-phenolic resins used in building wooden houses, and there have been a number of occasions in which the reaction has gone out of control and destroyed the entire plant. The reaction was investigated using differential thermal analysis (DTA) and isothermal calorimetry. When a catalyst was introduced, the heat rate suddenly rose “to a value determined by an Arrhenius relationship” (Gustin *et al*., 1993) and then increased with temperature. It was suggested that the sudden increase in heat production may be surprising to operators of plants in which this situation occurs. The results of this paper found a discrepancy between the experiments in the Dewar flask and in the vent-sizing package (VSP) experiments, explained in the discussion as “a wrong value of the adiabaticity coefficient” in the Dewar flask experiments.

A method of monitoring chemical reaction exotherms in pilot-scale batch reactors was described by Steele *et al*. (1993). The methodology used a bench scale experiment with a reaction involving dimsyl sodium production and ester coupling. The concept of overall heat transfer coefficient was used, but it was partially variable on the inside film of the reactor, depending on agitation speed, the geometry of the agitator and vessel, and the reaction fluid's density, thermal conductivity, specific heat capacity and viscosity. The calorimetry for both bench scale and pilot-scale experiment found a high degree of correlation.

Grau *et al*. (2000) modelled the thermal response to an exothermic reaction between thiosulphate and hydrogen peroxide in a batch and a semibatch reactor. Separate experiments were conducted in which the operating conditions of thiosulphate addition rate, initial temperature and initial concentration of reactants were varied. When a time delay was introduced into the model, the experimental results were closely matched by the model of the concentration profile. No cooling was present, as the results for temperature against time display a typical uncontrolled response in which the temperature increases to a maximum level and remains there (with a slight decrease due to natural heat loss).

Saw (2003) obtained data on an exothermic esterification reaction using calorimetric methods. The experimental results presented in Saw's thesis revealed the importance of correct sensor positioning and efficient mixing, in order to obtain accurate temperature measurements and therefore accurate calorimetry. The “limitations of the peripheral instruments have to be fully understood” (Saw, 2003). The control system and algorithms used must also be fully understood, as well as the uncertainties in measurements and control. Failure to take all these factors into account could lead to the possibility of an unexpected runaway reaction occurring.

Westerterp and Molga (2006) describe the systems in place to prevent runaway reactions in STRs. Correctly choosing the conditions of operation is the first priority. The equipment's cooling capacity, the temperature of the heat transfer medium, the rates and times of addition of the reactants, and the rates of agitation are all important factors. The second priority is to guard against improper operation, for example by selecting strict operating procedures and by using alarms and/or warning lights to indicate when the conditions are escaping the required safe limits. There are many possible causes of improper operation that can cause temperature to increase beyond the critical point where

runaway begins (Nolan and Barton, 1987). The cooling system can be hindered by power cuts or fouling, for example. Human error in operation or incorrect charging can contribute to accidents. Compared to laboratory scales, unexpected reaction mechanisms, for example autocatalysis, can be much more significant on an industrial scale. Finally, if all else fails, pressure relief and/or chemical containment systems can be installed to mitigate the damage that would otherwise happen if a runaway reaction proves to be inevitable. According to Nolan (1993), the incidence of runaway reactions occurring in industry increased towards the end of the 20th century, which prompted research on monitoring runaway reactions and attempts to model their behaviour.

2.5.2 CFD Modelling of Heat Transfer

Milewska and Molga (2007) used CFD to simulate the consequences of stirrer failures in a batch STR, "in which a strongly exothermic homogeneous reaction takes place in the liquid phase". At conditions usually considered safe when mixing, it was found that a serious runaway reaction could occur following failure of agitation.

Further to this work, Milewska and Molga (2010) formed models using both a perfectly mixed assumption and a CFD approach. The simulations used a simple second order reaction between two reactants with realistic kinetic parameters, where the rate of consumption of each reactant is directly proportional to the concentration (first order with respect to each reactant). The heat balance included effects due to reaction, jacket, accumulation in the vessel, loss through the head (ullage) region, as well as heat effects due to dilution and dosing. The models were all solved numerically. It was found that the perfectly mixed models could be very useful and pragmatic in situations where the mixing time is significantly greater than the reaction time, but the more time-consuming CFD models would have to be used if the reaction was fast enough that the agitator could not spread out the heat before it could cause significant temperature fluctuations.

Also in Milewska and Molga (2010), a model based safety analysis was also conducted for the second order reaction. Interestingly, damage to the cooling system causing a disturbance as little as a 2°C temperature rise was enough to cause a much more significant spike in the process temperature. For a reaction starting at room temperature and with a set jacket temperature of 28°C, the peak temperature in the reactor was about 45°C, but if the jacket temperature was set to 30°C at an early stage, the peak temperature in the reactor was 80°C. In another simulation, in which the coolant pump was stopped, the temperature increased exponentially from about 30°C to 60°C in about 10 minutes, and then suddenly jumped to a peak temperature of 140°C within seconds, before slowly

cooling naturally. In this case, the jacket temperature was controlled by the process temperature, which, in turn, was uncontrolled (except by the amount of reactant present at the start of the simulation). When damage to the stirring system was simulated, for example the stirrer slowing or stopping, perfect mixing could not be assumed, so the CFD models had to be used.

Rudniak *et al*. (2011) investigated further into CFD simulations of runaway reactions, finding that CFD could be a very robust and efficient method to provide an early warning. The spatial and temporal distributions of velocity, temperature and concentration were found, which were crucial for finding the important areas for temperature sensors to be located.

2.5.3 Condensation on the Outside Surfaces

During a cooling operation, a condensation film may form on the outside surface of reactors when the outside wall temperature of the jacket is low enough and the humidity of the surroundings is sufficiently high. This results in heat gains by the jacket, which reduces its cooling capacity.

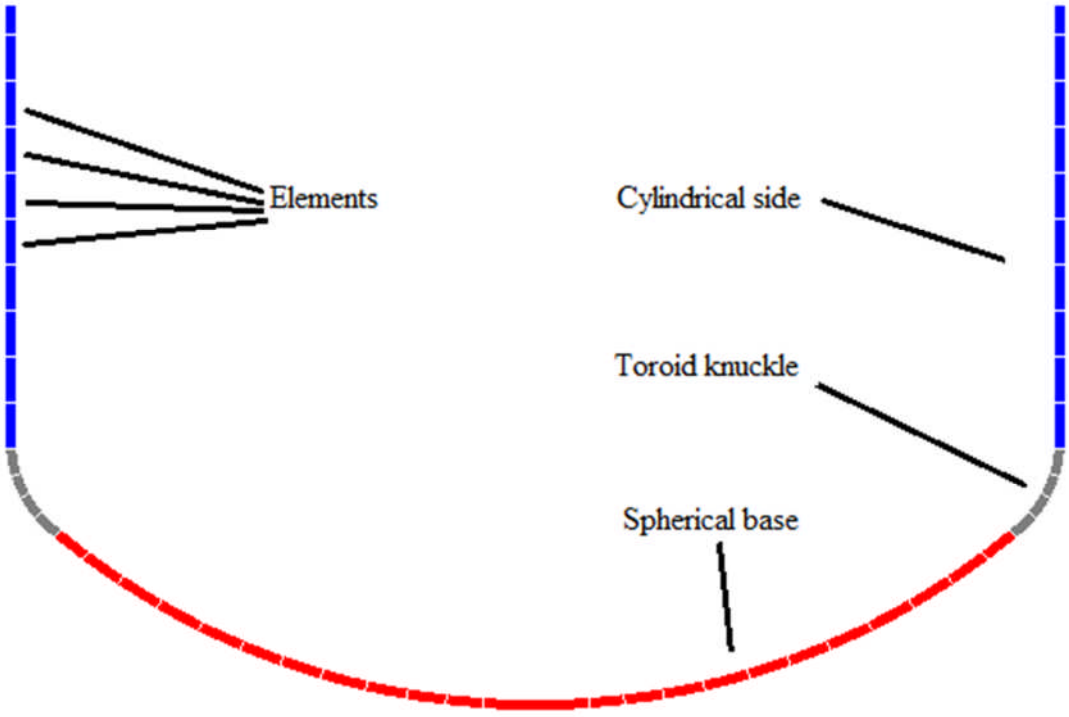

Figure 2.12– Sections of a torispherical reactor, divided into elements.

Perry and Geddes (2011) developed a localised condensation model to simulate heat transfer in a condensate film in kettle evaporators. Their model considered the side and

bottom surfaces of a torispherical vessel. This is a standard shape of many reactors of various sizes, including the ones used in the experimental investigation in this PhD thesis. The model notably accounted for the increase in average thickness of the condensate film towards the bottom of the reactor.

The model by Perry and Geddes (2011) provided equations for heat transfer coefficients on the 3 surface geometries – the spherical base, the toroid knuckle, and the cylindrical side. These surfaces were divided into elements along the length of the reactor, as displayed in figure 2.12. Rather than using mean heat transfer coefficients, separate coefficients are found for the different elements. This model did not take into account heat exchange with the surroundings or conduction between surface elements.

2.5.4 Lumped parameter and distributed parameter models

There are two types of lumped parameter ("simple") numerical models. The first take into account the thermal inertia of only the process contents, and the second also include the thermal inertia of the vessel itself, producing more realistic results. Lumped parameter models have been developed on MATLAB by Ali (2009) and Bentham (2011). Transient conduction in the walls of the vessel is also included in distributed parameter models. A distributed parameter model was developed to also include the effect of the glass lining of the vessel wall. Numerical solutions of the distributed parameter model yielded results that initially had a slower response, then rose to values between the results of the two types of lumped parameter models. This distributed parameter model used the assumption of isothermal operation (in this case, meaning a constant jacket temperature or infinite flow of the heat transfer medium). The experimental results in this case (example displayed in figure 2.13) had a delay in process temperature of a few hundred seconds before the temperature profile started to rise significantly. The isothermal distributed parameter model here had a much less significant delay, presumably because the temperature is assumed not to change across the jacket height. If this height profile was taken into account, the vessel wall would need to be heated transiently, and this might cause a longer delay, similar to the experimental ("observed") result depicted in figure 2.13. The "analytical" results simply used the UA values and simulated an exponential temperature curve with time (without thermal inertia).

Further testing has been done on the lumped parameter and distributed parameter models on MATLAB (Kairzhanova, 2010). When the thermal inertia of the vessel was taken into account, the results more closely matched the experimental data, which in this case were obtained by Saw (2003). Some inaccuracies were introduced when the assumption was

used that heat transfer only occurred in the cylindrical part of the vessel, and not the base. Kairzhanova (2010) also described some methods to determine the overall heat transfer coefficient when the jacket mass rate is unknown. A further assumption made in this literature was that the jacket inlet temperature was constant – however, the most likely case in industry is for this temperature to be regulated by another heat exchanger, with the jacket medium playing the role of a run-around coil. As run-around coils often have extensive pipework, the thermal response to control in the jacket would therefore be quite slow and the inlet temperature would also be a dependent variable.

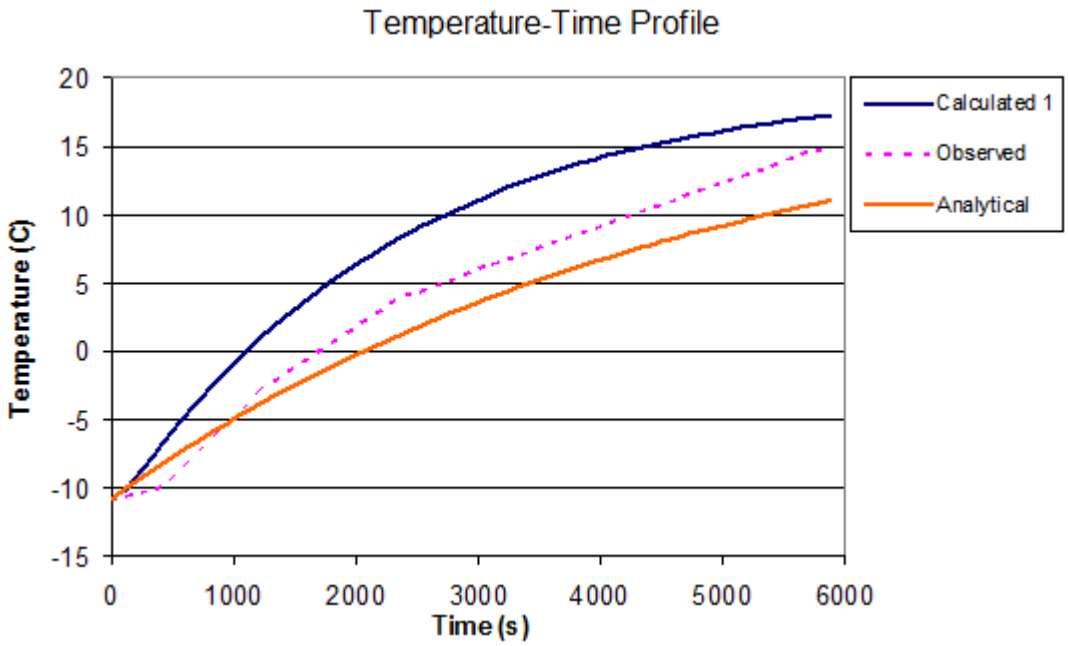

Figure 2.13 – Isothermal distributed parameter model ("calculated 1") results for heating methanol using water in a glass-lined jacketed vessel.

Bentham (2011) produced a numerical solution of the lumped parameter model under isothermal conditions, also including a simple first order exothermic reaction, and changed factors such as the pre-exponential factor, activation energy, heat of reaction and overall heat transfer coefficient. It was found that the cases with a higher heat of reaction in this case were also directly more likely to cause runaway situations, although this was easily anticipated from knowledge of simple reaction kinetics. The lumped parameter model in this case used constant jacket inlet temperatures.

In work by Bentham (2011) it was found that increasing the heat capacity rate of the heat transfer medium $\left(\dot{M}c_P\right)_m$, by increasing either $\dot{M}_m$ or $(c_P)_m$, cannot increase the cooling rate indefinitely. The controlling resistance, especially at larger industrial scales, is the resistance of the wall, and the only way for more heat to be exchanged across the solid wall (since convection is ruled out) is by increasing the temperature difference. In the

case of cooling the contents to prevent a runaway reaction, the only way to increase the cooling duty in the jacket is therefore to reduce the jacket inlet temperature.

Bentham (2011) previously developed the distributed parameter model to be non-isothermal by including changes in the jacket heat transfer medium temperature along the jacket height, and to include an independent algorithm to simulate changes in the jacket inlet temperature. In this model, the apparent heat capacity (and resultant time taken to produce a change in temperature) was approximately twice as large as in the lumped parameter model. However, this is because the reactor simulated in the distributed parameter model was based on arbitrarily selected values and not on realistic dimensions – in fact, the simulation used the inner wall diameter as 0.72 metres, and the pure metal wall (iron) thickness was set to 4 centimetres. This is why the heat capacity of the wall was about the same as the process contents themselves. In practical situations, most vessels this size would have a much thinner wall – not just to conserve material while still providing sufficient strength, but also because heat transfer is much more efficient with a thinner wall. In the reactor studied in this thesis, the glass wall is 6 millimetres thick, for example.

2.6 Summary of the Literature Review

Accurate modelling of the operating conditions is important. Mathematical models to simulate the conditions within stirred tank reactors have been developed and are becoming more sophisticated as research progresses. These models range from relatively simple analytical models, lumped parameter and distributed parameter models, to high level CFD models.

CFD modelling inside the vessel is much more prominent than modelling inside the jacket. Some specific models have been developed for isolated sections of the process, such as condensation on the outside surface of the jacket.

However, fully conjugate models incorporating both the distribution of temperature and flow in the jacket and simultaneous modelling of a free surface have not yet been thoroughly investigated and this thesis aims to work towards this goal.

3 EXPERIMENTAL WORK

3.1 Introduction to the Experimental Work

This chapter addresses the experimental data obtained, and details the equipment and its operation. Experimental data are presented.

The original purpose of the experiments was to investigate both heat transfer and batch distillation. The author supervised the experiments, assisted by two MEng project students (N. Fitch and S. Shaw). Fortuitously, much useful data were obtained from all the experiments. All the data taken during these experiments were analysed independently by the author.

Table 3.1 lists the experiments done in this context.

Table 3.1 – General list of experiments done.

Experiment name	Substances used	T_p range / °C	T_m range / °C	Impeller speed / rpm
Temperature Ramping 1	Water (20 L)	20.0 – 45.0	20.0 – 50.0	366
Temperature Ramping 2	Water (20 L)	17.5 – 31.5	17.5 – 32.5	366
Water Batch Distillation	Water (20 L)	20.8 – 100	20.0 – 150.0	366
Methanol Batch Distillation	Methanol (20 L)	21.0 – 64.7	25.0 – 100.0	264

3.2 Equipment Used

3.2.1 Agitated Vessel

The experimental data were obtained from experiments conducted in an unbaffled, pilot-scale, 25 litre agitated vessel. This reactor has at times been requested for use by the pharmaceuticals industry. The vessel is displayed in figure 3.1. It was situated in the Institute of Process Research and Development (iPRD) in the School of Chemistry, University of Leeds. It had a torispherical base. It was heated and cooled using only a plain jacket – single-chambered and with no vanes to guide the flow. The nominal capacity of this vessel was 20 litres (80% full). The main body and ullage region of the vessel were both constructed by QVF, entirely from borosilicate glass with a wall thickness of 6 mm on either side of the jacket. Details of the physical properties of this type of glass are displayed in the appendix, section 10.2.

Figure 3.1 – 25 litre jacketed stirred tank reactor, in iPRD, University of Leeds.

3.2.2 Heating and Cooling System

The controller for the vessel was a heating and cooling device (Huber Unistat 510). This uses a heating and cooling medium called DW-Therm (physical property data of DW-Therm are present in the Appendix, section 10.1). This substance remains in the liquid state under atmospheric pressure at temperatures as high as 200°C and as low as -90°C.

The Huber Unistat 510 had a maximum heating capacity of 6 kW and a maximum cooling capacity of 5.3 kW above 0°C. A table of further data on the unit, such as power requirements, is accessible by the Huber website (Huber, 2014). As it is a commercial product, information such as the control algorithms and heating and cooling mechanisms are difficult to obtain. It is likely that short “on-off” bursts of electrical current are applied through a resistant element every few seconds, producing heat (power supplied is equal to resistance multiplied by the square of the current, or equivalently, the square of the voltage divided by the resistance). When cooling, temperature profiles obtained every 12.5 seconds had fluctuations in the DW-Therm internal temperature.

The cooling system within the Huber unit predominantly used chilled water from the School of Chemistry's chilled water tank. This contained 1% glycol to help reduce its freezing point in rare cases when it is exposed to temperatures near 0°C. The temperature of this chilled water was kept somewhat around 10°C but varied periodically over an approximately 10 minute cycle. Heat from the surroundings would cause the temperature to increase to 12°C then an external cooling system would chill the water to 8°C to restart the cycle. To cool the vessel contents to temperatures near or below 12°C, the Huber would switch to the use of refrigerant. This is to avoid freezing the water.

The Huber can be programmed to ramp temperature or to produce exponential approaching functions. Once programmed, the set point will change gradually as desired. To set a ramping function, one inputs the starting set point, ending set point and time between set points. To set an exponential approaching function, one inputs the starting set point, ending set point and a “time constant”. Describing this “time constant”, the Huber operating manual (Huber, 2010) states: “when selecting an exponential ramp function (E-grade Professional) the end value (more precisely 99% of the end value) will be reached after 5 times the time constant has elapsed”.

The Huber operates in two main modes, named “process mode” and “internal mode”, depending on whether the controlled variable is the process temperature or the Huber internal temperature respectively. These modes are described in more detail in the following paragraphs.

When set to “process mode”, the Huber unit uses a cascade PID control system to attempt to directly control the process temperature to match the current set point temperature. In this mode, there is a set maximum temperature difference setting between the jacket and the process of 50°C. This is to prevent thermal shock. Incidentally, this means that if a runaway reaction occurred in this mode and the temperature difference $|T_p - T_{m1}|$ exceeded 50°C, the controller would attempt to heat up the jacket, furthering complications.

When set to “internal mode”, the Huber unit uses the same cascade PID control system, but instead attempts to control only the temperature of the oil inside the Huber. In this mode, the jacket temperature is able to be manually controlled. In this case, the user is responsible for watching the temperature difference $|T_p - T_{m1}|$ and keeping it below 50°C.

3.2.3 Process Flow Diagrams

Figure 3.2 displays a process flow diagram for the reactor and Huber system. Figure 3.3 displays a process flow diagram for the adjacent condenser and receiver.

The process liquid (water or methanol, depending on experiment) was charged into the five litre charge vessel. Four batches of five litres were transferred into the 25 litre reactor, filling it to the recommended 20 litre capacity. The impeller was pitched-blade type with three blades, each at a blade angle of 45° and a blade length of 72.5 mm.

Any vapour from the process side passed through a reflux condenser cooled with chilled water from the department's chilled water tank (the same supply as for the Huber coolant). An 80mm-diameter graphite “bursting disc” was installed in the vapour uplift stream. This would burst if the gauge pressure in the system rose above 0.4 bars. Any vapour that escaped the top of the condenser passed through a scrubber. The scrubber had clear plastic Raschig rings and a downflow of water.

In figure 3.3, the valve at the bottom of the receiver is open. During the distillation experiments, the condensed liquid was collected from the receiver and into a bottle with a weighing machine below it, from which it was pumped back into the charge hole of the 25 litre reactor, using a peristaltic pump. During boiling at a constant Huber set point temperature, the peristaltic pump was switched off, so that the rate of collection of vapour could be evaluated using the weighed bottle. This part of the process is described in more detail in section 3.3.3.

3.2.4 Data Logging

Most data from the instrumentation were sent to LabView, which automatically recorded the data on a Microsoft Excel spreadsheet. The parameters recorded with LabView are tabulated in table 3.2. These were later converted to SI units for analysis.

Additional variables were recorded manually. These were delayed by the time it took to plug the thermocouple lead into the reader. These are tabulated in table 3.3.

The type of thermocouples used was the “type ‘K’ general purpose probe” (T.M. Electronics, 2004).

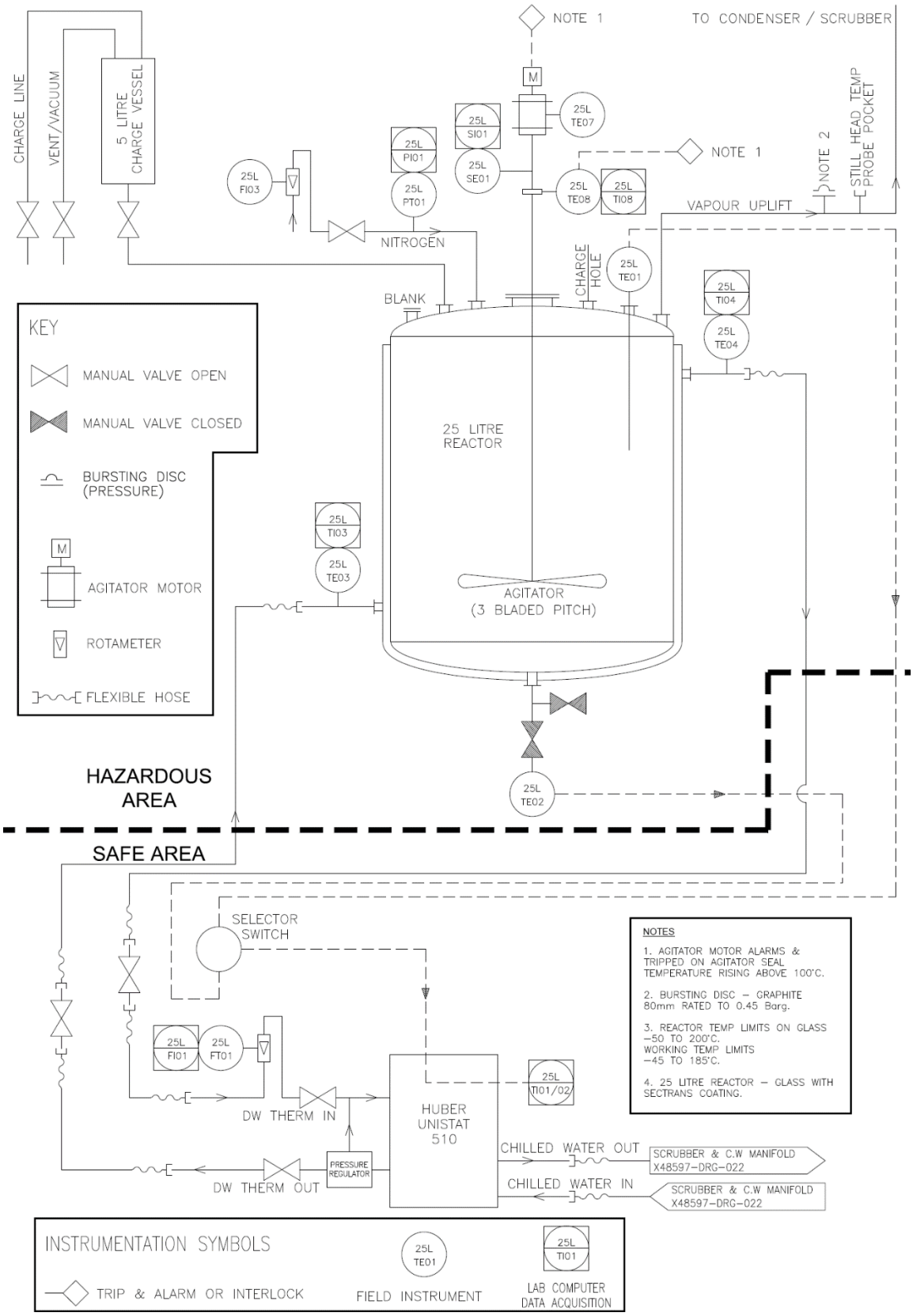

Figure 3.2 – Process flow diagram of the reactor and Huber (adapted from Fenney *et al.*, 2011).

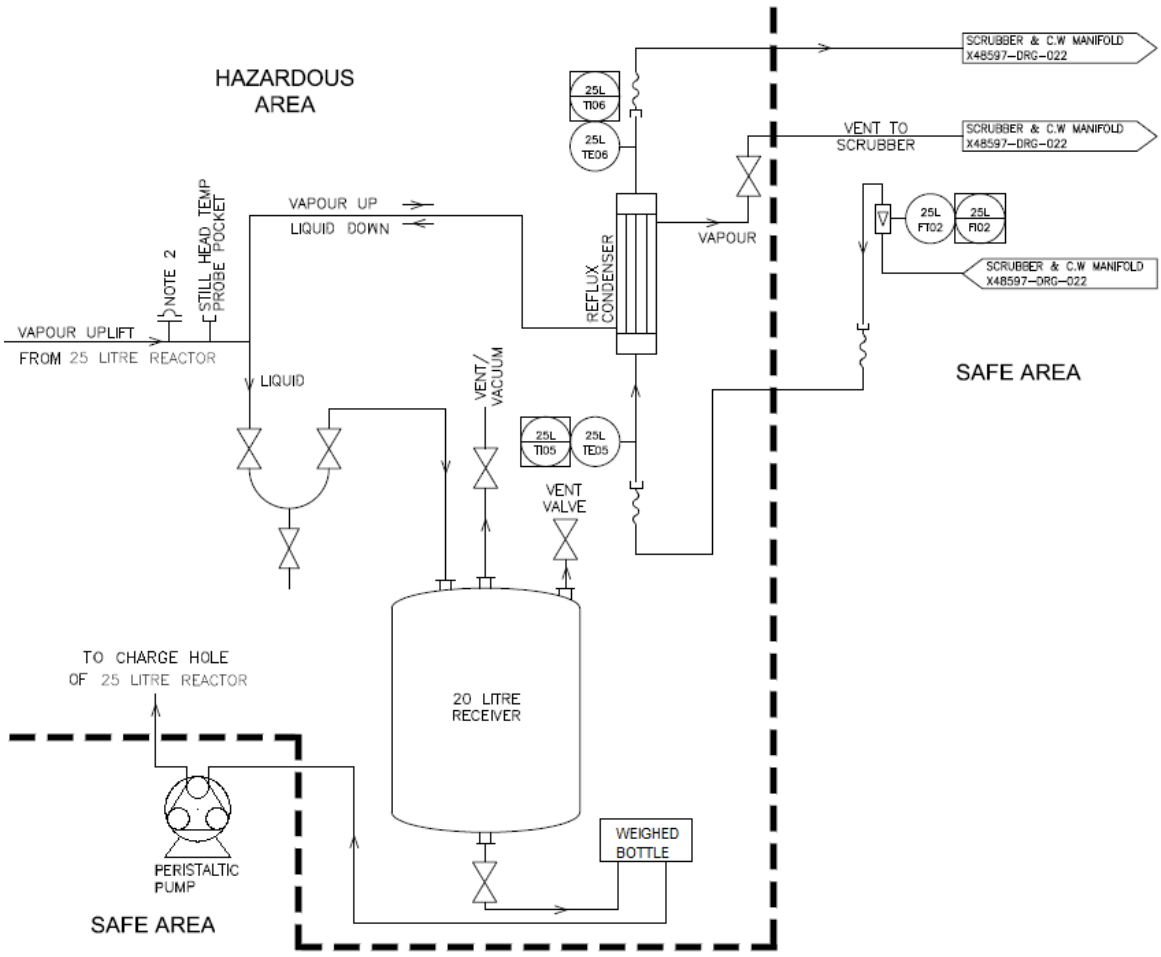

Figure 3.3 – Process flow diagram of the condenser and receiver (adapted from Fenney *et al.*, 2011).

Table 3.2 – Variables recorded with LabView.

Variable recorded with LabView	**Units recorded**
Time	Minutes
Huber Set Point Temperature (T_{set})	°C
Huber Oil Temperature (T_{huber})	°C
Process Temperature (T_p)	°C
Jacket Inlet Temperature (T_{m1})	°C
Jacket Outlet Temperature (T_{m2})	°C
Condenser Inlet Temperature (T_{cond1})	°C
Condenser Outlet Temperature (T_{cond2})	°C
Vessel Pressure	mbar absolute
Huber Oil Flow Rate	Litres per hour
Condenser Flow Rate	m^3 per hour
Impeller Speed	rpm
Impeller Motor Temperature	°C

Table 3.3 – Variables recorded manually.

Variable recorded manually	Units recorded
Ullage wall temperature (outer side) (T_{uo})	°C
Outer Wall Temperature (outer side) (T_{oo})	°C
Vapour Stream Temperature (T_v)	°C
Mass of substance in weighed bottle	kg

3.3 Experimental Investigations

3.3.1 Operation of the Equipment

The experiments were all conducted according to the University's regulations and the regulations of the School of Chemistry. For details on these standard operating procedures, safety precautions and risk assessment, see the Appendix, section 10.7.

Figure 3.4 displays the levels of water in the reactor when the agitator is set to “25 Hz”. The measured rotation frequency in these cases was 366 revolutions per minute, that is, 6.1 revolutions per second. When methanol was used (in the methanol batch distillation experiment), the agitator was instead set to “18 Hz”, which is 264 revolutions per minute (4.4 revolutions per second). Note that the Reynolds numbers are not quoted here because they change significantly with the viscosity and hence with the temperature of the vessel content.

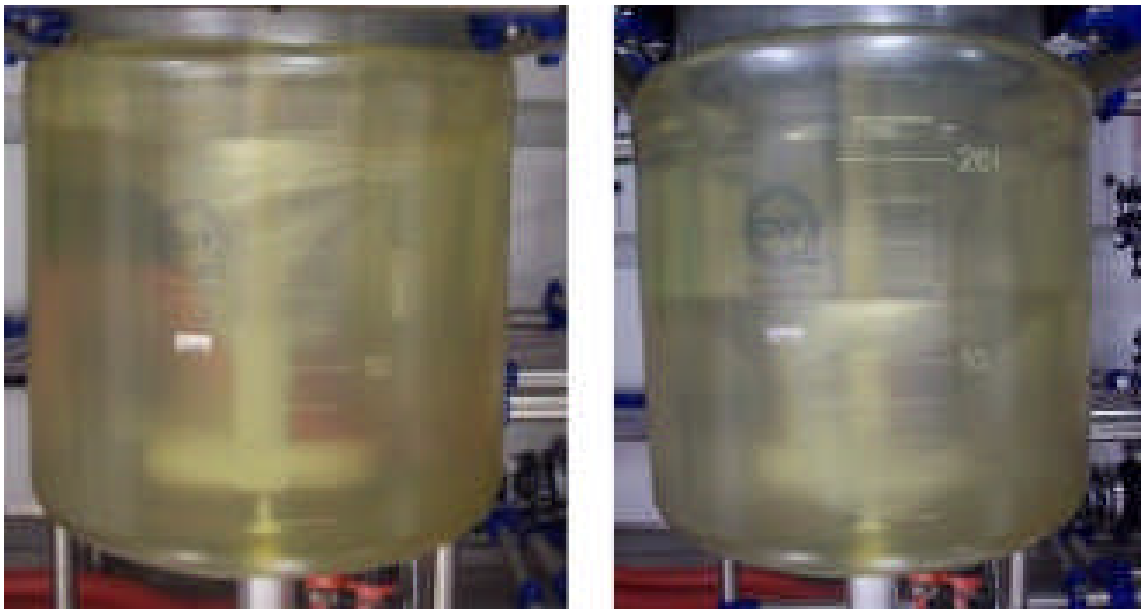

Figure 3.4 – Photographs of the vessel under agitation, with 20 litres (left) and 10 litres (right) of water inside. The vortex can be observed.

In figure 3.4, the image on the left displays the reactor filled with 20 litres of water, and the image on the right displays the reactor filled with 10 litres of water. In the latter image,

significant air entrainment can be observed at this agitation speed (366 rpm). At higher temperatures, particularly in the distillation experiments, the decreased viscosity of the water and methanol also allowed for some air entrainment when 20 litres of liquid were in the vessel.

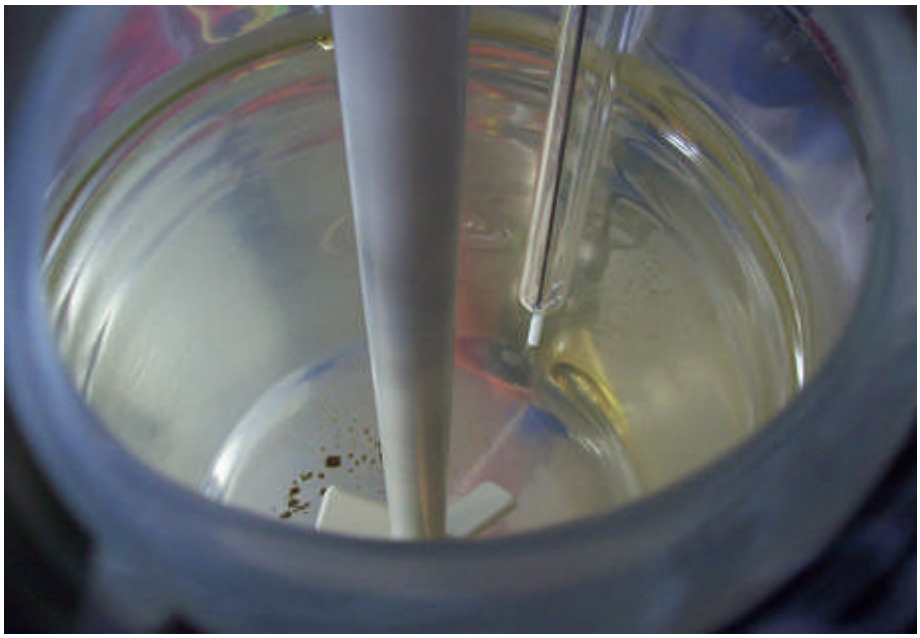

Figure 3.5 – Photograph of the internal content of the vessel when empty.

Figure 3.5 displays a view of the internal content of the vessel, including the thermocouple and the impeller. The thermocouple did not act as a baffle, because a large vortex can be observed during operation in figure 3.4. Some fouling can also be observed inside the vessel. Both the thermocouple and the fouling were ignored in all models in this thesis.

3.3.2 Temperature Ramping Experiments

In both temperature ramping experiments, “internal mode” was used.

The first temperature ramping experiment used 20 litres of water in the 25 litre reactor, and the agitation speed was 6.1 revolutions per second on average (366 rpm). The starting time in the results is at a point where both the process and jacket temperatures were at 20.0°C, and then the Huber was set to a temperature to 50.0°C on “internal mode”, as a square step. Under maximum heating rate, the oil temperature increased sharply, providing a ramped profile. As this oil is then pumped into the jacket, through insulated pipes, this deviates very little from the jacket inlet temperature. After approximately 2.5 hours, when the process temperature had almost become constant, a set point of 20.0°C was re-entered into the Huber, again a square step in which the oil cooled approximating a ramp (although the gradient of this ramp decreases with time until it overshoots the set

point). The contents were allowed to cool for approximately another 2 hours – until the allowed time was over. The results are displayed in figure 3.6. Here, T_{set} is the set point, T_{huber} is the Huber internal temperature, T_p is the process temperature, T_{m1} is the jacket inlet temperature and T_{m2} is the jacket outlet temperature.

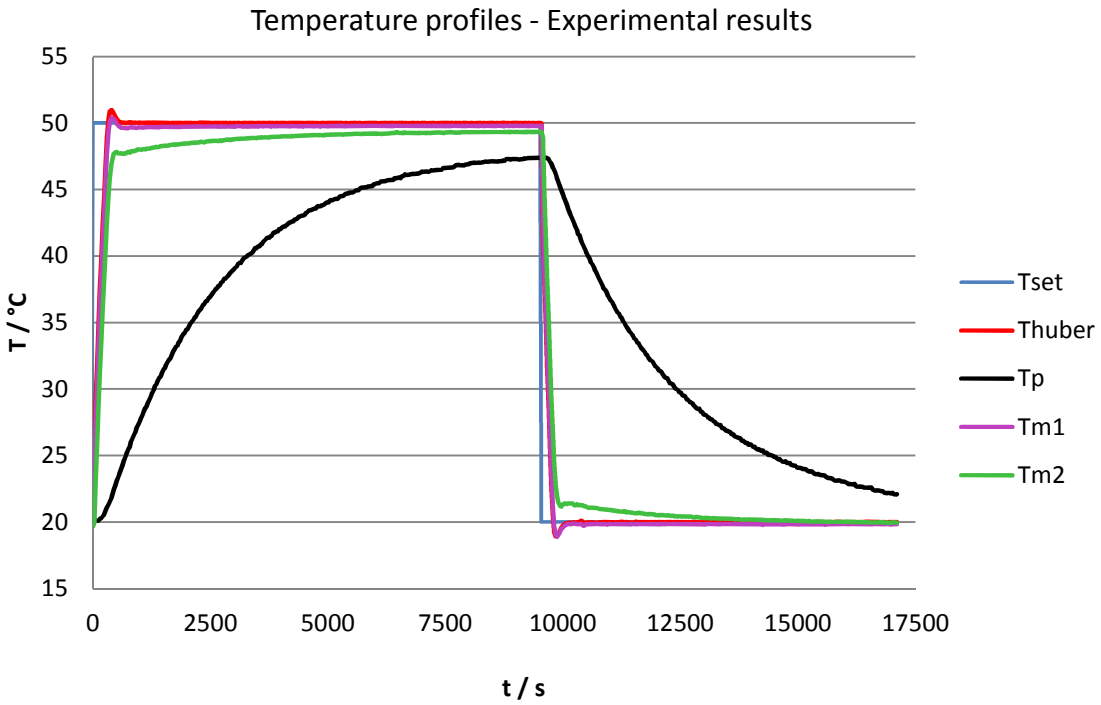

Figure 3.6 – Experimental results of the first temperature ramping experiment.

The second temperature ramping experiment also used 20 litres of water and an average agitation speed of 6.1 revolutions per second (366 rpm). The temperature control, again on "internal mode", was set at the ambient temperature of 17.5°C and then the set point was increased by 0.5°C every 30 seconds until the final set point of 32.5°C. This relatively low temperature was chosen to attempt to allow the process temperature to become almost constant. After approximately 3 hours, the allowed time was nearly over so the set point was reduced by 0.5°C every 30 seconds until it reached 17.5°C. After about 15 minutes, the controller was turned off and the monitoring software was deactivated shortly after. The results are displayed in figure 3.7.

In both the square step (figure 3.6) and programmed ramp (figure 3.7) profiles, the set points were overshot slightly before being corrected by the control system. This is due to the nature of the PID controller.

During the ramping, at the start of each experiment, the gradient of the process temperature only increases slowly, partly due to thermal inertia of the vessel and partly

due to the fact that a temperature ramp is a gradual increase in driving force for heating and cooling.

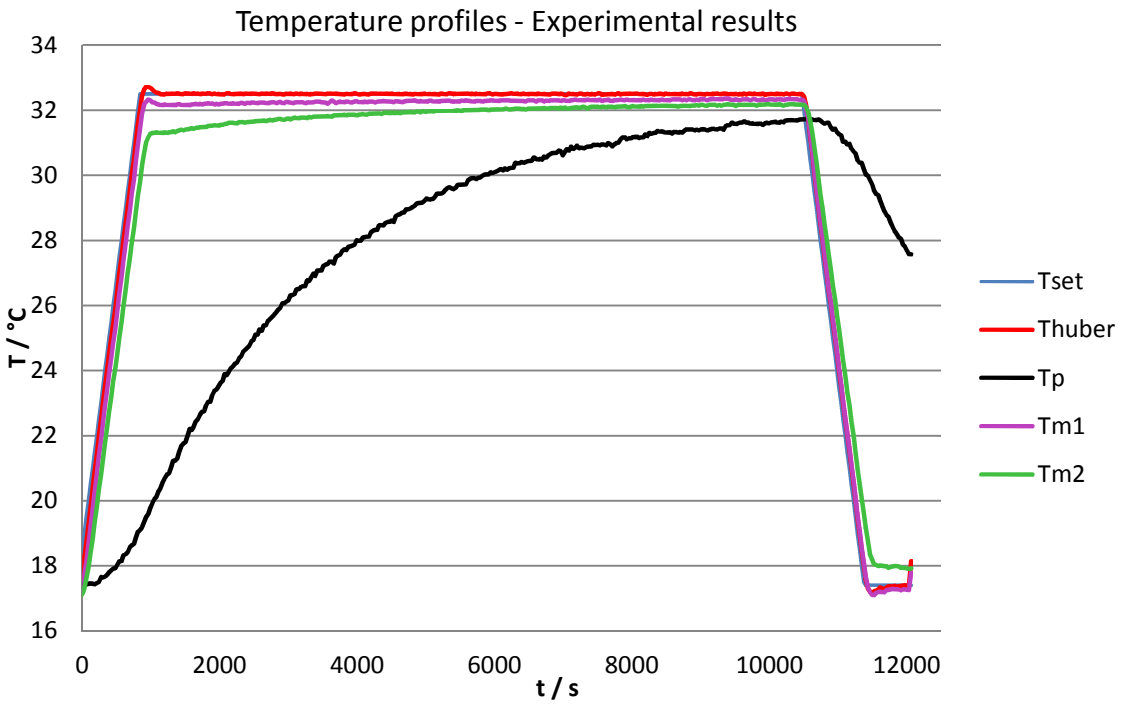

Figure 3.7 – Experimental results of the second temperature ramping experiment.

The process temperature tails off towards a value that does not quite reach the jacket temperature primarily because increased evaporation in the process side is taking heat off, providing a minimum temperature gradient across the internal walls which would persist even after an infinite amount of time. This is proportional to a function of the process temperature, and thus can be observed more readily in the first ramping experiment (where the Huber internal set point was 50°C and the process temperature tailed off at 47.5°C) compared to the second ramping experiment (where the Huber internal set point was 32°C and the process temperature tailed off at 31.7°C).

3.3.3 Batch Distillation Experiments

The distillation experiments used 20 litres of substance in the process side. The water distillation experiment distillation experiments had additional thermocouples (figure 3.8) compared to the ramping experiments – one taped to the outer glass surface, to measure the outer glass temperature, one taped to the top of the reactor, measuring the ullage outer temperature, and one inserted into the vapour stream to measure the vapour temperature before entering the condenser.

The collecting tank for the condensate had its valve opened during the times when the process was boiling, and the distillate was collected in a weighed bottle. A Watson Marlow 323E/D peristaltic pump was used to pump the distillate back into the reactor through a Marprene tube with 0.6 mm diameter. The pump was set to the maximum speed of 400 rpm.

After a set point had been entered, and once the desired jacket temperature had also been reached, the pump was switched off and the amount of distillate collected every two minutes over a ten minute period was recorded with the weighed bottle. The average of these amounts was taken as the rate of condensation of the distillate in the condenser. Separately, readings of condenser inlet and outlet temperature from the condenser were obtained. However, the variations over time in the condenser inlet temperature (coming from the chilled water tank) were about three times higher than the temperature difference between condenser inlet and outlet temperatures, so calculations of heat transfer using these was much more unreliable. A more detailed description of this is in section 3.3.4.

Once the distillate had been put back into the reactor, the jacket temperature was increased to the next step and the distillate was collected again. After the highest jacket temperature step, the jacket temperature was set to process mode and cooled down to 25°C before being turned off.

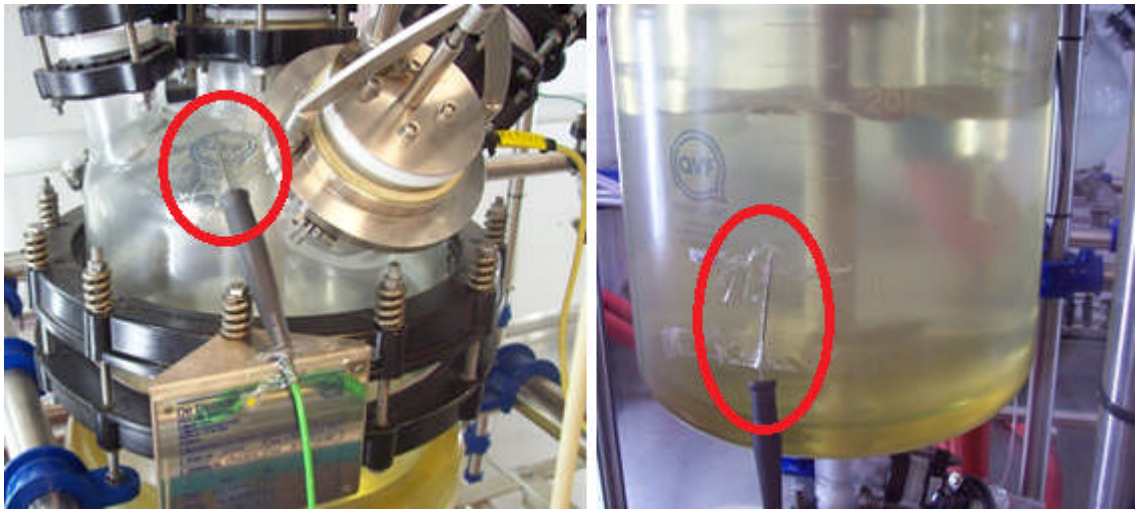

Figure 3.8 – Additional thermocouple positions for the 25 litre vessel during distillation experiments.

The water distillation experiment used an agitation speed set to “25 Hz”, and the measured impeller rotational speed was 6.1 revolutions per second (366 rpm). The methanol distillation experiment used an agitation speed set to “18 Hz”, and the measured impeller rotational speed was 4.4 revolutions per second (264 rpm).

Figure 3.8 displays additional thermocouples used to attempt to retrieve extra data from the ullage and outer walls respectively.

For these experiments, the set points of interest were for when the contents are boiling. The water distillation experiment used set points for the Huber internal temperature as 130°C, 135°C, 140°C, 145°C and 150°C. The methanol distillation experiment used set points for the Huber internal temperature of 80°C, 85°C, 90°C, 95°C and 100°C. In all cases, the jacket inlet temperature was slightly lower than than the Huber internal set temperature due to heat loss in the insulated pipes. This difference did not exceed 0.5°C. For example, at the highest set point of 140°C, with the strongest driving force for heat loss in the pipes, the jacket inlet temperature was 139.5°C. In any simulations, nevertheless, the measured value of jacket inlet temperature was used, rather than the Huber set point.

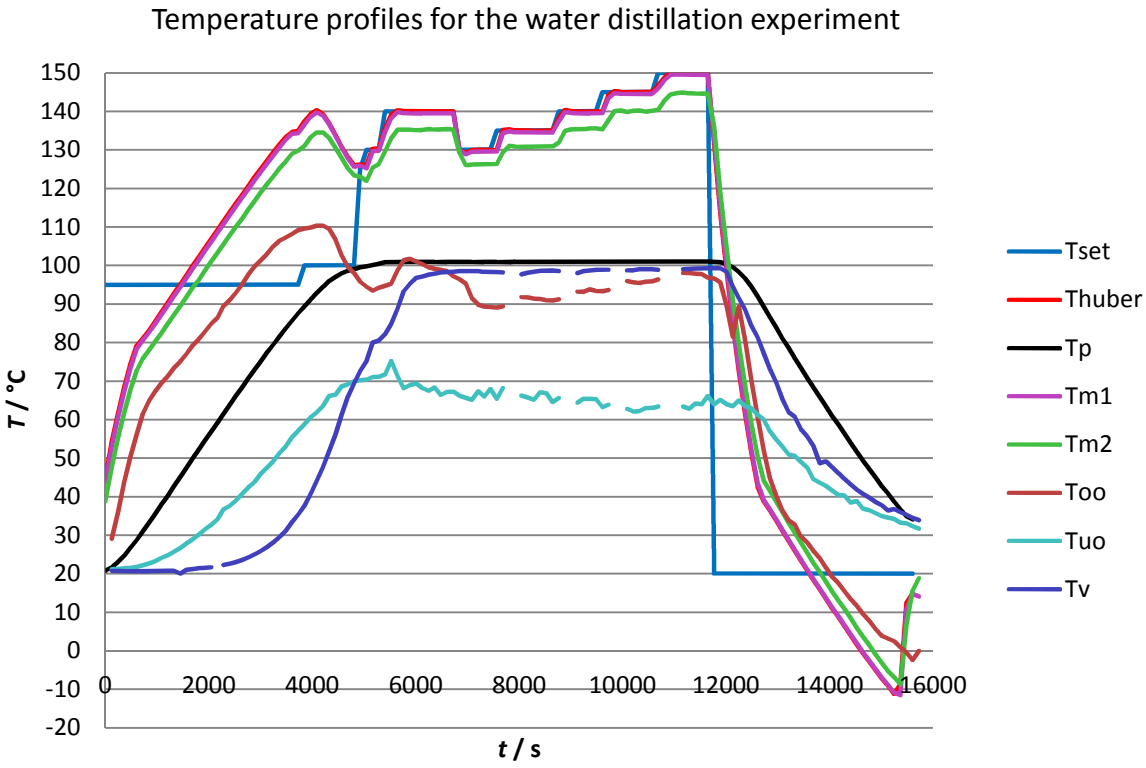

Figure 3.9 – Experimental results for the water distillation experiment. See nomenclature or description in text for the meaning of the symbols.

During heating and cooling, in the water distillation experiment, the system was set to "process mode". During boiling, the system was set to "internal mode" to control the jacket inlet temperature to desired set points. In the methanol distillation experiment, "internal mode" was used throughout the whole experiment.

Figures 3.9 and 3.10 display data plots from the thermocouples attached to the various points inside and outside of the 25 litre reactor during the water distillation experiment (figure 3.9) and the methanol distillation experiment (figure 3.10). Here, T_{oo} is the temperature of the thermocouple taped on the outer vertical side of the vessel (figure 3.8, right image), T_{uo} is the temperature of the thermocouple taped on the outside of the ullage region (figure 3.8, left image), and T_v is the temperature of the vapour stream going to the condenser and collection vessel.

It would be expected that the temperatures of the vapour stream T_v and the ullage region T_{uo} would remain at approximately the same value throughout all the boiling stages despite the increases in jacket temperature, as these are based on the saturation temperature of the process, but the outer wall temperature would increase with each stage as this is based on the jacket fluid temperature. This trend can be seen in figures 3.9 and 3.10, although there are notable deviations as discussed below.

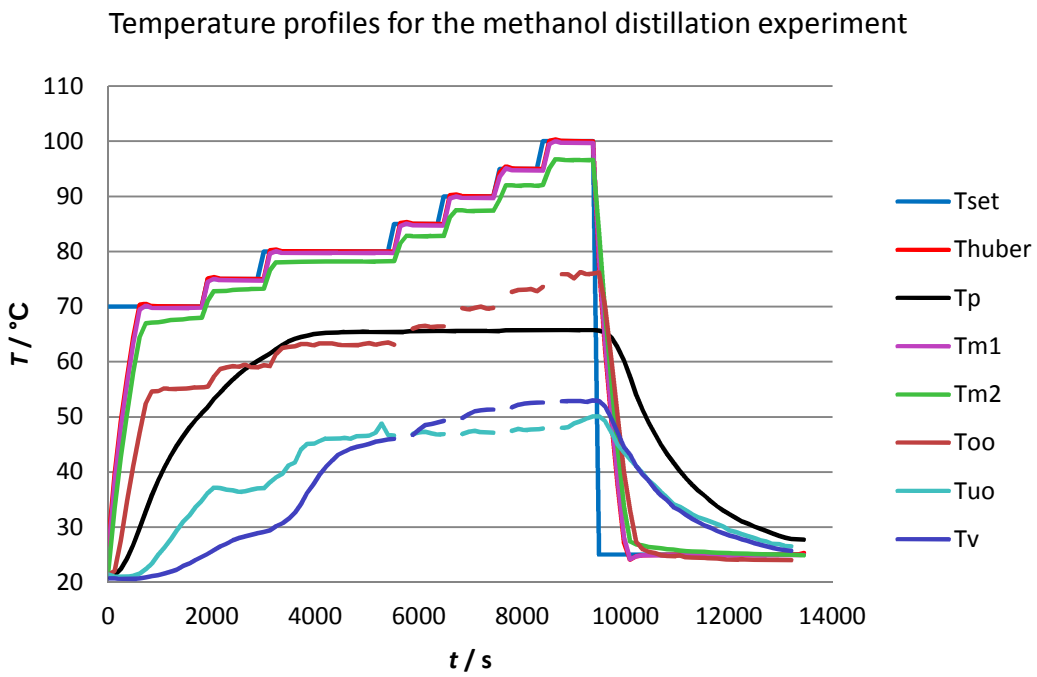

Figure 3.10 – Experimental results for the methanol distillation experiment. See nomenclature or description in text for the meaning of the symbols.

Firstly, the outer ullage temperature T_{uo} appears to decrease during the water boiling stages. Measurement was unreliable as the thermocouple was crudely taped onto the surface, and some variations of up to ±5°C were observed for this measurement. Plus the highest temperature boiling stage has slightly higher measured temperatures. The methanol boiling data give only a slow increase in outer ullage temperature and then a transient increase during the highest temperature setting. There could be several factors

at play here such as ambient temperature variations, and the fact that more vapour is driven off at the higher jacket temperature settings. In the water distillation case, the decrease could be caused by an increased amount of vapour on the internal walls of the ullage region evaporating, combined with the high latent heat of evaporation, thus resulting in an apparent decrease in outer ullage temperature on higher settings.

Secondly, the temperature of the vapour stream T_v in the methanol boiling case transiently increases during all the different boiling stages. Methanol is more volatile than water and has a lower heat capacity, so the vapour stream in the methanol distillation experiment turned out to be between 10°C and 20°C cooler than the boiling point of 64.7°C, whereas in the water case it was only 2°C cooler than the boiling point of 100°C and remained constant.

In figure 3.9, the Huber internal and jacket inlet and outlet temperatures briefly decreased below 0°C, even reaching -10°C, during the cooling cycle. This is because the system was in “process mode” during this time, providing the maximum cooling allowed (that is, a temperature difference of 50°C between process and Huber internal temperature). Deposited water (ice) could be seen on the outer surface of the Huber and the vessel during this time, although none was in the process side (and by the time the DW-Therm temperature had again risen above 0°C, the process temperature was still measured as at least 35°C and under an agitation rate of 366 revolutions per minute, so ice would have been unlikely to form in the process side).

3.3.4 Process Heat Rates

The amount of heat transferred to the process during boiling (in the distillation experiments) is the amount of heat to generate the vapour. Some of the vapour will be condensed in the ullage region and pipes before it reaches the condenser and a small amount will continue past the condenser (to the scrubbing system). The majority of the vapour is assumed to be condensed by the condenser and collected in the weighed bottle at the same rate as it is generated.

In the ramping experiments and during heating and cooling, the amount of heat is mostly sensible heat, but some heat loss due to evaporation will also occur. In any case, the condenser inlet and outlet temperatures were measured to see if they could be used.

The condenser consists of a glass shell with a glass coiled tube inside. The condensate condenses on the shell side of the condenser. In the tube side is chilled water, with 1% glycol. Note that at the lowest jacket temperatures (below 0°C), there was no danger of

freezing in the condenser, since the water vapour stream temperature had only dropped to 35°C before the experiment had ended).

The controller for the chilled water temperature only responds when the temperature deviates about 1.5°C away from its set point of 10°C, resulting in strong variations. The ambient temperature heats the chilled water tank to approximately 11.5°C and the controller cools it to 8.5°C then heats it to 10°C, then the process is repeated. This results in a saw-tooth-like profile. However, the difference in temperature across the condenser itself, from inlet to outlet, only goes up to about 0.5°C. Hence, the controller periodically forces the condenser inlet temperature below the outlet temperature, resulting in large variations in the apparent heat of the condenser (as displayed in figure 3.11).

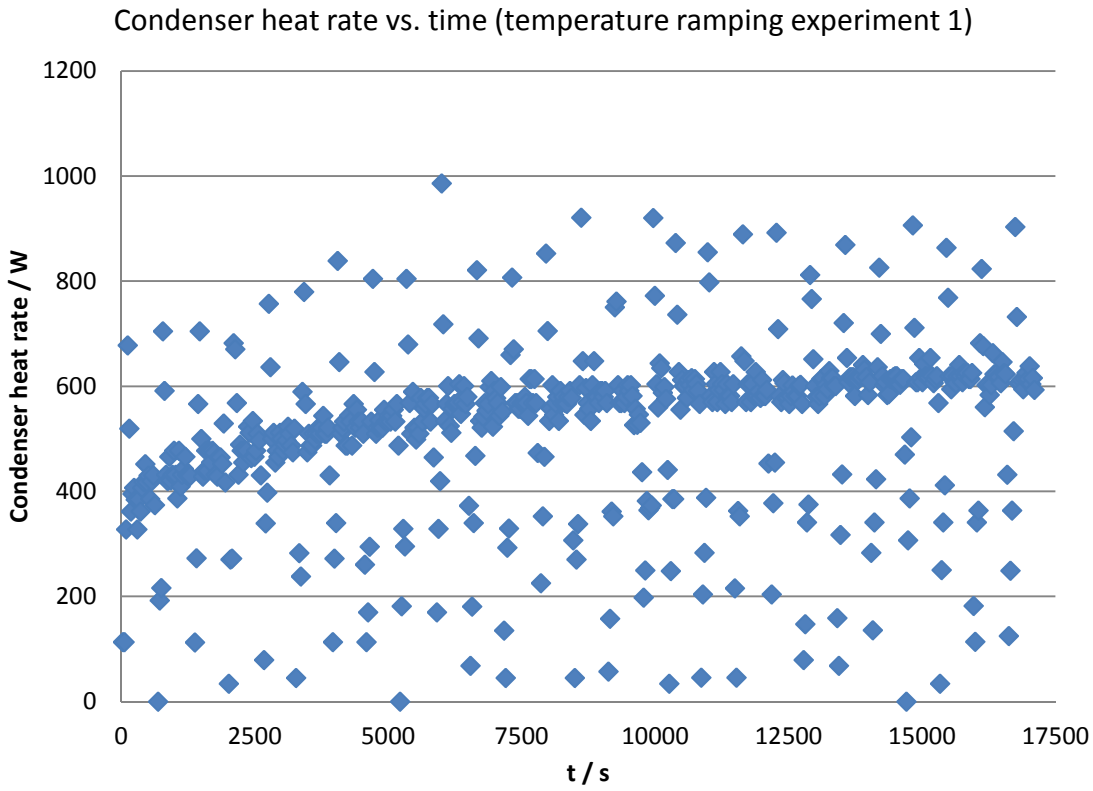

Figure 3.11 – Temperature ramping experiment 1 condenser heat rate based on the mass flow rate and heat capacity of the chilled water and the temperature difference between the inlet and outlet of the tube side of the condenser.

Figure 3.11 displays widely scattered points, but a heating curve can be seen where most of the points cluster. After almost 10 000 seconds, the first temperature ramping experiment switched from heating to cooling. This produces a gap in the curve where the clustered points lie. However, the condenser heat rate appears to stay high (and even rise slightly) during the cooling cycle, rather than returning to the original starting point. There are several factors that could cause this. Firstly, upon cooling, less vapour is produced and the vapour at a higher temperature condenses. Although it is only a small amount of

vapour (because it was not boiling; only heating to 50°C and cooling back to 22.5°C), this would still have produced a contraction, since every 1500 unit volumes of water vapour condense to a single unit volume of liquid water. Hence, the outside air would flow back into the system and the temperature in the condenser would not be influenced by the reactor. Secondly, the end of the experiment was later in the day, when the ambient temperature would have risen. Overall, the heat rate into the chilled water in the condenser tube side does not decrease during the process cooling cycle, and remains at around 600 W.

3.4 Errors Considered

The type 'K' general probe thermocouples were specified to have a calibration error of ±1.5°C and a measurement error of ±0.25°C (T.M. Electronics, 2004).

Measurement of T_{amb} was not recorded consistently. However, a thermocouple placed on the floor near the reactor read a temperature of 19.4°C during the experiment and this has been used in the diabatic simulations. The variation of T_{amb} from this value was not likely to have exceeded ±2°C, which is a maximum error in temperature difference of ±2.3% between T_{amb} and T_{m2} for the chosen boiling experiments.

The thermocouples taped onto the outside of the vessel and jacket (for measuring the outer jacket wall and outer ullage wall temperatures), as well as the thermocouple used for measuring the vapour stream temperature, were calibrated manually by the author and the assistants (N. Fitch and S. Shaw) according to the appropriate calibration procedure. This involved setting the 0°C point in a beaker of water filled with melting ice and the 100°C point in a beaker of boiling water.

As previously mentioned, because two thermocouples were crudely taped onto the surface, some variations of up to ±5°C were observed for these temperature readings (at the outer jacket wall and outer ullage wall). These temperatures were not used in the analysis.

The other thermocouples, for measuring the jacket inlet and outlet temperatures, the process temperature and the condenser inlet and outlet temperatures, had been calibrated by the School of Chemistry personnel.

Errors in the evaluation of condenser heat rate were introduced based on the fact that the condenser temperature was changing according to the chilled water cycle. This has already been described in the last part of section 3.3.4.

The measurement of the mass rate of the DW-Therm in the jacket varied by ±0.026 and kept relatively constant at about 0.269 kg s^{-1}; a variation of ±9.5%. The instantaneous measured mass flow was used in analysis and simulations, generating some variability in the evaluation of heat rates in the jacket.

3.5 Summary of the Experimental Work

Experimental work has been conducted for the 25 litre vessel involving heating, boiling and cooling of methanol and water. The experimental equipment used and the operating procedures have been described. Data on the temperature profiles and operating conditions in the reactor, condenser and jacket, have been obtained and presented.

These data are very useful for analysis and comparison with models of heat transfer, which is conducted in subsequent chapters. However, they do not describe the details of the flow or the distribution of temperature or pressure. Additional data from external thermocouples taped onto the reactor were obtained, but may not be reliable due to the effect of heat loss to the surrounding resulting in underestimation of the true surface temperatures.

4 THEORY AND ANALYSIS

4.1 Chapter Description

This chapter describes the initial analysis of the experimental results. The lumped parameter heat transfer model of the response to heating and cooling is described. This is developed for conditions when either a constant, linear or polynomial profile is used for the jacket inlet temperature, providing basic assumptions are involved.

The distributed parameter model is also described. This relaxes the assumptions of no thermal response through the wall, providing a result closer to a conjugate simulation.

4.2 Lumped Parameter Heat Transfer Model

4.2.1 Setup and Assumptions

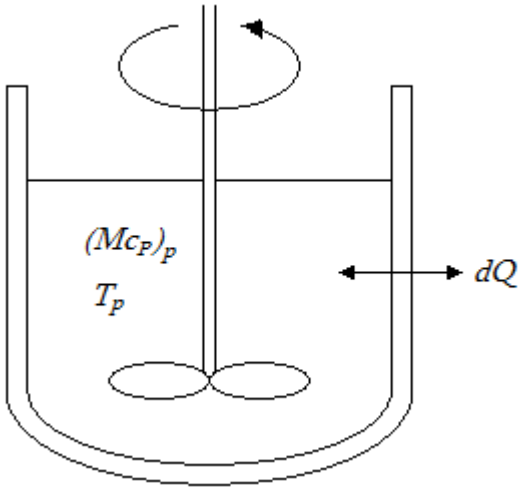

Figure 4.1 – Heat transfer in an agitated vessel.

The schematic in figure 4.1 illustrates the general heat transfer to or from an STR. The process content has an initial temperature of T_{p1} and a transient temperature of T_p. It has a heat capacity denoted by $(Mc_P)_p$. The overall conservation formula to be applied is displayed in equation (4.1).

$$input - output + generation - dissipation = accumulation \quad (4.1)$$

The rate of heat transfer to the process at any point in time, $\dot{Q}$, is the ratio of the infinitesimals dQ/dt. This is also the rate of accumulation. Thus, for an arbitrary time interval Δt, the $accumulation$ term in equation (4.1) is equal to ΔQ.

In this lumped parameter model, the following assumptions have been made about the reactor (Heggs and Hills, 1994):-

- The fluid is perfectly mixed, that is, the temperature of the content of the vessel is uniform throughout at any instant.
- The concept of an "overall heat transfer coefficient" (OHTC) applies.
- The OHTC is constant.
- The mass rate of the jacket medium does not change throughout the operation.
- All heat capacities remain constant throughout the operation.
- Heat losses or gains caused by anything other than the jacket cooling system are negligible.
- The heat capacity of the vessel content is much larger than that of the vessel wall, base, jacket and agitator.
- The thermal response of the jacket is instantaneous.

In all simulations, the values of the jacket medium inlet temperature (T_{m1}) were input from the experimental data.

Under these assumptions, for a constant process heat capacity $(M\tilde{c}_P)_p$, the change in process temperature (T_p) with time (t) is proportional to the difference between the temperatures T_{m1} and T_p. The proportionality constant in this case is denoted by χ, as in Heggs and Hills (1994).

4.2.2 With No Heat Loss to the Surroundings

When no reactions are occurring, the $generation$ and $dissipation$ terms in equation (4.1) are both equal to zero.

For the time interval Δt, a change in process temperature, ΔT_p, is observed. This is directly related to ΔQ, as seen in equation (4.2).

$$accumulation = \Delta Q = (Mc_P)_p \Delta T_p \tag{4.2}$$

Under the assumption that all heat losses or gains not caused by jacket-to-process heat transfer are negligible, the $output$ term is zero, and the $input$ term becomes the following:-

$$input = \chi(T_{m1} - T_p)\Delta t \tag{4.3}$$

where χ is the proportionality constant. Equation (4.1) then becomes equation (4.4).

$$\chi(T_{m1} - T_p)\Delta t = (Mc_P)_p \Delta T_p \tag{4.4}$$

Rearranging the terms, the overall equation is:-

$$(M\tilde{c}_P)_p \frac{dT_p}{dt} = \chi(T_{m1} - T_p) \tag{4.5}$$

where:-

$$\chi = EC_{min} = E(\dot{M}\tilde{c}_P)_m \tag{4.6}$$

and:-

$$E = 1 - exp\left[-\frac{(UA)_j}{(\dot{M}\tilde{c}_P)_m}\right] = \frac{\dot{Q}}{\dot{Q}_{max}} = \frac{T_{m1} - T_{m2}}{T_{m1} - T_p} \tag{4.7}$$

where U is the overall heat transfer coefficient and A is the area for heat transfer. Putting equations (4.6) and (4.7) into the overall equation gives:-

$$(M\tilde{c}_P)_p \frac{dT_p}{dt} = (\dot{M}\tilde{c}_P)_m \left\{1 - exp\left[-(UA)_j/(\dot{M}\tilde{c}_P)_m\right]\right\}(T_{m1} - T_p) \tag{4.8}$$

For the boundary conditions, the profile of $T_{m1}(t)$ is used, as well as the starting process temperature:-

When $t \leq 0,\ T_p = T_{p1}$ (4.9)

The jacket outlet temperature in this model is based only on how much heat was transferred to the process, represented by equation (4.10). The jacket outlet temperature can be calculated in this way because the effectiveness is also the ratio of temperature differences as in equation (4.7).

$$T_{m2} = (1 - E)T_{m1} + ET_p \tag{4.10}$$

This is solved numerically using a predictor-corrector method, the 2nd-order Runge-Kutta. This involves first predicting with the forward difference and then correcting using the modified central difference. Microsoft Excel was used to perform these calculations. As such, 4th order was not used because it would be more difficult to implement on Microsoft Excel.

Alternatively an analytical solution can be found when the jacket inlet temperature varies with time, by solving equation (4.8). If T_{m1} is a polynomial function of time, then, using the definitions in equations (4.6) and (4.7), the equation to solve is:-

$$\frac{\mathrm{d}T_p}{\mathrm{d}t} = \frac{\chi}{(M\tilde{c}_P)_p}\left(T_{m1} - T_p\right) \tag{4.11}$$

For a variable inlet temperature to the jacket, the solution for the following conditions is required:-

$$\text{when } t \leq 0, \qquad T_P = T_{p1} \tag{4.12}$$

$$\text{when } t \geq 0, \qquad T_{m1} = K_0 + K_1 t + K_2 t^2 + \cdots + K_n t^n \tag{4.13}$$

where $K_0, K_1, \ldots, K_n$ are constants. Theoretically any number of terms can be used, but as T_{m1} is set in a linear manner in the experiments, only $K_0 + K_1 t$ is essential. Higher order terms are included here in case more complex profiles of $T_{m1}(t)$ are used in future work.

$$\text{Let } \frac{\chi}{(M\tilde{c}_P)_p} = K_q \tag{4.14}$$

$$\text{Let } K_0 + K_1 t + K_2 t^2 + \cdots + K_n t^n = P_n(t) = P_n \tag{4.15}$$

This can be differentiated n times, until it becomes a constant:-

$$\frac{\mathrm{dP}_n}{\mathrm{d}t} = K_1 + K_2 t + K_3 t^2 + \cdots + K_n t^{n-1} \tag{4.16}$$

$$\frac{\mathrm{d}^{n-2}\mathrm{P}_n}{\mathrm{d}t^{n-2}} = K_{n-2} + K_{n-1} t + K_n t^2 \tag{4.17}$$

$$\frac{\mathrm{d}^{n}\mathrm{P}_n}{\mathrm{d}t^{n}} = K_n \tag{4.18}$$

Using equations (4.13), (4.14) and (4.15), equation (4.11) becomes:-

$$\frac{1}{K_q}\frac{\mathrm{d}T_p}{\mathrm{d}t} = \mathrm{P}_n - T_p \tag{4.19}$$

The polynomial term is substituted and differentiated n times:-

$$\text{Let } \mathrm{P}_n - T_p = y_1 \qquad \therefore \frac{\mathrm{d}y_1}{\mathrm{d}t} = \frac{\mathrm{dP}_n}{\mathrm{d}t} - \frac{\mathrm{d}T_p}{\mathrm{d}t} \qquad \therefore \frac{\mathrm{d}T_p}{\mathrm{d}t} = \frac{\mathrm{dP}_n}{\mathrm{d}t} - \frac{\mathrm{d}y_1}{\mathrm{d}t} \tag{4.20}$$

$$\therefore \frac{1}{K_q}\frac{\mathrm{dP}_n}{\mathrm{d}t} - \frac{1}{K_q}\frac{\mathrm{d}y_1}{\mathrm{d}t} = y_1 \quad \therefore \frac{1}{K_q}\frac{\mathrm{d}y_1}{\mathrm{d}t} = \frac{1}{K_q}\frac{\mathrm{dP}_n}{\mathrm{d}t} - y_1 \tag{4.21}$$

$$\text{Let } \frac{1}{K_q}\frac{\mathrm{d}\mathrm{P}_n}{\mathrm{d}t} - y_1 = y_2 \quad \therefore \frac{\mathrm{d}y_2}{\mathrm{d}t} = \frac{1}{K_q}\frac{\mathrm{d}^2\mathrm{P}_n}{\mathrm{d}t^2} - \frac{\mathrm{d}y_1}{\mathrm{d}t} \quad \therefore \frac{\mathrm{d}y_1}{\mathrm{d}t} = \frac{1}{K_q}\frac{\mathrm{d}^2\mathrm{P}_n}{\mathrm{d}t^2} - \frac{\mathrm{d}y_2}{\mathrm{d}t} \tag{4.22}$$

$$\therefore \frac{1}{K_q^2}\frac{\mathrm{d}^2\mathrm{P}_n}{\mathrm{d}t^2} - \frac{1}{K_q}\frac{\mathrm{d}y_2}{\mathrm{d}t} = y_2 \quad \therefore \frac{1}{K_q}\frac{\mathrm{d}y_2}{\mathrm{d}t} = \frac{1}{K_q^2}\frac{\mathrm{d}^2\mathrm{P}_n}{\mathrm{d}t^2} - y_2 \tag{4.23}$$

until:-

$$\text{Let } \frac{1}{K_q^{n-1}}\frac{\mathrm{d}^{n-1}\mathrm{P}_n}{\mathrm{d}t^{n-1}} - y_{n-1} = y_n \quad \therefore \frac{\mathrm{d}y_{n-1}}{\mathrm{d}t} = \frac{1}{K_q^{n-1}}\frac{\mathrm{d}^n\mathrm{P}_n}{\mathrm{d}t^n} - \frac{\mathrm{d}y_n}{\mathrm{d}t} \tag{4.24}$$

$$\frac{1}{K_q^n}\frac{\mathrm{d}^n\mathrm{P}_n}{\mathrm{d}t^n} - \frac{1}{K_q}\frac{\mathrm{d}y_n}{\mathrm{d}t} = y_n \quad \therefore \frac{1}{K_q}\frac{\mathrm{d}y_n}{\mathrm{d}t} = \frac{1}{K_q^n}\frac{\mathrm{d}^n\mathrm{P}_n}{\mathrm{d}t^n} - y_n \tag{4.25}$$

Combining with equation (4.18), equation (4.25) can then be solved using the initial condition from equation (4.12):-

$$\therefore \frac{-1}{K_q}\frac{\mathrm{d}y_n}{\mathrm{d}t} = y_n - \frac{K_n}{K_q^n} \quad \therefore \frac{-1}{K_q}\frac{\mathrm{d}\left(y_n - \frac{K_n}{K_q^n}\right)}{\mathrm{d}t} = y_n - \frac{K_n}{K_q^n} \tag{4.26}$$

$$\therefore \int_{y_{n(t=0)}}^{y_n} \frac{\mathrm{d}\left(y_n - \frac{K_n}{K_q^n}\right)}{\left(y_n - \frac{K_n}{K_q^n}\right)} = -\int_0^t K_q \mathrm{d}t \tag{4.27}$$

$$\therefore \ln\left(\frac{y_n - \frac{K_n}{K_q^n}}{y_{n(t=0)} - \frac{K_n}{K_q^n}}\right) = -K_q t \tag{4.28}$$

$$\therefore \frac{y_n - \frac{K_n}{K_q^n}}{y_{n(t=0)} - \frac{K_n}{K_q^n}} = \exp\left(-K_q t\right) \tag{4.29}$$

$$\therefore \frac{\frac{1}{K_q^{n-1}}\frac{\mathrm{d}^{n-1}\mathrm{P}_n}{\mathrm{d}t^{n-1}} - \frac{1}{K_q^{n-2}}\frac{\mathrm{d}^{n-2}\mathrm{P}_n}{\mathrm{d}t^{n-2}} + \cdots \pm \frac{1}{K_q^2}\frac{\mathrm{d}^2\mathrm{P}_n}{\mathrm{d}t^2} \mp \frac{1}{K_q}\frac{\mathrm{d}\mathrm{P}_n}{\mathrm{d}t} \pm \mathrm{P}_n \mp T_p - \frac{K_n}{K_q^n}}{\frac{K_{n-1}}{K_q^{n-1}} - \frac{K_{n-2}}{K_q^{n-2}} + \cdots \pm \frac{K_2}{K_q^2} \mp \frac{K_1}{K_q} \pm \mathrm{K}_0 \mp T_{p1} - \frac{K_n}{K_q^n}} = \exp\left(-K_q t\right) \tag{4.30}$$

$$\therefore T_p = \pm\left(+\frac{1}{K_q^{n-1}}\frac{\mathrm{d}^{n-1}\mathrm{P}_n}{\mathrm{d}t^{n-1}} - \cdots \pm \frac{1}{K_q^2}\frac{\mathrm{d}^2\mathrm{P}_n}{\mathrm{d}t^2} \mp \frac{1}{K_q}\frac{\mathrm{d}\mathrm{P}_n}{\mathrm{d}t} \pm \mathrm{P}_n - \frac{K_n}{K_q^n}\right)$$
$$\mp\left(\frac{K_{n-1}}{K_q^{n-1}} - \frac{K_{n-2}}{K_q^{n-2}} + \cdots \pm \frac{K_2}{K_q^2} \mp \frac{K_1}{K_q} \pm \mathrm{K}_0 \mp T_{p1}\right. \quad (4.31)$$
$$\left. - \frac{K_n}{K_q^n}\right)\exp(-K_q t)$$

In equations (4.30) and (4.31), the sign $\pm$ denotes a plus if n is odd, and a minus if n is even. Also in equations (4.30) and (4.31), the sign $\mp$ denotes denotes a minus if n is odd, and a plus if n is even. For the example of a linear profile of T_{m1} with time:-

$$n = 1 \therefore T_p = \left(-\frac{1}{K_q}\frac{\mathrm{dP}_1}{\mathrm{d}t} + \mathrm{P}_1\right) - \left(\mathrm{K}_0 - T_{p1} - \frac{K_1}{K_q}\right)\exp(-K_q t) \quad (4.32)$$

and:-

$$\mathrm{P}_n = T_{m1} = K_0 + K_1 t \quad (4.33)$$

$$\therefore T_p = K_0 + K_1 t - \frac{K_1}{K_q} - \left(K_0 - T_{p1} - \frac{K_1}{K_q}\right)\exp(-K_q t) \quad (4.34)$$

Alternatively, equations (4.11), (4.12) and (4.13) can be solved using a complementary function and particular integral. The solution must be in the following form:-

$$T_p = T_{CF} + T_{PI} \quad (4.35)$$

First, the constant term in equation (4.11) is shortened using equation (4.14), so that equation (4.11) becomes the following:-

$$\frac{\mathrm{d}T_p}{\mathrm{d}t} = K_q(T_{m1} - T_p) \quad (4.36)$$

The complementary function is obtained from the homogeneous part of equation (4.36), which is:-

$$\frac{\mathrm{d}T_p}{\mathrm{d}t} = -K_q T_p \quad (4.37)$$

The complementary function is:-

$$T_{CF} = C_1\exp(-K_q t) \quad (4.38)$$

where C_1 is an integration constant. Let us assume that the particular integral has the following form:-

$$T_{PI} = C_2 + C_3 t + C_4 t^2 + \cdots + C_{n+2} t^n \tag{4.39}$$

Differentiation of equation (4.39) gives:-

$$\frac{\mathrm{d}T_{\mathrm{PI}}}{\mathrm{d}t} = C_3 + C_4 t + \cdots + C_{n+2} t^{n-1} \tag{4.40}$$

Substitution of equations (4.13), (4.39), and (4.40) into equation (4.36) gives:-

$$\begin{aligned} C_3 + C_4 t + \cdots + C_{n+2} t^{n-1} \\ = K_q[K_0 - C_2 + (K_1 - C_3)t + \cdots + (K_n - C_{n+2})t^n] \end{aligned} \tag{4.41}$$

Collecting terms for values of t:-

$$t^0\ terms: \quad C_3 = K_q(K_0 - C_2) \tag{4.42}$$

$$t^1\ terms: \quad C_4 = K_q(K_1 - C_3) \tag{4.43}$$

$$t^{n-1}\ terms: \quad C_{n+2} = K_q(K_{n-1} - C_{n+1}) \tag{4.44}$$

$$t^n\ terms: \quad 0 = K_q(K_n - C_{n+2}) \tag{4.45}$$

From equations (4.42) to (4.45):-

$$C_{n+2} = K_n \tag{4.46}$$

$$C_{n+1} = K_{n-1} - \frac{K_n}{K_q} \tag{4.47}$$

$$C_3 = K_1 - \frac{K_2}{K_q} + \cdots \mp \frac{K_{n-1}}{K_q^{n-2}} \pm \frac{K_n}{K_q^{n-1}} \tag{4.48}$$

$$C_2 = K_0 - \frac{K_1}{K_q} + \cdots \pm \frac{K_{n-1}}{K_q^{n-1}} \mp \frac{K_n}{K_q^n} \tag{4.49}$$

From equations (4.35), (4.38), (4.39), the general solution is:-

$$T_{\mathrm{p}} = C_1 \exp(-K_q t) + C_2 + C_3 t + \cdots + C_{n+2} t^n \tag{4.50}$$

The integration constant C_1 is now obtained from the initial condition in equation (4.12), by substitution of the constants from equations (4.46) to (4.49) into equation (4.50):-

$$C_1 = T_{\mathrm{p}1} - K_0 + \frac{K_1}{K_q} - \cdots \mp \frac{K_{n-1}}{K_q^{n-1}} \pm \frac{K_n}{K_q^n} \tag{4.51}$$

Hence the solution is as follows:-

$$T_{\mathrm{p}} = \left(T_{\mathrm{p1}} - K_0 + \frac{K_1}{K_q} - \cdots \mp \frac{K_{n-1}}{K_q^{n-1}} \pm \frac{K_n}{K_q^n}\right)\exp\left(-K_q t\right) + \left(K_0 - \frac{K_1}{K_q} + \cdots \pm \frac{K_{n-1}}{K_q^{n-1}} \mp \frac{K_n}{K_q^n}\right) + \left(K_1 - \frac{K_2}{K_q} + \cdots \mp \frac{K_{n-1}}{K_q^{n-2}} \pm \frac{K_n}{K_q^{n-1}}\right)t + \cdots + K_n t^n \tag{4.52}$$

In equation (4.52), as in equation (4.31), the sign $\pm$ denotes a plus if n is odd, and a minus if n is even, and the sign $\mp$ denotes a minus if n is odd, and a plus if n is even. Equation (4.52) agrees with equation (4.31), which can be found by first rearranging the plus and minus terms:-

$$T_{\mathrm{p}} = \mp\left(\mp T_{\mathrm{p1}} \pm K_0 \mp \frac{K_1}{K_q} \pm \cdots + \frac{K_{n-1}}{K_q^{n-1}} - \frac{K_n}{K_q^n}\right)\exp\left(-K_q t\right) \pm \left[\pm\left(K_0 - \frac{K_1}{K_q} + \cdots \pm \frac{K_{n-1}}{K_q^{n-1}} \mp \frac{K_n}{K_q^n}\right) \pm \left(K_1 - \frac{K_2}{K_q} + \cdots \mp \frac{K_{n-1}}{K_q^{n-2}} \pm \frac{K_n}{K_q^{n-1}}\right)t \pm \cdots \pm (K_n)t^n\right] \tag{4.53}$$

Collecting all the individual terms, and considering equation (4.15), equation (4.53) can be rearranged into equation (4.31):-

$$\therefore T_p = \pm\left(+\frac{1}{K_q^{n-1}}\frac{\mathrm{d}^{n-1}\mathrm{P}_n}{\mathrm{d}t^{n-1}} - \cdots \pm \frac{1}{K_q^2}\frac{\mathrm{d}^2\mathrm{P}_n}{\mathrm{d}t^2} \mp \frac{1}{K_q}\frac{\mathrm{d}\mathrm{P}_n}{\mathrm{d}t} \pm \mathrm{P}_n - \frac{K_n}{K_q^n}\right) \mp \left(\frac{K_{n-1}}{K_q^{n-1}} - \frac{K_{n-2}}{K_q^{n-2}} + \cdots \pm \frac{K_2}{K_q^2} \mp \frac{K_1}{K_q} \pm \mathrm{K}_0 \mp T_{p1} - \frac{K_n}{K_q^n}\right)\exp\left(-K_q t\right) \tag{4.31}$$

For the example of a linear profile of T_{m1} with time, equation (4.52) becomes:-

$$n = 1 \therefore T_{\mathrm{p}} = \left(T_{\mathrm{p1}} - K_0 + \frac{K_1}{K_q}\right)\exp\left(-K_q t\right) + \left(K_0 - \frac{K_1}{K_q}\right) + (K_1)t \tag{4.54}$$

which agrees with equation (4.34):-

$$\therefore T_p = K_0 + K_1 t - \frac{K_1}{K_q} - \left(K_0 - T_{p1} - \frac{K_1}{K_q}\right)\exp\left(-K_q t\right) \tag{4.34}$$

To illustrate that equation (4.52) and (4.31) are equivalent; consider an example of a quartic profile of T_{m1} with time. Equation (4.52)'s solution is:-

$$\begin{aligned} n = 4 \therefore T_{\mathrm{p}} = &\left(T_{\mathrm{p1}} - K_0 + \frac{K_1}{K_q} - \frac{K_2}{K_q^2} + \frac{K_3}{K_q^3} - \frac{K_4}{K_q^4}\right)\exp\left(-K_q t\right) \\ &+ \left(K_0 - \frac{K_1}{K_q} + \frac{K_2}{K_q^2} - \frac{K_3}{K_q^3} + \frac{K_4}{K_q^4}\right) \\ &+ \left(K_1 - \frac{K_2}{K_q} + \frac{K_3}{K_q^2} - \frac{K_4}{K_q^3}\right)t + \left(K_2 - \frac{K_3}{K_q} + \frac{K_4}{K_q^2}\right)t^2 \\ &+ \left(K_3 - \frac{K_4}{K_q}\right)t^3 + K_4 t^4 \end{aligned} \tag{4.55}$$

Equation (4.31)'s solution is:-

$$\begin{aligned} n = 4 \therefore T_p = &-\left(+\frac{1}{K_q^3}\frac{\mathrm{d}^3\mathrm{P}_4}{\mathrm{d}t^3} - \frac{1}{K_q^2}\frac{\mathrm{d}^2\mathrm{P}_4}{\mathrm{d}t^2} + \frac{1}{K_q}\frac{\mathrm{dP}_4}{\mathrm{d}t} - \mathrm{P}_4 - \frac{K_4}{K_q^4}\right) \\ &+ \left(\frac{K_3}{K_q^3} - \frac{K_2}{K_q^2} + \frac{K_1}{K_q} - \mathrm{K}_0 + T_{p1} - \frac{K_4}{K_q^4}\right)\exp\left(-K_q t\right) \end{aligned} \tag{4.31}$$

$$\begin{aligned} \therefore T_p = &\frac{K_4}{K_q^4} - \frac{1}{K_q^3}\frac{\mathrm{d}^3\mathrm{P}_4}{\mathrm{d}t^3} + \frac{1}{K_q^2}\frac{\mathrm{d}^2\mathrm{P}_4}{\mathrm{d}t^2} - \frac{1}{K_q}\frac{\mathrm{dP}_4}{\mathrm{d}t} + \mathrm{P}_4 \\ &+ \left(T_{\mathrm{p1}} - K_0 + \frac{K_1}{K_q} - \frac{K_2}{K_q^2} + \frac{K_3}{K_q^3} - \frac{K_4}{K_q^4}\right)\exp\left(-K_q t\right) \end{aligned} \tag{4.56}$$

$$\mathrm{P}_4 = T_{m1} = K_0 + K_1 t + K_2 t^2 + K_3 t^3 + K_4 t^4 \tag{4.57}$$

$$\begin{aligned} \therefore T_p = &\frac{K_4}{K_q^4} - \frac{K_3 + K_4 t}{K_q^3} + \frac{K_2 + K_3 t + K_4 t^2}{K_q^2} - \frac{K_1 + K_2 t + K_3 t^2 + K_4 t^3}{K_q} \\ &+ K_0 + K_1 t + K_2 t^2 + K_3 t^3 + K_4 t^4 \\ &+ \left(T_{\mathrm{p1}} - K_0 + \frac{K_1}{K_q} - \frac{K_2}{K_q^2} + \frac{K_3}{K_q^3} - \frac{K_4}{K_q^4}\right)\exp\left(-K_q t\right) \end{aligned} \tag{4.58}$$

which agrees with equation (4.55).

In most cases, the Runge-Kutta (lumped parameter) model is more recommended than this analytical model because of the sensitivity of the coefficients in the polynomial. An attempt at the analytical model in Microsoft Excel, for example, was not accurate because of the high precision required. However, the analytical model could be easier for use in programming a controller if the coefficients are stored with sufficient precision.

4.2.3 With Heat Loss to the Surroundings

If heat loss to the surroundings is significant, the assumption that it is negligible must be relaxed. In this case the input term is based on the jacket temperature change and the output term is the heat loss to the surroundings, as seen in equations (4.56) and (4.57).

$$input = \left(\dot{M}\tilde{c}_P\right)_m (T_{m1} - T_{m2})\Delta t \tag{4.56}$$

$$output = Q_{loss} = (UA)_{loss}(T_{amb} - T_m)\Delta t \tag{4.57}$$

As the values of T_m in equation (4.56 and (4.57) are required along the jacket height Δz, the input and output terms must be based on the rates of transfer. These are represented in equations (4.58) and (4.59).

$$input\ rate = \left(\dot{M}\tilde{c}_P\right)_m (T_{m1} - T_{m2}) \tag{4.58}$$

$$output\ rate = (UA)_{loss}(T_{amb} - T_m) = (UA')_{loss}(T_{amb} - T_m)\mathrm{d}z \tag{4.59}$$

where A' is the area per unit height along the jacket. The accumulation rate can also be described by the following:-

$$accumulation\ rate = (UA)_j\left(T_p - T_m\right) = (UA')_j\left(T_p - T_m\right)\mathrm{d}z \tag{4.60}$$

Rearranging the rate terms above based on equation (4.1) gives the following equation:-

$$\left(\dot{M}\tilde{c}_P\right)_m \frac{\mathrm{d}T_m}{\mathrm{d}z} = (UA')_j\left(T_p - T_m\right) + (UA')_{loss}(T_{amb} - T_m) \tag{4.61}$$

Further rearrangement gives:-

$$\frac{\mathrm{d}T_m}{\mathrm{d}z} = \frac{-\left[(UA')_j + (UA')_{loss}\right]T_m}{\left(\dot{M}\tilde{c}_P\right)_m} + \frac{(UA')_j T_p}{\left(\dot{M}\tilde{c}_P\right)_m} + \frac{(UA')_{loss}T_{amb}}{\left(\dot{M}\tilde{c}_P\right)_m} \tag{4.62}$$

As only T_m is assumed to change with z, equation (4.62) can be put in the following form:-

$$\frac{\mathrm{d}T_m}{\mathrm{d}z} = -\mathrm{A}T_m + \mathrm{B} \tag{4.63}$$

where:-

$$\mathrm{A} = \frac{(UA')_j + (UA')_{loss}}{\left(\dot{M}\tilde{c}_P\right)_m} \tag{4.64}$$

$$\mathrm{B} = \frac{(UA')_j T_p + (UA')_{loss} T_{amb}}{\left(\dot{M}\tilde{c}_P\right)_m} \tag{4.65}$$

Equation (4.63) is rearranged and solved as follows:-

$$-\frac{\mathrm{d}T_m}{\mathrm{A}\mathrm{d}z} = T_m - \frac{\mathrm{B}}{\mathrm{A}} \tag{4.66}$$

$$\therefore \int_{T_{m1}}^{T_m} \frac{\mathrm{d}\left(T_m - \frac{\mathrm{B}}{\mathrm{A}}\right)}{T_m - \frac{\mathrm{B}}{\mathrm{A}}} = \int_0^z -\mathrm{A}\mathrm{d}z \tag{4.67}$$

$$\therefore ln\left(\frac{T_m - \frac{\mathrm{B}}{\mathrm{A}}}{T_{m1} - \frac{\mathrm{B}}{\mathrm{A}}}\right) = -\mathrm{A}z \tag{4.68}$$

$$\therefore \frac{T_m - \frac{\mathrm{B}}{\mathrm{A}}}{T_{m1} - \frac{\mathrm{B}}{\mathrm{A}}} = \exp(-\mathrm{A}z) \tag{4.69}$$

$$\therefore T_m = \frac{\mathrm{B}}{\mathrm{A}} - \left(\frac{\mathrm{B}}{\mathrm{A}} - T_{m1}\right)\exp(-\mathrm{A}z) \tag{4.70}$$

The total heat transferred from the jacket is:-

$$\dot{Q}_T = \left(\dot{M}\tilde{c}_P\right)_m (T_{m1} - T_{m2}) \tag{4.71}$$

The jacket outlet temperature T_{m2} is equal to T_m at the maximum height Z, which is defined using equation (4.70), therefore:-

$$T_{m2} = \frac{\mathrm{B}}{\mathrm{A}} - \left(\frac{\mathrm{B}}{\mathrm{A}} - T_{m1}\right)\exp(-\mathrm{A}Z) \tag{4.72}$$

$$\therefore \dot{Q}_T = \left(\dot{M}\tilde{c}_P\right)_m \left(T_{m1} - \frac{\mathrm{B}}{\mathrm{A}} + \left(\frac{\mathrm{B}}{\mathrm{A}} - T_{m1}\right)\exp(-\mathrm{A}Z)\right) \tag{4.73}$$

$$\therefore \dot{Q}_T = \left(\dot{M}\tilde{c}_P\right)_m \left(T_{m1} - \frac{\mathrm{B}}{\mathrm{A}}\right)[1 - \exp(-\mathrm{A}Z)] \tag{4.74}$$

The total heat transfer comprises the heat transferred to the process ($\dot{Q}_p$) and the heat lost to the surroundings ($\dot{Q}_{loss}$):-

$$\dot{Q}_T = \dot{Q}_p + \dot{Q}_{loss} \tag{4.75}$$

where:-

$$\dot{Q}_p = \int_0^Z (UA')_j \left(T_m - T_p\right) dz \tag{4.76}$$

$$\dot{Q}_{loss} = \int_0^Z (UA')_{loss} (T_m - T_{amb}) dz \tag{4.77}$$

Equation (4.76) is combined with equation (4.70) and solved:-

$$\dot{Q}_p = \int_0^Z (UA')_j \left[\frac{\mathrm{B}}{\mathrm{A}} - T_p - \left(\frac{\mathrm{B}}{\mathrm{A}} - T_{m1}\right) \exp(-\mathrm{A}z)\right] dz \tag{4.78}$$

$$\therefore \dot{Q}_p = (UA')_j \left[\left(\frac{\mathrm{B}}{\mathrm{A}} - T_p\right) z + \frac{1}{\mathrm{A}} \left(\frac{\mathrm{B}}{\mathrm{A}} - T_{m1}\right) \exp(-\mathrm{A}z)\right]_0^Z \tag{4.79}$$

$$\therefore \dot{Q}_p = (UA')_j \left[\left(\frac{\mathrm{B}}{\mathrm{A}} - T_p\right) Z + \frac{1}{\mathrm{A}} \left(\frac{\mathrm{B}}{\mathrm{A}} - T_{m1}\right) \exp(-\mathrm{A}Z) - \frac{1}{\mathrm{A}} \left(\frac{\mathrm{B}}{\mathrm{A}} - T_{m1}\right)\right] \tag{4.80}$$

Re-arrangement gives:-

$$\dot{Q}_p = \left(\frac{(UA')_j \mathrm{B} - \mathrm{A}T_p}{\mathrm{A}}\right) Z - \frac{(UA')_j}{\mathrm{A}^2} (\mathrm{B} - \mathrm{A}T_{m1})[1 - \exp(-\mathrm{A}Z)] \tag{4.81}$$

Combining equation (4.81) with the definitions of the constants from equations (4.64) and (4.65):-

$$\begin{aligned} \dot{Q}_p &= \frac{(UA')_j (UA')_{loss} \left(T_{amb} - T_p\right) Z}{(UA')_j + (UA')_{loss}} \\ &- \frac{(UA')_j \left(\dot{M}\tilde{c}_P\right)_m^2}{\left[(UA')_j + (UA')_{loss}\right]^2} \left(\frac{(UA')_j \left(T_p - T_{m1}\right) + (UA')_{loss} (T_{amb} - T_{m1})}{\left(\dot{M}\tilde{c}_P\right)_m}\right) \\ &\times \left[1 - \exp\left(-\frac{(UA')_j + (UA')_{loss}}{\left(\dot{M}\tilde{c}_P\right)_m} Z\right)\right] \end{aligned} \tag{4.82}$$

$$\begin{aligned} \therefore \dot{Q}_p &= \frac{\left(T_{amb} - T_p\right) Z}{\frac{1}{(UA')_j} + \frac{1}{(UA')_{loss}}} \\ &- \frac{\left(\dot{M}\tilde{c}_P\right)_m}{\left[1 + \frac{(UA')_{loss}}{(UA')_j}\right]^2} \left(T_p - T_{m1} + \frac{(UA')_{loss}}{(UA')_j} (T_{amb} - T_{m1})\right) \\ &\times \left[1 - \exp\left(-\frac{(UA')_j + (UA')_{loss}}{\left(\dot{M}\tilde{c}_P\right)_m} Z\right)\right] \end{aligned} \tag{4.83}$$

Now, based on equation (4.5), the process temperature equation can be written as:-

$$(M\tilde{c}_P)_p \frac{\mathrm{d}T_p}{\mathrm{d}t} = \dot{Q}_p(T_p) \tag{4.84}$$

$$\therefore (M\tilde{c}_P)_p \mathrm{d}T_p = \dot{Q}_p(T_p)\mathrm{d}t \tag{4.85}$$

The experimental values of T_{m2} can be used to find a value of $(UA')_{loss}$ which can then be used in the overall model in equation (4.83). Based on equations (4.75) and (4.84):-

$$\dot{Q}_T(t) = (M\tilde{c}_P)_p \frac{\mathrm{d}T_p}{\mathrm{d}t} + \dot{Q}_{loss}(t) \tag{4.86}$$

Combining the terms in equation (4.86) with those in equations (4.71) and (4.77) gives:-

$$\left(\dot{M}\tilde{c}_P\right)_m [T_{m1}(t) - T_{m2}(t)] = (M\tilde{c}_P)_p \frac{\mathrm{d}T_p}{\mathrm{d}t} + \int_0^Z (UA')_{loss}(\tilde{T}_m - T_{amb})\mathrm{d}z \tag{4.87}$$

where, using the mean of the jacket inlet and outlet temperatures:-

$$\tilde{T}_m = [T_{m1}(t) + T_{m2}(t)]/2 \tag{4.88}$$

$$\therefore \left(\dot{M}\tilde{c}_P\right)_m [T_{m1}(t) - T_{m2}(t)] = (M\tilde{c}_P)_p \frac{\mathrm{d}T_p}{\mathrm{d}t} + (UA')_{loss}\left\{\frac{[T_{m1}(t) + T_{m2}(t)]}{2} - T_{amb}\right\}Z \tag{4.89}$$

The time derivative of T_p can be inferred from an analytical solution designed to fit the curve (as in equation (4.31) or (4.52)) or from the experimental T_p values and previously guessed $(UA)_j$ values (from equation (4.11)).

$$\dot{Q}_p = \left(\dot{M}\tilde{c}_P\right)_p \frac{\mathrm{d}T_p}{\mathrm{d}t} = (UA)_j(\tilde{T}_m - T_p) \tag{4.90}$$

Equation (4.90) is used to find $\dot{Q}_p$ directly from the experimental data in order to find an approximate value for $\dot{Q}_{loss}$ using equation (4.86), and therefore $(UA')_{loss}$ using equation (4.89). This is then used in equation (4.83) for the analytical model. A more accurate approach is to use the log mean temperature difference instead of the average temperature difference, so, in equation (4.87), equation (4.91) would be used instead of equation (4.88).

$$\tilde{T}_m - T_{amb} = LMTD_o = \frac{[T_{m1}(t) - T_{amb}] - [T_{m2}(t) - T_{amb}]}{\ln\left\{\frac{[T_{m1}(t) - T_{amb}]}{[T_{m2}(t) - T_{amb}]}\right\}} \tag{4.91}$$

The analytical solution of equation (4.83) can be found by combining with equation (4.84) and re-arranging:-

$$\frac{\mathrm{d}T_p}{\mathrm{d}t} = \mathrm{A}_2 T_{amb} + \mathrm{B}_2 T_{m1} - \mathrm{D}_2 T_p \tag{4.92}$$

where:-

$$\mathrm{A}_2 = \frac{Z/(M\tilde{c}_P)_p}{\frac{1}{(UA')_j} + \frac{1}{(UA')_{loss}}} - \frac{\frac{(\dot{m}\tilde{c}_P)_m}{\left[1 + \frac{(UA')_{loss}}{(UA')_j}\right]^2}\left[\frac{(UA')_{loss}}{(UA')_j}\right]\left[1 - \exp\left(-\frac{(UA')_j + (UA')_{loss}}{(\dot{m}\tilde{c}_P)_m}Z\right)\right]}{(M\tilde{c}_P)_p} \tag{4.93}$$

$$\mathrm{B}_2 = \frac{\frac{(\dot{m}\tilde{c}_P)_m}{\left[1 + \frac{(UA')_{loss}}{(UA')_j}\right]^2}\left[1 - \exp\left(-\frac{(UA')_j + (UA')_{loss}}{(\dot{m}\tilde{c}_P)_m}Z\right)\right]\left[1 + \frac{(UA')_{loss}}{(UA')_j}\right]}{(M\tilde{c}_P)_p} \tag{4.94}$$

$$\mathrm{D}_2 = \frac{\frac{Z}{\frac{1}{(UA')_j} + \frac{1}{(UA')_{loss}}} + \frac{(\dot{m}\tilde{c}_P)_m}{\left[1 + \frac{(UA')_{loss}}{(UA')_j}\right]^2}\left[1 - \exp\left(-\frac{(UA')_j + (UA')_{loss}}{(\dot{m}\tilde{c}_P)_m}Z\right)\right]}{(M\tilde{c}_P)_p} \tag{4.95}$$

For a ramped jacket temperature profile and constant ambient temperature, the same initial conditions as equations (4.12) and (4.13) can be used, in linear form:-

when $t \leq 0$, $\quad T_P = T_{p1}$ (4.12)

when $t \geq 0$, $\quad T_{m1} = K_0 + K_1 t$ (4.13)

$$\frac{\mathrm{d}T_{m1}}{\mathrm{d}t} = K_1 \tag{4.96}$$

Let $y = \mathrm{A}_2 T_{amb} + \mathrm{B}_2 T_{m1} - \mathrm{D}_2 T_p = \mathrm{A}_2 T_{amb} + \mathrm{B}_2 K_0 + \mathrm{B}_2 K_1 t - \mathrm{D}_2 T_p$ (4.97)

$$\therefore \frac{\mathrm{d}y}{\mathrm{d}t} = \mathrm{B}_2 K_1 - \mathrm{D}_2 \frac{\mathrm{d}T_p}{\mathrm{d}t} \quad \therefore \frac{\mathrm{d}T_p}{\mathrm{d}t} = \frac{\mathrm{B}_2}{\mathrm{D}_2} K_1 - \frac{1}{\mathrm{D}_2} \frac{\mathrm{d}y}{\mathrm{d}t} \tag{4.98}$$

From the initial conditions:-

$$y_0 = \mathrm{A}_2 T_{amb} + \mathrm{B}_2 K_0 - \mathrm{D}_2 T_{p1} \tag{4.99}$$

Combining equations (4.92), (4.97) and (4.98), and considering the constant terms:-

$$\frac{\mathrm{B}_2}{\mathrm{D}_2} K_1 - \frac{1}{\mathrm{D}_2} \frac{\mathrm{d}y}{\mathrm{d}t} = y \quad \therefore \frac{-1}{\mathrm{D}_2} \frac{\mathrm{d}\left(y - \frac{\mathrm{B}_2}{\mathrm{D}_2} K_1\right)}{\mathrm{d}t} = \left(y - \frac{\mathrm{B}_2}{\mathrm{D}_2} K_1\right) \tag{4.100}$$

$$\therefore \int_{y_0}^{y} \frac{\mathrm{d}\left(y - \frac{\mathrm{B}_2}{\mathrm{D}_2} K_1\right)}{\left(y - \frac{\mathrm{B}_2}{\mathrm{D}_2} K_1\right)} = \int_{0}^{t} -\mathrm{D}_2 \mathrm{d}t \tag{4.101}$$

$$\therefore \left[\ln\left(y - \frac{\mathrm{B}_2}{\mathrm{D}_2} K_1\right)\right]_{y_0}^{y} = \ln\left(\frac{y - \frac{\mathrm{B}_2}{\mathrm{D}_2} K_1}{y_0 - \frac{\mathrm{B}_2}{\mathrm{D}_2} K_1}\right) = -\mathrm{D}_2 \mathrm{t} \tag{4.102}$$

$$\therefore \frac{y - \frac{\mathrm{B}_2}{\mathrm{D}_2} K_1}{y_0 - \frac{\mathrm{B}_2}{\mathrm{D}_2} K_1} = \exp(-\mathrm{D}_2 \mathrm{t}) \tag{4.103}$$

$$\begin{aligned} &\therefore \mathrm{A}_2 T_{amb} + \mathrm{B}_2 K_0 + \mathrm{B}_2 K_1 t - \mathrm{D}_2 T_p - \frac{\mathrm{B}_2}{\mathrm{D}_2} K_1 \\ &= \left(\mathrm{A}_2 T_{amb} + \mathrm{B}_2 K_0 - \mathrm{D}_2 T_{p1} - \frac{\mathrm{B}_2}{\mathrm{D}_2} K_1\right) \exp(-\mathrm{D}_2 \mathrm{t}) \end{aligned} \tag{4.104}$$

$$\begin{aligned} \therefore T_p = \frac{\mathrm{A}_2}{\mathrm{D}_2} T_{amb} + \frac{\mathrm{B}_2}{\mathrm{D}_2} K_0 + \frac{\mathrm{B}_2}{\mathrm{D}_2} K_1 t - \frac{\mathrm{B}_2}{\mathrm{D}_2^2} K_1 \\ - \frac{1}{\mathrm{D}_2}\left(\mathrm{A}_2 T_{amb} + \mathrm{B}_2 K_0 - \mathrm{D}_2 T_{p1} - \frac{\mathrm{B}_2}{\mathrm{D}_2} K_1\right) \exp(-\mathrm{D}_2 \mathrm{t}) \end{aligned} \tag{4.105}$$

For a constant T_{m1}, K_1 is set to zero.

4.3 Boiling Heat Transfer

Although the analytical model generally uses *U* for the overall heat transfer coefficient, the individual resistances between the jacket and the vessel can be separated. Presuming there is no fouling on either surface:-

$$\frac{1}{UA} = \frac{1}{(\alpha A)_p} + \frac{\ln\left(\frac{d_o}{d_i}\right)}{2\pi\lambda_w L} + \frac{1}{(\alpha A)_j} \tag{4.106}$$

The wall resistance equation is the middle term on the right hand side of equation (4.106). This wall resistance and the heat capacity rate of the jacket $(\dot{m}\tilde{c}_P)_m$ are assumed to remain constant during boiling.

4.3.1 Adiabatic Operation

If there is no heat loss to the surroundings, the heat transferred by the jacket is put into the process and the following equations apply:-

$$\dot{Q} = \left(\dot{M}\tilde{c}_P\right)_m (T_{m1} - T_{m2}) = (UA)_{boil} LMTD_i \tag{4.107}$$

where:-

$$LMTD_i = \left[\left(T_{m1} - T_p\right) - (T_{m2} - T_p)\right] / \ln\left(\frac{T_{m1} - T_p}{T_{m2} - T_p}\right) = (T_{m1} - T_{m2}) / \ln\left(\frac{T_{m1} - T_p}{T_{m2} - T_p}\right) \tag{4.108}$$

To find the inside coefficient α_{ii}, a correlation is needed for pool boiling combined with a constant stirring rate. This method is described in the literature review, section 2.3.5.

4.3.2 Diabatic Operation

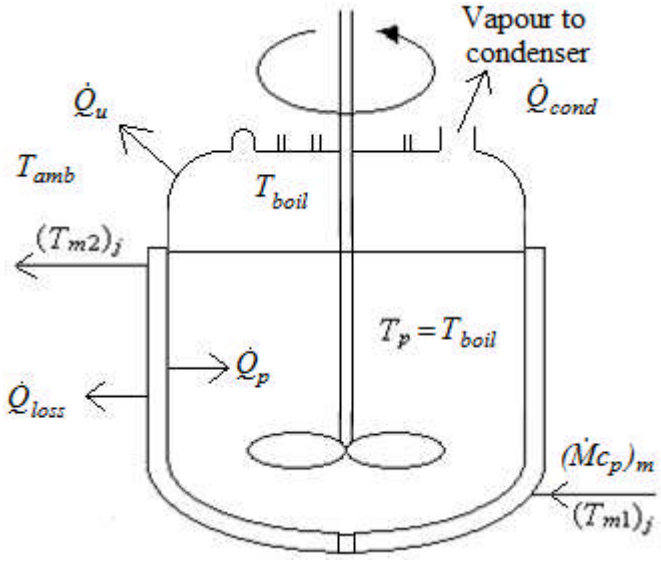

Figure 4.2 – Paths of heat in the reactor during boiling.

The total heat transferred by the jacket has three main pathways, illustrated in figure 4.2. Firstly, heat loss from the jacket ($\dot{Q}_{loss}$), which has been covered in section 4.2.3. Secondly, heat loss from the ullage region ($\dot{Q}_u$). This is assumed to be constant during boiling even at different values of T_{m1}, because it is assumed that the temperature on the

inside surface of the ullage region is the same as the boiling point of the vessel contents. Thirdly, heat carried by the vapour to the condenser.

The vapour taken to the condenser is condensed and cools down as it is collected. The main path of the heat in this process is the condensation itself, which is represented in equation (4.109).

$$\dot{Q}_{cond} = \dot{M}_{evap} h_{fg} \tag{4.109}$$

A correlation for a film heat transfer coefficient can be found for the outer wall. This is a combination of convection and radiation coefficients. The convection coefficient for the outer surface of the outer wall is:-

$$\alpha_{conv} = Nu_{air} \lambda_{air} / z_j \tag{4.110}$$

where:-

$$\mathrm{Nu}_{air} = 0.59(\mathrm{Gr}_{air}\mathrm{Pr}_{air})^{0.25} \tag{4.111}$$

$$\mathrm{Gr}_{air} = L^3 \rho_{air}^2 g \beta_{air} \Delta T / \mu_{air} \tag{4.112}$$

$$\mathrm{Pr}_{air} = c_P \, \mu_{air} / \lambda_{air} \tag{4.113}$$

and the radiation coefficient (where the temperatures in the radiation equation are in Kelvins and σ is the Stefan-Boltzmann constant) is:-

$$\alpha_{rad} = \frac{\varepsilon_g \sigma (T_g^4 - T_{amb}^4)}{T_g - T_{amb}} \tag{4.114}$$

The combined coefficient for the outer wall is:-

$$\alpha_{oo} = \alpha_{conv} + \alpha_{rad} \tag{4.115}$$

4.4 Analysis of the Experiments

The analysis of the results used the experimental profile of the jacket inlet temperature T_{m1} as the input. Detail about the experimental data has been covered in chapter 3.

4.4.1 Temperature Ramping Experiments (Internal Mode)

The lumped parameter model simulation of the first temperature ramping experiment was run in Microsoft Excel. A value of UA was searched for, using the maximum process temperature. This was a temperature of 47.4°C at 9540 seconds, which was also the first

measured value after the set point of the Huber temperature was changed from 50°C to 20°C. The UA value was initially guessed to be 29.0 W K^{-1}. "Goal seek" was used on the data to adjust the UA value so that the same peak temperature occurred at the same time. The UA value here was 23.1 W K^{-1} (U = 50.7 W m^{-2} K^{-1}). The solution is displayed in figure 4.3. The disagreement with experimental values is likely because external heat loss is not accounted for. This is particularly visible as the experimental results have a lower peak temperature and lower temperatures during cooling.

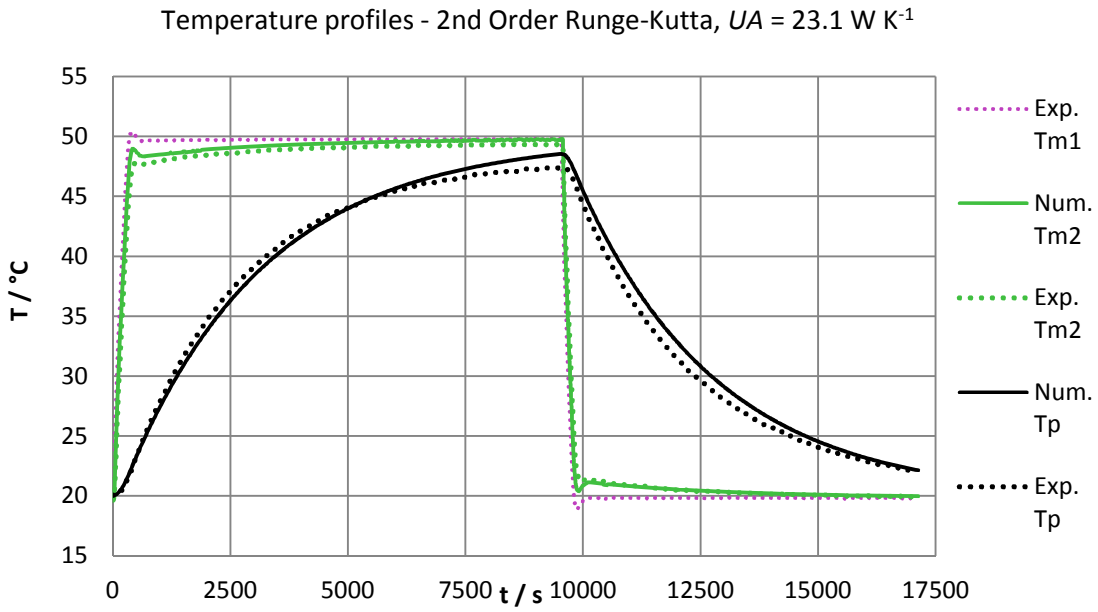

Figure 4.3 – Lumped parameter simulation of the first temperature ramping experiment for the 25 litre vessel. Using UA = 23.1 W K^{-1}.

An overshoot occurs in the experimental data, once heating and cooling are completed, which is reflected in the Runge-Kutta simulations of T_{m2} but not in the experimental data. This is because the response of T_{m2} is assumed to be instant in the numerical solution but in reality the DW-Therm takes some time to go round the jacket and the outlet temperature is not instantly responsive to sudden changes in T_{m1}.

In the second temperature ramping experiment, the values of T_{m1}, T_{m2} and T_p were approximated using the following conditions (temperatures in these equations are represented in Kelvins and without displayed units, for mathematical purposes):-

$$\text{when } 0 \leq t \leq 870.18, \qquad K_0 = 290.5, \qquad K_1 = 0.016815, \tag{4.116}$$

$$T_{m1} = K_0 + K_1 t \tag{4.117}$$

$$\text{and } T_p = K_0 + K_1 t - \frac{K_1}{K_q} - \left(K_0 - T_{p1} - \frac{K_1}{K_q}\right) \exp\left(-\frac{(UA)_j}{(M\tilde{c}_P)_p} t\right) \tag{4.118}$$

$$\text{when } 0 \leq t \leq 900.18, \qquad T_{m2} = 289.6 + 0.015844 \times t \tag{4.119}$$

when $900.18 \leq t \leq 10501.26$, $T_{m1} = 305.4$ (4.120)

and $T_p = T_{m1} + (T_{p1} - T_{m1}) \exp\left(-\frac{(UA)_j}{(M\tilde{c}_P)_p} t\right)$ (4.121)

when $900.18 \leq t \leq 10561.26$,
$T_{m2} = 305.3 - 1.00 \times \exp(-0.0004 \times t)$ (4.122)

when $10531.26 \leq t \leq 11401.56$, $K_0 = 403.45$,
$K_1 = -0.016906$, (4.123)

$T_{m1} = K_0 + K_1 t$ (4.117)

and $T_p = K_0 + K_1 t - \frac{K_1}{K_q} - \left(K_0 - T_{p1} - \frac{K_1}{K_q}\right) \exp\left(-\frac{(UA)_j}{(M\tilde{c}_P)_p} t\right)$ (4.118)

when $10591.26 \leq t \leq 11431.56$, $T_{m2} = 470.6 - 0.015646 \times t$ (4.124)

when $11431.56 \leq t \leq 12061.56$, $T_{m1} = 290.4$ (4.125)

and $T_p = T_{m1} + (T_{p1} - T_{m1}) \exp\left(-\frac{(UA)_j}{(M\tilde{c}_P)_p} t\right)$ (4.121)

when $11461.56 \leq t \leq 12061.56$, $T_{m2} = 291.1$ (4.126)

The numerical values of K_0 and K_1, displayed in equations (4.116), (4.119), (4.120), (4.123), (4.124), (4.125) and (4.126), were obtained from the data using specific data points from the experimental results, with the gradients obtained using equation (4.127) which is based on a well-known technique for finding the gradient of a straight line. Where data point 1 on the temperature-time graph has coordinates (T_1, t_1) and data point 2 has coordinates (T_2, t_2):-

$$K_1 = \frac{T_2 - T_1}{t_2 - t_1} \quad (4.127)$$

The K_0 values were obtained using the same formula but with T_1 as the intercept, becoming:-

$$K_0 = T_2 - K_1 t_2 \quad (4.128)$$

The constants in the exponential function of T_{m2} in equation (4.122) were chosen arbitrarily to closely match the data. Equation (4.117) is the form of the linear function for T_{m1} during ramping, and equations (4.121) and (4.123) are the analytical solutions of T_p using the general polynomial function, in equation (4.52), for n values of 0 and 1 respectively.

For the conditions in equations (4.116) and (4.123), which describe the ramping up and down respectively, the $(UA)_j$ value from equation (4.118) was initially selected as 26.0 W K^{-1}. For the conditions in equation (4.120), which describes the constant jacket inlet temperature at the higher temperatures, the $(UA)_j$ value from equation (4.121) was initially selected as 29.0 W K^{-1}. For the conditions in equation (4.125), the $(UA)_j$ value from equation (4.121), which describes the constant jacket inlet temperature at the lower temperatures, was initially selected as 28.0 W K^{-1}. These $(UA)_j$ values were arbitrarily selected so that the results could be seen visually to closely match the experimental data. When the curves are fitted using these $(UA)_j$ values with equations (4.116) to (4.126), they match the experimental results very closely, as can be seen in figure 4.4.

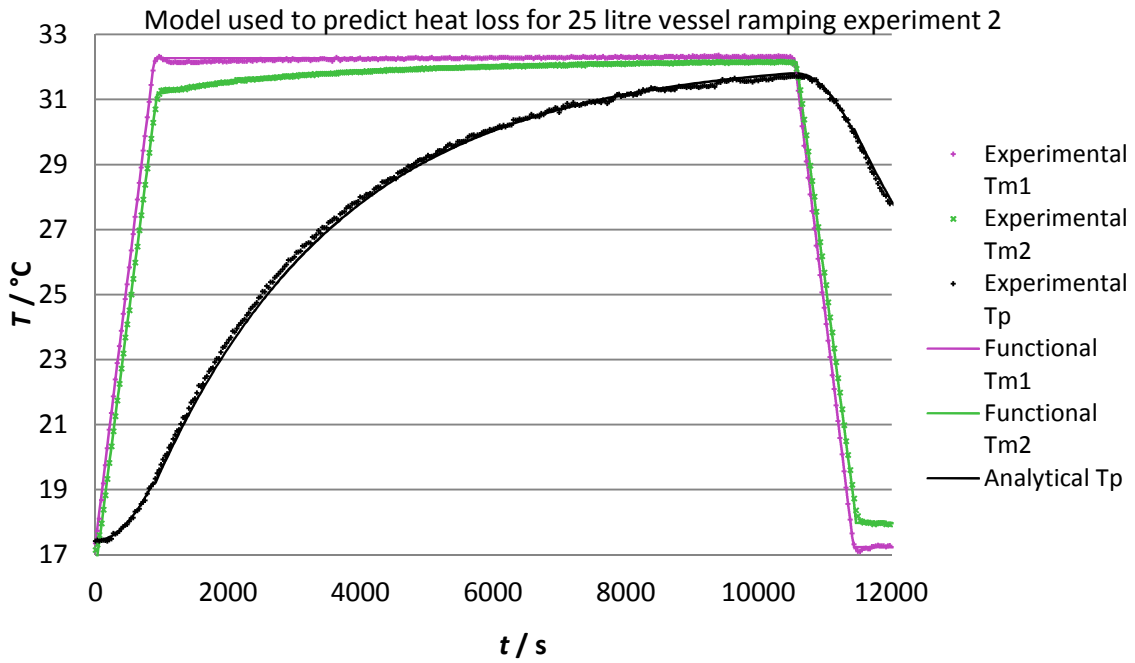

Figure 4.4 – Experimental data for jacket inlet and outlet temperatures and process temperature, compared to the functional values for jacket inlet and outlet temperatures and analytical values for process temperature.

Figure 4.4 seems to illustrate visibly that the curvature was stronger in the experiments than in this simulation, which has a constant UA value. This would mean that the actual UA value between the jacket and the process temperature was higher with higher set temperatures, but the equivalent UA value was reduced due to heat losses to the surroundings by both surface evaporation and through the outer side of the un-insulated jacket. This could also explain why the simulated UA values were more significantly lower when the desired temperature was higher. That is, a set point of 50°C (the first temperature ramping experiment) yielded a simulated UA value of 23.1 W K^{-1} and a set

point of 32.5°C (the second temperature ramping experiment) yielded a simulated UA value of 27.7 W K^{-1}.

The lumped parameter solution to the second temperature ramping experiment is displayed in figure 4.5. The UA value for the simulation of this experiment was also initially set as 29.0 W K^{-1}, based on the first temperature ramping experiment, then adjusted using Goal Seek. For the alternative UA value, the experimental peak temperature here was 31.7°C at 10530 seconds. The UA value found in this case was 27.7 W K^{-1} (U = 60.8 W m^{-2} K^{-1}).

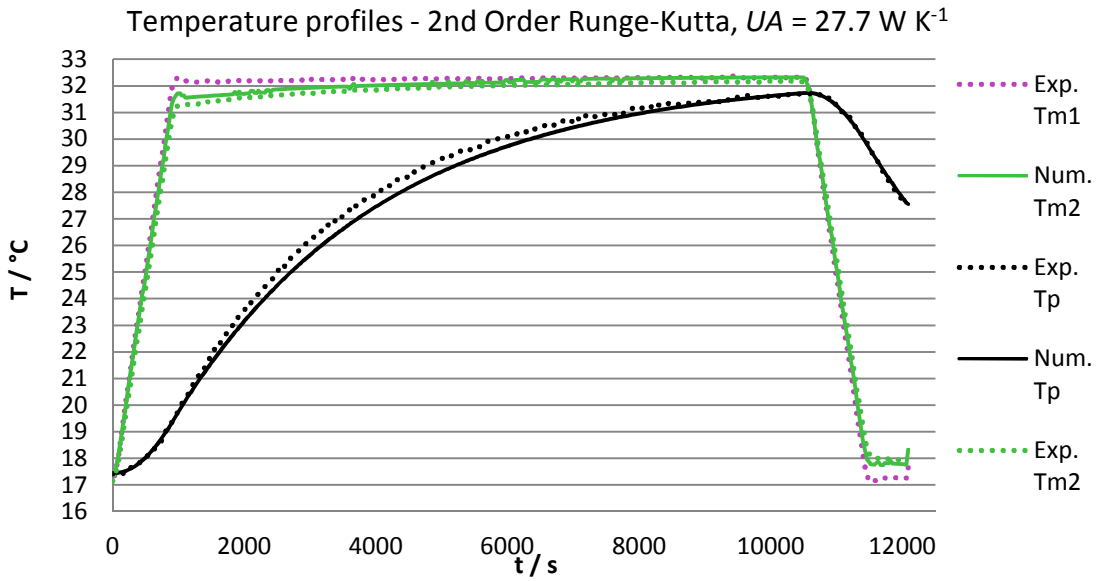

Figure 4.5 – Lumped parameter simulation of the second temperature ramping experiment for the 25 litre vessel. UA = 27.7 W K^{-1}.

Some of the discrepancy between the final UA value in figure 4.3 (23.1 W K^{-1}) compared to figures 4.4 and 4.5 (27.7 W K^{-1}) may arise from slightly different levels of water in the vessel. To take this into account, the following equations may be used to account for the distance along the vessel (height, z):-

$$\left(\dot{M}\tilde{c}_P\right)_m \frac{dT_{m(j)}}{dz} = U'A'(T_p - T_{m(j)}) \tag{4.129}$$

$$\text{At } z = 0,\ T_{m(j)} = T_{m1} \tag{4.130}$$

Where U' is the overall heat transfer coefficient when the water surface is at a specified level, and A' is the area per unit height. The overall value of U' is the average value of U in this case, and is expected to be lower if the water level is lower, due to the lowered overall thermal conductivity inside the vessel.

At heights $z > 0$, U changes depending on whether the jacket is transferring heat to either air or water in the vessel. The average process temperature for a specified water level is denoted T_p'. The effectiveness at a specified water level is E'. Note that at the maximum height Z, there is still some air being heated at the top of the jacket.

Figure 4.6 displays the results of the analytical model of the second temperature ramping experiment including heat loss to the surroundings. Here, the heat transfer coefficient per unit height (UA') was used. The heat transfer coefficients were initially chosen to visually match the data. In this experiment, there was only a small amount of heat loss due to the small difference between the jacket inlet temperature and the ambient temperature (this difference was 13°C). As a result, setting the heat loss to zero would result in very little deviation from the experimental values. To make the analytical solution of the process temperature curve most closely match the experimental results, a jacket UA' value of 94.1 W m^{-1} K^{-1} (U_j = 65.7 W m^{-2} K^{-1}) and a heat loss UA' value of 27.4 W m^{-1} K^{-1} (U_{loss} = 12.9 W m^{-2} K^{-1}) were required. These were found using "Goal Seek" and the sum of squares of difference between the analytical solution and the experimental values. The average residual error (root mean square) for T_p was 0.107°C for the full run.

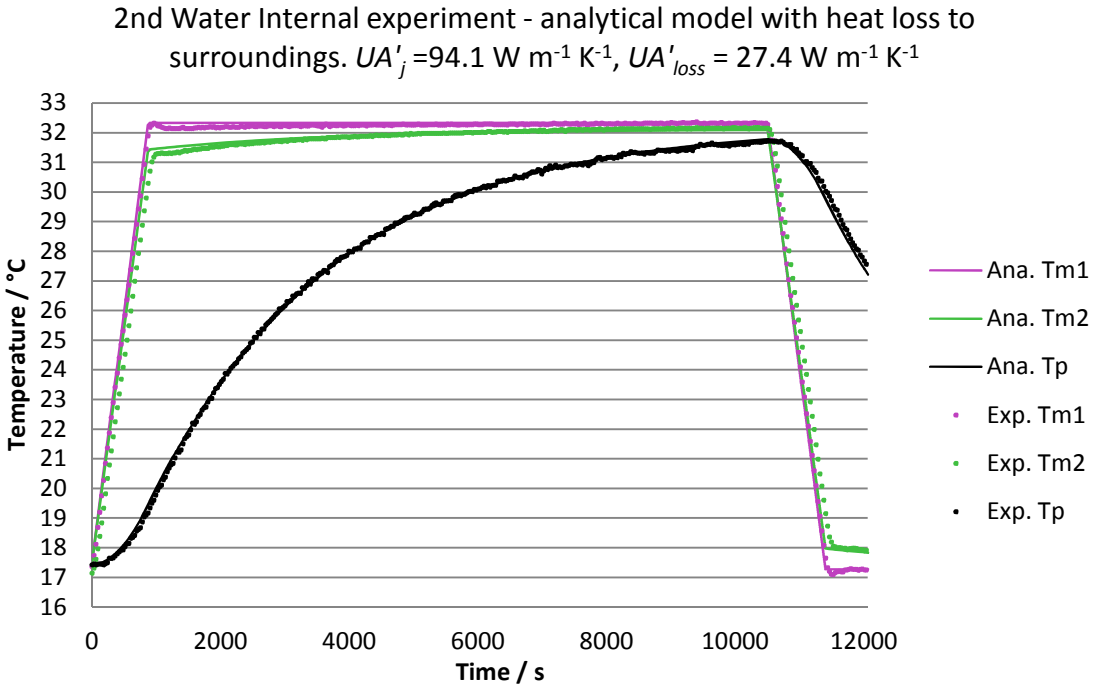

Figure 4.6 – Results of the analytical model including heat loss, with $(UA')_j$ and $(UA')_{loss}$ found with Goal Seek.

During heating, the average residual error in this analytical model was 0.086°C. As a rule of thumb, most temperature measurements in this context are taken to have an error of about 0.1°C, so this model produces some quite accurate results.

During cooling, the model seems to under-predict the temperature and the average residual error is 0.285°C. This may be caused by a slight underestimation of the delay in response to cooling in the current model.

Figures 4.7 and 4.8 display the values of $(UA')_{loss}$ in the second temperature ramping experiment for the 25 litre vessel. The experimental and predicted values were both worked out as displayed in equations (4.131) to (4.133). The difference is that the experimental values used only the raw data and the predicted values used the analytical approximations of T_{m1} and T_{m2} and the analytical solution of T_p which used only T_{m1} and the operating conditions. In this way, T_{m2} was used to find the heat loss coefficient.

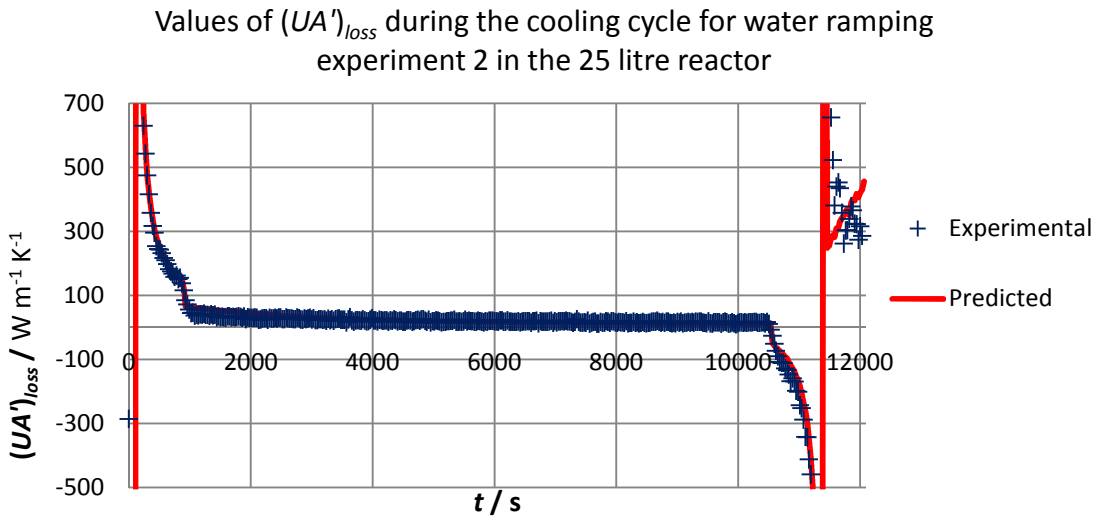

Figure 4.7 – A graph displaying values of the heat transfer coefficient for heat loss, multiplied by area per unit height. The predicted values use analytical approximations of the experimental values of temperature.

$$\dot{Q}_m = \left(\dot{M}c_P\right)_m (T_{m1} - T_{m2}) \tag{4.131}$$

$$\dot{Q}_p = \left(\dot{M}c_P\right)_p \frac{T_p(t_2) - T_p(t_1)}{t_2 - t_1} \tag{4.132}$$

$$UA'_{loss} = \frac{\dot{Q}_m - \dot{Q}_p}{\frac{(T_{m1} + T_{m2})}{2} - T_{amb}} \tag{4.133}$$

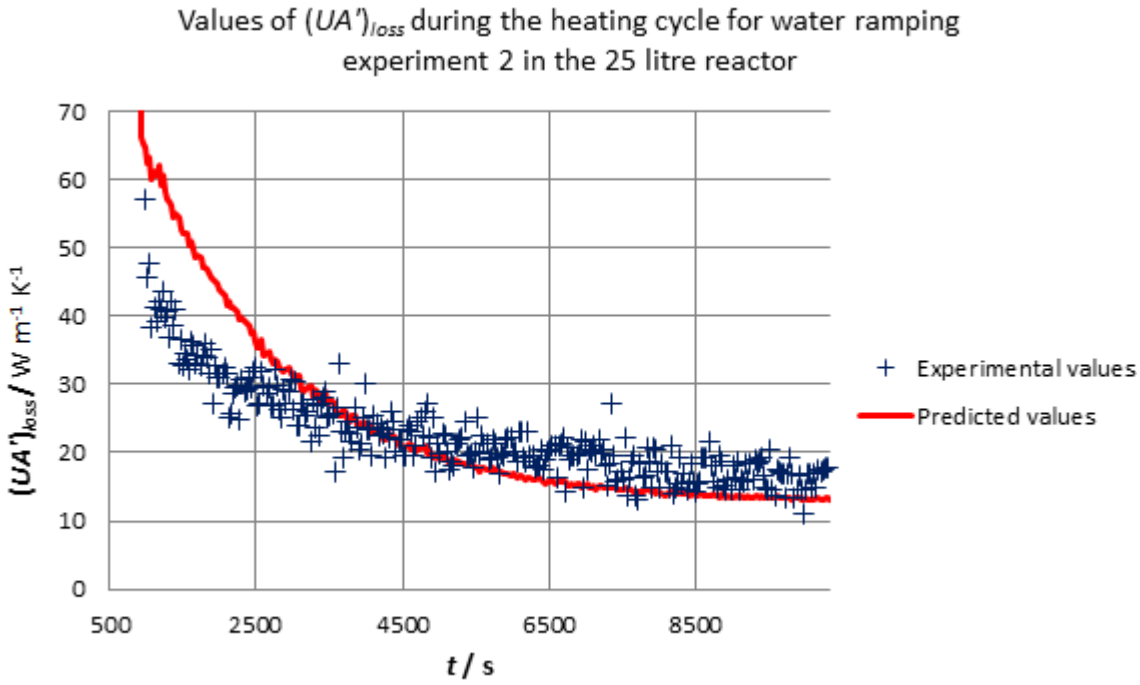

Figure 4.8 – Part of figure 4.7; a closer graph displaying values of the heat transfer coefficient for heat loss, multiplied by area per unit height, during the heating period only. The predicted values use analytical approximations of the experimental values of temperature.

All results used the experiment's measured transient data of the jacket flow and the densities based on the measured temperatures, thus some noise can be seen in the "predicted" values as well as the "experimental" values. The results closely match except during the cooling cycle, where the "predicted" values increase while the empirical values are much more scattered but seem overall to decrease instead.

The asymptotes in figure 4.7 occur when the temperature difference briefly passes by zero (as displayed in figure 4.6), at which point the instantaneous heat transfer coefficient cannot be defined. Towards the start of the experiment, in figure 4.8, the difference between the analytical solution of T_{m2} and the experimental values are due to the thermal capacity of the vessel, temporarily increasing the value of $(UA')_{loss}$ to much higher values, as seen in figures 4.7 and 4.8.

4.4.2 Batch Distillation Experiments

Figures 4.9 and 4.10 display results for the analytical model with heat loss included. In figures 4.9 and 4.10, the pure methanol and pure water distillation experiments, the analytical solution for the T_{m2} curve was much closer to the experimental values at the start, compared to figure 4.6, despite the same thermal capacity of the vessel. This is

because the temperature difference between the jacket and the process was larger at the start (49°C in figure 4.9, compared to 14°C in figure 4.6) and the vessel thus heated up proportionately faster, causing less of a lag in T_{m2}. Once boiling started, during the steady phases (at constant T_{m1} values), the experimental values of T_{m2} also became constant. At these steady states, at constant pressure and jacket heat capacity rate, the difference between the experimental values of T_{m1} and T_{m2} depended only on the ambient temperature (T_{amb}), which was assumed as a constant 19.4°C in these experiments (based on a reading from a spare temperature probe that was placed near the reactor).

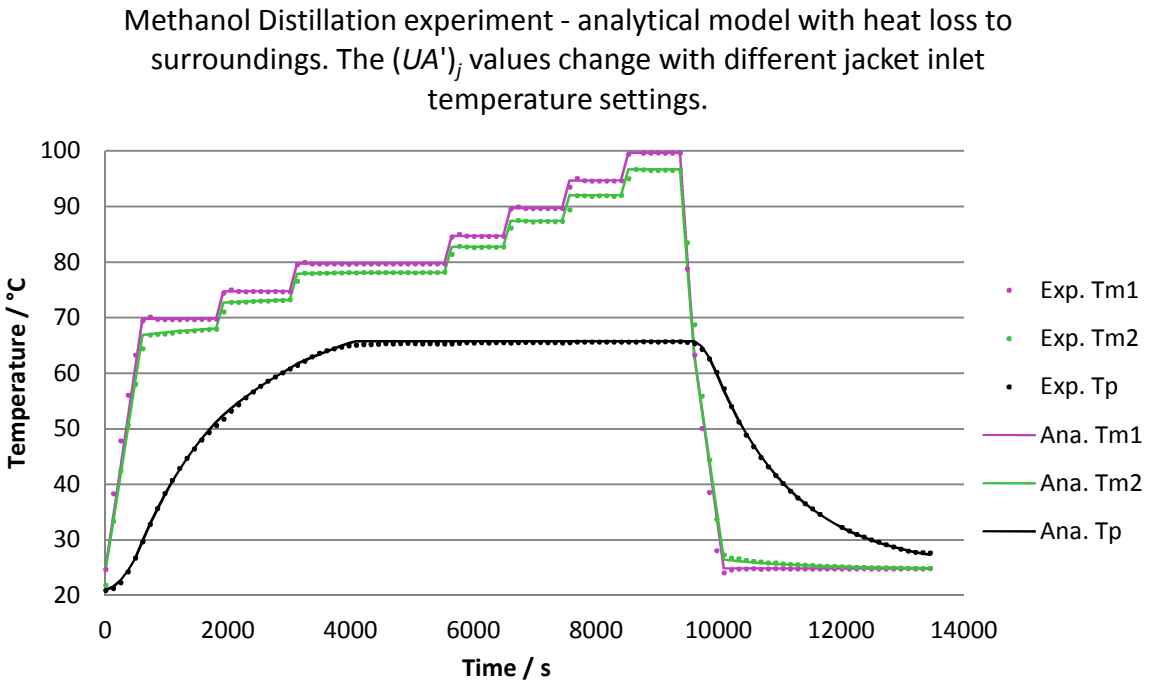

Figure 4.9 – Results of the analytical model with heat loss, for the methanol distillation experiment, with $(UA')_j$ and $(UA')_{loss}$ found during all constant-temperature times with Goal Seek.

The (UA') values used to produce the analytical solutions in figures 4.9 and 4.10 are the heat transfer coefficient multiplied by the area per unit length. As previously mentioned, the area A for the 25 litre vessel was 0.422 m^2 (QVF, 2005). The liquid height at 20 litres capacity Z was 0.318 m. The area per unit length, A', is the ratio of these two values, which is 1.327 for the 25 litre vessel. For the pure methanol distillation experiment, the $(UA)_j$ value of 27.7 W K^{-1} would correspond to a $(UA')_j$ value of 87.1 W m^{-1} K^{-1} (U_j = 60.8 W m^{-2} K^{-1}). For the deionised water distillation experiment, the $(UA)_j$ value of 34.0 W K^{-1} would correspond to a $(UA')_j$ value of 106.9 W m^{-1} K^{-1} (U_j = 80.6 W m^{-2} K^{-1}).

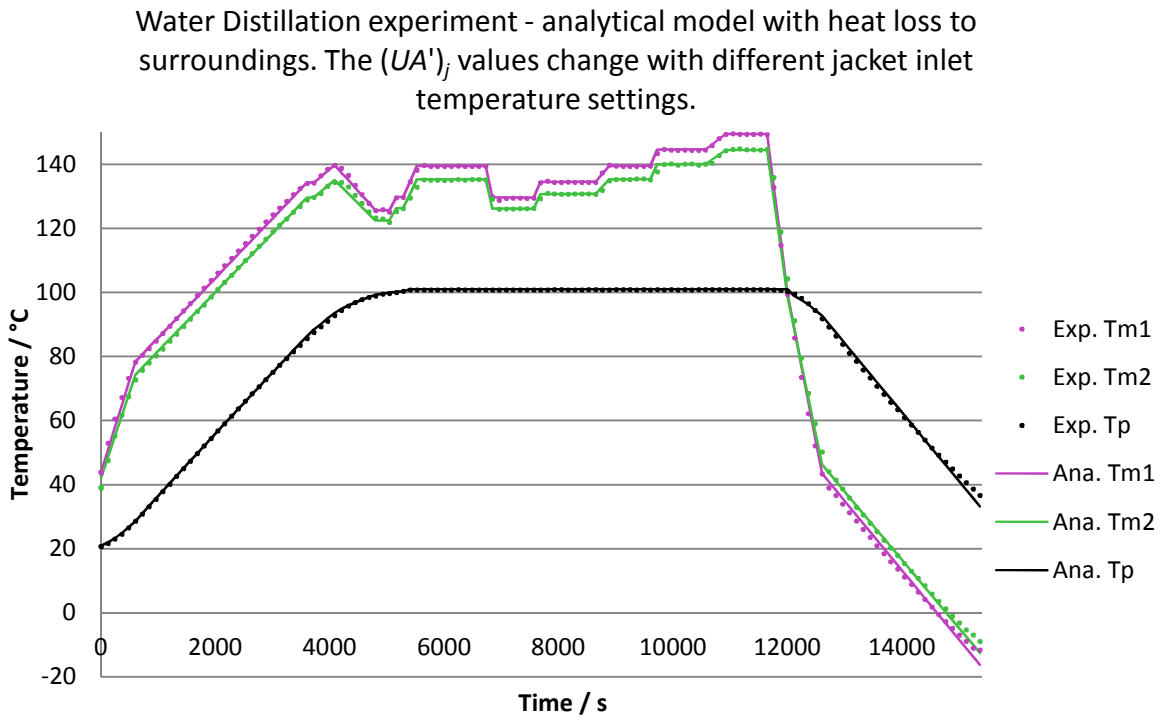

Figure 4.10 – Results of the analytical model with heat loss, for the water distillation experiment, with $(UA')_j$ and $(UA')_{loss}$ found for all constant-temperature times with Goal Seek.

Note that a uniform distribution of flow in the jacket has been assumed, although it is likely that in reality, the flow would be non-uniform. Also, the Reynolds number calculated inside the jacket using this assumption varied between 673 and 791 at the different jacket temperatures during the methanol boiling. This would correspond to a laminar flow. However, because the viscosity changes significantly with temperature (as displayed in figure 4.11), it was assumed that the correlation for turbulent flow in concentric annuli found in ESDU 81045 (1981) could be used.

Nevertheless, the ESDU 81045 (1981) correlation for the jacket side heat transfer coefficients (see the literature review, section 2.3.4) yielded impossible results because the heat transfer coefficients were too low (21.5 W m^{-2} K^{-1} to 23 W m^{-2} K^{-1}). This would correspond to a large temperature drop of 63°C in the jacket film heat transfer coefficient, when the maximum possible is 4.1°C if the process side film heat transfer coefficient is infinite. Simply guessing the values of α_j as between 635 W m^{-2} K^{-1} and 1170 W m^{-2} K^{-1}, as suggested by Hewitt *et al.* (1994), would have yielded better results. The Reynolds number range for this correlation is from 4×10^3 to 3×10^6. It is expected that because the expected Reynolds number is out of the range applicable to this correlation, the calculated values of α_j are not applicable here. It would also seem that in reality, the non-uniform

flow distribution significantly helps the heat transfer in this regard by enhancing turbulence.

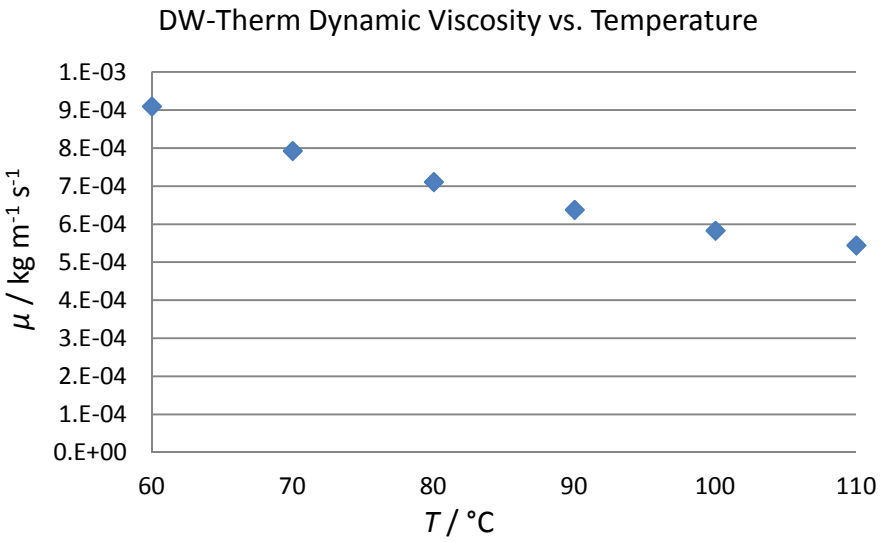

Figure 4.11 – DW-Therm dynamic viscosity vs. temperature.

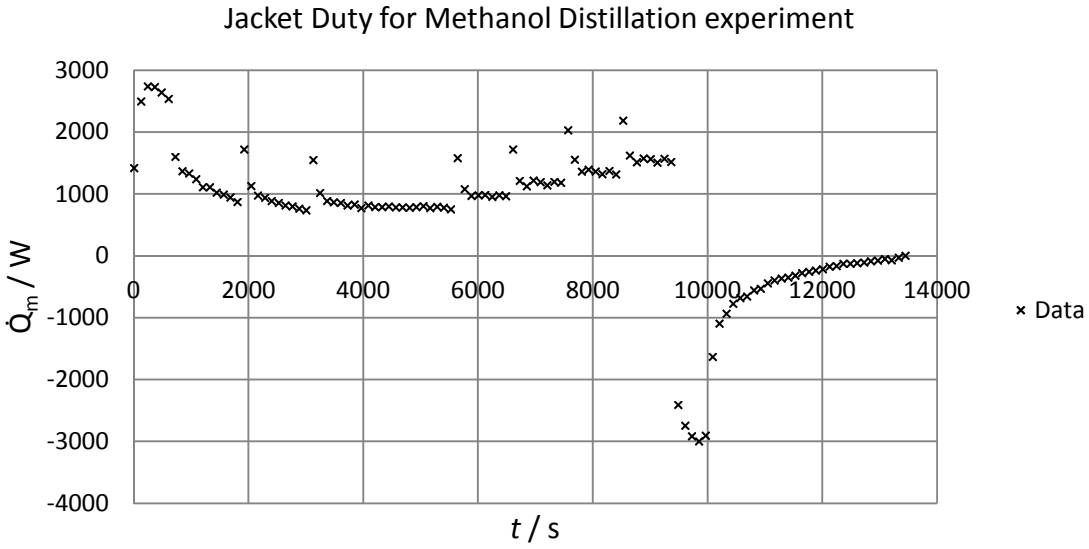

Figure 4.12 – Jacket heat duties for the methanol distillation experiment.

The values of the overall heat transfer coefficient were expected to change slightly depending on the temperature, due to different boiling stages, changing physical properties of the Huber oil, and radiation effects.

In figure 4.12, the methanol was boiling from approximately 5000 to 9000 seconds into the experiment. In this region, the jacket temperature was increased in stages. The important times are when the jacket temperatures were constant and the methanol was boiling.

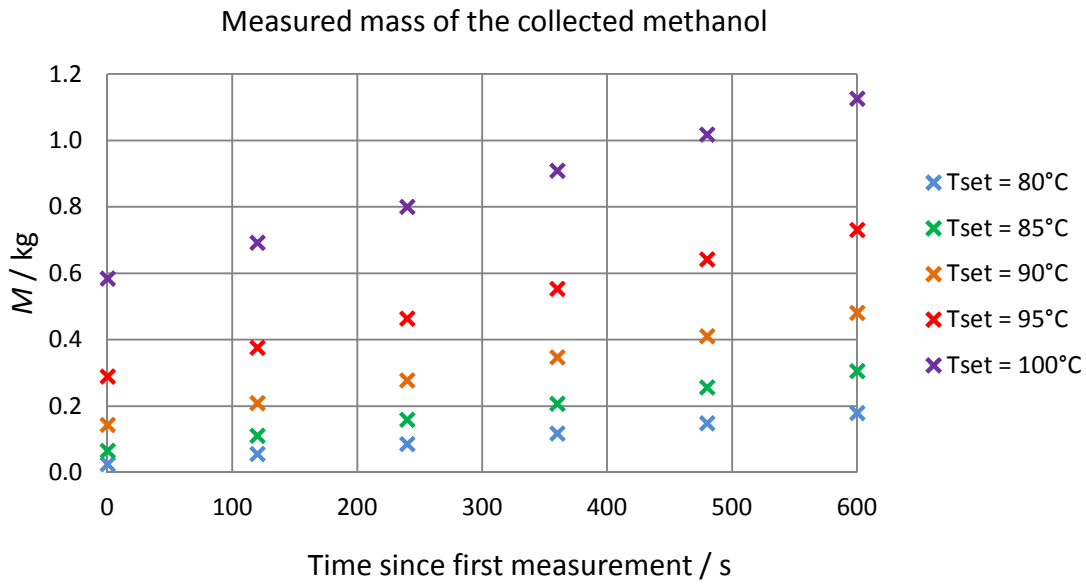

Figure 4.13 – Mass of the collected methanol.

The collected amount of methanol was recorded during the five times during the experiment in which boiling took place with a constant jacket inlet temperature. A graph displaying the measurements of mass collected is in figure 4.13. The difference between these data points was taken as the mass rate ($\dot{M}$). Multiplying this by the latent heat of vaporisation of methanol at 1 atmosphere pressure (1094.5 kJ kg^{-1}) gives the value of $\dot{M}h_{fg}$, which is the heat rate required to condense the collected methanol. These results are displayed in figure 4.14.

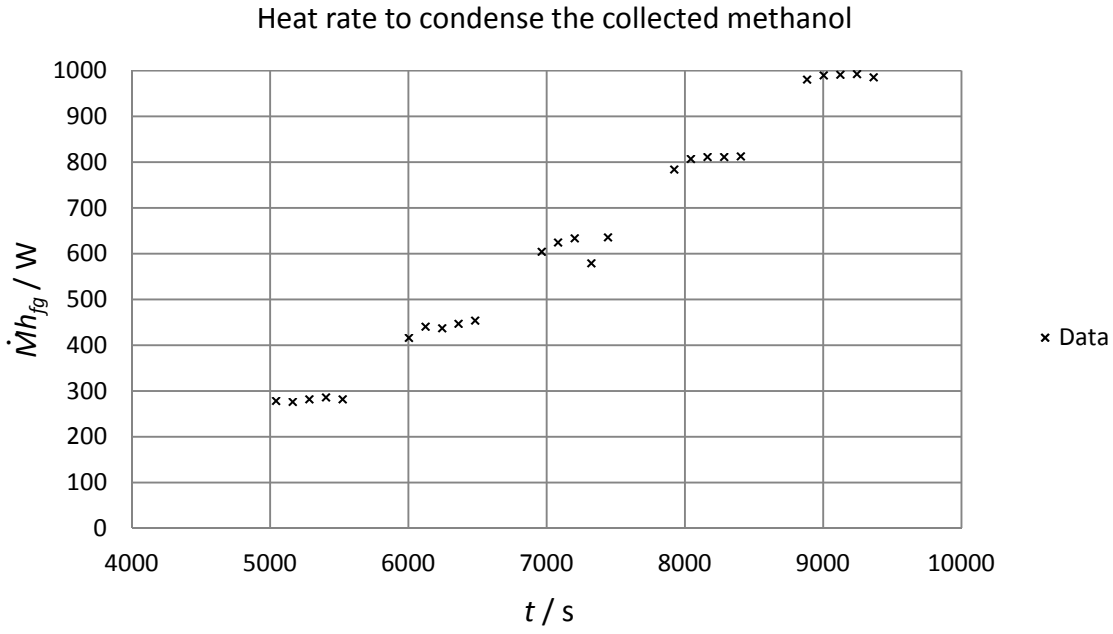

Figure 4.14 – Heat transfer rate needed to condense the collected methanol.

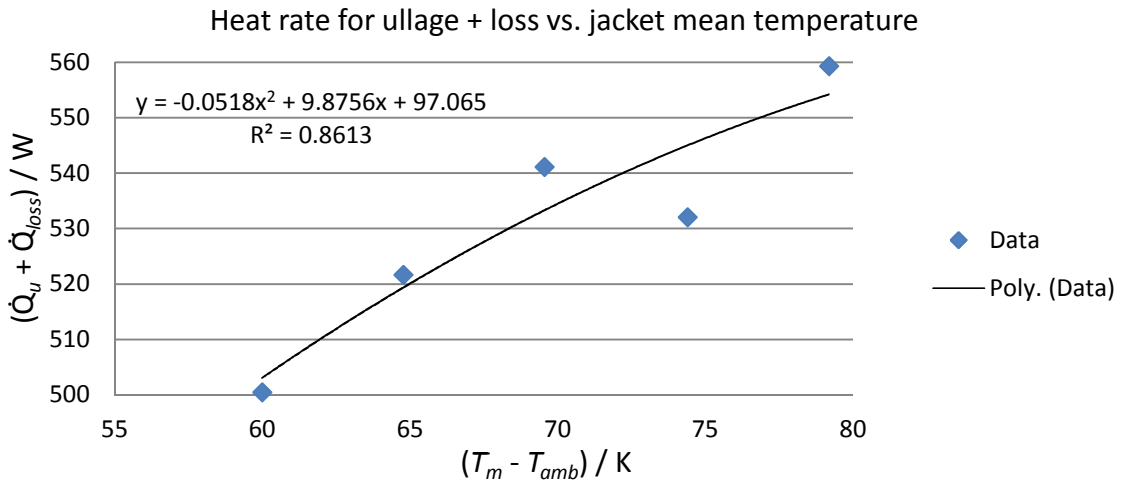

Figure 4.15 – Remaining heat rate for each temperature step.

The mode values of $\dot{M}h_{fg}$ were taken as the average, eliminating some anomalies caused by the condensation process, as it was still transient during recording. When these values are taken from $\dot{Q}_m$, the remaining heat values ($\dot{Q}_u + \dot{Q}_{loss}$) are displayed in figure 4.15. A contentious second-order polynomial line has been fitted to account for some possible variation in heat transfer coefficients with temperature (that is, a non-linear relationship between heat transferred and temperature difference). However, it is not recommended to use this because there is too much extrapolation and there are too few data points.

If the experiment were repeated, it would be suggested to find a jacket temperature at which the rate of collection is zero, that is, all the methanol re-condenses before it reaches the condenser. Also, the effects of heat loss through the ullage and the sides of the jacket may be reduced by using insulation providing a more accurate calculation of the jacket-to-process heat transfer coefficient, although some heat would still escape through the insulation.

If the heat loss term has the polynomial relationship to $\tilde{T}_m - T_{amb}$, displayed in figure 4.15, the constant value of $\dot{Q}_u$ during the methanol boiling experiment would be 97.1 W (the intercept of the curve). The difference between $\dot{Q}_{loss}$ values at different jacket temperatures can also be worked out from figure 4.12. The $\dot{Q}_p$ values are found from equation (4.134).

$$\dot{Q}_p = \dot{Q}_m - \dot{Q}_{loss} = \dot{Q}_u + \dot{M}h_{fg} \tag{4.134}$$

With the values of $\dot{Q}_p$ and $\dot{Q}_{loss}$ known, an attempt to find individual heat transfer coefficients for the jacket can be undertaken. The correlation found in Garvin (1999)

predicts different coefficients for the surfaces inside the jacket on the inner wall (α_{io}) and outer wall (α_{oi}), based on the different viscosities caused by the different temperatures on either surface. The Garvin (1999) correlation does seem to give plausible values for either α_{io} or α_{oi}, and the ratio between these two values can be used to infer one from the other when one of them could be found by solving equation (4.135) for the whole wall.

$$\dot{Q} = UA(T_h - T_c) = (\alpha A)_h(T_h - T_{hw}) = \frac{2\pi L\lambda_w}{\ln\left(\frac{d_o}{d_i}\right)}(T_{hw} - T_{cw}) = (\alpha A)_c(T_{cw} - T_c) \quad (4.135)$$

In the most reliable method found to determine the heat transfer coefficients, the value of α_{oi} was found first by substituting the values for the outer jacket wall into equation (4.135) to give equation (4.136).

$$\dot{Q}_{loss} = UA\left(\tilde{T}_m - T_{amb}\right) = (\alpha A)_{oi}\left(\tilde{T}_m - T_{oi}\right) = \frac{2\pi L\lambda_g}{\ln\left(\frac{d_{oo}}{d_{oi}}\right)}(T_{oi} - T_{oo}) = (\alpha A)_{oo}(T_{oo} - T_{amb}) \quad (4.136)$$

In equation (4.136), α_{oo} is a combination of heat transfer by free convection and radiation, which is found by the correlations described in section 4.3.2.

The ratio found by the Garvin (1999) correlation is then used to find α_{io} and expected values for the combined coefficient of boiling with agitation (α_{ii}) by substituting the values for the outer jacket wall into equation (4.135) to give equation (4.137).

$$\dot{Q}_p = UA\left(\tilde{T}_m - T_p\right) = (\alpha A)_{io}\left(\tilde{T}_m - T_{io}\right) = \frac{2\pi L\lambda_g}{\ln\left(\frac{d_{io}}{d_{ii}}\right)}(T_{io} - T_{ii}) = (\alpha A)_{ii}\left(T_{ii} - T_p\right) \quad (4.137)$$

Tables 4.1, 4.2 and 4.3 display various parameters measured or calculated during the methanol experiment. In these three tables, T_p is 64.7 °C and T_{amb} is 19.0 °C.

Table 4.1 displays the average jacket temperature and calculated values of heat passing from the jacket to the process ($\dot{Q}_p$) and from the jacket to the surroundings ($\dot{Q}_{loss}$). It also displays the inner and outer wall jacket heat transfer coefficients predicted by the Garvin (1999) correlation. These values provide a useful ratio between the inner and outer walls, which could be used in other correlations.

Table 4.1 – Comparison of heat transfer coefficients in the methanol distillation experiment, using correlations from the literature.

Parameter	T_{set} **=80°C**	T_{set} **=85°C**	T_{set} **=90°C**	T_{set} **=95°C**	T_{set} **=100°C**
$\tilde{T}_m$ / °C	78.9	83.7	88.5	93.3	97.8
$\dot{Q}_p$ / W	375.5	550.8	751.1	905.4	1090.1
$\dot{Q}_{loss}$ / W	405.9	422.4	436.4	447.9	457.2
U_j / W m^{-2} K^{-1}	62.4	67.1	72.2	72.0	73.8
U_{loss} / W m^{-2} K^{-1}	10.7	10.3	9.9	9.5	9.1
α_{io} / W m^{-2} K^{-1} (Garvin, 1999) (equation 2.47)	226.9	229.8	237.1	238.3	240.5
α_{oi} / W m^{-2} K^{-1} (Garvin, 1999)	227.5	230.5	237.9	239.2	241.5
α_{boil} / W m^{-2} K^{-1} (Cooper, 1984) (equation 2.63)	337.1	435.9	536.6	608.1	688.7
α_a / W m^{-2} K^{-1} (Penney, 1983) (equation 2.28)	196.4	196.6	196.6	196.6	196.6
α_{ii} / W m^{-2} K^{-1} (Alane, 2007) (equation 2.59)	1589	1635	1681	1714	1751

Additionally, in table 4.1, the agitation (Penney, 1983) and boiling (Cooper, 1984) heat transfer coefficients are displayed, as well as the Penney-Cooper correlation developed by Alane (2007) for the inner wall.

In the equations used to find the combined boiling and agitation coefficient, described by Alane (2007), the values of vapour mass quality and boiling number in the process side were difficult to assess because the cross sectional flow is harder to define within the vessel. In this case a ballpark estimated vapour mass quality of 0.05 and a boiling number of 6.7×10^{-4} were used, resulting in reasonable values. However, the Cooper correlation (with no agitation) has more well-defined parameters and is used in this thesis by default.

The Garvin (1999) correlation produced reasonable values of heat transfer coefficient in the jacket (displayed in table 4.1). Values for both α_{io} and α_{oi} could be found, and it was investigated whether the ratio between these could be used to predict an alternate value of α_{io} if α_{oi} is known, using back-calculated values of α_{oi} from equation 4.136. This method started by finding the temperature T_{oo} using the convection and radiation formulae as described in section 4.3.2.

Table 4.2 – Calculated values of the outside film heat transfer coefficient.

Parameter	T_{set} **=80°C**	T_{set} **=85°C**	T_{set} **=90°C**	T_{set} **=95°C**	T_{set} **=100°C**
α_{conv} / W m^{-2} K^{-1} (Convection, outside)	5.30	5.34	5.37	5.39	5.41
α_{rad} / W m^{-2} K^{-1} (Radiation, outside)	6.05	6.11	6.15	6.19	6.21
α_{oo} / W m^{-2} K^{-1} (Total, outside)	11.36	11.44	11.52	11.58	11.63

Table 4.3 – Back-calculated values of jacket and process film heat transfer coefficients.

Parameter	T_{set} **=80°C**	T_{set} **=85°C**	T_{set} **=90°C**	T_{set} **=95°C**	T_{set} **=100°C**
α_{oi} / W m^{-2} K^{-1} (Using equation 4.136)	450.0	255.9	208.9	175.1	158.5
α_{io} / W m^{-2} K^{-1} (Using the ratio of α_{io} to α_{oi} from Garvin, 1999)	447.1	251.0	201.9	167.4	149.4
α_{ii} / W m^{-2} K^{-1} (Using equation 4.137)	70.0	124.3	279.8	690.9	-1130 (negative)

Table 4.4 – Alternative pool boiling coefficients.

Parameter	T_{set} **= 80°C**	T_{set} **= 85°C**	T_{set} **= 90°C**	T_{set} **= 95°C**	T_{set} **= 100°C**
α_{boil} / W m^{-2} K^{-1} (Forster and Zuber, 1955)	662.1	805.6	948.3	1045.8	1152.3
α_{boil} / W m^{-2} K^{-1} (Cooper, 1984)	337.1	435.9	536.6	608.1	688.7
α_{boil} / W m^{-2} K^{-1} (Mostinskii, 1963)	204.4	267.3	332.1	378.5	431.0
α_{boil} / W m^{-2} K^{-1} (Palen *et al.*, 1972)	199.2	260.5	323.7	369.0	420.1
α_{boil} / W m^{-2} K^{-1} (Bier *et al.*, 1983)	192.3	251.4	321.4	356.0	405.4

Displayed in table 4.2 are the calculated heat transfer coefficients for convection and radiation, and the combined outer wall coefficient, which can be used in equations 4.136 and 4.137. This can then be used to find the expected temperatures and heat transfer coefficients throughout the system if Garvin's (1999) ratio is used to make the jump between the outer and inner sides of the jacket. The results gave some apparent values of heat transfer coefficient (displayed in table 4.3); however, this method is not recommended because the calculated heat transfer coefficient passes an asymptote and

becomes negative, which is impossible because it would mean the net heat is travelling from cold to hot.

Table 4.4 displays alternative values for the pool boiling coefficients, for use in finding other correlations for α_{ii}. The range of possible values is quite large, for example the largest values (predicted by the correlation in Forster and Zuber, 1955) are about three times larger than the smallest values (predicted by Bier *et al*., 1983).

4.5 Distributed Parameter Model

The distributed parameter model (developed by Bentham, 2011) relaxes assumptions of instant heat conduction through the walls. It simulates transient operation by allowing the walls to heat up over time. In Bentham (2011), it was assessed that in large industrial scale reactors, perhaps as much heat goes into heating the walls and equipment as it does into the process, as the total heat capacity of the wall may be similar to the total heat capacity of the content of the vessel. A time delay in the heating or cooling response is present due to the thermal inertia of the solid.

4.5.1 Derivation of the Distributed Parameter Model

Neglecting the source term (from diffusion and convection at small scales), the general energy equation in cylindrical coordinates for pure Newtonian fluids with constant density ρ and thermal conductivity λ is as follows (adapted from Bird *et al.*, 2002):-

$$\rho c_P \left(\frac{\partial T}{\partial t} + v_r \frac{\partial T}{\partial r} + \frac{v_\theta}{r}\frac{\partial T}{\partial \vartheta} + v_z \frac{\partial T}{\partial z}\right) = \lambda \left[\frac{1}{r}\frac{\partial}{\partial r}\left(r\frac{\partial T}{\partial r}\right) + \frac{1}{r^2}\frac{\partial^2 T}{\partial \vartheta^2} + \frac{\partial^2 T}{\partial z^2}\right] \qquad (4.138)$$

where c_P is the heat capacity, T is the temperature, t is the time, r is the radius, ϑ is the angle around the cylinder, z is the height, and v is the velocity component (with the subscripts denoting its direction).

The following subsets of this equation will be derived, assuming perfect symmetry around the jacket, perfect mixing in the vessel and no longitudinal conduction of heat in the wall:-

In the jacket:-

$$\left.\frac{\partial T_m}{\partial z}\right|_{t'} = -K_m\left(T_m - T_w|_{r=r_o}\right) \qquad (4.139)$$

where:-

$$K_m = \alpha_o A'_o / \left(\dot{M} c_P\right)_m \tag{4.140}$$

In the wall:-

$$\left.\frac{\partial T_w}{\partial t'}\right|_z = K_w \left(\left.\frac{\partial^2 T_w}{\partial r^2}\right|_z + \frac{1}{r} \left.\frac{\partial T_w}{\partial r}\right|_z \right) \tag{4.141}$$

where:-

$$K_w = \lambda_w / (\rho c_P)_w \tag{4.142}$$

In the vessel:-

$$\frac{\mathrm{d}T_p}{\mathrm{d}t'} = K_p \left(\left.\tilde{T}_w\right|_{r=r_i} - T_p \right) \tag{4.143}$$

where:-

$K_p = \alpha_i A_i / (M c_P)_p$ and $\left.\tilde{T}_w\right|_{r=r_i}$ is the mean inner wall temperature. (4.144)

Assuming symmetry (neglecting any changes with ϑ), for the conditions in equation (4.145) equation (4.146) applies to the glass wall, where the subscript w denotes the values in the vessel wall, and the radius r is the distance from the central axis of the vessel.

$$t > 0, \qquad r_i \le r \le r_o, \qquad 0 < z < Z \tag{4.145}$$

$$(\rho c_P)_w \frac{\partial T_w}{\partial t} = \lambda_w \left(\frac{\partial^2 T_w}{\partial r^2} + \frac{1}{r} \frac{\partial T_w}{\partial r} + \frac{\partial^2 T_w}{\partial z^2} \right) \tag{4.146}$$

Assuming either an isothermal jacket fluid or no longitudinal (vertical) heat conduction, $Z >> (r_o - r_i)$. That is, the height is far greater than the thickness of the vessel wall, the partial derivative with respect to z is insignificant, and thus equation (4.146) becomes equation (4.147).

$$(\rho c_P)_w \frac{\partial T_w}{\partial t} = \frac{\lambda_w}{r} \frac{\partial}{\partial r} \left(r \frac{\partial T_w}{\partial r} \right) \tag{4.147}$$

Here T_w is itself still a function of z, provided that the jacket fluid is non-isothermal. Heat transfer to or from the jacket fluid will affect its temperature as it travels in the z direction, and this will affect the adjacent wall temperature.

The equations can be further simplified by converting Eulerian time to Lagrangian time (where $\boldsymbol{v}$ is the velocity vector of the heat transfer fluid), as follows:-

$$t' = t - \frac{z}{\boldsymbol{v}} \tag{4.148}$$

$$\therefore T(t,z) \rightarrow T(t',z) \tag{4.149}$$

The derivative of the temperature is as follows:-

$$\mathrm{d}T = \left.\frac{\partial T}{\partial t'}\right|_z \mathrm{d}t' + \left.\frac{\partial T}{\partial z}\right|_{t'} \mathrm{d}z \tag{4.150}$$

$$\therefore \left.\frac{\mathrm{d}T}{\mathrm{d}t}\right|_z = \left.\frac{\partial T}{\partial t'}\right|_z \left.\frac{\mathrm{d}t'}{\mathrm{d}t}\right|_z + \left.\frac{\partial T}{\partial z}\right|_{t'} \left.\frac{\mathrm{d}z}{\mathrm{d}t}\right|_z \tag{4.151}$$

$$\text{and } \left.\frac{\mathrm{d}T}{\mathrm{d}z}\right|_t = \left.\frac{\partial T}{\partial t'}\right|_z \left.\frac{\mathrm{d}t'}{\mathrm{d}t}\right|_t + \left.\frac{\partial T}{\partial z}\right|_{t'} \left.\frac{\mathrm{d}z}{\mathrm{d}t}\right|_t \tag{4.152}$$

Using equation (4.148) and visually evaluating the exact derivatives in the right hand side of equations (4.151) and (4.152) results in equations (4.153) and (4.154):-

$$\left.\frac{\mathrm{d}T}{\mathrm{d}t}\right|_z = \left.\frac{\partial T}{\partial t'}\right|_z \tag{4.153}$$

$$\left.\frac{\mathrm{d}T}{\mathrm{d}z}\right|_t = \left.\frac{\partial T}{\partial z}\right|_{t'} - \frac{1}{\boldsymbol{v}} \left.\frac{\partial T}{\partial t'}\right|_z \tag{4.154}$$

For the heat transfer fluid, where A' is the heat transfer area per unit length and the subscripts i and o denote the inner and outer wall surface respectively:-

$$\left(\dot{M} c_P\right)_m \left.\frac{\partial T_m}{\partial z}\right|_t + \frac{\left(\dot{M} c_P\right)_m}{\boldsymbol{v}} \left.\frac{\partial T_m}{\partial t}\right|_z = -\alpha_o A'_o \left(T_m - T_w|_{z,r=r_o}\right) \tag{4.155}$$

Using equations (4.153) and (4.154), equation (4.155) becomes:-

$$\left(\dot{M} c_P\right)_m \left(\left.\frac{\partial T_m}{\partial z}\right|_{t'} - \frac{1}{\boldsymbol{v}} \left.\frac{\partial T_m}{\partial t'}\right|_z\right) + \frac{\left(\dot{M} c_P\right)_m}{\boldsymbol{v}} \left.\frac{\partial T_m}{\partial t'}\right|_z = -\alpha_o A'_o \left(T_m - T_w|_{r=r_o}\right) \tag{4.156}$$

In equation (4.156), the velocity vector terms cancel out to become:-

$$\left(\dot{M} c_P\right)_m \left.\frac{\partial T_m}{\partial z}\right|_{t'} = -\alpha_o A'_o \left(T_m - T_w|_{r=r_o}\right) \tag{4.157}$$

A detailed numerical solution and MATLAB code for these equations is provided in the appendix, section 10.6.

4.5.2 MATLAB Model Results

Figures 4.16 and 4.17 display the results of heating water in the vessel using the distributed parameter model on MATLAB. In the example displayed, the initial process temperature was set to 293.15 K (20°C). the jacket inlet temperature T_{m1} first rises from 20°C (293.15 K) to 100°C (373.15 K) from 0 to 2000 seconds and remains constant at 373.15 K until the end time of 10 000 seconds. Water is used as the process fluid, assumed at a constant heat capacity of 4184 J kg^{-1} K^{-1}. The DW-Therm is assumed to be at a constant heat capacity of 1950.9 J kg^{-1} K^{-1}, which is at 100°C.

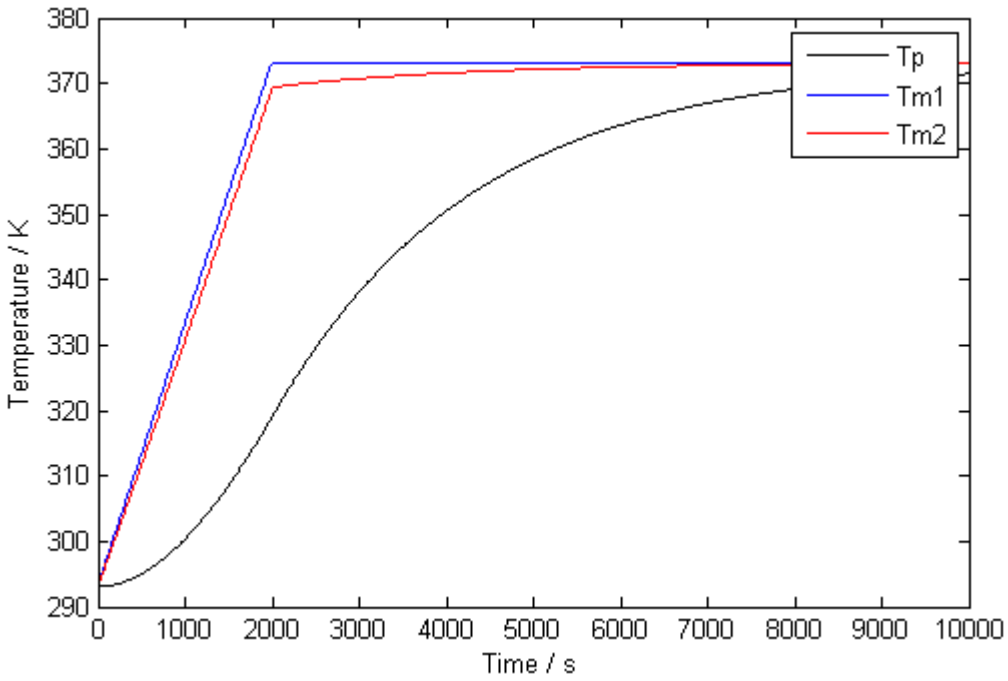

Figure 4.16 – MATLAB simulation of heating water – temperature vs. time.

In figure 4.16, the jacket outlet temperature T_{m2} changes rapidly at first, along with the jacket inlet temperature, until it is held constant. The process temperature T_p at first takes a while to form an upward trend, because the vessel wall is heated first. After this, both profiles follow the expected exponential curve approaching a steady state when all temperatures are the same. This is because of the assumption of a closed system. In reality, some heat would be escaping from the jacket (into the surroundings), as well as from the process (predominantly through the ullage region), so the temperatures would never equalise as they do in this simulation.

Figure 4.17, displays the heat transfer rates of the DW-Therm as it passes through the jacket ($\dot{Q}_m$) and the rate of heating the process itself ($\dot{Q}_p$). From these figures, it can be seen that there is an initial period of a few hundred seconds when there is more heat being transferred between the jacket and the wall than between the wall and the process, and

that when the jacket inlet temperature turns constant (at 2000 seconds), the wall heating profile (through the glass) evens out quickly and both heat transfer rates decrease exponentially as the system reaches equilibrium.

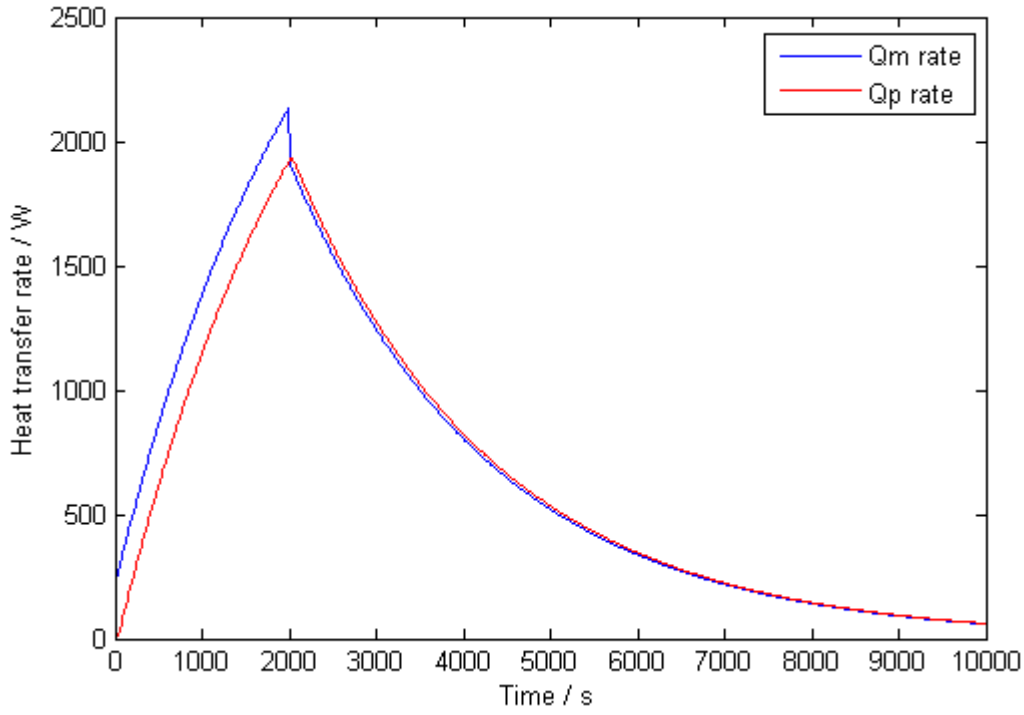

Figure 4.17 – MATLAB simulation of heating water – heat transfer rate vs. time.

After 2000 seconds, the simulation displays more heat being transferred to the process than from the jacket. Although it is only a small amount, this is not realistic in experimental settings as the jacket will lose some heat to the surroundings. However, in this simulation, the reason this phenomenon occurs is due to the thermal inertia of the glass wall – as the system is approaching equilibrium, this heat present in the wall preferentially passes to the process side because it is colder. As the wall profile evens out, this causes a little more heat transfer to the process side than is coming from the jacket at that time.

Note that the MATLAB model is not currently developed well enough to compare with experimental data because the experimental values of T_{m1} would have to be input at every time step. Currently it can only show an idealised profile of T_{m1}.

4.6 Summary of the Analysis

The data obtained in the experiments (from chapter 3) have been simulated using an analytical model to describe the jacket operation with time and to account for heat transfer

between the jacket and the process, as well as heat loss to the surroundings. Analysis of the experiments during boiling was also conducted.

The lumped parameter model and analytical solutions used several important assumptions to simplify the mathematics behind the process. Heat transfer coefficients were predicted using the analytical model as well as industrially used engineering correlations found in the literature.

A distributed parameter model has been derived which accounts for the thermal inertia of the vessel wall, although the assumptions of perfect mixing, symmetry, uniform upward jacket flow and no longitudinal conduction through the vessel wall have not yet been relaxed.

5 MODELS TO INVESTIGATE THE PLAIN JACKET

5.1 Basic Description of the Jacket Models

Precisely what happens inside the jacket in terms of the distribution of pressure, velocity and heat transfer coefficients has not yet been thoroughly investigated in the literature.

The 25 litre stirred tank reactor in the iPRD laboratory (see chapter 4) was used as the basis for this investigation, although experimental measurements could not be established because of the high predicted cost of extra equipment and installation. Pressure measurements at the inlet and outlet points of the jacket, as well as at various points inside the jacket, would be useful for completing a more thorough investigation.

A low-level model using Bernoulli's equations and basic textbook fluid mechanics for sudden contractions and expansions was used as an idealised model for pressure drop calculation. High-level modelling of the flow and heat transfer was then conducted using the CFD software packages ANSYS FLUENT and ANSYS CFX.

Using the Bernoulli model, two extreme cases were investigated, and these are described as low-level models due to the simple formulae used. The first of these is for a flow that suddenly turns into a uniform upwards flow through the jacket, as in previous idealised models, for the ones developed by Ali (2009), Kaiyrzhanova (2010) and Bentham (2011). The second of the low-level models is for a flow that expands very little upon entry, and then swirls tangentially around inside the jacket in a coil-like manner, without spreading out as it rises. In reality, the flow is expected to spread out considerably, and thus the results are expected to be much closer to the first low-level model.

A further case was investigated using the Bernoulli model – one with an ‘equivalent flow area’ derived from the CFD simulation (from which an equivalent length scale is obtained). In both cases, the hydraulic diameter was taken as the difference in diameter between the inside wall and outside wall of the jacket (which is 0.058 m). In the equivalent flow area case, the Reynolds number found in the CFD is used. The jacket pressure drop from the CFD is taken to be the same as that for the equivalent flow area, from which an equivalent length scale is derived from the friction factor formula (discussed below).

Figure 5.1 displays the locations of the profiles in the CFD models. In the cylindrical coordinates used in the descriptions in this chapter, the radius r is the magnitude of distance from the central axis, the height z starts at 0 from the middle of the inlet pipe, and the angle ϑ starts at 0° from the place where the flow direction of inlet pipe is

perpendicular to the radial direction. The outlet pipe therefore exits the jacket parallel to the radial direction, at the angle position of 270° (in cylindrical coordinates).

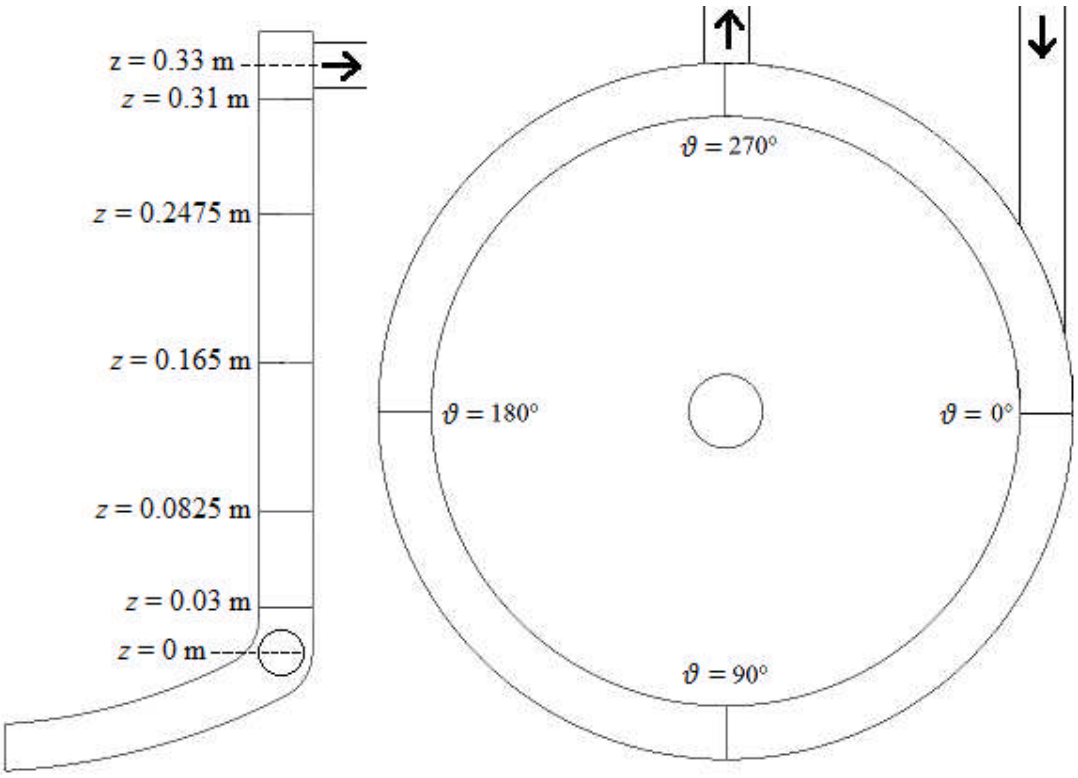

Figure 5.1 – Locations of the profiles in the CFD model, in cylindrical coordinates. The left image indicates the designated heights of the inlet pipe (0 m) and outlet pipe (0.33 m). The right image is a view from the top.

In the CFD models, the inlet and outlet pipe lengths 1 metre away from the plane that crosses the angular positions of 0° and 180°. This distance was selected in order to achieve fully developed flow at the end of each pipe. Based on this geometry, the actual pipe lengths in the model (the minimum distance to where they connect to the outer wall) are 0.8994 m for the inlet pipe and 0.811 m for the outlet pipe. Table 5.1 displays other important dimensions used in the models. The dimensions in this table, as well as other specific geometry dimensions such as knuckle radii, were supplied by the manufacturer of the reactor.

The flow inside the jacket will change due to the change in viscosity and density affecting the pump. Dead zones in the jacket are expected at the bottom (below the inlet pipe) and at the top, where the flow has lost swirl compared to the lower walls.

Table 5.1 – Important geometrical dimensions used in the models.

Dimension	Symbol	Value / m
Radius of the inner jacket wall	r_{io}	0.16
Radius of the outer jacket wall	r_{oi}	0.189
Gap between the inner and outer jacket wall	r_{io}- r_{oi}	0.029
Hydraulic diameter of the jacket	D_H	0.058
Jacket height (from the centres of the inlet pipe to the outlet pipe)	Δz	0.33
Inlet and outlet pipe diameter	d_{pipe}	0.025

5.2 The Bernoulli Model

The Bernoulli equation is:-

$$\frac{p_1}{\rho g} + \frac{v_1^2}{2g} + z_1 = \frac{p_2}{\rho g} + \frac{v_2^2}{2g} + z_2 + \left(h_f + \Sigma h_L\right) \tag{5.1}$$

Using the Bernoulli equation accounting for frictional losses, two extreme cases of uniform axial flow and tangential flow, replicating a strongly swirling flow path, were calculated. The aim of this investigation is to find out the extent to which the results from the CFD lie between the two cases, so an empirical swirl factor can be found. The two cases are, firstly, uniform distribution in the jacket (axial flow) and, secondly, a tangential flow through a rectangular cross sectional area with dimensions of the width of the jacket by the diameter of the pipe (see figure 5.2).

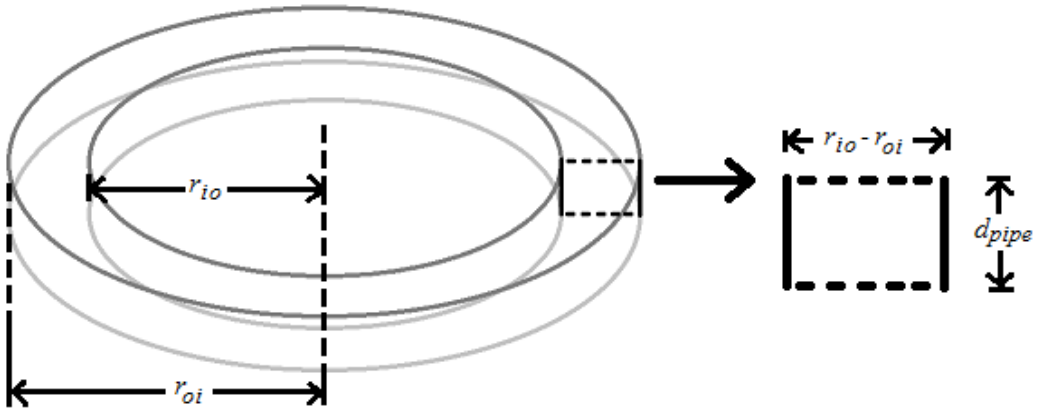

Figure 5.2: Cross section for the tangential flow case.

The cases of axial flow and tangential flow were compared. In the axial flow case, the hydraulic diameter (D_H) was taken as the difference in diameter between the inside wall and outside wall of the jacket (which is 0.058 m). In the tangential flow case, the hydraulic diameter is the same, as the equation (5.2) for hydraulic diameter comes to the same value when the wetted perimeter consists of only the two vertical edges displayed in the right

hand image on figure 5.2. The horizontal lines here are assumed to be frictionless surfaces, as the flow is going in the same direction above and below.

$$D_H = 4A_X/P_W \quad (5.2)$$

The shortest distance between different flow points in the jacket in the axial flow case (Δz) was used to compare the pressure drops for the different scenarios. However, interestingly, the total length of the path taken by the flow in the tangential flow case in the jacket itself is 16.6 metres, that is 46.9 times longer than the axial flow case.

In both cases, the pressure drop in the inlet and outlet pipe was assumed to be by frictional losses only. The relative roughness (ϵ/D) for the glass pipes was sufficiently small (2.4×10^{-7}) to be considered a smooth surface, for the pipe Reynolds number (Re) of 14237, the Blasius equation (Blasius, 1913) gave a Moody (1944) friction factor of 0.029 (Coulson & Richardson, 1999).

The pressure head and pressure are related by:-

$$h_p = p/\rho g \quad (5.3)$$

The velocity head (h_v) in the inlet pipe or jacket is related to the cross sectional average velocity (v) by:-

$$h_v = v^2/2g \quad (5.4)$$

The head loss due to friction along the length of pipe or jacket (L) was worked out by the Moody (1944) friction factor formula (Coulson & Richardson, 1999):-

$$h_f = f_M(L/D)(v^2/2g) \quad (5.5)$$

The entry point was treated as a sudden expansion and the exit point was treated as a sudden contraction. The formula used for entry and exit losses (where v is the pipe velocity in both cases) is as follows:-

$$h_L = K_L(v^2/2g) \quad (5.6)$$

where for the inlet point, the formula for a sudden expansion (Douglas *et al*., 2006) was used:-

$$K_L = (1 - A_2/A_1)^2 \quad (5.7)$$

and for the outlet point, K_L was found using a chart (Douglas *et al*., 2006), for a sudden contraction.

In the axial flow case, the full cross sectional area of the jacket was used (about 100 times larger than that of the pipes, hence almost all of the velocity head was converted into pressure in the jacket entry point and back to velocity in the jacket exit point. In the tangential flow case, the cross sectional area of the jacket was taken as the area displayed on the right side in figure 5.2.

There are different definitions of friction factor – Stanton-Pannell (f_{SP}), Fanning (f_F) and Moody (also known as Darcy or Darcy-Weisbach) (f_M). These are closely related to each other, as displayed in equation (5.8).

$$\frac{\tau_w}{\rho v_f^2} = f_{SP} = \frac{f_F}{2} = \frac{f_M}{8} \tag{5.8}$$

It was decided that the Moody (Darcy or Darcy-Weisbach) friction factor (f_M) would be used, because it is used in the equations for annular flow by Kakaç *et al*. (1987) and Gnielinski (2009). In these equations, firstly, a radius ratio was defined:-

$$r^* = r_i / r_o \tag{5.9}$$

For the laminar axial flow case (Kakaç *et al*., 1987):-

$$f_M = (4/\mathrm{Re}) \times 24 \times r^{*0.035} \tag{5.10}$$

For the turbulent tangential flow case (Gnielinski, 2009):-

$$\mathrm{Re}^* = \mathrm{Re} \times \left[\left(1 + r^{*2}\right) \ln(r^*) + \left(1 - r^{*2}\right)\right] / \left[(1 - r^*)^2 \ln(r^*)\right] \tag{5.11}$$

$$f_M = \left[1.8 \log_{10}(\mathrm{Re}^*) - 1.5\right]^{-2} \tag{5.12}$$

Although the flow path in the tangential flow case was a spiral rather than an annulus, the dimensionless friction factor was calculated based on annular formulae purely because the jacket has annular geometry.

Points along the fluid path were labelled point 0 to 5. This is displayed in figure 5.3. To perform the manual calculations, the final outlet pressure (p_5) was firstly assumed to be 101325 Pa (1 atmosphere). The pressure head (h_p) at each point was converted to actual pressure using equation (5.3). The inlet pressure was found by working out all the other pressures backwards from the known outlet pressure.

The hydrostatic (potential) head change is not included in these pressure drop calculations because this change is not due to friction factor.

At any defined point in the Bernoulli model, equation (5.3) can be used to convert the pressure head into the absolute pressure at that point.

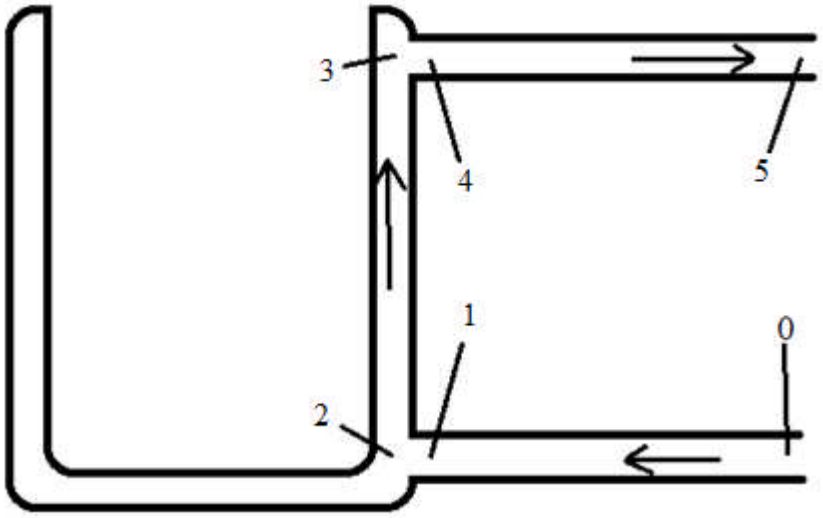

Figure 5.3: Designated points in the pipes and jacket.

5.3 CFD Modelling of the Jacket

CFD simulations provide deeper insight into the possible phenomena within the limits of the model itself. For example, details of the flow that would be much more difficult and/or expensive to measure in the experiment. The drawback is that it cannot provide an exact simulation taking into account everything (again without excessive cost and/or difficulty), so a compromise has to be reached between the two approaches.

One specific instance of the experiments conducted was chosen to be analysed in detail at first – part of the methanol distillation experiment (see section 3.3.3 and section 4.4.2). In this case, the methanol was boiling (providing a constant T_p of 64.7°C). The experimentally measured values of T_{m1} and T_{m2} stayed constant at 89.8°C and 87.4°C respectively, which evaluates to a steady total heat transfer rate of 1174.9 W based on the measured jacket mass flow of 0.2631 kg s^{-1} and average heat capacity of 2831 J kg^{-1} K^{-1}.

An ambient temperature of 19.4°C was measured during the experiment and this has been used in the diabatic simulations.

5.3.1 Basic Mathematics Behind the CFD Models

Much of the mathematics presented here for the CFD models is present in the ANSYS Help files (ANSYS, 2012). Within ANSYS Help 14.5, the section on “Mechanical ADPL”, sub-section “Theory Reference”, part 7.1, contains the description and equations for fluid flow fundamentals. The section on “CFX”, sub-section “Modeling Guide” (sic), part 2.7.5, contains the equations for heat transfer used in the CFD simulations. The

section on “CFX”, sub-section “Theory Guide”, part 2.8.1, contains the equations for mathematical formulations such as “near-wall” values and definitions thereof.

The fluid flow problem is defined by the laws of conservation of mass and momentum (Navier-Stokes equations) and heat transfer by the law of conservation of energy. These laws are expressed in terms of partial differential equations, which are discretized with a finite difference or finite volume based technique. They are considered “common knowledge” and their derivations can be found in many CFD text books, such as Versteeg and Malalasekra (2009).

The primary assumption is that there is only one fluid phase in each zone analysed. Also, the user must determine whether the problem is laminar or turbulent.

The first equation used is the continuity equation (5.13), which represents the law of conservation of mass. In tensor notation:-

$$\frac{\partial \rho}{\partial t} + \frac{\partial \left(\rho v_j\right)}{\partial s_j} = 0 \tag{5.13}$$

where v is the velocity, s is distance, t is time and ρ is density. The subscript j denotes that the x, y and z components are summed, for example:-

$$\frac{\partial \left(\rho v_j\right)}{\partial s_j} = \frac{\partial (\rho v_x)}{\partial x} + \frac{\partial \left(\rho v_y\right)}{\partial y} + \frac{\partial (\rho v_z)}{\partial z} \tag{5.14}$$

Tensor notation for the momentum equation (Navier-Stokes):-

$$\frac{\partial (\rho v_i)}{\partial t} + \frac{\partial \left(\rho v_i v_j\right)}{\partial s_j} = \frac{\partial}{\partial s_j}\left(\mu \frac{\partial v_i}{\partial s_j}\right) - \frac{\partial p}{\partial s_i} + \rho g_i + \frac{\partial}{\partial s_j}\left(\mu \frac{\partial v_j}{\partial s_i}\right), \quad i = 1, 2, 3 \tag{5.15}$$

In equation (5.15), the letter s is used to denote spatial distance and the subscripts i and j denote the directions. In Cartesian coordinates (used in the CFD simulations), these equations expand into three each, corresponding to the subscript i being x, y and z, and the subscript j within each equation referring to the sum of the x, y and z components. The last term in equation (5.15) is the viscous loss term, which is eliminated in incompressible constant property cases.

The energy equation includes heat and work done on the fluid:-

$$\frac{\partial(\rho c_p T_0)}{\partial t} + \frac{\partial(\rho v_j c_p T_0)}{\partial s_j} = \frac{\partial}{\partial s_j}\left(\lambda \frac{\partial T_0}{\partial s_j} - v_j p\right) + \frac{\partial(v_i \tau_{ij})}{\partial s_j} \tag{5.16}$$

where T_0 is defined in 'CFX Help' as "the total (or stagnation) temperature". This is related to the static temperature (T) by equation (5.17), although the difference is extremely small and its calculation was deactivated during all the CFD models presented in this thesis.

$$T_0 = T + \frac{v_j^2}{2c_p} \tag{5.17}$$

The final term in equation (5.16) contains the heating contribution by viscous work, viscous dissipation and viscous kinetic energy (which were also deactivated during all the CFD models presented in this thesis) and can be expanded as follows:-

$$\frac{\partial(v_i \tau_{ij})}{\partial s_j} = v_j \mu \left[\frac{\partial}{\partial s_i}\left(\frac{\partial v_j}{\partial s_i}\right) + \frac{\partial}{\partial s_k}\left(\frac{\partial v_k}{\partial s_j}\right)\right] + \Phi - \frac{\partial}{\partial s_j}\left[\frac{\lambda}{c_p}\frac{\partial}{\partial s_j}\left(\frac{v_j^2}{2}\right)\right] \tag{5.18}$$

where Φ is the viscous heat generation term:-

$$\Phi = \mu\left(\frac{\partial v_i}{\partial s_k} + \frac{\partial v_k}{\partial s_i}\right)\frac{\partial v_i}{\partial s_k} \tag{5.19}$$

Note that the letters i, j and k in equations (5.16), (5.18) and (5.19) do not refer to different equations as in equation (5.15), but to the different combinations of the dimensions used.

Under turbulence, the velocity fluctuates seemingly randomly about its average value. It is thus assumed to be divided into a mean component and a fluctuating component, as in equation (5.20).

$$v_j = \bar{v}_j + v_j' \tag{5.20}$$

Substituting equation (5.20) into the three momentum equations (5.15) leads to the following additional terms, labelled Reynolds stress terms:-

$$\sigma_{R_i} = -\frac{\partial}{\partial s_j}\overline{\left(\rho v_i' v_j'\right)}, \qquad i = 1, 2, 3 \tag{5.21}$$

The Reynolds stress terms in equation (5.21) are related to the mean velocity gradients through the eddy viscosity or turbulent viscosity (μ_t), using Boussinesq's Eddy Viscosity model, as follows:-

$$-\overline{\rho v_i' v_j'} = \mu_t \left(\frac{\partial v_i}{\partial s_j} + \frac{\partial v_j}{\partial s_i} \right) - \frac{2}{3} \rho k \delta_{ij} = 2\mu_t S_{ij} - \frac{2}{3} \rho k \delta_{ij} \tag{5.22}$$

where:-

$$S_{ij} = \frac{1}{2} \left(\frac{\partial v_i}{\partial s_j} + \frac{\partial v_j}{\partial s_i} \right) \tag{5.23}$$

5.3.2 Turbulence Models

The standard k-ε model and the shear stress transport (SST) model are both academic and industrial standard CFD models and are a primary focus of study in this thesis. The baseline (BSL) Reynolds Stress model will also be described because it was used in modelling the jacket and was intended for use in all models. It is also used often as standard in many investigations in the literature, because it is generally considered more accurate (although more computationally expensive and difficult to converge). Many other CFD models exist, including Low-Re turbulence models. However, these were not used in any of the CFD simulations in this thesis and therefore will not be described here.

In the standard k-ε model (Launder and Spalding, 1974), the terms k and ε refer to the turbulent kinetic energy and turbulence dissipation rate respectively, which are standard parameters describing eddies within the turbulent flow. They are also written as follows:-

$$k = \frac{1}{2} \overline{\left(v_j' \right)^2}, \qquad \varepsilon = \frac{\mu}{\rho} \overline{\left(\frac{\partial v_i'}{\partial s_k} \right)^2} \tag{5.24}$$

The k-ε model description begins with the definitions of the velocity scale (v_t) and length scale (l_t) associated with the large-scale turbulence:-

$$v_t = k^{1/2} \tag{5.25}$$

$$l_t = \frac{k^{3/2}}{\varepsilon} \tag{5.26}$$

The turbulent viscosity (μ_t) is associated to the above terms by:-

$$\mu_t = \rho C_\mu v_t l_t = \rho C_\mu \frac{k^2}{\varepsilon} \tag{5.27}$$

where C_μ is a dimensionless constant (Versteeg and Malalasekra, 2009).

The transport equations for k and ε are as follows:-

$$\frac{\partial(\rho k)}{\partial t}+\frac{\partial\left(\rho v_j k\right)}{\partial s_j}=\frac{\partial}{\partial s_j}\left(\frac{\mu_t}{\sigma_k}\frac{\partial k}{\partial s_j}\right)+2\mu_t\left(S_{ij}\cdot S_{ij}\right)-\rho\varepsilon \tag{5.28}$$

$$\frac{\partial(\rho \varepsilon)}{\partial t}+\frac{\partial\left(\rho v_j \varepsilon\right)}{\partial s_j}=\frac{\partial}{\partial s_j}\left(\frac{\mu_t}{\sigma_\varepsilon}\frac{\partial \varepsilon}{\partial s_j}\right)+2C_{1\varepsilon}\mu_t\frac{\varepsilon}{k}\left(S_{ij}\cdot S_{ij}\right)-C_{2\varepsilon}\rho\frac{\varepsilon^2}{k} \tag{5.29}$$

The default coefficients used for closure of the standard k-ε model model are as follows (Versteeg and Malalasekra, 2009):-

$$C_\mu = 0.09 \tag{5.30}$$

$$\sigma_k = 1 \tag{5.31}$$

$$\sigma_\varepsilon = 1.3 \tag{5.32}$$

$$C_{1\varepsilon} = 1.44 \tag{5.33}$$

$$C_{2\varepsilon} = 1.92 \tag{5.34}$$

The standard k-ε model works better further from walls and the standard k-ω model (Wilcox, 2006 and 2008) works better closer to walls. The Shear Stress Transport (SST) model (Menter, 1994), primarily used in the CFD analysis, is a modification of the standard k-ε model, which combines the advantages of both the standard k-ε and k-ω models.

To introduce the SST model, the formulae for the standard k-ω model and the transformed k-ε model (ANSYS, 2013) must first be introduced.

The SST model begins with the following relation:-

$$\mu_t = \rho\frac{k}{\omega} \tag{5.34}$$

where ω is the specific turbulence dissipation rate:-

$$\omega = \frac{\varepsilon}{C_\mu k} \tag{5.35}$$

Equations (5.37) and (5.38) display the formulae for the standard k-ω model (Wilcox, 1986).

$$\frac{\partial(\rho k)}{\partial t}+\frac{\partial\left(\rho v_j k\right)}{\partial s_j}=\frac{\partial}{\partial s_j}\left[\left(\mu+\frac{\mu_t}{\sigma_{k1}}\right)\frac{\partial k}{\partial s_j}\right]+P_k-\beta'\rho k\omega \tag{5.37}$$

$$\frac{\partial(\rho\omega)}{\partial t}+\frac{\partial\left(\rho v_j \omega\right)}{\partial s_j}=\frac{\partial}{\partial s_j}\left[\left(\mu+\frac{\mu_t}{\sigma_{\omega 1}}\right)\frac{\partial \omega}{\partial s_j}\right]+\alpha_1\frac{\omega}{k}P_k-\beta_1\rho\omega^2 \tag{5.38}$$

where P_k is the "turbulence production due to viscous forces" (ANSYS, 2013), displayed in equation (5.39). The other as-yet-unexplained constants and terms will be listed after all the SST model equations.

$$P_k=\min\left\{\left[\mu_t\left(\frac{\partial v_i}{\partial s_j}+\frac{\partial v_j}{\partial s_i}\right)\frac{\partial v_i}{\partial s_j}-\frac{2}{3}\frac{\partial v_k}{\partial s_k}\left(3\mu_t\frac{\partial v_k}{\partial s_k}+\rho k\right)\right], 10\rho\varepsilon\right\} \tag{5.39}$$

Equations (5.40) and (5.41) display the transformed *k*-*ε* model formulae.

$$\frac{\partial(\rho k)}{\partial t}+\frac{\partial\left(\rho v_j k\right)}{\partial s_j}=\frac{\partial}{\partial s_j}\left[\left(\mu+\frac{\mu_t}{\sigma_{k2}}\right)\frac{\partial k}{\partial s_j}\right]+P_k-\beta'\rho k\omega \tag{5.40}$$

$$\begin{aligned}\frac{\partial(\rho\omega)}{\partial t}+&\frac{\partial\left(\rho v_j \omega\right)}{\partial s_j}\\&=\frac{\partial}{\partial s_j}\left[\left(\mu+\frac{\mu_t}{\sigma_{\omega 2}}\right)\frac{\partial \omega}{\partial s_j}\right]+2\rho\frac{1}{\sigma_{\omega 2}\omega}\frac{\partial k}{\partial s_j}\frac{\partial \omega}{\partial s_j}+\alpha_2\frac{\omega}{k}P_k\\&\quad-\beta_2\rho\omega^2\end{aligned} \tag{5.41}$$

The baseline (BSL) *k*-*ω* model is a stage closer to the SST model. It combines these two by combining equations (5.37) to (5.41) with an extra function, here denoted by $F_{k\omega 1}$. Additional buoyancy effects were included, to account for the possibility of natural convection. The BSL *k*-*ω* model formulae are then as follows:-

$$\frac{\partial(\rho k)}{\partial t}+\frac{\partial\left(\rho v_j k\right)}{\partial s_j}=\frac{\partial}{\partial s_j}\left[\left(\mu+\frac{\mu_t}{\sigma_{k3}}\right)\frac{\partial k}{\partial s_j}\right]+P_k-\beta'\rho k\omega+P_{kb} \tag{5.42}$$

$$\begin{aligned}\frac{\partial(\rho\omega)}{\partial t}+\frac{\partial\left(\rho v_j \omega\right)}{\partial s_j}&=\frac{\partial}{\partial s_j}\left[\left(\mu+\frac{\mu_t}{\sigma_{\omega 3}}\right)\frac{\partial \omega}{\partial s_j}\right]\\&+(1-F_{k\omega 1})2\rho\frac{1}{\sigma_{\omega 2}\omega}\frac{\partial k}{\partial s_j}\frac{\partial \omega}{\partial s_j}+\alpha_3\frac{\omega}{k}P_k-\beta_3\rho\omega^2+P_{\omega b}\end{aligned} \tag{5.43}$$

where the full buoyancy terms (with no extra options selected) are as follows:-

$$P_{kb}=-\frac{\mu_t}{\rho}g_i\frac{\partial\rho}{\partial s_i} \tag{5.44}$$

$$P_{\omega b} = \frac{\omega}{k}[(\alpha_3 + 1)C_3 \max(P_{kb}, 0) - P_{kb}] \tag{5.45}$$

In equations (5.42) and (5.43), the function $F_{k\omega 1}$ is a function of the distance y from the nearest wall:-

$$F_{k\omega 1} = \tanh(arg_1^4) \tag{5.46}$$

where:-

$$arg_1 = \min\left[\max\left(\frac{\sqrt{k}}{\beta'\omega y}, \frac{500\mu}{\rho\omega y^2}\right), \frac{4\rho k}{CD_{k\omega}\sigma_{\omega 2} y^2}\right] \tag{5.47}$$

where:-

$$CD_{k\omega} = \max\left(2\rho\frac{1}{\sigma_{\omega 2}\omega}\frac{\partial k}{\partial s_j}\frac{\partial \omega}{\partial s_j}, 10^{-10}\right) \tag{5.48}$$

The SST model is then formed by limiting the turbulent viscosity as follows:-

$$\mu_t = \frac{\rho\alpha_1 k}{\max(\alpha_1\omega, S_R F_2)} \tag{5.49}$$

where:-

$$F_2 = \tanh(arg_2^2) \tag{5.50}$$

where:-

$$arg_2 = \max\left(\frac{2\sqrt{k}}{\beta'\omega y}, \frac{500\mu}{\rho\omega y^2}\right) \tag{5.51}$$

and S_R is “an invariant measure of the strain rate” (ANSYS, 2013). S_R is later described in non-invariant form, as follows:-

$$S_R = \sqrt{2S_{ij}S_{ij}} \tag{5.52}$$

where S_{ij} is as defined in equation (5.23).

The default coefficients (ANSYS, 2013) used for closure of the SST model are as follows:-

$$\beta' = 0.09 \tag{5.53}$$

$$\alpha_1 = 5/9 \tag{5.54}$$

$$\beta_1 = 0.075 \tag{5.55}$$

$$\sigma_{k1} = 2 \tag{5.56}$$

$$\sigma_{\omega 1} = 2 \tag{5.57}$$

$$\alpha_2 = 0.44 \tag{5.58}$$

$$\beta_2 = 0.0828 \tag{5.59}$$

$$\sigma_{k2} = 1 \tag{5.60}$$

$$\sigma_{\omega 2} = 1/0.856 \tag{5.61}$$

$$\alpha_3 = F_{k\omega 1}\alpha_1 + (1 - F_{k\omega 1})\alpha_2 \tag{5.62}$$

$$\beta_3 = F_{k\omega 1}\beta_1 + (1 - F_{k\omega 1})\beta_2 \tag{5.63}$$

$$\sigma_{k3} = F_{k\omega 1}\sigma_{k1} + (1 - F_{k\omega 1})\sigma_{k2} \tag{5.64}$$

$$\sigma_{\omega 3} = F_{k\omega 1}\sigma_{\omega 1} + (1 - F_{k\omega 1})\sigma_{\omega 2} \tag{5.65}$$

The Reynolds Stress models (RSM) are a type of "seven-equation model", solving for the six Reynolds stresses and either ε or ω. The ε-based models are divided into three possible models. Two of them were developed by Launder *et al*. (1975) and are named the Launder, Reece and Rodi Isotropization of Production (LRR-IP) and Quasi-Isotropic (LRR-QI) models. The remaining ε-based model "uses a quadratic relation for the pressure-strain correlation" (ANSYS, 2013) and is named the Speziale, Sarkar and Gatski (SSG) model (Speziale *et al*., 1991). The ω-based model is described in ANSYS (2013). These models are better suited to swirling flows with stronger 3D directionality of motion, for example the vortex in an unbaffled stirred tank (which is highly relevant to the experiments conducted).

The BSL RSM, which includes the features just described, is formed as a blend of the LRR and SSG models with the ω-based model described in ANSYS (2013), in the same way that the BSL k-ω model is a blend of the k-ε and k-ω models. The equations for the Reynolds stresses take the following form (ANSYS, 2013):-

$$\begin{aligned}\frac{\partial\left(\rho\overline{v_i'v_j'}\right)}{\partial t} + \frac{\partial\left(v_k\rho\overline{v_i'v_j'}\right)}{\partial s_k} \\ = P_{ij} - \frac{2}{3}\beta'\rho\omega k\delta_{ij} + \varphi_{ij} + P_{ij,b} \\ + \frac{\partial}{\partial s_k}\left[\left(\mu + \frac{\mu_t}{\sigma_k}\right)\frac{\partial\left(\overline{v_i'v_j'}\right)}{\partial s_k}\right]\end{aligned} \tag{5.66}$$

where the buoyancy term is expanded:-

$$P_{ij,b} = B_{ij} - \mathrm{C}_{buo}\left(B_{ij} - \frac{1}{3}B_{kk}\delta_{ij}\right) \tag{5.67}$$

In equation (5.67), according to ANSYS (2013), "the second term represents the buoyancy contribution from the pressure-strain term" given by Launder (1989). The term C_{buo} may be found from Launder (1989). The term B_{ij} is expanded:-

$$B_{ij} = g_i \mathrm{b}_j + g_j \mathrm{b}_i \tag{5.68}$$

Using the full buoyancy model, the b terms take the form:-

$$\mathrm{b}_i = -\frac{\mu_t}{\rho\sigma_\rho}\beta\frac{\partial\,\rho}{\partial\,s_i} \tag{5.69}$$

The omega equation for the BSL Reynolds stress model takes the following form:-

$$\begin{aligned}\frac{\partial(\rho\omega)}{\partial\,t} + \partial(v_k\rho\omega) \\ = \alpha_3\frac{\omega}{k}P_k + P_{\omega b} - \beta_3\rho\omega^2 + \frac{\partial}{\partial\,s_k}\left[\left(\mu + \frac{\mu_t}{\sigma_{\omega 3}}\right)\frac{\partial\,\omega}{\partial\,s_k}\right] \\ + (1 - F_{RS1})\cdot 2\rho\frac{1}{\sigma_2\omega}\frac{\partial\,k}{\partial\,s_k}\frac{\partial\,\omega}{\partial\,s_k}\end{aligned} \tag{5.70}$$

where:-

$$F_{RS1} = \tanh(arg_{RS}^4) \tag{5.71}$$

where:-

$$arg_{RS} = \min\left[\max\left(\frac{\sqrt{k}}{\beta'\omega y}, \frac{500\mu}{\rho\omega y^2}\right), \frac{4\rho k}{CD_{k\omega}\sigma_{k-\varepsilon}y^2}\right] \tag{5.72}$$

where:-

$$CD_{k\omega} = \max\left(2\rho\frac{1}{\sigma_{k-\varepsilon}\omega}\frac{\partial\,k}{\partial\,s_j}\frac{\partial\,\omega}{\partial\,s_j}, 10^{-10}\right) \tag{5.73}$$

and the default coefficients used for closure are the same as for the BSL *k-ω* model (equations (5.53) to (5.65).

The remaining terms P_{ij} and φ_{ij} in equation (5.66) are from the pressure-strain correlation. The production term:-

$$P_{ij} = -\overline{\rho v_i' v_k'} \frac{\partial v_j}{\partial s_k} - \overline{\rho v_j' v_k'} \frac{\partial v_i}{\partial s_k} \tag{5.74}$$

and:-

$$\varphi_{ij} = \beta' C_1 \rho \omega \left(-\overline{v_i' v_j'} + \frac{2}{3} k \delta_{ij} \right) - \hat{\alpha} \left(P_{ij} - \frac{1}{3} P_{kk} \delta_{ij} \right) - \hat{\beta} \left(D_{ij} - \frac{1}{3} P_{kk} \delta_{ij} \right) - \hat{\gamma} \rho k \left(S_{ij} - \frac{1}{3} S_{kk} \delta_{ij} \right) \tag{5.75}$$

where:-

$$D_{ij} = -\overline{\rho v_i' v_k'} \frac{\partial v_k}{\partial s_j} - \overline{\rho v_j' v_k'} \frac{\partial v_k}{\partial s_i} \tag{5.76}$$

and:-

$$\hat{\alpha} = (8 + C_2)/11 \tag{5.77}$$

$$\hat{\beta} = 8(C_2 - 2)/11 \tag{5.78}$$

$$\hat{\gamma} = 60(C_2 - 4)/55 \tag{5.79}$$

where the default coefficients are:-

$$\beta' = 0.09 \tag{5.80}$$

$$C_1 = 1.8 \tag{5.81}$$

$$C_2 = 0.52 \tag{5.82}$$

As an alternative to the Reynolds Stress models, the SST model can be modified by a "curvature correction" term. This enables the model to more accurately simulate strongly swirling flows without resolving all the individual Reynolds stresses. Compared to the normal SST model, this provides results much closer to experiments, comparable to the RST model (Smirnov and Menter, 2009).

For the curvature correction, the production term (P_k) in the *k* equation of the SST model is multiplied by a factor f_r, which is limited by ANSYS CFX in the following way (ANSYS, 2013):-

$$f_r = \max\left[0, 1 + C_{scale}\left(\tilde{f}_r - 1\right)\right] \tag{5.83}$$

where C_{scale} is unity by default but can be set by the user to tune the level of curvature correction, and:-

$$\tilde{f}_r = \max[\min(f_{rotation}), 1.25] \tag{5.84}$$

where $f_{rotation}$ is the factor used by Smirnov and Menter (2008) based on Spalart and Shur (1997), which is:-

$$f_{rotation} = (1 + c_{r1})\frac{2r^*}{1 + r^*}[1 - c_{r3}\tan^{-1}(c_{r2}\tilde{r})] - c_{r1} \tag{5.85}$$

where the constants c_{r1}, c_{r2} and c_{r3} are set "based on performed tests" (ANSYS, 2013) as:-

$$c_{r1} = 1 \tag{5.86}$$

$$c_{r2} = 2 \tag{5.87}$$

$$c_{r3} = 1 \tag{5.88}$$

and:-

$$r^* = S/\Omega \tag{5.89}$$

$$\tilde{r} = 2\Omega_{ik}S_{jk}\left[\frac{DS_{ij}}{Dt} + (\varepsilon_{mn}S + \varepsilon S)\Omega_{r_m}\right]\frac{1}{\Omega D^3} \tag{5.90}$$

where:-

$$S^2 = 2S_{ij}S_{ij} \tag{5.91}$$

$$\Omega^2 = 2\Omega_{ij}\Omega_{ij} \tag{5.92}$$

$$D^2 = \max(S^2, 0.09\omega^2) \tag{5.93}$$

and where:-

$$S_{ij} = \frac{1}{2}\left(\frac{\partial U_i}{\partial s_j} + \frac{\partial U_j}{\partial s_i}\right) \tag{5.94}$$

$$\Omega_{ij} = \frac{1}{2}\left(\frac{\partial U_i}{\partial s_j} + \frac{\partial U_j}{\partial s_i}\right) + 2\varepsilon_{mji}\Omega_{r_m} \tag{5.95}$$

Also, in equation 5.90, the term DS_{ij}/Dt denotes the components of the Lagrangian derivative of the strain rate tensor, which is the second velocity gradient (ANSYS, 2013). The term ε_{mn} denotes the tensor of Levi–Civita (Smirnov and Menter, 2009) and Ω_{r_m} denotes the components of the system rotation vector (Smirnov and Menter, 2009).

Details of the numerical discretisation schemes used in CFD are found in many text books, for example Versteeg and Malalasekra (2009). The most common are first-order

upwind and second-order upwind, and the Quadratic Upstream Interpolation for Convective Kinematics (QUICK) scheme, used by ANSYS FLUENT. ANSYS CFX uses the “High Resolution” scheme, which is a blend of first-order upwind and second-order upwind. The “High Resolution” scheme was used in the main simulations presented in this thesis.

5.3.3 Geometry and Mesh Creation

Using ANSYS Workbench, the geometry was first sketched in Design Modeller based on diagrams provided by QVF, the manufacturer of the vessel. Unstructured, automatically generated meshes were made on ANSYS Mesher. These consisted only of tetrahedral cells. They were used for the preliminary FLUENT models, which used water as the medium in the jacket.

The procedure for making these automatic meshes was relatively simple – a cross-sectional sketch of the wall of the reactor was constructed, using the dimensions provided for the reactor, and rotated 360° to form the shape of the wall with the jacket fluid inside. Then on ANSYS Meshing, the default settings were used to create an automatic mesh that was composed entirely of tetrahedral elements.

ANSYS ICEM was used to create a more regular mesh, made purely from hexahedral cells (cubes), rather than tetrahedral cells. Both meshes classified as ‘unstructured’ by strict definition. ICEM saves its meshes as a file with the extension “.uns”, which stands for ‘unstructured’.

The procedure for creating the meshes in ICEM was much more complex and tedious. This is detailed in the appendix, section 10.3.

5.3.4 Isothermal Models on ANSYS FLUENT

The purpose of using ANSYS FLUENT was to establish a preliminary, qualitative view of the jacket flow, to know roughly what flow pattern to expect, before learning how to use ANSYS CFX. Initially, water was used in the jacket, and the jacket was simulated isothermally on ANSYS FLUENT at the default temperature (in this case 15°C). This was to establish an initial qualitative view of the expected flow pattern in the jacket.

In this CFD simulation, the realizable k-ε model was used, with standard wall functions (with the no-slip condition), and the flow boundary conditions were a constant atmospheric pressure at the end of the outlet pipe and a constant velocity of 0.653 m s^{-1} at the start of the inlet pipe. This is the mean pipe velocity that occurs at the default mass

flow set by the Huber system. Two tetrahedral meshes were produced, one with 6.6×10^5 cells and one with 1.7×10^6 cells. In both meshes, the cells were smaller near the walls. These gave similar results, but the finer mesh was selected for extra accuracy.

The convergence criteria for the residuals of the ANSYS FLUENT models were set to the standard value of 10^{-4}. The maximum number of iterations was set to 50,000.

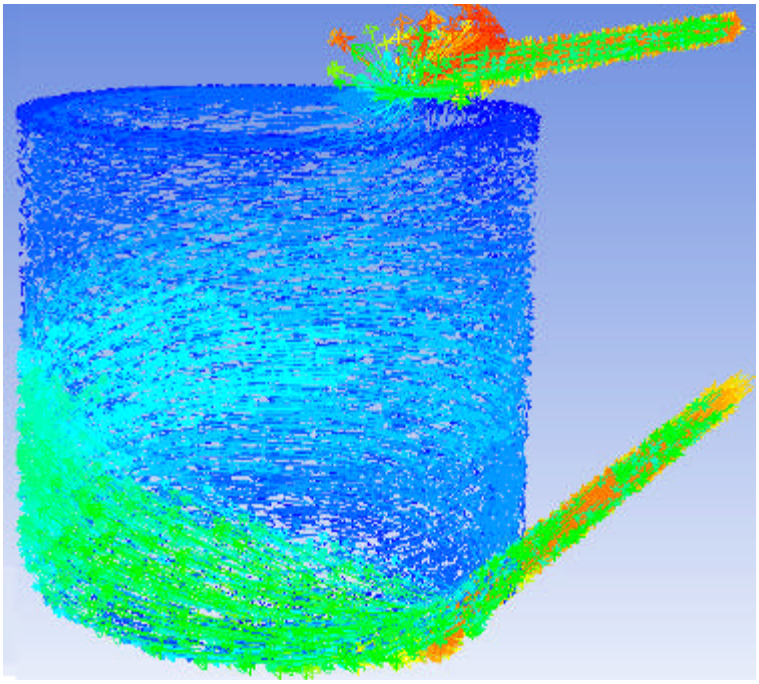

Figure 5.4 – Direction vectors of the flow in the jacket in the CFD model, providing a qualitative representation of the expected flow pattern.

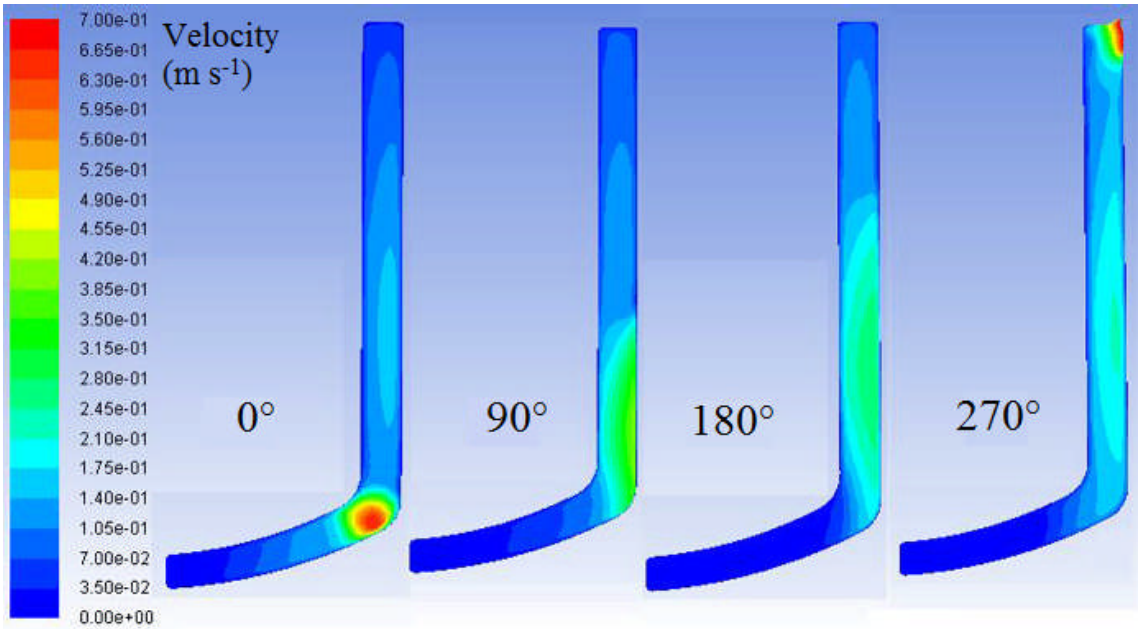

Figure 5.5 – Contours of velocity in the jacket at 90 degree intervals. Displayed velocities range from 0 (blue) to 0.7 m s^{-1} (red).

Figure 5.4 displays the result of this simulation. In this figure, the vectors are coloured by velocity. Blue indicates zero velocity (dead zones) and red indicates the highest velocity, which in this case is 0.892 m s^{-1}, at a point in the outlet pipe. Aside from this, the highest velocities are observed in the middle of the pipes (as expected due to their smaller cross sectional area of flow).

Figure 5.5 displays velocity contours at cross sections in the jacket at 90 degree intervals. In combination with figure 5.4, it can be deduced that in this simulation, the bulk of the flow misses the bottom of the reactor and rises along the walls, spreading out over one revolution and with a smaller stream breaking off towards the outlet port. Additional flow at the top of the reactor is drawn towards the outlet. The regions of lowest flow are at the top rim of the jacket and the bottom section (below the main stream).

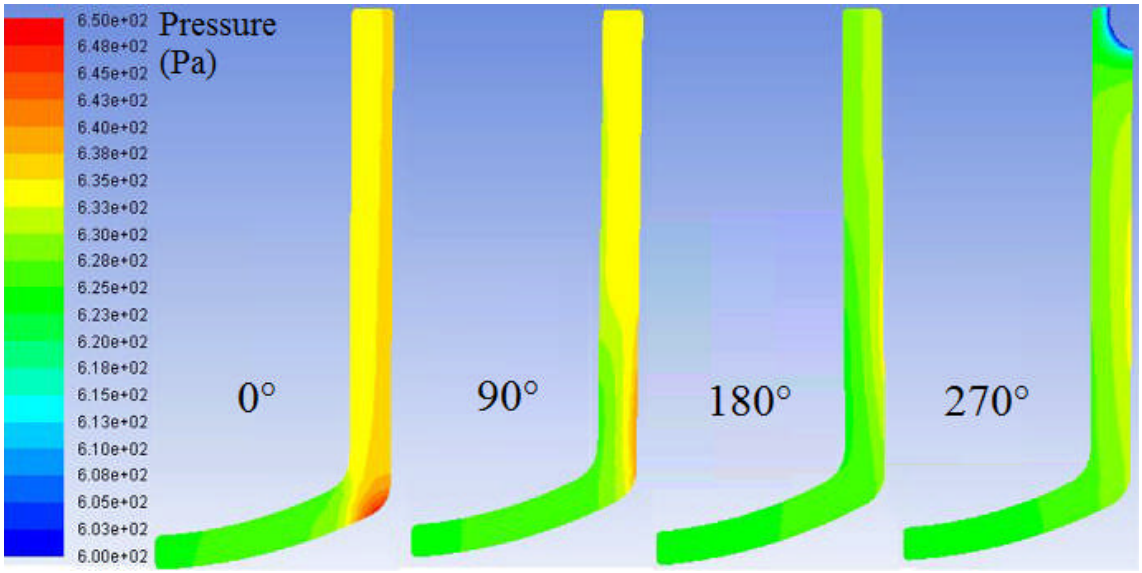

Figure 5.6 – Contours of pressure (negating the hydrostatic head) in the jacket at 90 degree intervals. Displayed pressures range from 600 Pa (blue) to 650 Pa (red).

Figure 5.6 displays pressure contours at cross sections in the jacket at 90 degree intervals. It is observed that the highest pressure is at the outer wall, due to the centripetal force, and that this pressure at the wall is highest at and above the inlet port.

5.3.5 Non-Isothermal Models on ANSYS CFX

ANSYS CFX offered several advantages over ANSYS FLUENT, one of the major advantages being that it would simulate the flow using the more structured and customised meshes which were created in ANSYS ICEM. In the attempts made, it seemed CFX could not deal with the mesh made of tetrahedral cells that did work in FLUENT, whereas the mesh made in ICEM with hexahedral cells worked well on CFX but not on FLUENT. It is unknown why the tetrahedral mesh was preferred by FLUENT and the

hexahedral mesh was preferred by CFX, as CFX does not inherently have difficulty working with tetrahedral meshes and FLUENT does not inherently have difficulty working with hexahedral meshes (this was discussed with a CFX programmer, A. D. Burns).

For the main CFD models (using ANSYS CFX), monitor points were set up to check the velocity at points inside the simulation where flow was expected. When these monitors flat-lined (did not change with iteration number), this would indicate converged values. The convergence criteria for the residuals were set to 10^{-10}, because time was the main factor in the runs rather than convergence. The run-time was set high enough for maximum convergence to be observed within the simulation. Graphs of the residuals vs. time, as well as mass and energy balances, for all relevant simulations, are displayed in the appendix, sections 10.4 and 10.5.

DW-Therm was added to ANSYS CFX as a custom material with user-defined properties. Firstly, the physical properties of DW-Therm (see appendix, section 10.1) were input into Microsoft Excel. Graphs were generated and equations describing the trends on these graphs (the change in physical property with temperature at atmospheric pressure) were found using the 'add trendline' option and selecting 'display equation'. These equations were then entered into the 'CFX-Pre' program as user-defined functions using CFX Expression Language (CEL).

The physical properties of methanol and water were already known by the program, so these did not require extra inputs.

The models used within ANSYS CFX for the jacket side were the "BSL Reynolds Stress" (the Baseline Reynolds Stress model) and "Shear Stress Transport" (the SST model). These used automatic wall functions if the dimensionless distance y^+ was less than 2 at the walls, however, this was calculated to be approximately 70 μm (Pointwise, 2014), so the mesh would have to be built fine enough to be close enough to this. During analysis of the walls post-process, it was found that the y^+ was still too large (for the coarse mesh, used in most of this analysis, an area weighted average y^+ of 8.34 on the outer wall and 5.26 on the inner wall). The distribution of y^+ was very non-uniform, reaching values around 25 in the outer wall where flow impinged on the surface.

At the inlet face the flow boundary condition was a constant mass rate, of 0.2631 kg s^{-1} for the methanol boiling simulations and 0.2761 kg s^{-1} for the water boiling simulations. The jacket inlet temperature was 89.8°C for the methanol boiling simulations and 134.6°C for

the water boiling simulations. All these jacket inlet values were the same as those measured in the experiments detailed in section 3.3.3.

The flow boundary condition at the outlet was a static pressure of zero (gauge) on the outlet face. The reference pressure was 101325 Pa. All walls had a non-slip condition (which was the CFD program's default).

The inner and outer walls used the ANSYS CFX method called “heat transfer coefficient”, in which a combined external heat transfer coefficient and external temperature were input: the process temperature of 100°C on the inner wall and the ambient temperature of 19.4°C on the outer, coupled with a modified overall heat transfer coefficient accounting for the conductive resistance of each wall and the outside thermal resistance – boiling on the process side and free convection and radiation on the outer side. The other walls of the model, including the pipes, were adiabatic.

The combined heat transfer coefficient for the inner wall was:-

$$\frac{1}{U_i^*} = \frac{\delta_g}{(A_{ii}/A_{ig})\lambda_g} + \frac{1}{(A_{ii}/A_{io})\alpha_{boil}} \tag{5.96}$$

where the Cooper (1984) correlation, using the properties of methanol or water (depending on the simulation), was used to assess the boiling coefficient:-

$$\alpha_{boil} = \frac{55 p_r^{0.12} \dot{q}^{0.67}}{[-\log(p_r)]^{0.55} M_R^{0.5}} \tag{5.97}$$

and the inner wall glass area is:-

$$A_{ig} = (A_{io} - A_{ii}) / \ln(A_{io}/A_{ii}) \tag{5.98}$$

The combined heat transfer coefficient for the outer wall was:-

$$\frac{1}{U_o^*} = \frac{\delta_g}{(A_{oo}/A_{og})\lambda_g} + \frac{1}{(A_{oo}/A_{oi})(\alpha_{conv} + \alpha_{rad})} \tag{5.99}$$

where the outer wall glass area is:-

$$A_{og} = (A_{oo} - A_{oi}) / \ln(A_{oo}/A_{oi}) \tag{5.100}$$

and the convection coefficient for the outer surface of the outer wall is:-

$$\alpha_{conv} = Nu_{air}\lambda_{air}/z_j \tag{5.101}$$

where:-

$$\mathrm{Nu}_{air} = 0.59(\mathrm{Gr}_{air}\mathrm{Pr}_{air})^{0.25} \tag{5.102}$$

$$\mathrm{Gr}_{air} = L^3\rho_{air}^2 g\beta_{air}(T_{oo} - T_{amb})/\mu_{air} \tag{5.103}$$

$$\mathrm{Pr}_{air} = c_P\,\mu_{air}/\lambda_{air} \tag{5.104}$$

and the radiation coefficient (where the temperatures in the radiation equation are in Kelvins and σ is the Stefan-Boltzmann constant) is:-

$$\alpha_{rad} = \frac{\varepsilon_g\sigma\left(T_{oo}^4 - T_{amb}^4\right)}{T_{oo} - T_{amb}} \tag{5.105}$$

The convection coefficient used the formula for laminar free convection on a vertical surface, with the physical properties of air evaluated at the arithmetic mean of the surface temperature and the ambient temperature. The length scale *L* used in the Grashof number (equation 5.103) is the jacket height z_j (0.33 metres), which is also used in the Nusselt number (equation 5.102). Laminar flow was used because the criterion is that $\mathrm{Gr}_{air}\mathrm{Pr}_{air}$ (the product of the Grashof number and the Prandtl number) is less than 10^9. The calculated value of $\mathrm{Gr}_{air}\mathrm{Pr}_{air}$ was 1.49×10^8.

5.3.6 Grid and Model Independence (ANSYS CFX models only)

Table 5.2 – Details of the grids used in the jacket.

Jacket Mesh	No. of cells	Max cell edge length / mm	Approx. desktop run time / days
Fine	9.22×10^6	1.6×10^{-3}	8
Medium	6.16×10^6	2.0×10^{-3}	4
Coarse	3.25×10^6	2.5×10^{-3}	2
Coarsest	1.75×10^6	4.0×10^{-3}	1

In ANSYS CFX, four different meshes were made, with different cell sizes ('coarsest', 'coarse', 'medium' and 'fine'). Figure 5.7 displays a cross-section of the coarse jacket mesh used in ANSYS CFX. All three meshes used hexahedral cells only and used smaller cell widths near the wall. The minimum width of the computational cells near the wall was chosen to equate the y^+ value less than 2, to resolve the laminar sublayer near the wall. Table 5.2 displays details of the grid sizing and number of cells in the jacket meshes. In this case, the near-wall cell distance was set to 5×10^{-5} metres (50 micrometres), as this was thought to be within the approximate value of 70 micrometres, corresponding to the

desired distance calculated using the online y^+ calculator in Pointwise, Inc. (see references section). The maximum cell size of 1.6 mm was chosen for the fine mesh rather than 1.5 mm because using a cell size any smaller would require too much computer memory. In fact, even the computer memory used by this fine mesh (with 1.6 mm maximum cell size) was slightly more than the system RAM of 16.340 GB.

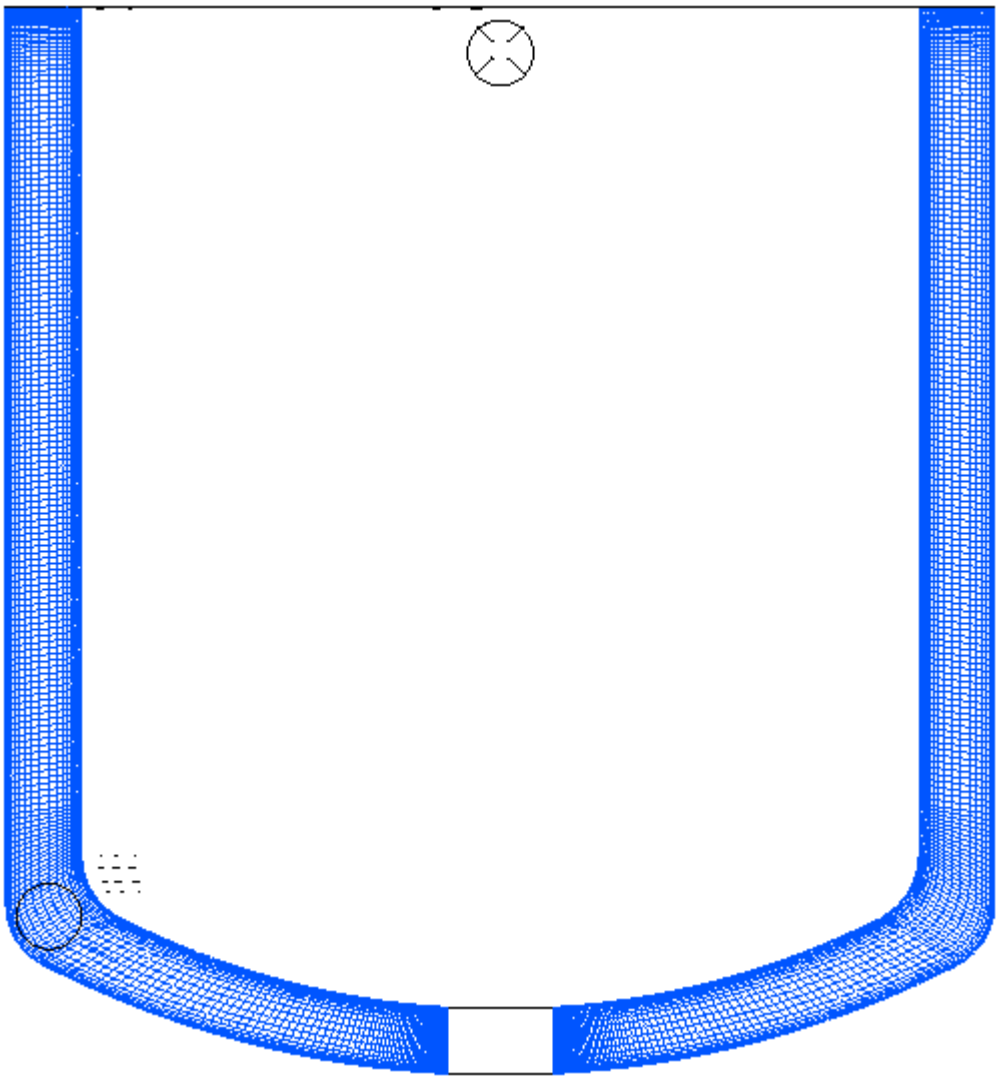

Figure 5.7 – Cross section of the coarse jacket mesh used in the ANSYS CFX simulations.

The results of the grid independence tests are displayed in figures 5.8 and 5.9. The coarsest mesh was an outlier and the coarse, medium and fine meshes are very similar. As a result, the coarse mesh was selected to test the effect of turbulence model.

The effect of turbulence model independence was a comparison between only the SST model and the BSL RSM. The reason why the standard k-ε model was not included here was because it was not recommended, because the jacket flow was expected to be more

dominated by wall effects, which are much better dealt with using the SST model than the k-ε model.

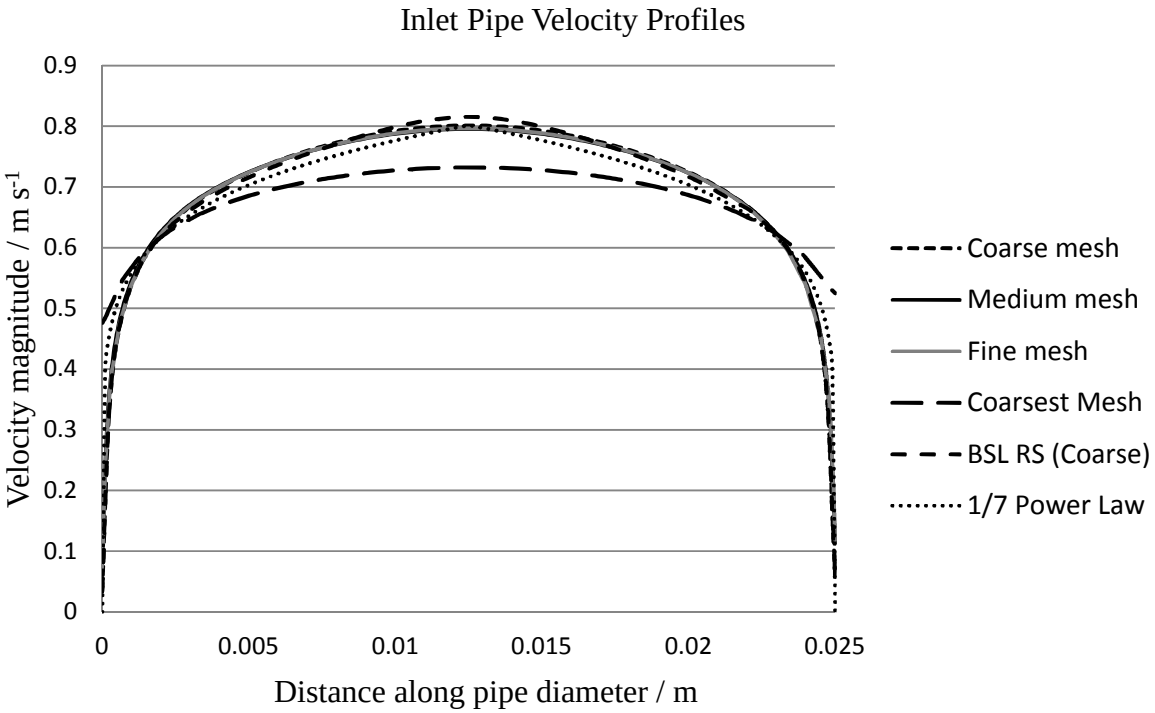

Figure 5.8 – Grid independence tests (SST model) and model independence test (BSL RS) for the fully developed pipe flow entering the jacket.

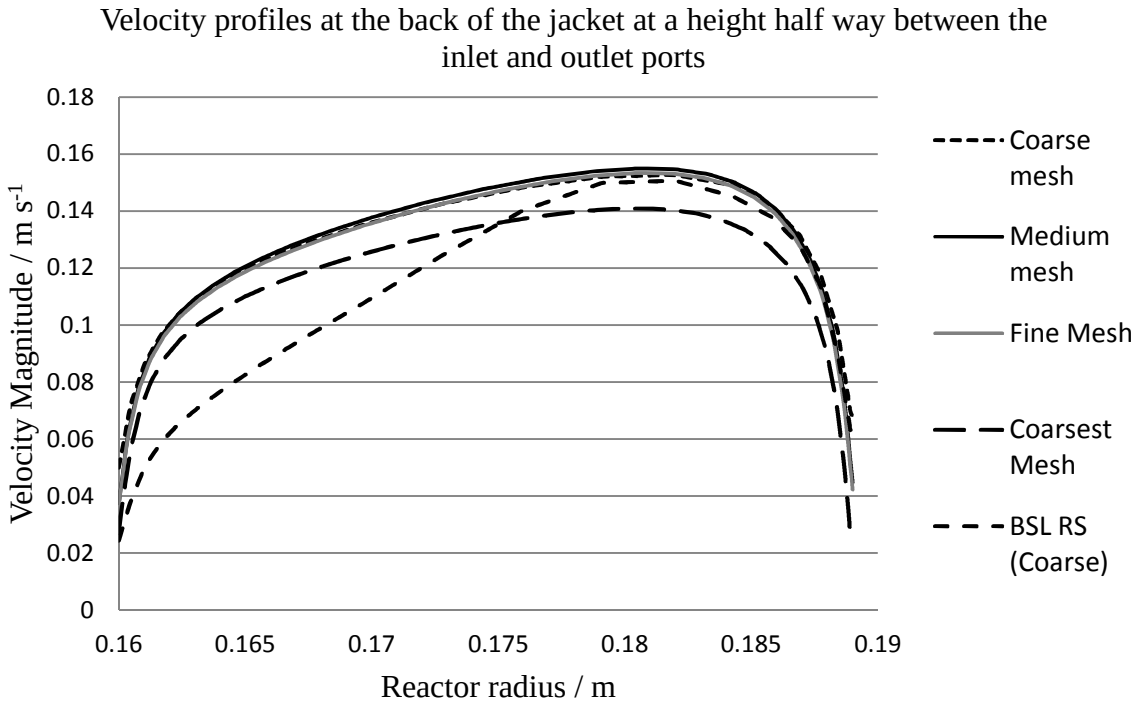

Figure 5.9 – Grid independence tests (SST model) and model independence test (BSL RS) for the velocity in the back of the jacket, at ϑ = 180° and z = 0.165 m.

Different models yielded very similar results for fully developed pipe flow, as displayed in figure 5.8, but there can be significantly different results for individual locations in the jacket. In figure 5.9, the BSL RSM results appear quite different from the SST results. Compared to the SST model, from the peak velocity (which is the same in both models), the BSL RSM results display a sharper decrease in velocity with decreasing radius until the transition layer (at which point the velocity decrease is lesser as it tends towards zero). This could be due to the unusual position in which small details of the flow may be highly sensitive to different models. Additionally, the BSL RSM results in figure 5.8 display a higher peak velocity and unusual shape of the velocity profile, indicating that these results have not converged sufficiently. The BSL RSM is known to have more difficulty converging than the SST and k-ε models, and therefore the SST model was chosen to be the main model to use in the jacket-only simulations.

In both figures 5.8 and 5.9, the results for the coarsest mesh were consistent outliers, predicting a lower velocity. This indicated that the coarsest mesh was too coarse to provide valid results.

Table 5.3 displays the area averaged values for heat transfer coefficients, wall temperatures and shear stresses for the inner and outer walls for to compare the two models for the conditions of a Huber set point of 135°C and boiling water in the process side.

Table 5.3 – Comparison of average values at the walls between the SST and BSL RS models.

Variable	SST model	BSL Reynolds Stress model
Area averaged inner wall heat transfer coefficient (α_{io}) / W m^{-2} K^{-1}	293.5	271.0
Area averaged inner wall temperature (T_{io}) / °C	118.1	117.2
Area averaged inner wall shear / Pa	0.0679	0.0478
Area averaged outer wall heat transfer coefficient (α_{oi}) / W m^{-2} K^{-1}	376.3	380.3
Area averaged outer wall temperature (T_{oi}) / °C	125.3	125.0
Area averaged outer wall shear / Pa	0.1639	0.1643

Interestingly, the BSL Reynolds Stress model outputs an average inner wall shear stress 30% lower than the SST model, but an average inner wall heat transfer coefficient only 8% lower. The temperature at the inner wall is predicted to be 0.9°C lower for the BSL Reynolds Stress model in this particular case.

As the BSL Reynolds Stress model is more accurate for swirling flows with vortices, it was assessed that it may be more appropriate to have used this model for the jacket. However, the run times would be significantly longer, it is computationally significantly more expensive and convergence is known to be more difficult to achieve.

5.3.7 Mass, Momentum and Energy Balances

The results of each run were recorded automatically by ANSYS CFX in a file with the extension '.out'. These provided detailed reports of the iterations, residuals and balances. The section of the file entitled "Normalised Imbalance Summary" gives a summary of any differences between inlets and outlets of each domain (in the case of the jacket-only mesh, this is the whole jacket). These summaries are given in the Appendix, section 10.4.

5.4 Jacket Flow and Pressure Drop Comparison

5.4.1 Velocity Distribution

The velocity distributions in this section are based on the results of the isothermal DW-Therm model for the methanol boiling experiment during a Huber set point of 90°C. The physical properties of the DW-Therm were set as constant, for the average temperature of 88.58°C. The results of velocity flow distribution for the variable property model were also extracted but did not vary significantly from the isothermal case in the areas depicted (along the wall of the jacket).

Figure 5.10 depicts axial velocity profiles of the fluid in the jacket. Figure 5.11 depicts the tangential velocity profiles. It should be noted that the scale is conserved only within each figure. That is, the axial velocities in figure 5.10 are to scale with each other, but not to scale with the tangential velocities in figure 5.11. Similarly, the tangential velocities in figure 5.11 are to scale with each other, but not to scale with the axial velocities in figure 5.10.

In figure 5.10 in particular, areas of higher axial velocity rise as the flow moves from the 90° position, through 180°, to the 270° position. Due to the path of momentum travelling from the inlet to the outlet, an overall upward motion is expected. There is no depiction of velocity below the inlet port, because it is negligible.

In the 90° and 180° positions, a significant downward component of velocity is also observed closer to the inner wall. As displayed in figure 5.11, the flow is more tangential

than axial. The main reason for this downward velocity is likely to be due to a vortex effect, where the pressure is higher on the outer walls. As the higher pressure areas tend to force fluid towards the outlet, this is balanced by the lower pressure areas on the inner walls. When the flow is stronger, which is closer to the bottom, the lower pressure on the inner walls draws some fluid downwards.

It also seems that this downward flow may be at least partly the result of natural convection opposing the jacket flow during heating – the flow should be opposed on both sides of the jacket because the jacket fluid is hotter than both the surroundings and the process. The air on the outside insulates the outer wall more, so the effect should be observed more on the inner wall.

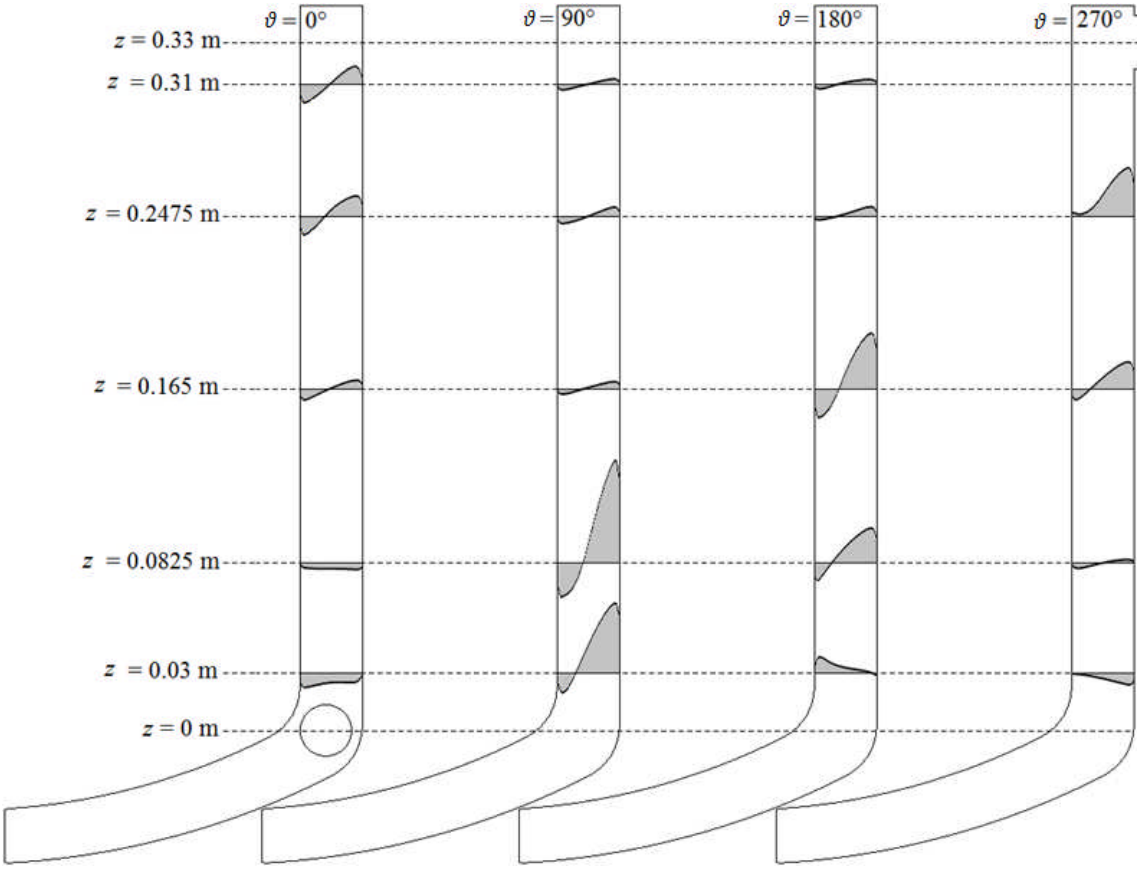

Figure 5.10 – Profiles of axial velocity in the jacket, to scale. Cylindrical coordinates are given. The maximum velocity that is displayed, in the 3rd image, is 0.145 m s^{-1}.

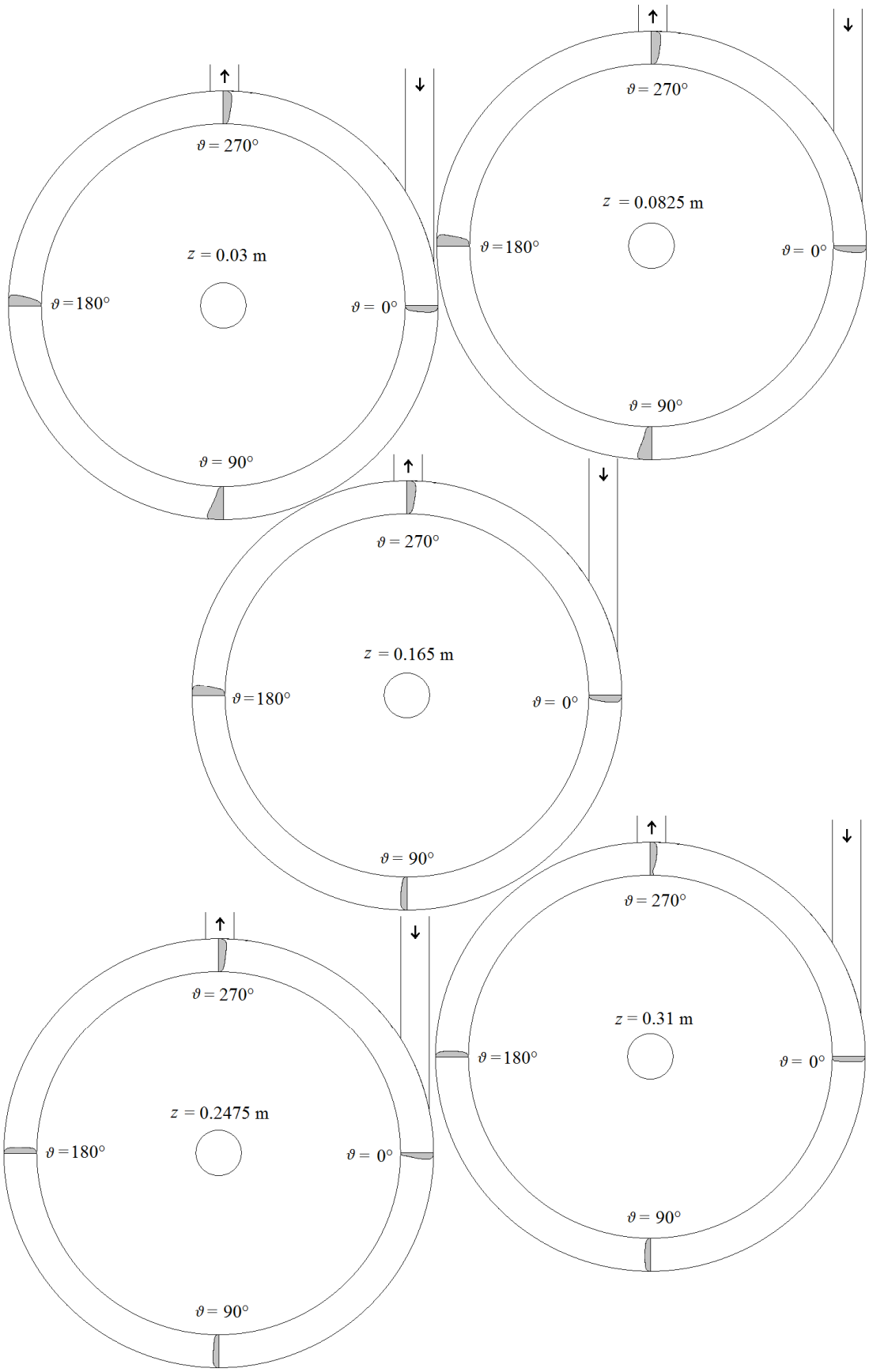

Figure 5.11 – Profiles of tangential velocity in the jacket, to scale. Cylindrical coordinates are given. The maximum velocity that is displayed (in the top left image at 90°) is 0.4 m s^{-1}.

It is important to consider that when the components of the velocity magnitudes are analysed, the tangential component of the flow in the CFD simulation is greater than the axial component, particularly in the areas with greater velocity. See figures 5.10 and 5.11, particularly the images of the 90° position. As the flow moves around, from the 0° position to the 90°, 180° and 270° position, a single major tangential flow is present at the lower heights (though this is still above the inlet point). By the time it reaches back round to 0°, this tangential flow has decayed from an average velocity of 0.65 m s^{-1} (in the pipe) to just above 0.1 m s^{-1} (in the top left image of figure 5.11 at the 0° position), and has risen slightly due to the axial component.

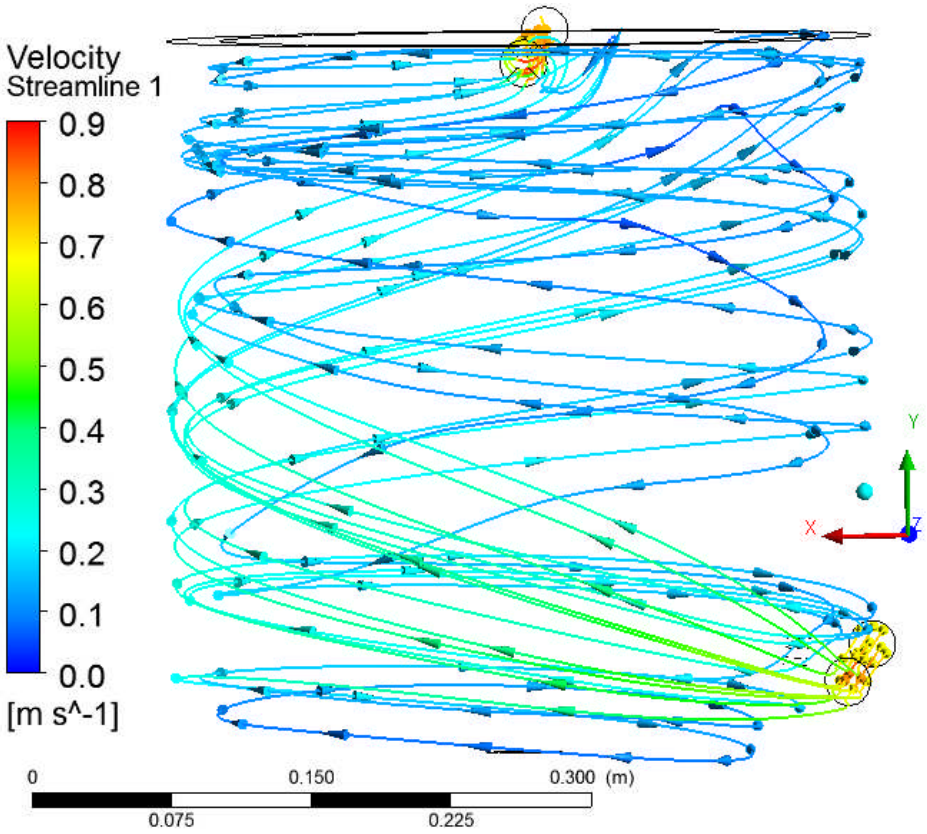

Figure 5.12 – Streamlines in the methanol batch distillation experiment when the Huber set point temperature is 90°C.

Figure 5.12 displays flow streamlines and velocity distributions inside the jacket. Note that most streamlines appear to circulate about three or four times in the jacket before reaching the outlet.

If a uniform upwards flow was assumed, using the hydraulic diameter (58 mm) with the density and viscosity in the jacket, the Reynolds number would be between 962 and 1090 (laminar flow), but based on the average velocity in the whole jacket in the CFD simulations, the average Reynolds number in the jacket is calculated to be between 14779 and 16875

(turbulent flow). It is likely that laminar flow occurs in the base of the jacket, below the inlet port, where the flow stagnates, so the use of a transitional flow model may be advisable for more detail in the bottom.

5.4.2 Pressure Drop

A correlation factor ($factor_1$) was developed for the pressure drop in the jacket alone, Δp_{total}, which can be either measured from the actual equipment or simulated by a CFD program. The factor is described by the following relationship:-

$$\Delta p_{total} = \Delta p_{axial} \times factor_1 \tag{5.106}$$

Table 5.4 displays Reynolds numbers, mean velocities and pressure drops in the jacket in the manual cases and the pipes. Within in the jacket itself, the pressure drop due to friction was much lower than the pressure drop due to the entry and exit effects. The exception is the tangential flow case, but this unrealistically assumed that the flow would not spread out at all in the jacket. Note that the Reynolds number is higher in the tangential flow case than in the pipes because the hydraulic diameter (0.058 m) is more than double that of the pipes (0.025 m) while the velocity (displayed in table 5.4) is close to two thirds of the velocity in the pipes.

Table 5.4 – Reynolds numbers, mean velocities and pressure drops in different regions and cases in the Bernoulli model.

Region and case	**Re**	**Flow type**	**Mean v / m s^{-1}**	**Δp_{modj} / Pa**	**$\Delta p_{friction}$ / Pa**	***factor*$_1$**
Inlet and outlet pipes, all cases	20720	Turbulent	0.6549	185 / metre	185 / metre	N/A
Jacket, axial flow case	742	Laminar	0.0101	258	0.031	1.00
Jacket, tangential flow case	32547	Turbulent	0.4434	595	505	2.31

Table 5.5 displays the pressures in the jacket and inlet and outlet pipes and the pressure drop factors for the manual and selected CFD cases. The factors for the CFD cases (except the “coarsest” mesh) all cases have about 10% more pressure drop in the jacket overall than the axial flow case. The CFD model produced results that lay in between the tangential flow and axial flow cases of the Bernoulli model (described in section 5.2). Therefore, despite some swirl being clearly present in the jacket in the CFD model, the pressure loss is much closer to that of the uniform flow case than the tangential flow case.

Table 5.5 – Pressure drop factors.

Model	Δp_{modt} / Pa	Δp_{modj} / Pa	Δp_{pi} / Pa	Δp_{po} / Pa	*factor*$_1$
Axial	575	258	167	150	1.00
Tangential	912	595	167	150	2.31
(SST) Coarsest mesh	530	274	141	115	1.06
(SST) Coarse mesh	618	283	176	160	1.10
(SST) Medium mesh	631	282	180	168	1.10
(SST) Fine mesh	637	281	186	171	1.09
BSL RS (Coarse mesh)	612	281	178	153	1.09
(SST) Variable Property (Coarse VP)	622	291	174	157	1.13

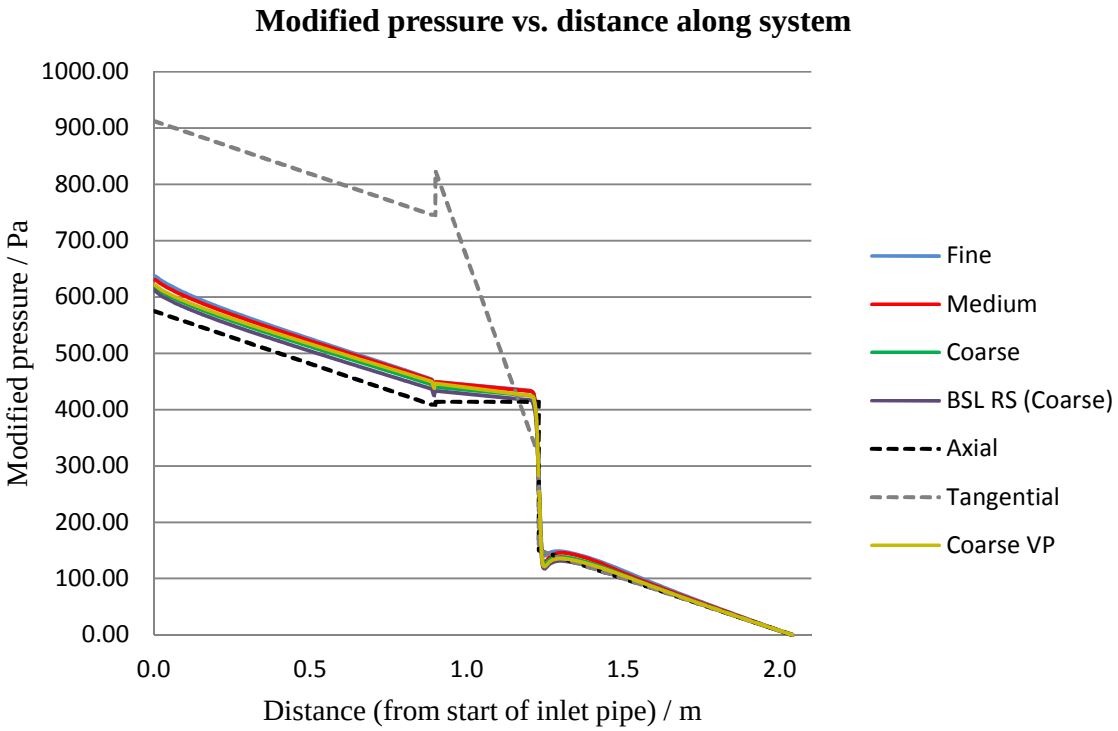

Figure 5.13 – Graph of modified pressure vs. distance for the models across the system when the Huber set point temperature is 90°C. The final outlet pressure was set to 1 atmosphere in all cases.

The modified pressure drop (Δp_{modj} for the jacket only and Δp_{modt} for the total pressure drop in the system) displayed in tables 5.4 and 5.5 negates both the ambient pressure and the pressure differences due to height differences, leaving only frictional losses and entry or exit effects (including the velocity head conversion into pressure and back). A graph of the modified gauge pressure in the system and the pressure drop across the pipes,

according to manual calculations for the two cases and for the CFD models, is displayed in figure 5.13.

In Figure 5.13, the dashed lines represent the results of the Bernoulli models while the unbroken lines represent the CFD results from different grids. For the modified pressure the contribution of height was removed. The distance was normalised so that the curves match each other for display purposes. That is, the distance inside the jacket is represented by the jacket height for all models. Compared to the axial case, the actual distance travelled by the flow is slightly higher in the CFD cases and much higher in the tangential case. This contributes to the higher pressure drop inside the jacket in the tangential case. In the axial flow case, the pressure drop inside the jacket itself (negating all entry and exit losses) was negligible.

In figure 5.13, the distance of zero represents the start of the inlet pipe (this corresponds to point 0 in figure 5.3, section 5.2). The fluctuation in pressure at about 0.9 metres is at the inlet port (points 1 and 2 in figure 5.3). The sudden large dip in pressure at about 1.25 metres is the pressure change at the outlet port (points 3 and 4 in figure 5.3). Zero pressure represents the end of the outlet pipe (point 5 in figure 5.3).

The profile for the “coarsest” mesh is excluded from figure 5.13 because it was producing unreliable results. The “Coarse VP” line represents the results of the diabatic variable property model (including heat transfer), while the other CFD models represented are isothermal models. The difference between these pressure profiles is negligible.

One major difference between the pressure drop calculations for the cases of the tangential flow and axial flow cases was in the hydraulic diameter (and subsequently area for the expansion coefficients). This causes the great difference in entry and exit losses for the tangential flow case.

There is a rise in pressure upon entering the jacket which occurs at the end of the inlet pipe, because of the conversion of velocity head from the pipe into additional pressure head. In the axial flow case, although the difference in velocity head is greater, the entry loss is also greater, and this cancels out most of the velocity head difference. Hence, the overall entry pressure rise is greater in the tangential case. In the CFD model, the predicted losses were somewhere in between the axial flow case and the tangential flow case.

For the pressure drop at the exit region, the sudden contraction of areas again causes a greater difference in velocity head for the axial case and the pressure drop here is greater in the axial case. The pressure drop at the exit predicted by the Bernoulli model in the axial case very closely matched the pressure drop predicted by the CFD model. In all cases, the CFD model predicted results much closer to the axial case than the tangential case in the Bernoulli model.

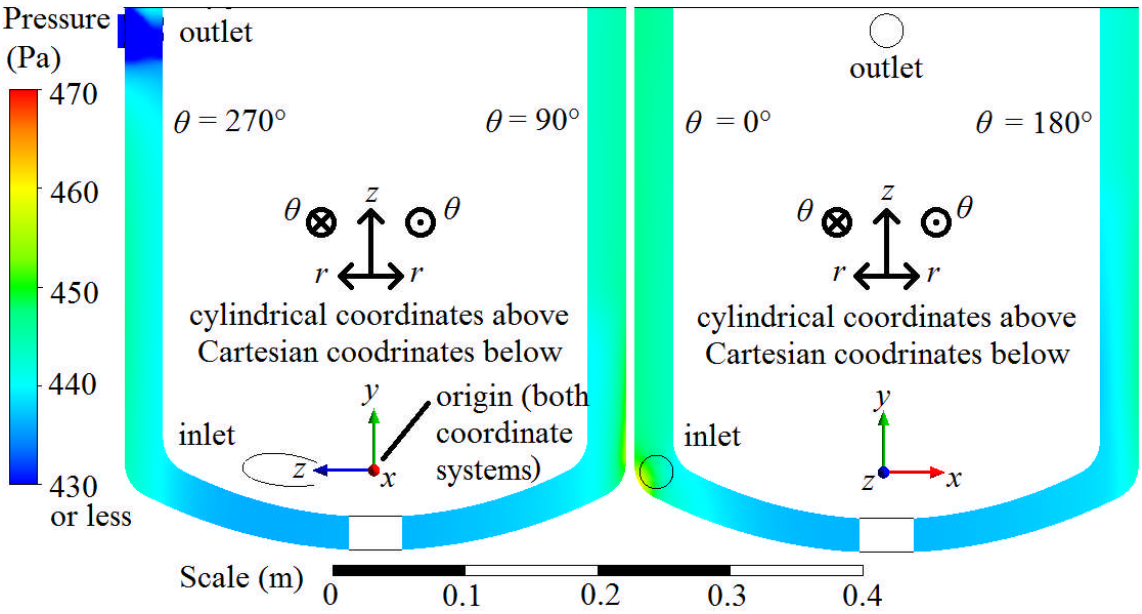

Figure 5.14 – Pressure contours in the jacket under the conditions when the Huber set point temperature is 90°C, for the coarse mesh with the isothermal SST model.

Figure 5.14 displays the pressure contours inside the jacket for the CFD model at 90° intervals. It can be seen, similarly to the preliminary FLUENT results, that the higher pressure generally occurs at the outer walls and is much more defined at the bottom half of the straight section, and much more uniform in the top half of the reactor. The pressure at the very bottom (the dish section) is generally lower than the pressure in the reactor walls, due to the centripetal force from the outer wall. The flow is moving upwards overall because of the much lower pressure at the outlet port.

Table 5.6 displays separate inlet (sudden expansion) and outlet (sudden contraction) pressure drops. A negative value of pressure drop (Δp) indicates a pressure rise. It turns out that the pressure change calculation for a sudden expansion into a much larger area (such as the uniform axial flow case) is closer to the CFD values for the expansion and contraction head losses than using an equivalent flow area derived from the average velocity in the CFD values. The similarity between the jacket pressure drops in the last two cases displayed (25 Pa) is a direct result of using the equivalent flow area that would

produce the same result as the CFD calculations, so this is to be expected. Interestingly, the flow length would be 4.91 metres (5.07 circumferences). This is similar to the qualitative representation in figure 5.12 of the flow circulating three or four times.

Table 5.6 – Pressure drop comparison with 'equivalent flow area' Bernoulli Model case.

Model	Inlet (expansion) Δp / Pa	Jacket Δp / Pa	Outlet (contraction) Δp / Pa	Flow Area / m^2	Flow Length / m
Axial flow	-5.60	0.023	276.4	3.2×10^{-2}	0.33
Tangential flow	-80.9	490.4	133.6	7.3×10^{-4}	14.47
Equivalent flow area	-67.6	25.0	250.2	2.1×10^{-3}	4.91
CFD SST	-8.31		269.6	N/A	N/A

5.5 Jacket Heat Transfer

5.5.1 Main Analysis

The distribution of individual heat transfer coefficients within the jacket conforms to the flow.

The external heat transfer coefficient is calculated by ANSYS CFX, using a reduced temperature (T^+) defined in equation (5.107) (ANSYS, 2013), which is rearranged into equation (5.108).

$$T^+ = \frac{\rho c_p u^* \left(T_w - T_f\right)}{q_w} \tag{5.107}$$

$$q_w = \frac{\rho c_p u^*}{T^+}\left(T_w - T_f\right) \tag{5.108}$$

where T_w is the wall temperature, T_f is the near-wall fluid temperature (the temperature in of the nearest computational node to the wall), c_p is the fluid heat capacity, q_w is the heat flux at the wall, and u^* is the velocity. The heat transfer coefficient is therefore defined as in equation (5.109) (ANSYS, 2013):-

$$\alpha_j = \frac{\rho c_p u^*}{T^+} \tag{5.109}$$

As automatic wall treatment is used in the SST model, the dimensionless temperature is modelled using equation (5.110) (ANSYS, 2013):-

$$T^+ = \mathrm{Pr} \cdot y^* \cdot e^{-\Gamma} + [2.12 \ln(y^*) + \boldsymbol{\beta}] e^{-1/\Gamma} \quad (5.110)$$

where

$$\boldsymbol{\beta} = \left(3.85 \mathrm{Pr}^{1/3} - 1.3\right)^2 + 2.12 \ln(\mathrm{Pr}) \quad (5.111)$$

and

$$\Gamma = \frac{0.01(\mathrm{Pr} \cdot y^*)^4}{1 + 5\mathrm{Pr}^3 \cdot y^*} \quad (5.112)$$

An investigation was conducted to see if the heat transfer coefficient could be defined another way. Heat transfer coefficients (α) take the form:-

$$\alpha_j = \dot{q} / \left(T_{fluid} - T_{wall}\right) \quad (5.113)$$

The temperature T_{fluid} must be defined to compare coefficients. This could be from using the bulk fluid temperature at a particular height using either the area averaged formula:-

$$T_{bulk} = \frac{\Sigma(AT)}{\Sigma A} \quad (5.114)$$

or the mass flow averaged formula:-

$$T_{mfa} = \frac{\Sigma(\dot{M}T)}{\Sigma \dot{M}} \quad (5.115)$$

The "absolute mass flow averaged" values were also considered (not taking into account whether the fluid was moving up or down):-

$$T_{amfa} = \frac{\Sigma(|\dot{M}|T)}{\Sigma|\dot{M}|} \quad (5.116)$$

Using the jacket fluid inlet temperature was also taken into account, to provide a lower limit for possible heat transfer coefficients, as this provides the maximum temperature difference.

ANSYS CFX can calculate the wall temperatures using the "function calculator", but by default uses "conservative values" (adjacent cell temperature) rather than "hybrid values" (wall surface temperature), so the "hybrid" button must be clicked to calculate the correct values.

The individual heat transfer coefficients for the glass wall could be calculated based on the areas and physical properties of the glass (such as thermal conductivity) and the total heat transferred through these surfaces, and the process wall temperature (T_{ii}) and outer surface temperature (T_{oo}) could then be calculated. These could then be used to evaluate expected values of α_{ii} and α_{oo} as displayed in table 5.7.

Table 5.7 – Experimental and CFD results for the different Huber set point temperatures in the methanol distillation experiment.

T_{set} / °C	80	85	90	95	100
$T_{m1,expt} = T_{m1,CFD}$ / °C	79.7	84.8	89.8	94.7	99.7
$T_{m2,expt}$ / °C	78.1	82.7	87.4	91.9	96.6
$T_{m2,CFD}$ / °C	78.0	82.6	87.2	91.7	96.2
$\dot{Q}_{m,expt}$ / W	788.0	987.9	1185.4	1386.7	1555.4
$\dot{Q}_{m,CFD}$ / W	848.8	1072.1	1302.7	1527.2	1750.7
$\dot{Q}_{m,CFD} / \dot{Q}_{m,expt}$	1.077	1.085	1.099	1.101	1.126
T_{oi} (*) / °C	77.0	81.4	85.8	90.3	94.7
α_{oi} (*) / W m^{-2} K^{-1}	345.1	348.9	356.2	358.2	360.1
Area weighted $\dot{q}_{oi}$ (*) / W m^{-2}	635.2	688.5	744.2	796.3	848.8
$\dot{Q}_{o,CFD} = \dot{q}_{oi} \times A_{oi,CFD}$ / W	342.0	370.7	400.6	428.7	457.0
$\dot{Q}_{o,calc} = \dot{q}_{oi} \times A_{oi,expt}$ / W	318.3	339.9	362.0	389.9	401.0
$T_{oo,calc}$ (using wall conductivity) / °C	74.6	78.8	83.1	87.3	91.6
$\alpha_{oo,calc} = \dot{q}_{oo}/(T_{oo,calc} - T_{amb})$ / W m^{-2} K^{-1}	9.2	9.2	9.3	9.3	9.4
$U_o = U_{loss}$ / W m^{-2} K^{-1}	8.6	8.6	8.7	8.7	8.8
T_{io} (*) / °C	76.4	80.4	84.5	88.5	92.5
α_{io} (*) / W m^{-2} K^{-1}	275.8	278.4	282.8	284.7	286.6
Area weighted $\dot{q}_{io}$ (*) / W m^{-2}	1197.4	1657.2	2131.4	2595.5	3056.7
$\dot{Q}_{i,CFD} = \dot{q}_{io} \times A_{io,CFD}$ / W	506.8	701.4	902.1	1098.5	1293.7
$\dot{Q}_{i,calc} = \dot{q}_{io} \times A_{io,expt}$ / W	469.8	648.0	823.5	996.8	1154.4
$\dot{Q}_{cond}$ (**) / W	280.9	438.9	615.7	805.5	988.0
$\dot{Q}_{u,calc} = \dot{Q}_{i,calc} - \dot{Q}_{cond}$ / W	188.8	209.1	207.8	191.3	166.4
$T_{ii,calc}$ (using wall conductivity) / °C	71.1	73.0	75.1	77.1	79.3
$\alpha_{ii,calc} = \dot{q}_{ii}/(T_{ii,calc} - T_p)$ / W m^{-2} K^{-1}	223.9	226.4	227.5	227.8	225.7
$U_i = U_j$ / W m^{-2} K^{-1}	76.4	76.9	77.3	77.5	77.4
Wall superheat $(T_{ii,calc} - T_p)$ / °C	6.4	8.3	10.4	12.4	14.6
(*) = CFD only (not measured). (**) = Experimental only (not simulated).					

Table 5.7 displays experimental and CFD results as a comparison as well as calculated values of heat transfer coefficients on the process side and outer surface. The total heat transferred by the jacket ($\dot{Q}_m$) in the experiment compared to the CFD differs by only about

10%. This is displayed in table 5.7 with the different values of $\dot{Q}_i$, $\dot{Q}_o$ and $(T_{m2} - T_{m1})$. As well as this, the evaluated heat transfer coefficients, as well as the overall heat transfer coefficients U_j and U_{loss}, are notably similar to the values calculated in chapter 4 (section 4.4.1). The difference may largely be due to a difference in areas used in the CFD compared to the experiment, as well as a difference in the definition of T_{fluid}. These areas are tabulated in table 7.2 (page 190). These factors will need to be corrected for, upon further investigation. Additional errors are due to rounding of values in calculation.

Another factor influencing the difference in heat assumed to have been transferred through the outer vs inner walls in the experimental analysis (in chapter 4) was the amount of condensate collected. It was assumed that 100% of the heat transferred to the methanol was used to boil it, and the amount of condensate collected was taken to match up with $\dot{Q}_{cond}$ in the experimental results.

As described in chapter 3, the re-condensed methanol was collected in a weighed bottle to record the rate of condensation, and returned to the process at an unmeasured temperature (most likely close to ambient temperature) after the condensation rate at each incremental Huber set point temperature had been measured. This ensured that the heat required to heat up the returned methanol to its boiling point was not transferred during these times in the experiment.

Table 5.8 – Jacket side heat transfer coefficients when the Huber set point temperature is 90°C.

Correlation	$\boldsymbol{\alpha_{io}}$ / W m^{-2} K^{-1}	$\boldsymbol{\alpha_{oi}}$/ W m^{-2} K^{-1}
Petukov (1970) equation for flow in pipes	523.9	
ESDU 81045 (1981) modification of Petukov (1970) for annuli	445.8	434.8
Gnielinski (2009) model for turbulent flow in annuli	511.0	506.2
Hewitt *et al*. (1994), from Brown et al. (1947)	635 to 1170	
Bondy and Lippa (1983) turbulent correlation	163.7	165.0
CFD (SST model in ANSYS CFX)	282.8	356.2

The jacket heat transfer coefficients (α_{io} for the inner and α_{oi} for the outer) were significantly lower than common correlations, as displayed in table 5.8, with the exception of the Bondy and Lippa (1983) correlation. Standard correlations such as the Petukov (1970) equation for pipe flow and the ESDU 81045 (1981) modification for annuli, as well as the Gnielinski (2009) correlation, result in significantly higher values,

and hence these correlations are not considered suitable for this investigation. The suggested values in Hewitt *et al.* (1994) based on Brown et al. (1947) are especially unsuitable, as they use liquid water rather than DW-Therm.

$$\alpha_{ii} = \left(\alpha_{nb}^3 + \alpha_{fc}^3\right)^{1/3} \tag{5.117}$$

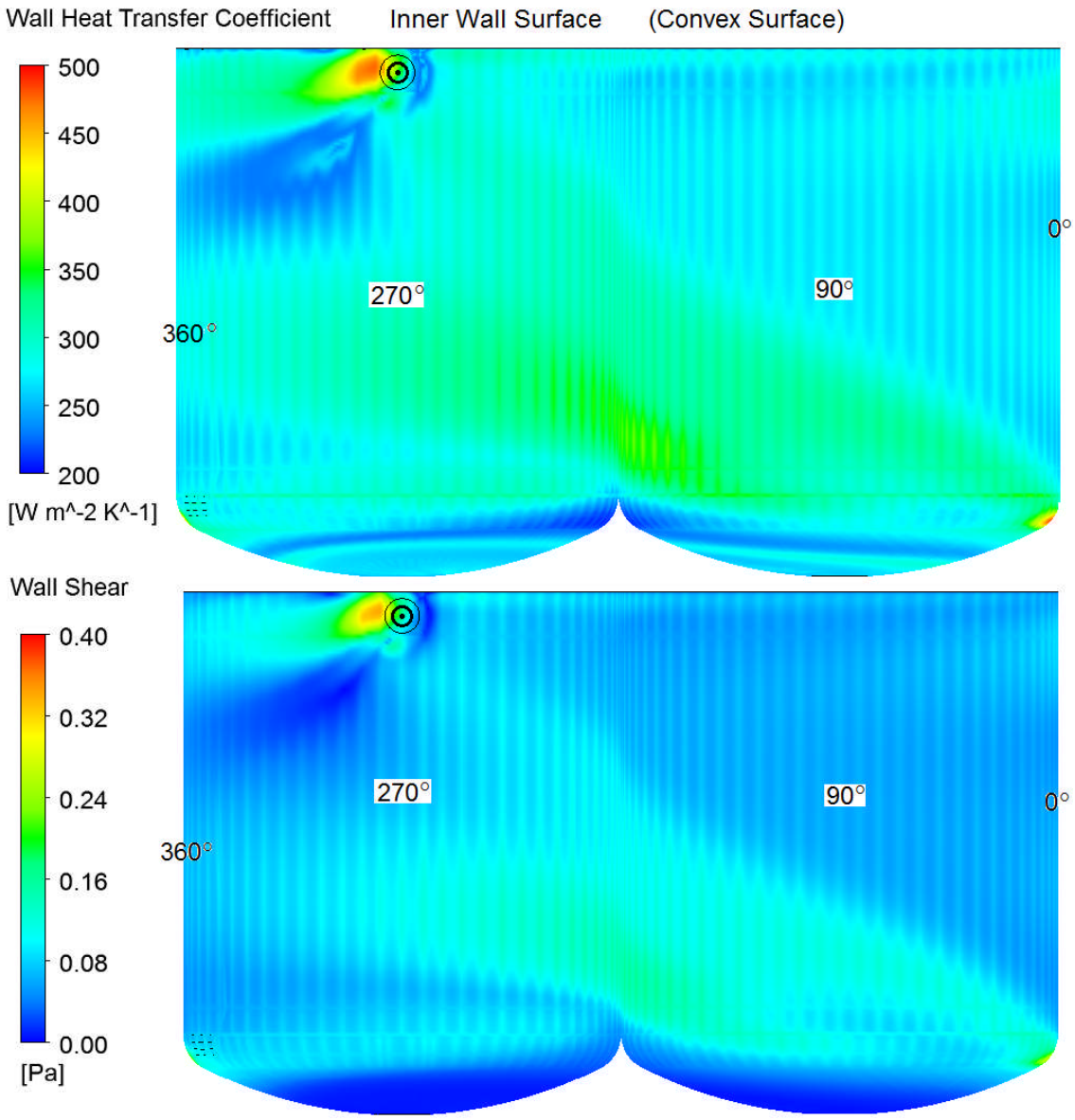

Figure 5.15 – Distributions of wall heat transfer coefficient and wall shear for the inner wall in the methanol batch distillation experiment when the Huber set point temperature is 90°C. View from the outside.

Table 5.9 displays the results of some correlations for nucleate boiling coefficients (α_{nb}) from different sources based on the inner vessel wall, for different Huber set points of the methanol distillation experiment. The Nagata *et al.* (1971) correlation suggested a forced convection heat transfer coefficient due to the stirrer (α_{fc}) of 531.3 W m^{-2} K^{-1}. Steiner and Taborek (1992) suggest combining these two as in equation (5.117), which would

result in higher values than α_{fc} alone, whereas the calculated values displayed in table 5.7 have a process heat transfer coefficient staying almost constant at around 225 W m^{-2} K^{-1}.

Table 5.9 – Boiling coefficients for methanol in the vessel, according to different sources found in Hewitt *et al.* (1994).

Huber set point temperature	**80°C**	**85°C**	**90°C**	**95°C**	**100°C**
Forster-Zuber (1956) / W m^{-2} K^{-1}	883	1487	2125	2808	3508
Cooper (1984) / W m^{-2} K^{-1}	231	287	337	383	422
Montinskii (1963) / W m^{-2} K^{-1}	138	173	204	233	259
Montinskii-Palen (Palen, 1972) / W m^{-2} K^{-1}	134	168	199	227	252
Montinskii-Bier (Bier *et al.*, 1983) / W m^{-2} K^{-1}	130	162	192	220	243

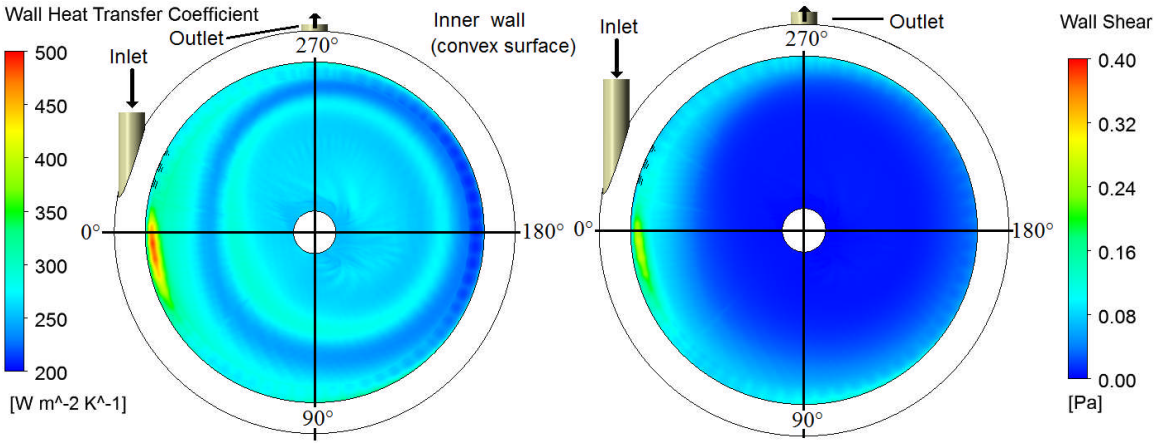

Figure 5.16 – Distribution of wall heat transfer coefficient and wall shear for the inner wall in the methanol batch distillation experiment when the Huber set point temperature is 90°C. View from the bottom.

Figures 5.15 to 5.21 display the CFD results for the wall heat transfer coefficient and wall shear stress on the jacket side (inner and outer walls), when the Huber set point temperature is 90°C. Both sets of data have a similar pattern. In these data, the average values for wall heat transfer coefficient were 282.8 W m^{-2} K^{-1} on the inner surface and 356.2 W m^{-2} K^{-1} on the outer surface.

For the CFD results of wall shear stress, the average values were 0.071 Pa on the inner wall surface and 0.175 Pa on the outer wall surface. Much greater values of wall shear stress are observed at certain points on the walls, where the flow impinges.

Engineering correlations in the literature usually predict higher values of wall shear stress on the inner surface because they do not account for the flow impinging on the outer surface. Attachment of flow is predominantly on the outer wall. Attachment to the inner wall due to the Coandă effect occurs comparatively little – some at the back of the jacket, but most prominently just after the flow passes by the outlet point.

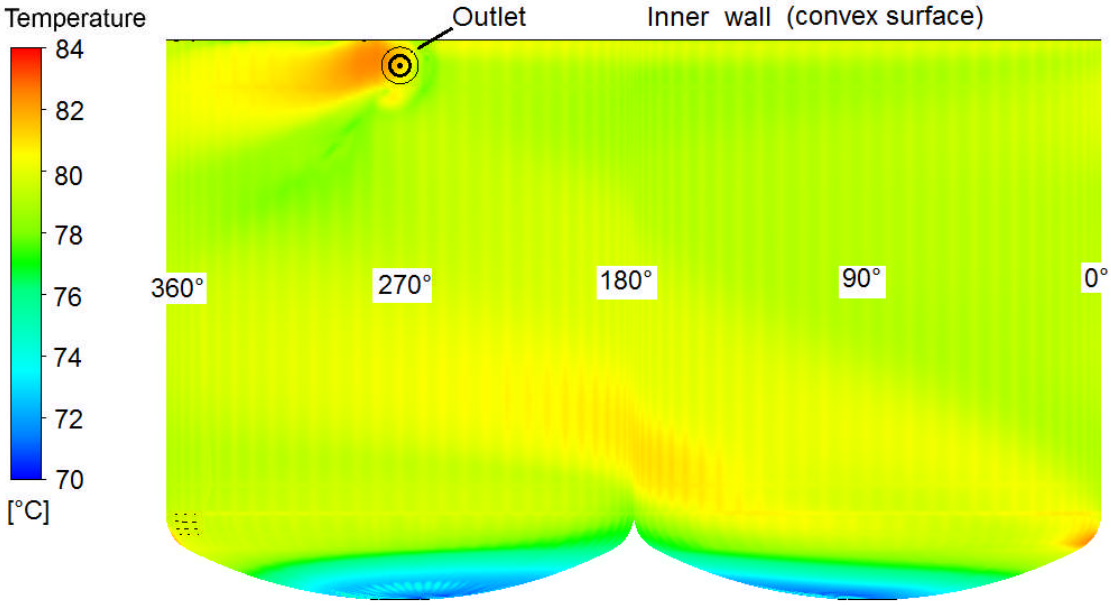

Figure 5.17 – Distribution of wall temperature for the inner wall in the methanol batch distillation experiment when the Huber set point temperature is 90°C. View from the outside.

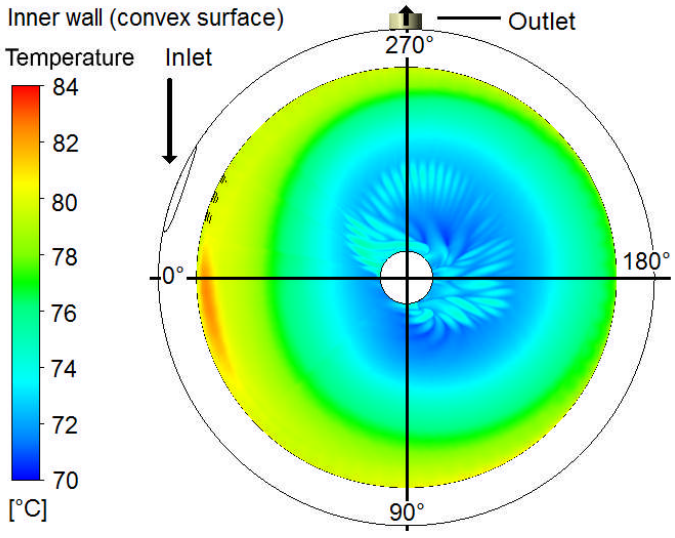

Figure 5.18 – Distribution of wall temperature for the inner wall in the methanol batch distillation experiment when the Huber set point temperature is 90°C. View from the bottom.

Note that the visual distortions in figures 5.15 to 5.21 (apparent vertical lines or “waves”) are a result of the polygonal structure of the mesh, a necessary component of the CFD

model. These minor distortions in the values at the wall occur at regular intervals no matter whether temperature, shear stress, heat transfer coefficient, wall heat flux or wall temperature is displayed. The distortions correspond to the polygonal (prismatic) structure of the original geometry generated in ANSYS Design Modeler. Re-associating the block faces with the geometry surfaces in the meshing program ICEM made no difference, as it ensured that the mesh would conform to the polygonal geometry. Also, attempting to disassociate the block faces with the surface – so that they were only definable by the curves in the geometry, which did not have a polygonal structure – prevented the mesh from being generated.

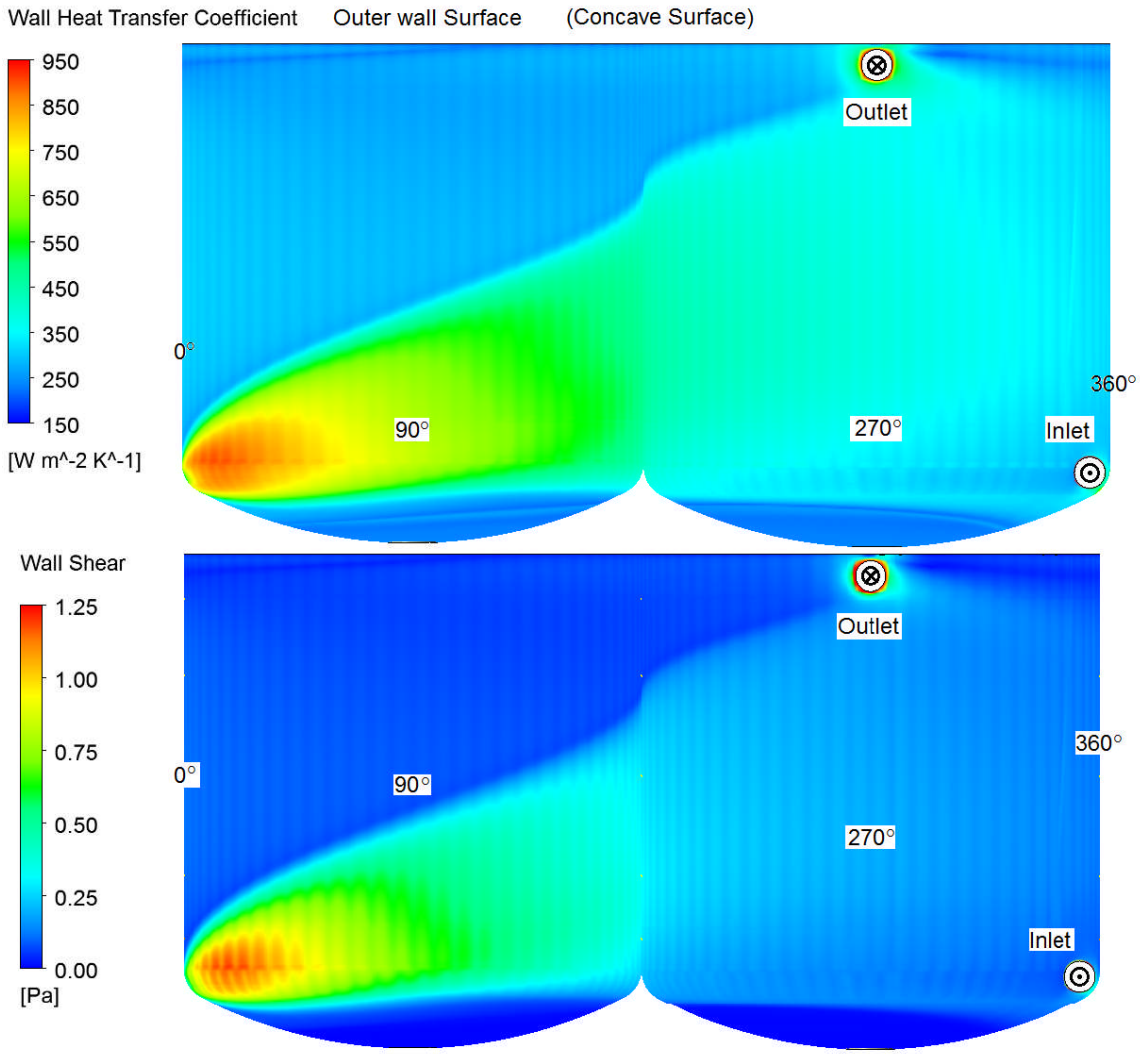

Figure 5.19 – Distributions of wall heat transfer coefficient and wall shear for the outer wall in the methanol batch distillation experiment when the Huber set point temperature is 90°C. View from the inside.

The highest temperatures inside the jacket (just below the jacket inlet temperature) occurred when the inlet stream impinged against the outer wall surface. The higher temperatures on

the inner wall surface (approximately 88°C) were observed at the inlet point and the outlet point, when the flow was disturbed by the presence of the outlet port. Additionally, a small region of higher temperature was observed at the back of the reactor. The lowest temperatures (approximately 58°C) were observed at the bottom of the jacket, where the flow stagnated. It is likely that laminar flow and natural convection dominate in this region. Figures 5.16 and 5.18 appear to display a pattern produced by natural convection at the bottom.

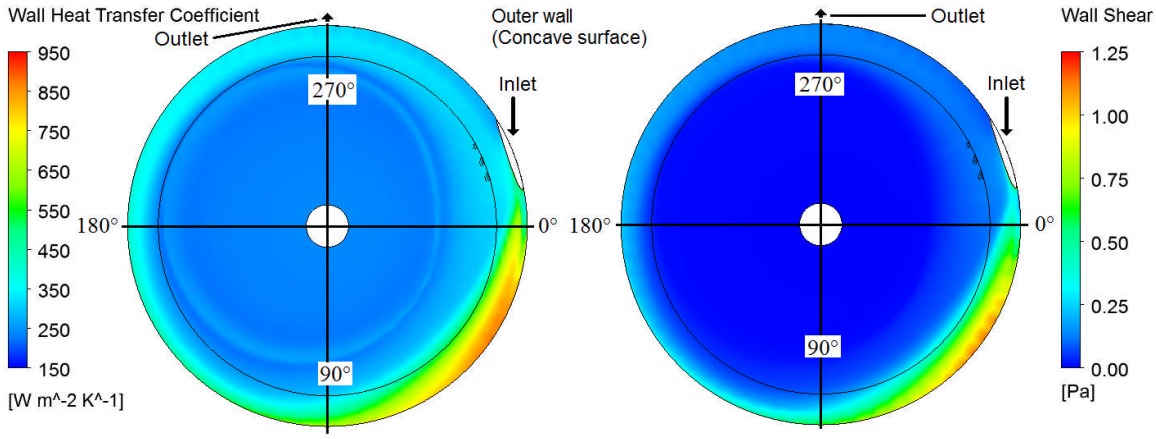

Figure 5.20 – Distributions of wall heat transfer coefficient and wall shear for the outer wall in the methanol batch distillation experiment when the Huber set point temperature is 90°C. View from the top.

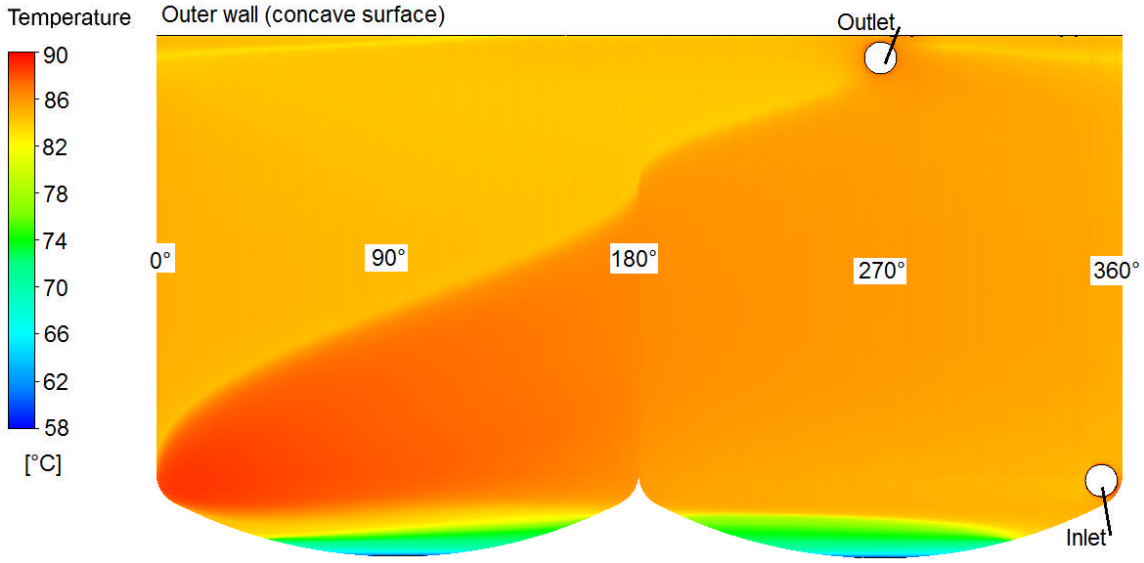

Figure 5.21 – Distribution of wall temperature for the outer wall in the methanol batch distillation experiment when the Huber set point temperature is 90°C. View from the inside.

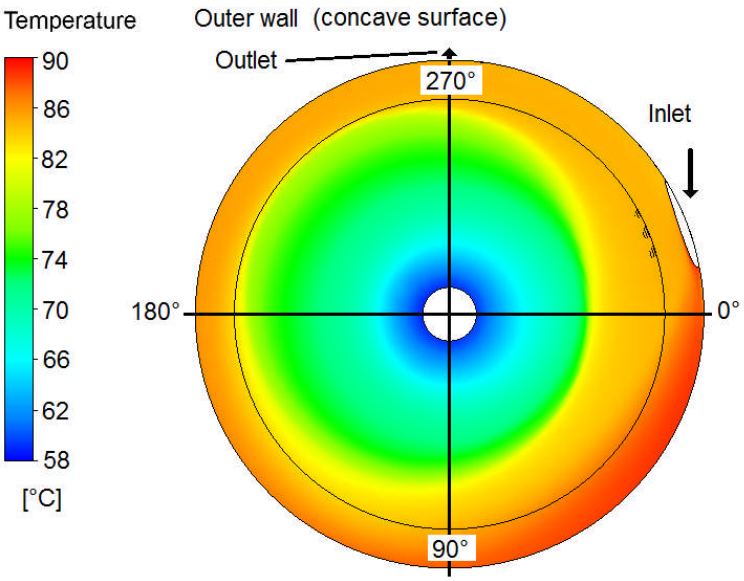

Figure 5.22 – Distribution of wall temperature for the outer wall in the methanol batch distillation experiment when the Huber set point temperature is 90°C. View from above.

5.5.2 Reversed Flow Conditions

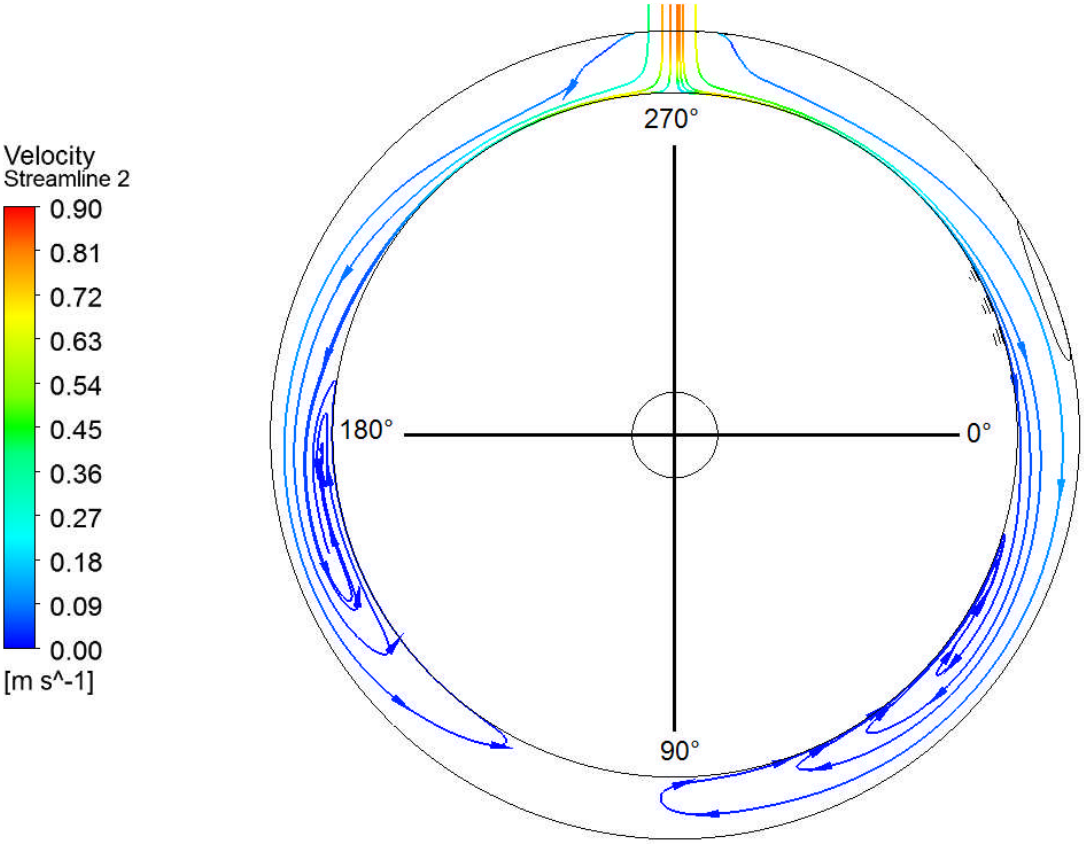

Figure 5.23 – Streamlines with vector arrowheads at the plane of the 'inlet' pipe for the reversed flow simulation of the water batch distillation experiment when the Huber set point temperature is 135°C. The plane displayed is at the height of the centre of the top pipe.

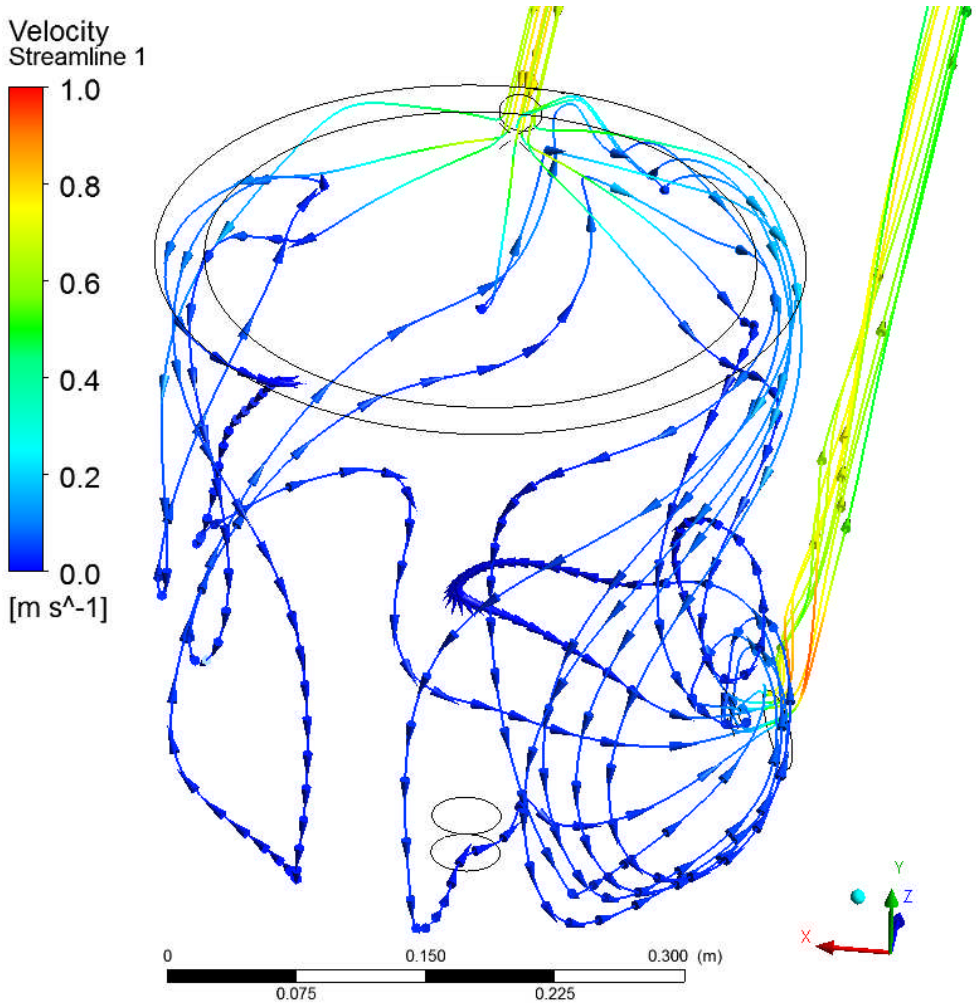

Figure 5.24 – Streamlines with vector arrowheads for the reversed flow simulation of the water batch distillation experiment when the Huber set point temperature is 135°C. Along each line, an arrowhead is displayed for every 1 second a DW-Therm particle travels along the streamline.

To test what the CFD would produce for different flow conditions, the inlet and outlet ports were swapped. This meant that the jacket flow would come in at the top radially and exit near the bottom tangentially.

The direction of feed can have a dramatic effect on the distribution of heat transfer coefficients, although the area averaged heat transfer coefficients do not change as much as might be expected. Figures 5.23 and 5.24 each display 9 streamlines based on particle tracks with starting points on the inlet face (in this case, for the pipe at the top of the reactor).

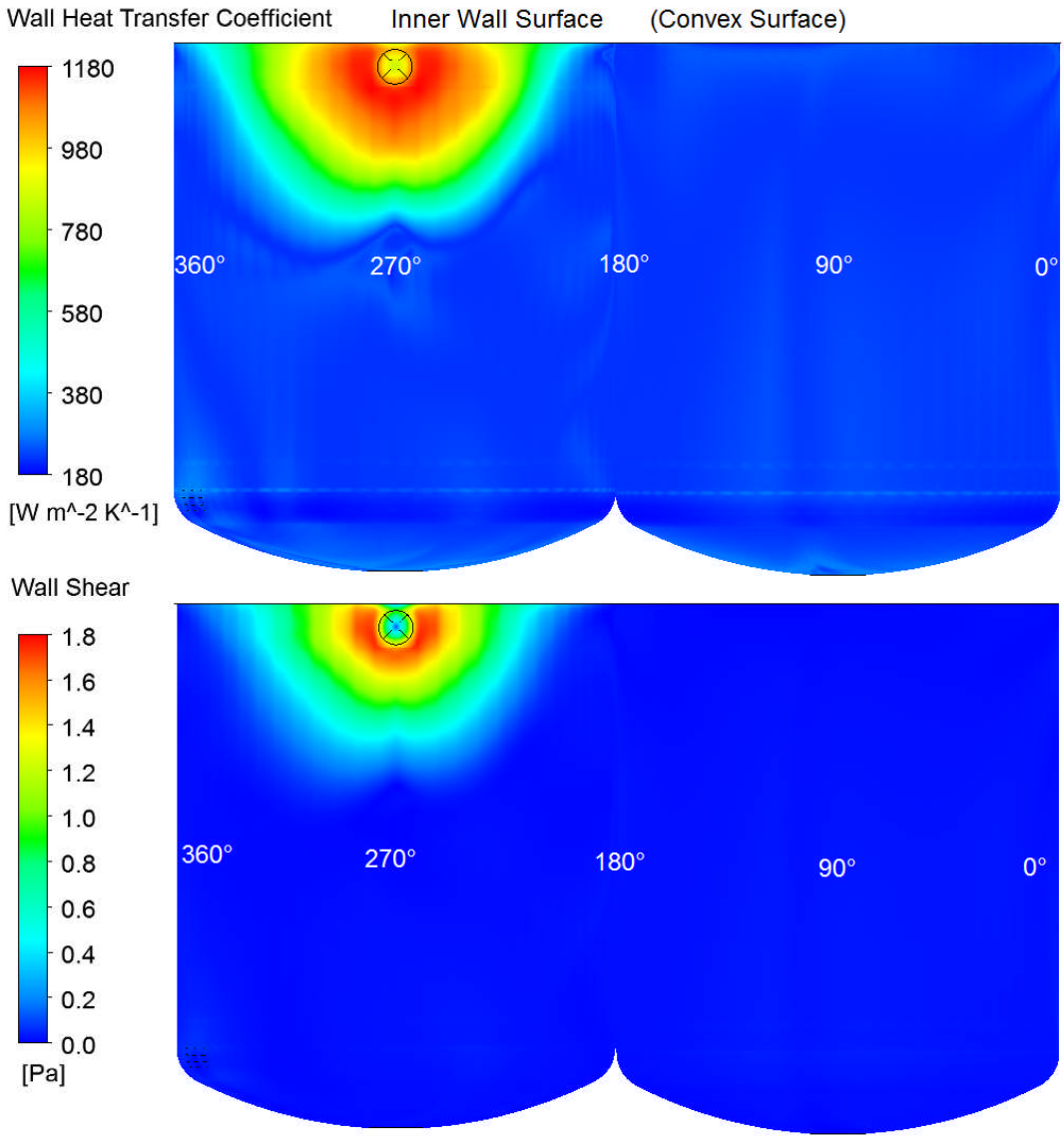

Figure 5.25 – Distributions of heat transfer coefficient and wall shear stress on the inner wall (convex surface, viewed from outside) for the reversed flow simulation of the water batch distillation experiment when the Huber set point temperature is 135°C.

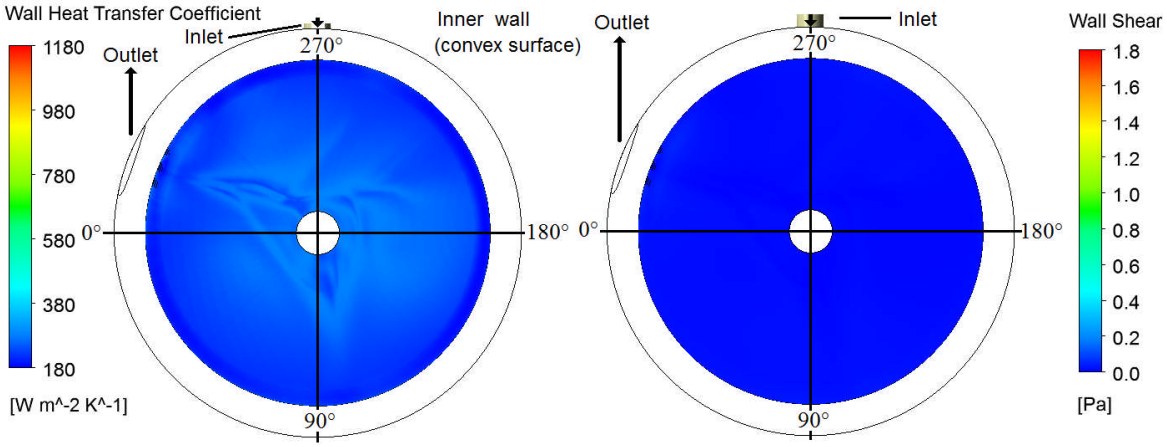

Figure 5.26 – Distributions of heat transfer coefficient and wall shear stress on the inner wall (convex surface, viewed from the bottom) for the reversed flow simulation of the water batch distillation experiment when the Huber set point temperature is 135°C.

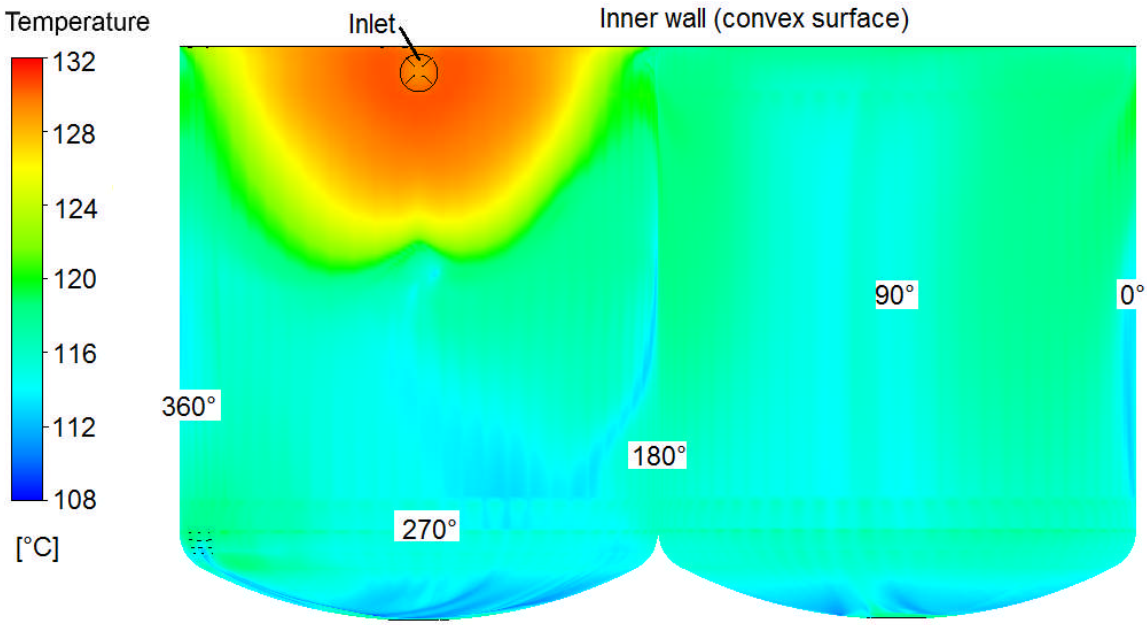

Figure 5.27 – Distribution of wall temperature on the inner wall (convex surface, viewed from outside) for the reversed flow simulation of the water batch distillation experiment when the Huber set point temperature is 135°C.

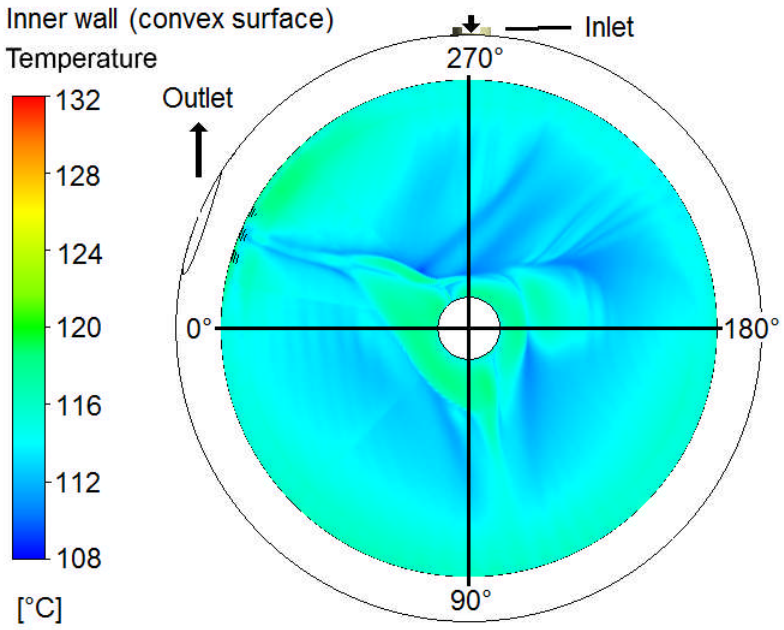

Figure 5.28 – Distribution of wall temperature on the inner wall (convex surface, viewed from the bottom) for the reversed flow simulation of the water batch distillation experiment when the Huber set point temperature is 135°C.

The distance between two arrowheads on the same path in figures 5.23 and 5.24 indicates a time of 1 second, hence the fluid is moving very slowly in most areas inside the jacket. Note that these starting points are not distributed in specific symmetrical positions at the inlet face, and this means that the paths tracked by the streamlines may not be evenly or symmetrically distributed in the jacket. In addition, the slow flow in the jacket makes the

particle tracks very susceptible to slight changes in the flow, further increasing the apparent asymmetry, particularly in figure 5.24.

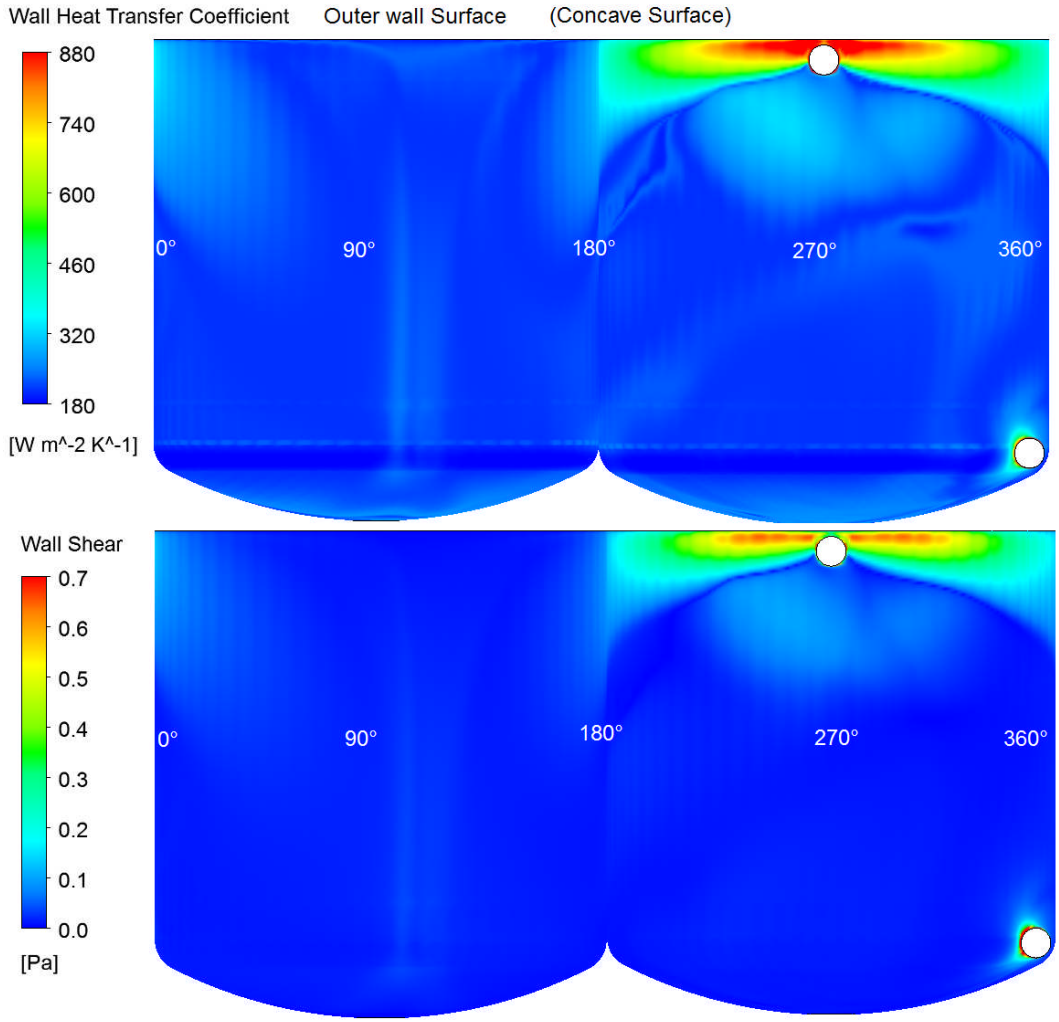

Figure 5.29 – Distributions of heat transfer coefficient and wall shear stress on the outer wall (concave surface, viewed from inside) for the reversed flow simulation of the water batch distillation experiment when the Huber set point temperature is 135°C.

Figures 5.25 and 5.26 display the distributions of heat transfer coefficient and wall shear in the inner wall. In both cases, the greatest heat transfer coefficient and the greatest shear stress both occur at the point where the ‘inlet’ jet impinges on the inner wall. This is a highly concentrated region, so there is maldistribution of heat transfer, but the advantage is that the higher heat transfer occurs on the inner wall, rather than the outer wall. Figures 5.27 and 5.28 display the inner wall temperature distributions. A similar pattern is observed to the heat transfer, where a large non-uniform distribution of temperature occurs and the highest wall temperature occurs at the point where the inlet jet impinges against the inner wall. There is a sudden jump from this region of high temperature (about 130°C) to the rest of the jacket (about 118°C).

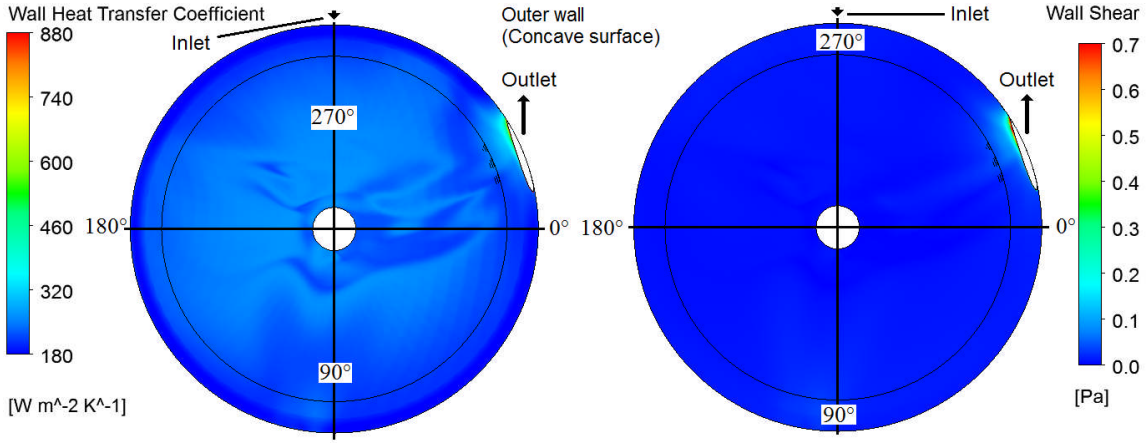

Figure 5.30 – Distributions of heat transfer coefficient and wall shear stress on the outer wall (concave surface, viewed from the top) for the reversed flow simulation of the water batch distillation experiment when the Huber set point temperature is 135°C.

Figures 5.29 and 5.30 display the distributions of heat transfer coefficient and wall shear in the outer wall. There is a high heat transfer coefficient and high shear stress at the top of the jacket, where the inlet jet enters the jacket, the flow is spreading throughout the jacket and the highest velocities occur at this inlet point.

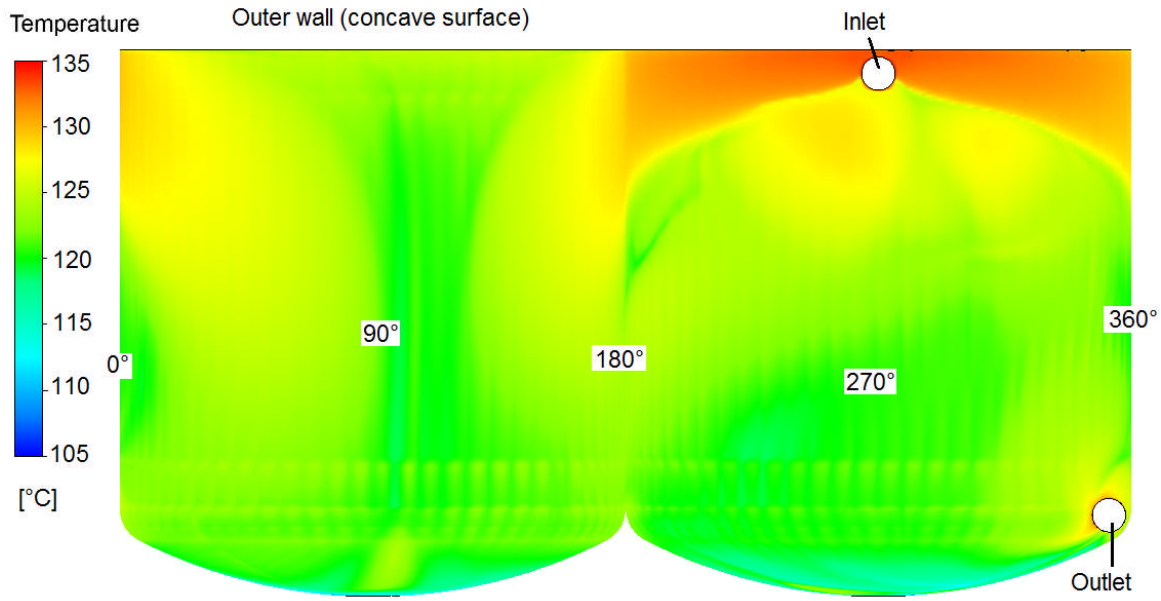

Figure 5.31 – Distribution of wall temperature on the outer wall (concave surface, viewed from inside) for the reversed flow simulation of the water batch distillation experiment when the Huber set point temperature is 135°C.

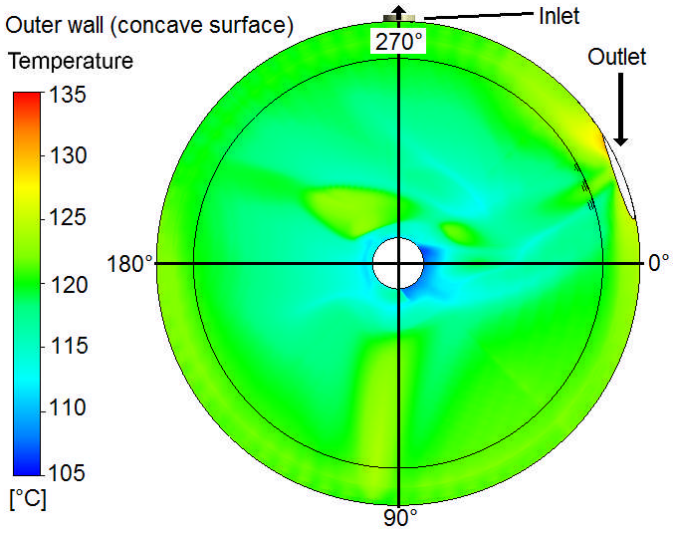

Figure 5.32 – Distribution of wall temperature on the outer wall (concave surface, viewed from the top) for the reversed flow simulation of the water batch distillation experiment when the Huber set point temperature is 135°C.

Figures 5.31 and 5.32 display the outer wall temperature distributions. Compared to the inner wall temperature distributions, most outer wall temperatures are higher (about 125°C). This is due to a lower overall heat transfer coefficient, where less heat is being transferred at the outer wall.

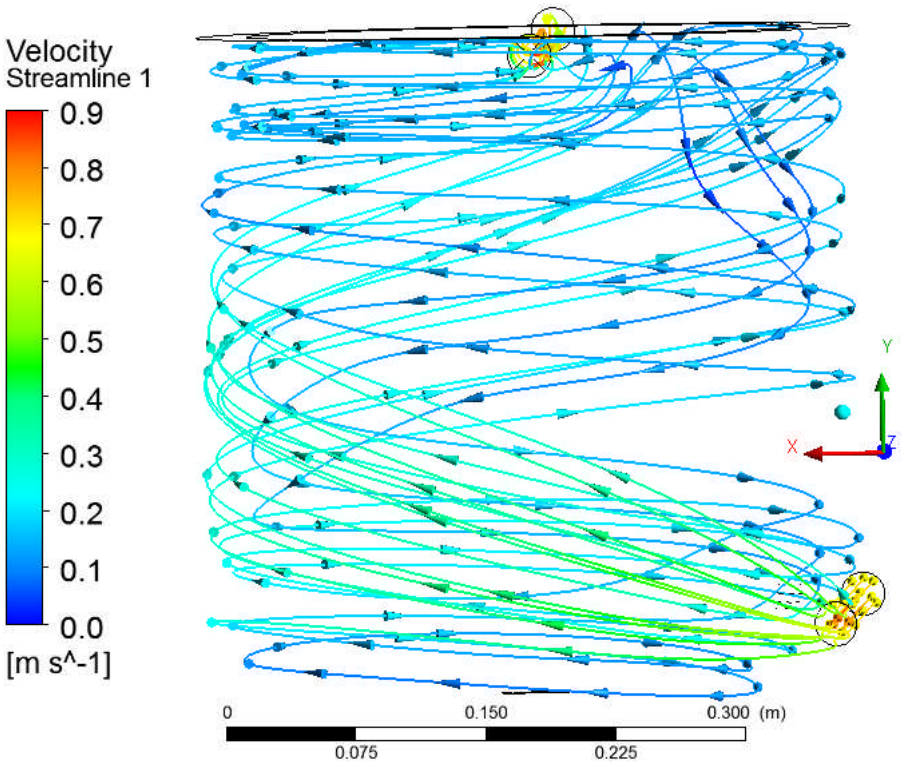

Figure 5.33 – Streamlines with vector arrowheads for the forwards flow simulation of the water batch distillation experiment when the Huber set point temperature is 135°C. Along each line, an arrowhead is displayed for every 1 second a DW-Therm particle travels along the streamline.

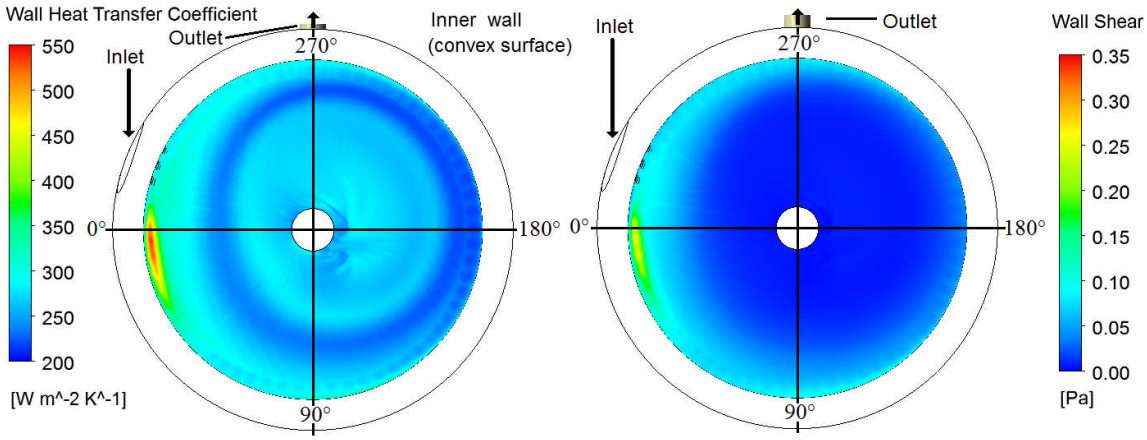

Figure 5.34 – Distributions of heat transfer coefficient and wall shear stress on the inner wall (convex surface, viewed from the bottom) for the forwards flow simulation of the water batch distillation experiment when the Huber set point temperature is 135°C.

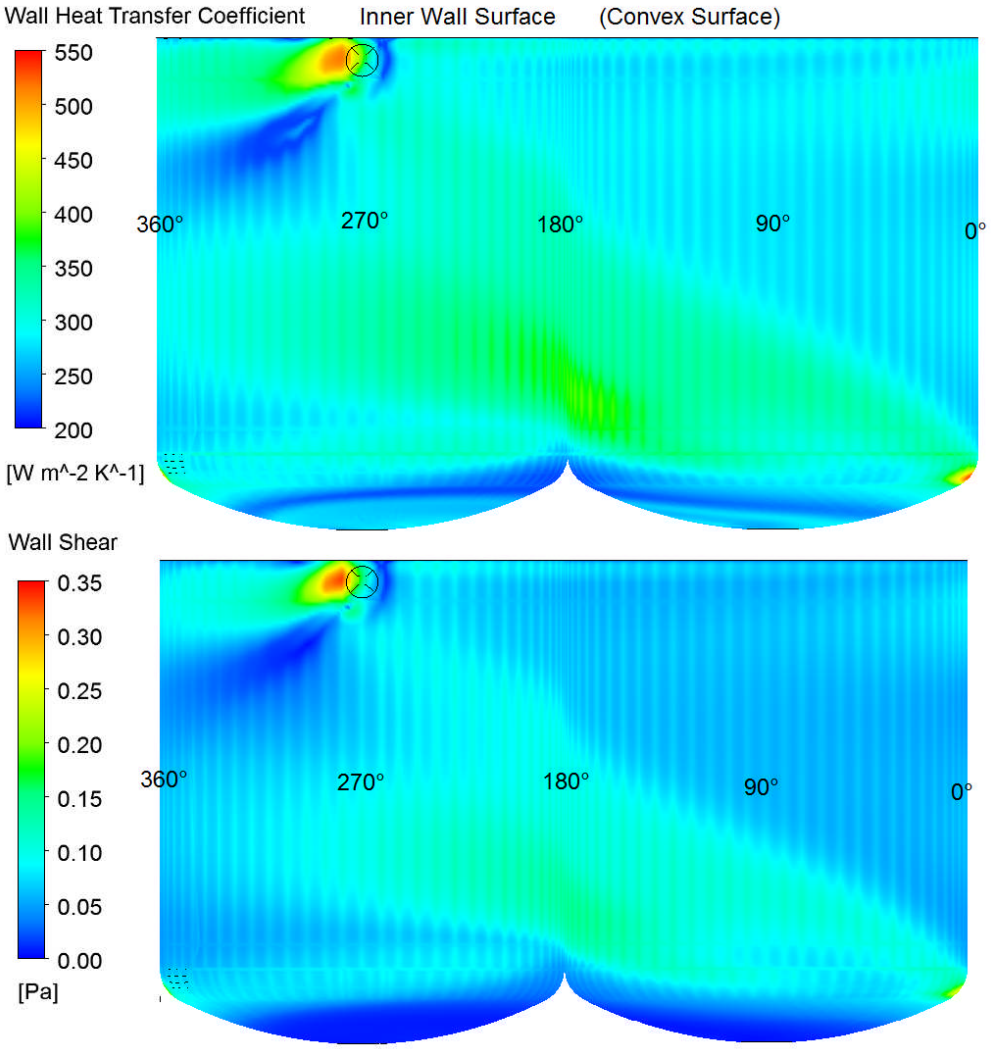

Figure 5.35 – Distributions of heat transfer coefficient and wall shear stress on the inner wall (convex surface, viewed from outside) for the forwards flow simulation of the water batch distillation experiment when the Huber set point temperature is 135°C.

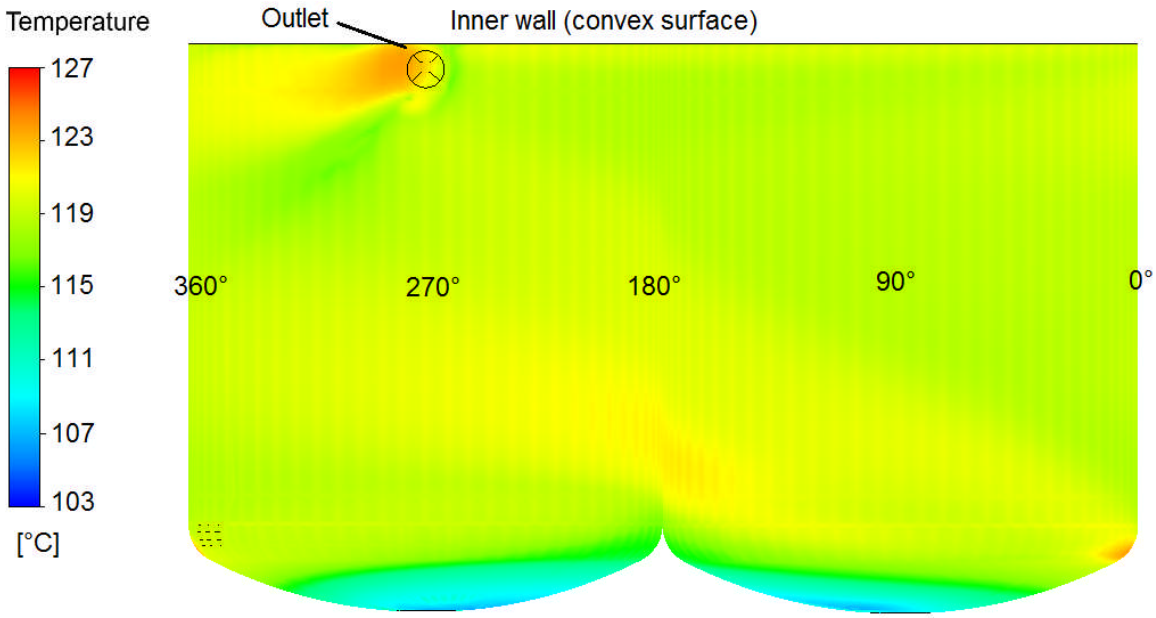

Figure 5.36 – Distribution of wall temperature on the inner wall (convex surface, viewed from outside) for the forwards flow simulation of the water batch distillation experiment when the Huber set point temperature is 135°C.

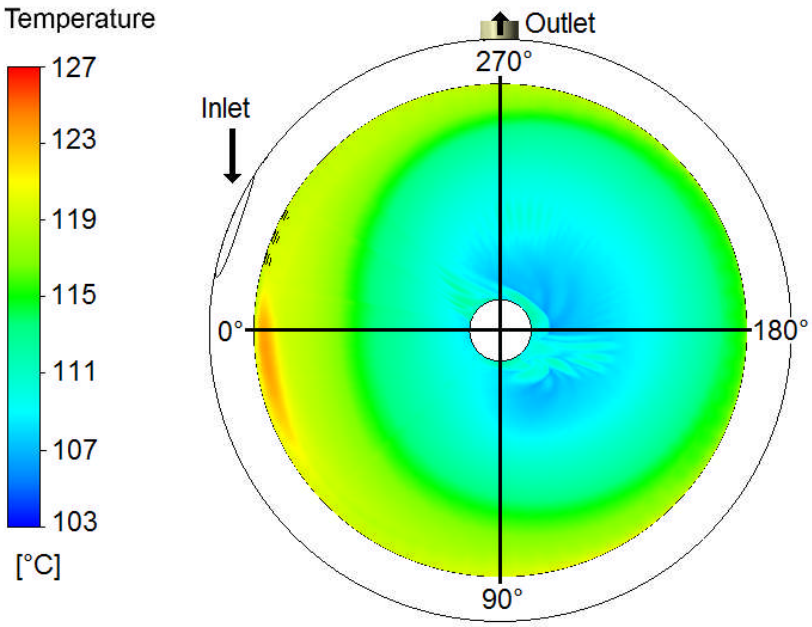

Figure 5.37 – Distribution of wall temperature on the inner wall (convex surface, viewed from the bottom) for the forwards flow simulation of the water batch distillation experiment when the Huber set point temperature is 135°C.

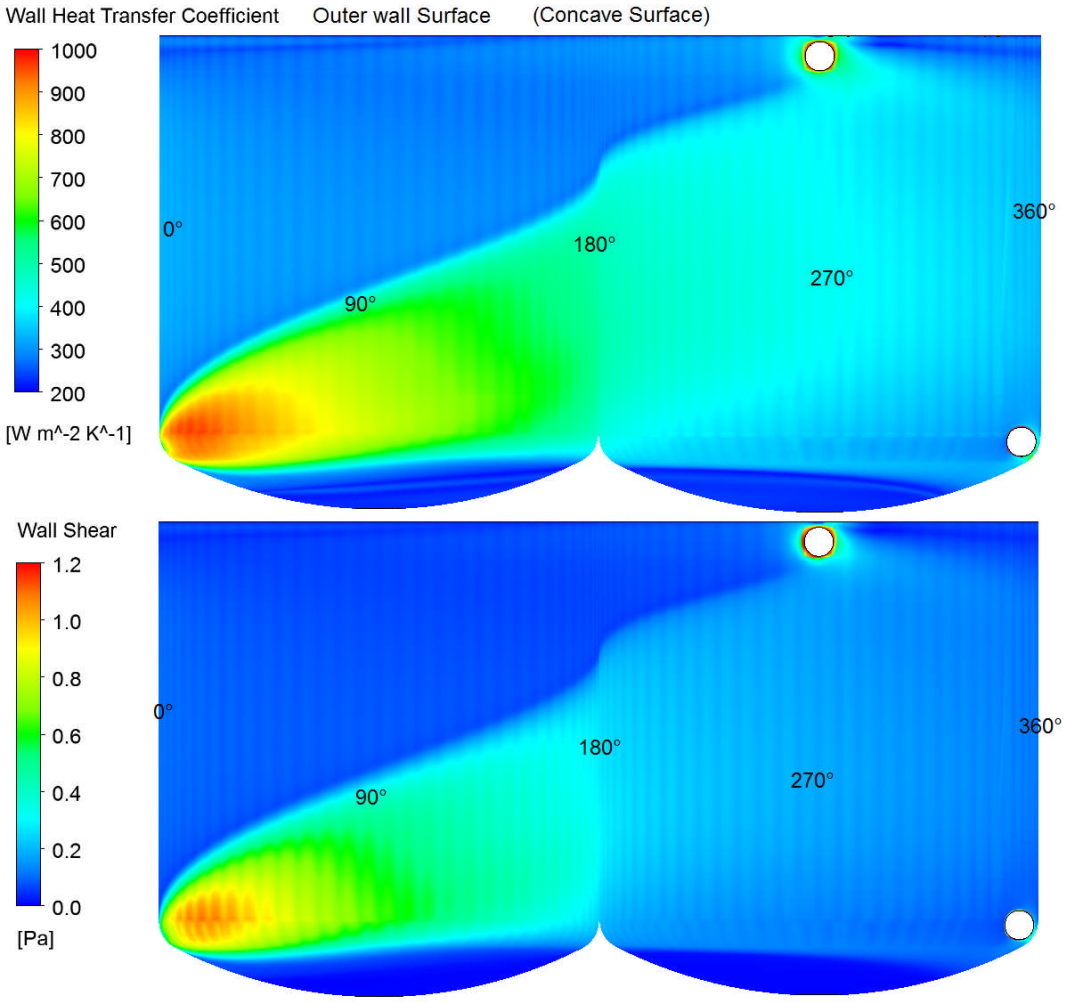

Figure 5.38 – Distribution of heat transfer coefficient and wall shear stress on the outer wall (concave surface, viewed from inside) for the forwards flow simulation of the water batch distillation experiment when the Huber set point temperature is 135°C.

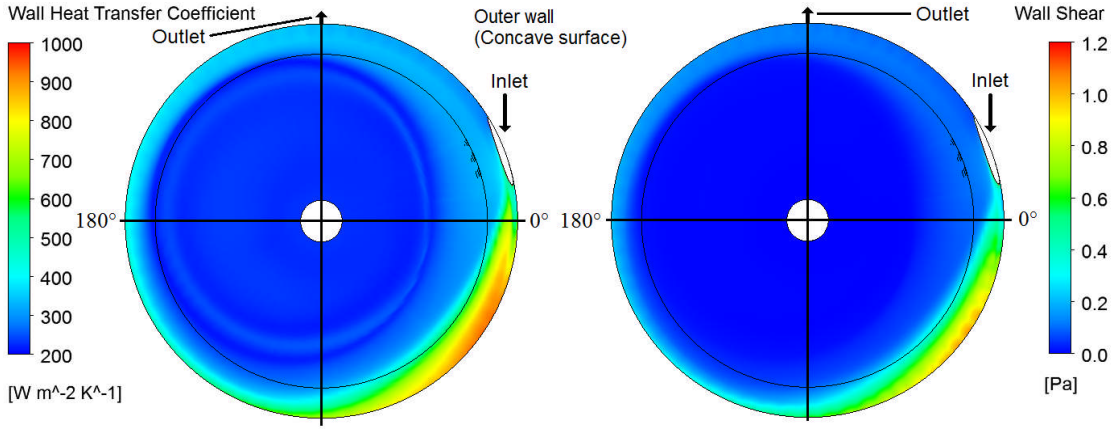

Figure 5.39 – Distribution of heat transfer coefficient and wall shear stress on the outer wall (concave surface, viewed from the top) for the forwards flow simulation of the water batch distillation experiment when the Huber set point temperature is 135°C.

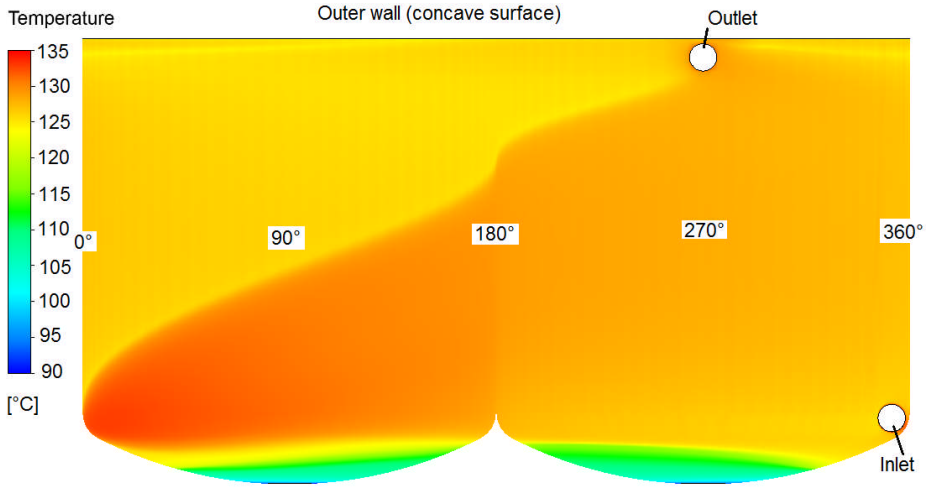

Figure 5.40 – Distribution of wall temperature on the outer wall (concave surface, viewed from inside) for the forwards flow simulation of the water batch distillation experiment when the Huber set point temperature is 135°C.

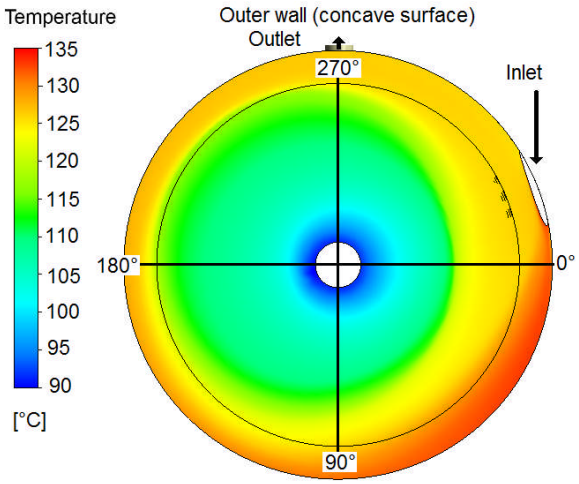

Figure 5.41 – Distribution of wall temperature on the outer wall (concave surface, viewed from the top) for the forwards flow simulation of the water batch distillation experiment when the Huber set point temperature is 135°C.

To compare the reverse flow with the forwards flow, the conditions were set to the same values. Figure 5.33 displays the streamlines in the forward flow simulation. Relative distributions of heat transfer coefficient, wall shear stress and wall temperature (and explanations thereof) are the same as those in the previous section (5.5.1), but the temperatures are higher because this experiment was boiling water rather than methanol. These results are displayed in figures 5.34 to 5.41.

Table 5.10 – Comparison of data for the forward and reversed flow CFD simulations.

Variable	**Water batch distillation, T_{set} = 135°C (forwards flow)**	**Water batch distillation, T_{set} = 135°C (reversed flow)**
T_{m1} / °C	134.6	134.6
T_{m2} / °C	130.8	131.1
T_p / °C	100.0	100.0
T_{amb} °C	19.4	19.4
Average T_{io} / °C	118.2	127.1
Average T_{oi} / °C	125.2	128.7
U_i^* (input) / W m^{-2} K^{-1}	153	153
U_o^* (input) / W m^{-2} K^{-1}	12.3	12.3
$\overline{\alpha_{io}}$ (output) / W m^{-2} K^{-1}	293	268
$\overline{\alpha_{oi}}$ (output) / W m^{-2} K^{-1}	376	242
Average inner wall shear / Pa	0.068	0.062
Average outer wall shear / Pa	0.164	0.034
q_i / W m^{-2}	2999	2765
q_o / W m^{-2}	1692	1660
$factor_1$	1.11	1.07

The heat transfer coefficients and wall shear stresses are more spread out in the forwards flow simulation. Despite the inlet jet impinging on the inner wall in reversed flow, the average heat transfer coefficients and wall shear stresses are higher in the forwards flow simulation. These variables are displayed in table 5.10. The value of $factor_1$ (see section 5.4.2 for explanation), and therefore the pressure drop, is also found to be slightly higher in the forwards flow simulation. Overall, the reversed flow conditions are thus less desirable than forwards flow, but not drastically so.

5.5.3 Heat Transfer as a Function of Height

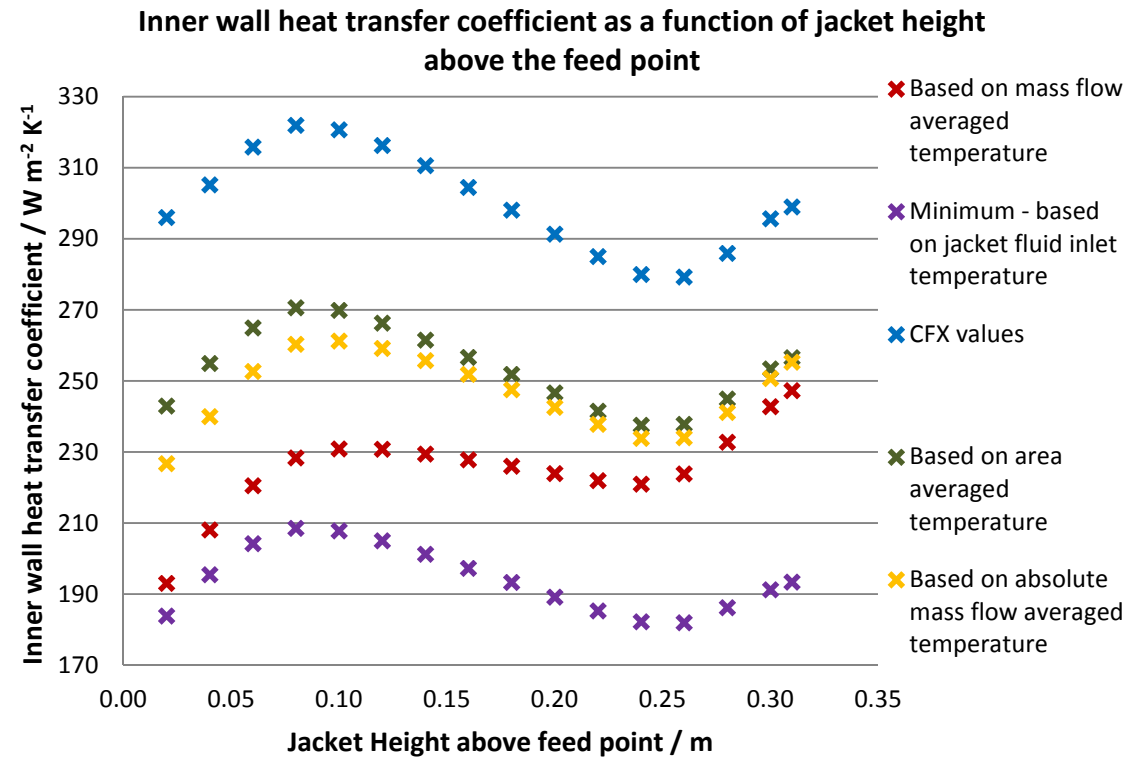

Figure 5.42 – Possible heat transfer coefficient as a function of jacket height above the feed point, for the inner wall, in the annular part of the jacket.

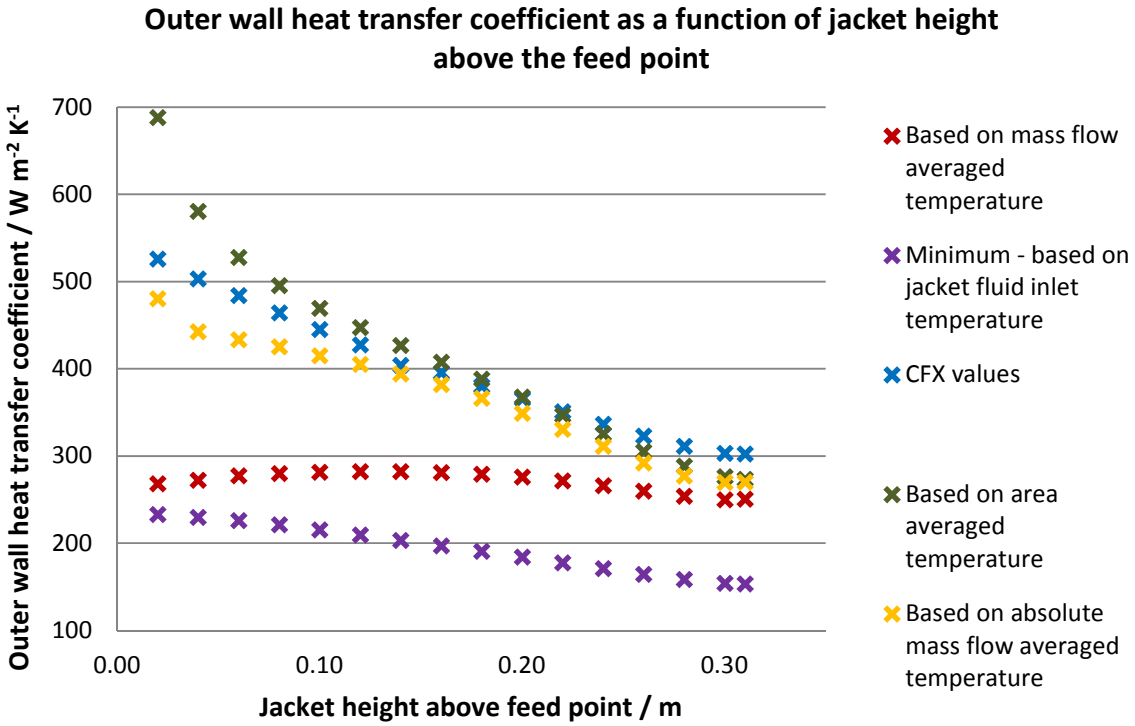

Figure 5.43 – Possible heat transfer coefficient as a function of jacket height above the feed point, for the outer wall, in the annular part of the jacket.

The temperature of the wall at a particular height was found in CFD-Post by setting an iso-clip on the wall within a set height, in this case one millimetre thick. For example, for the lowest analysed plane at height 0.02 metres, the corresponding wall temperature was area-averaged over the height 0.0195 to 0.0205 metres. This was done in intervals of 0.02 metres from height values of 0.02 metres to 0.30 metres, and at 0.31 metres. The reason why a height of zero was not included is because this would include the temperatures of the inlet pipe (the centre of which is defined as a height of zero). The reason why results at 0.31 metres rather than 0.32 metres were taken is because 0.32 metres would include the temperatures of the outlet pipe (which ranges from the z values of 0.3175 to 0.3425 m). The pipes were not included in the height calculations because doing so would have to involve working out the area excluding the pipes; an unnecessary complication.

Figures 5.42 and 5.43 display these selected possible heat transfer coefficients as a function of jacket height above the feed point. For the inner wall, the coefficient increases up to about 0.09 metres (27% of the jacket height). This is due to the flow partly attaching itself to the back of the jacket on the inner wall (the Coandă effect). The coefficient then steadily decreases as heat is lost, up to about 0.25 metres (76% of the jacket height), where it begins to increase again due to further flow attachment because the flow is disrupted near the outlet point. For the outer wall, the coefficient is predominantly higher, and steadily decreases along the entire jacket height, as the flow preferentially attaches to the outer side due to the centripetal force directing the fluid around the jacket.

5.5.4 Comparison with the Resistance Model

Engineering correlations to describe jacket side heat transfer coefficients are present in the literature. However, they have some significant drawbacks. The correlations by Bondy and Lippa (1983), Dream (1999) and Garvin (1999) consider only the inner film coefficient (α_{io}), and the correlations by Gnielinski (2009) and Kakaç *et al*. (1987) do not have formulae for scenarios with heat transfer from both walls of the annulus.

Bondy and Lippa (1983) and Dream (1999) both use a correlation found in Perry and Chilton (1973) for turbulent flow, the only difference being that Bondy and Lippa suggest neglecting a term in unbaffled jackets. It makes a greatly significant difference whether this term is included or not. Kakaç *et al*. (1987) uses laminar flow only, so their correlation is excluded in the table below.

To compare these heat transfer coefficients, the CFD values were included, as well as results from a typical 1D resistance model of the form displayed in figure 5.44. The resistance

model schematic displayed has historically been the standard overall method of calculating the temperatures in a heat transfer process such as this. In this model, a constant heat Q passes from side 1 to side 2, through three layers of resistance: the film resistance on side 1, the wall resistance, and the film resistance on side 2.

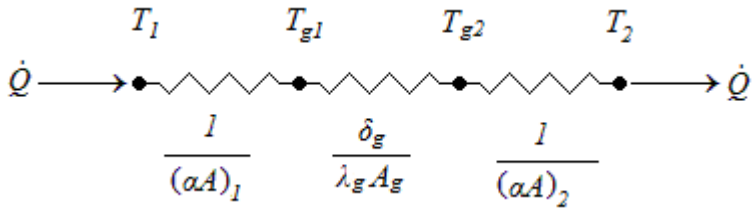

Figure 5.44 – Model of heat transfer through three layers of resistance.

The inputs for the resistance model were all the values of temperatures and heat transfer coefficients except the heat transfer coefficient on the jacket side. Putting in the same temperatures, areas and heat transfer coefficients as were used as the boundary conditions into the CFD defines all inputs but the temperature on side 1. This can either be the average of the jacket inlet and outlet temperatures, or the volume-averaged temperature in the entire jacket from the CFD values ($\overline{T_m}$). For most purposes, $\overline{T_m}$ was used.

Table 5.11 displays the results of the calculations for heat transfer coefficients, including correlations and the resistance model. Noticeably, the values predicted using the correlation by Bondy and Lippa (1983) (when using $\overline{T_m}$) are similar to the results of the resistance model when using the mean of the jacket inlet and outlet temperatures. In either of these cases, however, the value of α_{io} is underpredicted compared to the values derived from the CFD simulations. The Garvin (1999), Dream (1999) and Gnielinski (2009) correlations are considered to be less suitable because the values are much higher, implying different definitions of temperatures or different flow and heat transfer arrangements were used.

The results of evaluating correlations using the average of T_{m1} and T_{m2} rather than $\overline{T_m}$ are not significantly different, so only the values using $\overline{T_m}$ are displayed in table 5.11. This occurs because the correlations do not directly use the values of temperature, but rather use Reynolds number, Prandtl number and viscosity. A small difference in temperature thus will hardly impact the correlations, but will significantly impact the values given by the resistance model. In a similar manner, there is very little difference between the inner and outer wall when using the engineering correlations, because the only difference is the wall viscosity, which is raised to the power of 0.14 (and thus has a relatively small influence on the overall equation).

Table 5.11 – Average heat transfer coefficient comparison for the inner wall in the water boiling experiment.

Experiment mean jacket inlet temperature / °C		**129.4**	**134.6**	**139.5**	**144.5**	**149.5**
Inner wall heat transfer coefficient α_{io} / W m^{-2} K^{-1}	CFD values (using $\overline{T_m}$)	239.9	238.9	241.0	246.8	252.3
	Bondy and Lippa (1983) correlation	185.8	184.8	186.8	193.4	198.5
	Dream (1999) correlation	421.6	419.2	423.9	438.9	450.3
	Garvin (1999) correlation	274.1	272.8	276.6	288.1	296.9
	Gnielinski (2009) correlation	728.4	726.6	738.4	770.9	796.0
	resistance model using CFD $\overline{T_m}$	239.8	237.6	240.5	246.3	252.1
	resistance model using $(T_{m1}+ T_{m2})/2$	192.4	191.8	194.3	201.3	207.7
	Minimum (resistance model using T_{m1} only)	169.9	169.6	172.5	180.0	185.9

In table 5.11, differences between the CFD values and the resistance model were negligible if the CFD geometry model's area and the CFD simulation's volume-averaged bulk temperature ($\overline{T_m}$) were used in both cases. This is a direct consequence of using the same values for everything except wall temperature (ANSYS CFX calculates wall temperature as a distribution across the surface).

The surface area of the experimental setup must be well known, as this can greatly affect the film heat transfer coefficients when using the resistance model. For example, putting the originally assumed jacket side outer wall area of 0.6356 m^2 instead of the CFD geometry's own area (based on the known dimensions of the jacket) of 0.5384 m^2 into the resistance model changes the predicted outer wall heat transfer coefficient from 278 W m^{-2} K^{-1} to 52 W m^{-2} K^{-1}. This is because of the much larger temperature drop on the outside surface (side 2), so if this is reduced by a small percentage, since the overall temperature drop is constant, the smaller temperature drop on the jacket side (side 1) is added to the large temperature drop caused by the area change.

5.6 Summary of Modelling the Plain Jacket

This chapter has relaxed the assumption of uniform upwards flow in the jacket, using a model for pressure drop in the jacket with the Bernoulli equation, and CFD simulations have been conducted on the jacket and process sides separately. The simulations appear to agree reasonably with the experimental results and analysis.

Much can be learned from studying the results of the CFD models. Flow in the jacket is non-uniform and heat transfer is greater near the inlet and outlet ports of the jacket.

Running a mesh-intensive CFD simulation may reveal details such as temperature hotspots that could affect the process. Comparatively, the commonly used resistance model combined with engineering correlations can be reliable as an estimate to expected average temperatures. Predicted values of heat transfer coefficient for the inner wall in the case of Bondy and Lippa (1983) are at most 5% different from the CFD values in the inner wall, at most 15% different in the outer wall. However, comparing the results of the resistance model, this translates into a temperature error only up to about 1.1°C in both the inner and outer wall. Other correlations would have higher errors in this case, but may be more suitable for other geometries such as uniform annular flow, flow guided by vanes, or different jacket types such as half-pipe or dimple jackets.

In cases such as when high mixing and/or boiling coefficients are used for the process side – though these have a high degree of uncertainty – the values are usually high enough not to be the controlling factor for heat transfer. On the other hand, in the outer wall, the input values often become the controlling resistance and require specific known conditions to estimate, such as free convection of air on a vertical surface (as detailed in section 4.3.2).

6 MODELS TO INVESTIGATE THE PROCESS SIDE

6.1 Introduction to Modelling the Process Side

According to the literature, the assumption of perfect mixing in the process side (that is, inside the vessel) is very robust for most applications. However, for very fast reactions or very temperature-sensitive reactions “CFD models should be definitely used” (Milewska and Molga, 2010). Detailed understanding of the heat transfer and fluid flow in the specific type of reactor under operation is therefore important in such situations. Knowledge of the distributions of heat transfer coefficients is an essential part of this, because this will highlight areas of the reactor in which temperature peaks (or “hot spots”) may occur.

The dominant direction of flow in unbaffled vessels agitated using a pitched blade turbine, as with most impellers, is tangential. In an unbaffled vessel, the bulk of the fluid will thus create a vortex. A lack of baffles will mean mixing and turbulence are reduced, and resistance to flow is reduced. The primary flow pattern generated by a pitched three-blade turbine is that the flow is directed downwards at the blades and moves upwards axially along the wall. Secondary flow effects may include an outer, slower-moving flow circulation that moves downwards closer to the wall. This is especially promoted if the contents are cooling, as natural convection will aid downward flow at the walls. During heating, natural convection will aid upward flow at the walls – however, in this CFD simulation, the secondary effects of forced convection still result in net downward flow near the walls despite the heating condition.

Areas for temperature peaks are known to occur in the centres of the recirculation zones of the secondary flow, “since heat transfer is dominated by the secondary flow” (Pedrosa and Nunhez, 2003). These zones are slower-moving than the primary flow zones generated directly by the turbine and thus are less well mixed.

Brennan (1976) reviewed the vortex models developed by Nagata *et al*. (1955), Braginskii (1967) and Zlokarnik (1971). In these models, the flow was separated into an inner forced vortex, which is like a rotating cylinder of liquid, and an outer free vortex. This model of a forced vortex in the centre and a free vortex on the outside, joined at a ‘critical radius’, is widely used in predicting the free-surface profile, for example in Nataga (1975), but the focus has been on Rushton turbines and flat-blade impellers, rather than pitched blade turbines.

Correlations for predicting the vortex depth, defined as the distance between the initial surface height and the surface height at the centre of the vortex, for various impeller types, have been reported by Rieger *et al*. (1979). Equation (6.1) is such a correlation, derived from an experimental investigation to provide the vortex depth for a pitched three-blade turbine, for a Galileo number between 10^8 and 10^{10}, using an empirically derived constant (B_1) of 0.71 ± 0.03 under these conditions.

$$h_V/d = B_1 \mathrm{Ga}^{0.069}(D/d)^{-0.038}\mathrm{Fr}^{1.14\mathrm{Ga}^{-0.008}(D/d)^{-0.008}} \tag{6.1}$$

Nagata (1975) provided equations to describe the vortex profile in a six-bladed Rushton turbine, which were later used by many authors, including Haque *et al*. (2006). This profile is compared to the CFD results for the three-bladed pitched turbine used in this investigation.

Nagata *et al*. (1972) provided a correlation, equation (6.2), for predicting the average wall film heat transfer coefficient on the inside surface of an unbaffled agitated vessel from the Nusselt number in terms of a Reynolds number, a Prandtl number, a viscosity ratio and parameters related to the turbine: b is the turbine blade width, ϑ_{bl} is the blade angle measured from the horizontal, d is the turbine diameter and n_{bl} is the number of blades. This equation alone is not suitable for the type of problem discussed in chapter 4, as it does not account for boiling.

$$\mathrm{Nu}_{ii} = 0.54\mathrm{Re}_a^{0.67}\mathrm{Pr}^{0.33}\mathrm{Vi}^{0.14}\left[\frac{5b\sin(\vartheta_{bl})}{d}\right]^{0.2}\left(\frac{n_{bl}}{6}\right)^{0.2}[\sin(\vartheta_{bl})]^{0.5} \tag{6.2}$$

6.2 CFD Modelling of the Process Side

6.2.1 CFD Simulation Methodology

Figure 6.1 displays the ‘domains’ used in the CFD simulation (on ANSYS CFX) for the impeller (purple) and tank (green). An optional wall mesh (red) was used in non-isothermal simulations. The ‘ANSYS Meshing’ program was used to automatically generate a mesh for the impeller using tetrahedral elements, because of the complex geometry involved. ANSYS ICEM was used to make the mesh for the rest of the tank, which had a height 0.2 metres higher than the top of the jacket. This was to ensure no water could reach the top of the tank domain, which would cause problems as it would be deleted from the simulation.

The ‘2D bump tutorial’ in ANSYS CFX was first practised to learn how to simulate a two-phase problem with water and air. The initial volume fraction distribution and pressure distribution had to be set. This required knowledge of an initial water level.

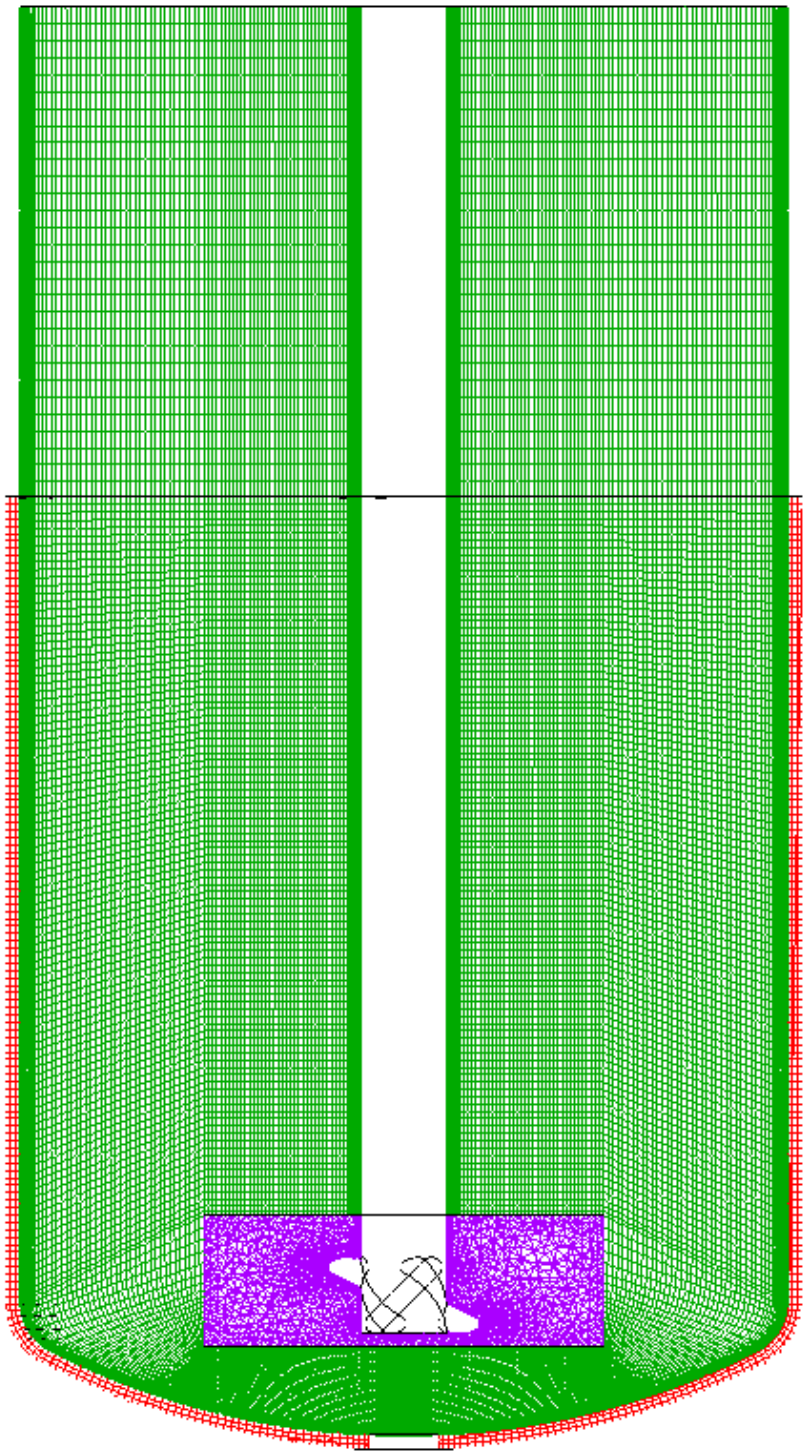

Figure 6.1 – The computational domains of the process side and wall mesh.

In the ANSYS program ‘DesignModeler’, clicking on any “body” (which means any 3D part of the model), automatically displays values such as the volume. For example the “process” body, when clicked on without the stirrer, takes up 26.589 litres. The volume

of the stirrer is then taken off this value, and the volume of a cylinder with a hole in it (hole diameter the same as the stirrer shaft, which is 0.034 m) and outer diameter the same as the process side of the vessel, which is 0.308 m) can be used to calculate the liquid height at which 20 litres of substance is in the process side. This can then be used to set the initial volume fraction of air and water in the process side.

The conservation equations for mass, momentum and energy were used by all CFD programs and implemented in the simulations in this thesis. These have been discussed in section 5.3.1. Both the standard *k-ε* turbulence model and the shear stress transport (SST) model were used to model turbulence. These models have been described in detail in section 5.3.2. The BSL RSM was also attempted, however, all attempts failed for unknown reasons. This is discussed more in section 6.2.3.

According to ANSYS Help (2013), the 'homogeneous model' should be selected if "the interface is distinct and well-defined everywhere". This condition applies in this simulation. The homogeneous model solves the conservation equations using the same velocity and temperature fields across both fluids.

The interface capturing method described in Zwart *et al*. (2003) was used. 'Aggressive interface compression' is used by default in ANSYS CFX, although an option exists to disable it if needed.

The detailed equations describing the 'homogeneous' two-phase model in ANSYS CFX are provided in Zwart (2005). For two-phase liquid-vapour systems, as in this thesis, the liquid continuity equation is used, where the subscripts l and v represent the liquid and vapour phases respectively, and $\dot{\rho}_{lv}$ represents the rate of mass transfer from vapour to liquid:-

$$\frac{\partial\, x_l \rho_l}{\partial\, t} + \frac{\partial\, x_l \rho_l v_i}{\partial\, s_i} = \dot{\rho}_{lv} \tag{6.3}$$

The volume continuity equation, assuming incompressible phases (as is the case with water and subsonic air) is:-

$$\frac{\partial\, v_i}{\partial\, s_i} = \dot{\rho}_{lv}\left(\frac{1}{\rho_v} - \frac{1}{\rho_l}\right) \tag{6.4}$$

The bulk momentum equation is:-

$$\frac{\partial(\tilde{\rho}v_i)}{\partial t} + \frac{\partial(\tilde{\rho}v_j v_i)}{\partial s_j} = -\frac{\partial p}{\partial s_i} + \tilde{\rho}g_i + \frac{\partial \tilde{\tau}_{ji}}{\partial s_j} \quad (6.5)$$

where:-

$$\tilde{\rho} = x_l\rho_l + x_v\rho_v \quad (6.6)$$

and:-

$$\tilde{\tau}_{ji} = \tilde{\mu}\left(\frac{\partial v_i}{\partial s_j} + \frac{\partial v_j}{\partial s_i}\right) \quad (6.7)$$

where:-

$$\tilde{\mu} = x_l\mu_l + x_v\mu_v \quad (6.8)$$

Finally, the volume fraction constraint is:-

$$x_l + x_v = 1 \quad (6.9)$$

According to Zwart (2005), this system involves six equations for the six unknowns, which are v_i (three directions), p, x_l and x_v.

ANSYS Help section 7.18 of the CFX Modelling Guide states that the inhomogeneous model is to be used when entrainment of one phase into the other is expected, so that the phases can separate. Hence, as no entrainment is expected in this simulation, the homogeneous model was selected.

The University of Leeds's 'ARC2' computing facility could not run the internal simulation at first and produced an output file suggesting to set the expert parameter 'topology estimate factor zif' to a value above 1.0 but not as high as 1.2.

The description of the expert parameter 'topology estimate factor zif' in ANSYS Help, CFX Modeling Guide section 17.3.4 (Convergence Control Parameters) (ANSYS, 2013) was that it was an internal memory factor, so shouldn't affect the results.

A 'topology estimate factor zif' value of 1.15 was initially put into the ARC2 simulation with the internal content and wall with heat transfer (thermal run). The corresponding desktop run had no such expert parameter set. A different level of convergence was the only other difference in these runs as a result of the difference in running time (momentum

equation residuals of approximately 10^{-4} in the desktop run and 10^{-6} in the ARC2 run). Note that these residual values were not part of the convergence criteria in this case, as minimum residuals were turned off and the simulation was left to converge for two days in the desktop run and 8 hours in the ARC2 run. Comparison of these results produced apparently different values – a visually deeper vortex (by about 1 centimetre) was present in the ARC2 run (with the expert parameter active). An inquiry submitted to ANSYS customer support confirmed that this difference could not be due to the 'topology estimate factor zif' because it is a memory allocation factor.

Consequently, a further set of isothermal runs were conducted, with the convergence criteria of 10^{-5} as the stopping condition. Again, the desktop run had no expert parameters and the ARC2 run had the expert parameter 'topology estimate factor zif' set to 1.05. This value was sufficient in this case. This time, there was no significant difference in vortex depth or maximum velocity between the two runs.

One of the suggested options to more accurately resolve the interface between the air and water was 'mesh adaption'. This is the process of refining the mesh (decreasing the cell size) at the place where the interface is expected. ANSYS CFX does offer an option to do this automatically – however, when 'mesh adaption' was selected, CFX-Pre (version 15) did not allow it, instead producing the message: "Mesh Adaption is unavailable for multi domain cases, cases with external solver coupling, elapsed time control, transient, mesh motion, radiative tracking or particle transport cases or until a Domain has been created!"

Parallel processing was thought to be a factor as to why some problems kept occurring with the simulation, as ANSYS Help, CFX Modeling Guide section 7.18.5.9 (ANSYS, 2013) suggested that a free surface model where a portion of the partition boundary is aligned with the free surface can cause problems with parallel processing. The guide suggested using "coupled partitioning" or reducing the value of the expert parameter 'overlap relaxation fluids' from its default value of 1. However, this parameter was not adjusted during these simulations. Additionally, serial processing on the desktop may be sufficient to overcome this problem, although the computational power of the desktop used is far lower and the maximum memory may be insufficient.

6.2.2 Boundary and Setup Conditions

For the flow calculation, a non-slip boundary condition was implemented on all walls. The log law of the wall was used by default. The top of the ullage region was set as an 'opening' with an 'entrainment' type selected, which was set to 1 atmosphere pressure

and a constant volume fraction of 1 for air and 0 for water. In the non-isothermal simulations, the 'opening' was set to a constant temperature of 30°C. Any air escaping the boundary due to convection would thus be replaced with air at 30°C. When heated, this would induce natural convection in the air, where air at 30°C would come down at the centre of the vessel while hotter air would rise at the walls, because the walls are hotter due to the jacket heating the contents.

Figure 6.2 displays the thermal boundary conditions used for the non-isothermal flow (semi-conjugate) calculation. The walls were divided into an upper (ullage) section and a lower (jacket) section. The upper wall was exposed to the ambient temperature (T_{amb}) and the lower wall (the outside of the wall mesh) was exposed to the mean jacket heat transfer medium temperature (T_m), which was treated as constant.

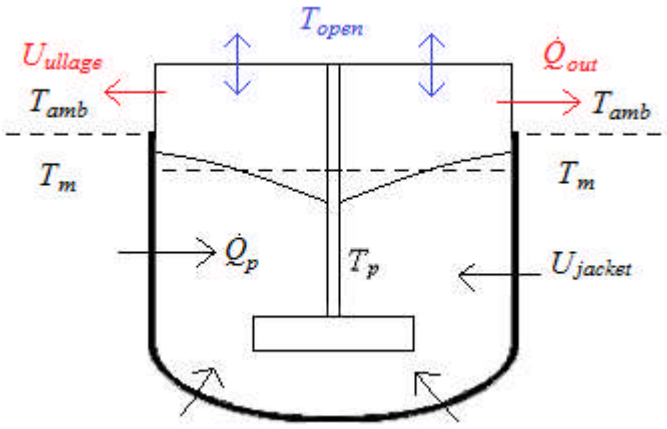

Figure 6.2 – Thermal boundary conditions for the semi-conjugate simulation.

At the walls, an external heat transfer coefficient including conduction and convection resistances and external temperature were specified. This procedure is the same as discussed in section 5.3.5.

For the lower wall, the mean jacket temperature was set to 78.2°C, based on the experiment, and the heat transfer coefficient was set to 220 W m^{-2} K^{-1}; a reasonable guess based on the values discussed in section 5.5.4.

The upper wall used the ambient temperature of 20°C. The heat transfer coefficient in the upper wall accounts for the conductive resistance of the upper wall and the outside thermal resistance – free convection and radiation on the outer side. The assessed value used in this case was 12 W m^{-2} K^{-1}; again based on the possible values discussed in section 5.5.4.

To connect the different meshes (tank to impeller and tank to wall), 'general grid interfaces' (GGI) were set up at the boundaries between them. According to the 'CFX Help' documentation, "a control surface approach is used to perform the connection across a GGI attachment or periodic condition". Additionally, "A physically based intersection algorithm is employed to provide the complete freedom to change the grid topology and physical distribution across the interface." The documentation does not provide the equations used, for commercial reasons.

ANSYS CFX cannot simulate different fluids in different domains unless the settings for "constant domain physics" and "default domain" are disabled. In ANSYS 15, this is a 'beta feature'. In future versions it might become a more standard feature of ANSYS CFX.

The shaft (inner tank domain wall) and the impeller domain were set to rotate at 180 rpm (corresponding to a Reynolds number of 7.67×10^4 at 30°C). Gravity was set as -9.81 m s^{-1} in the vertical direction. The homogeneous multiphase flow model was used. For heat transfer, the separate 'homogeneous' option was selected (which means the same temperature field will be used for both phases) and the 'thermal energy' option was chosen, which means the energy contribution due to viscous work is ignored – this is recommended for subsonic flow.

An initial pressure and volume fraction of water had to be specified in the simulation, so an initial height was required. The liquid level in the reactor when 20 litres full was the same as the tank diameter (0.308 m) when measured from the bottom of the vessel. Based on the coordinate system in the simulation (with the centre of the jacket inlet pipe marking the base height of zero), the water level was assessed to be at a height of 0.2733 metres. Above this height, the initial volume fraction of air was set to 1 and the initial volume fraction of water was set to 0. Below this height, the initial volume fraction of air was set to 0 and the initial volume fraction of water was set to 1.

The initial pressure was set as the hydrostatic pressure of the water, proportional to height under the surface pressure of 1 atmosphere. This was set using equation (6.10), where z is the height value in the simulation's coordinates.

$$p_{water} = x_{water}\rho_{water}g(0.2733 - z) \tag{6.10}$$

The initial pressure of the air above the surface was set to 1 atmosphere (independent of height).

The simulation was set to ‘steady state’ in order to investigate the heat transfer rates. It should be noted that the heat transfer process to be modelled is intrinsically transient (non-steady state) in reality, but the calculation method uses “pseudo time steps”, in which the water gradually heats up from the initial temperature (30°C). This was deemed sufficient for an initial investigation, although it meant that the final water temperature needed to be used in estimating the temperature difference for the heat transfer investigation.

The typical maximum time scale to be used (in each pseudo time step) was worked out by using the reciprocal of the rotational speed in radians per second. This worked out as 0.053 seconds, but a smaller value (0.026 seconds) was used to provide greater stability in the solution's convergence.

6.2.3 Grid and Turbulence Model Independence Tests

Coarse, medium and fine meshes were constructed for the tank, while only medium and fine meshes were made for the turbine. A single size of mesh was also used for the inner jacket wall in the lower half of the vessel. Table 6.1 lists some details of the grids used for the simulation (impeller, tank and wall) – number and type of cells, maximum cell edge lengths and the refined cell edge lengths of the cells adjacent to the wall (labelled as the “near-wall cell edge length”). Note that the ‘coarse’ impeller mesh was used with the ‘coarse’ tank mesh, and the ‘fine’ impeller mesh was used with the ‘medium’ and ‘fine’ tank meshes.

Table 6.1 – Details of the grids for the tank and impeller.

Mesh	Number of cells × 10^{-5}	Type of cells	Maximum cell edge length / mm	Near-wall cell edge length / mm
Impeller (Coarse)	3.69	Tetrahedral	6.8	0.034
Impeller (Fine)	5.42	Tetrahedral	5.0	0.022
Tank (Coarse)	6.90	Hexahedral	5.4	0.800
Tank (Medium)	27.5	Hexahedral	2.9	0.100
Tank (Fine)	96.2	Hexahedral	1.5	0.100
Wall	1.68	Hexahedral	2.0	N/A

Figure 6.3 displays the predicted tangential velocity profiles for the three grid sizes (see Table 6.1) obtained using the standard k-ε model. The results are very similar for all grid sizes. On the other hand, Figure 6.4 displays some different profiles depending on the grid used with the SST model. Further refinement is required for the SST model, although this was not practical without further investment of time and computational resources. In

the main simulations and analysis, the medium mesh was used with the standard k-ε model.

The curvature corrected SST model was also tested, but the results again were inconsistent, so further refinement will be needed.

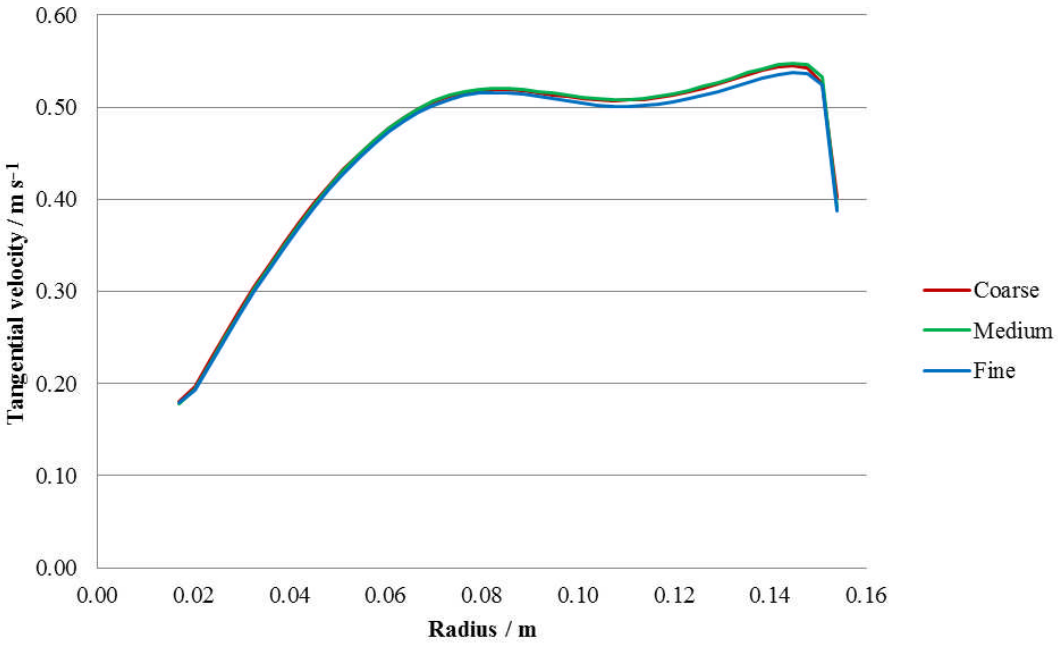

Figure 6.3 – Predicted tangential velocities, at a height of 0.1 m above the jacket inlet port, using three mesh sizes and the standard k-ε model.

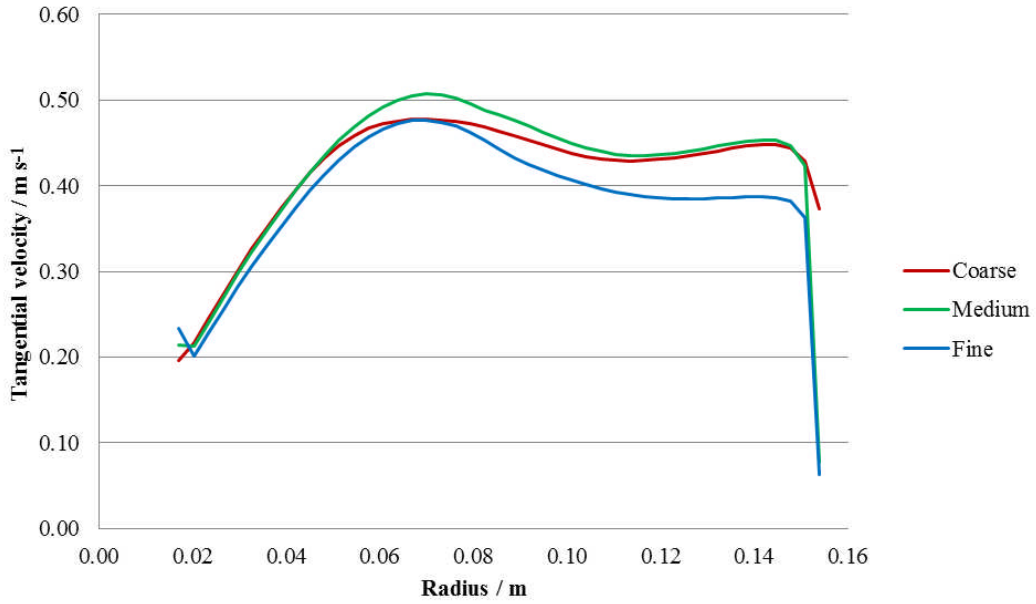

Figure 6.4 – Predicted tangential velocities above the gap between the blades, at a height of 0.1 m above the jacket inlet port, using three mesh sizes and the SST model.

The BSL Reynolds Stress model could not run when the process side simulation was involved, and an investigation into this lead to the use of the Explicit Algebraic Reynolds Stress Model (EARSM), which produced results that had a very large error in mass conservation (such as the water level dropping by about 50%). This was speculated to be due to poor mesh quality in the automatically generated, tetrahedral ANSYS mesh (in which one single cell was identified to be over the acceptable skewness), although it is unknown if the automatic mesh generator in ANSYS Meshing can alter individual cells to reach any acceptable level. Further development of automatic meshing software may be required.

6.2.4 Flow Pattern

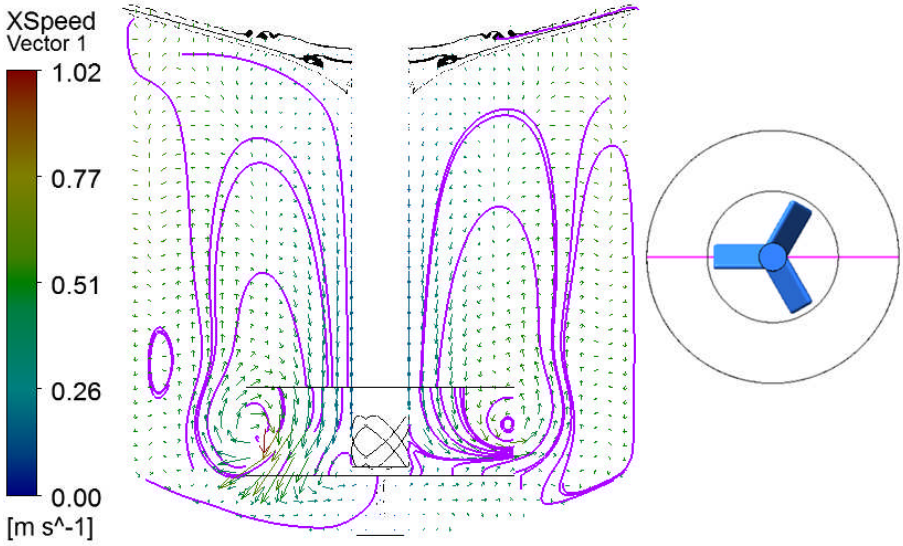

Figure 6.5 – Predicted velocity vectors (coloured by tangential velocity) and streamlines (purple) using the standard k-ε model and the medium grid.

Figure 6.5 displays the flow pattern in the tank using the velocity vectors and streamlines obtained with the k-ε model and the medium grid. The magenta line in the right-hand image displays the position of the vertical plane seen from above. As expected, the motion of the water in the vessel agitated by the pitched blade turbine creates a toroidal vortex around the impeller, with the liquid being drawn down along the impeller shaft and up further away. However, this effect does not reach the walls, so there is also an outer, slower toroidal vortex and a small downward velocity close to the walls. This is considered part of the secondary flow, so “hot spots” are more likely to occur in these regions as well as nearer the surface where the turbulence is lower.

At the blades, there is a much stronger downward motion, due to the blade pushing the fluid downwards. The asymmetry in the flow field is due to the position of the turbine

blades with respect to the vertical plane as displayed in the right-hand image in figure 6.5. Heat transfer and turbulence are greater in this part of the vessel.

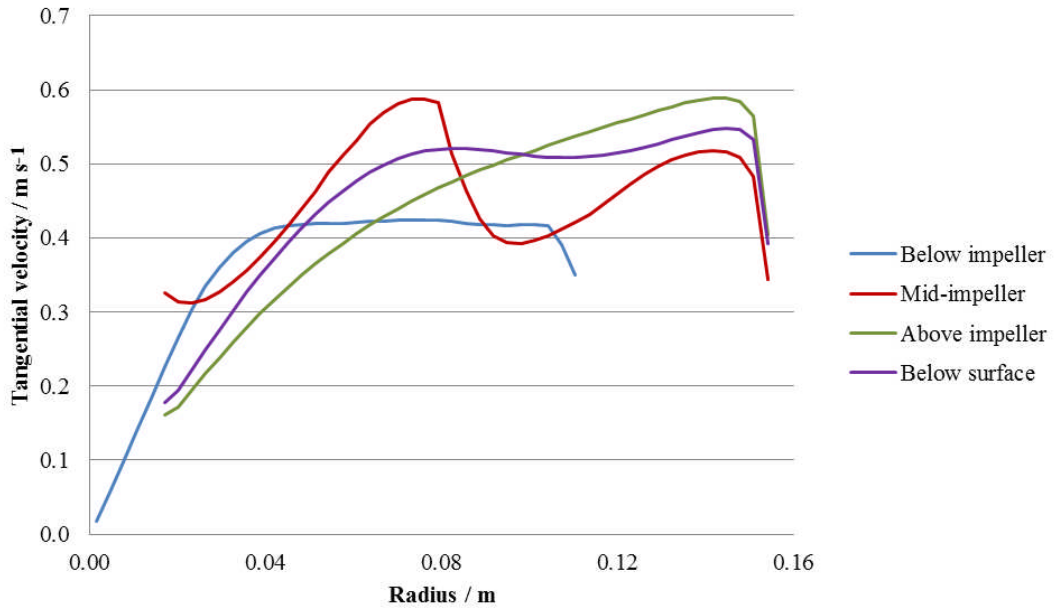

Figure 6.6 – Tangential velocities at different heights (between the blades) predicted using the standard k-ε model.

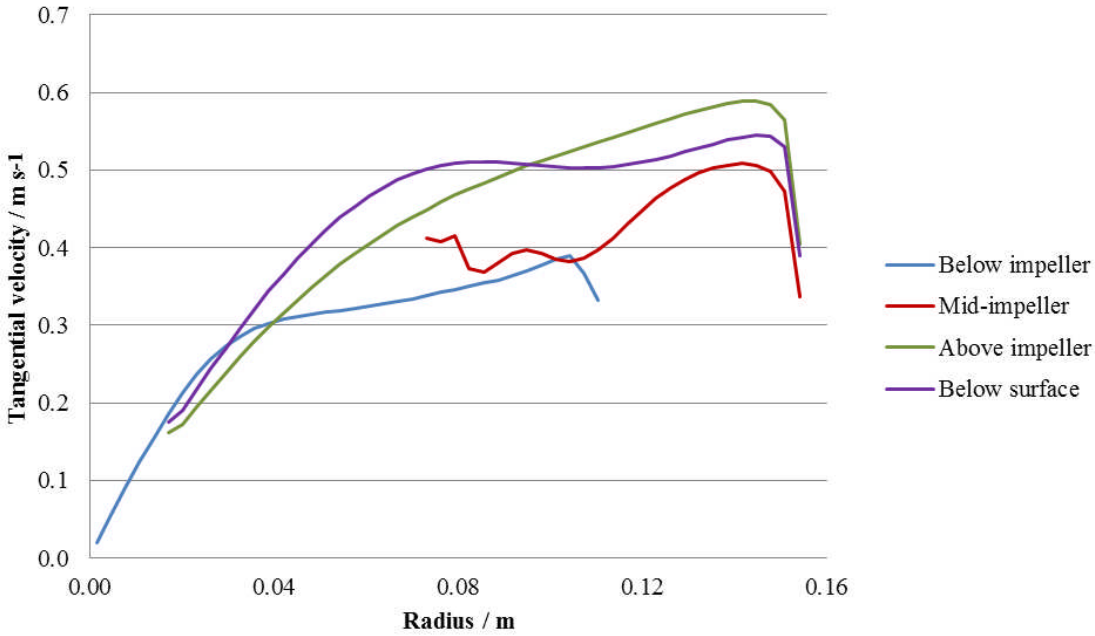

Figure 6.7 – Tangential velocities at different heights (at the blades) predicted using the standard k-ε model.

Figures 6.6 and 6.7 display the radial profiles of the tangential velocity obtained using the k-ε turbulence model at key vertical locations along the liquid height. Figure 6.8 displays all of these heights relative to the liquid depth in the reactor as magenta lines, as a visual indicator, as well as the location of the vertical plane with respect to the impeller position.

Figure 6.6 displays the velocities in the vertical plane located between two turbine blades, whereas figure 6.7 displays the velocities in the plane aligned with the turbine blade itself. Above and even at the impeller, there is little change in the flow as the blade passes. Below the impeller, the tangential velocity increases rapidly – when the blade is passing, closer to the shaft, the tangential velocity drops from 0.4 to 0.3 m s^{-1}. This is due to the flow being re-directed downwards at this point. The velocity vectors in figures 6.5 and 6.8 also display this effect.

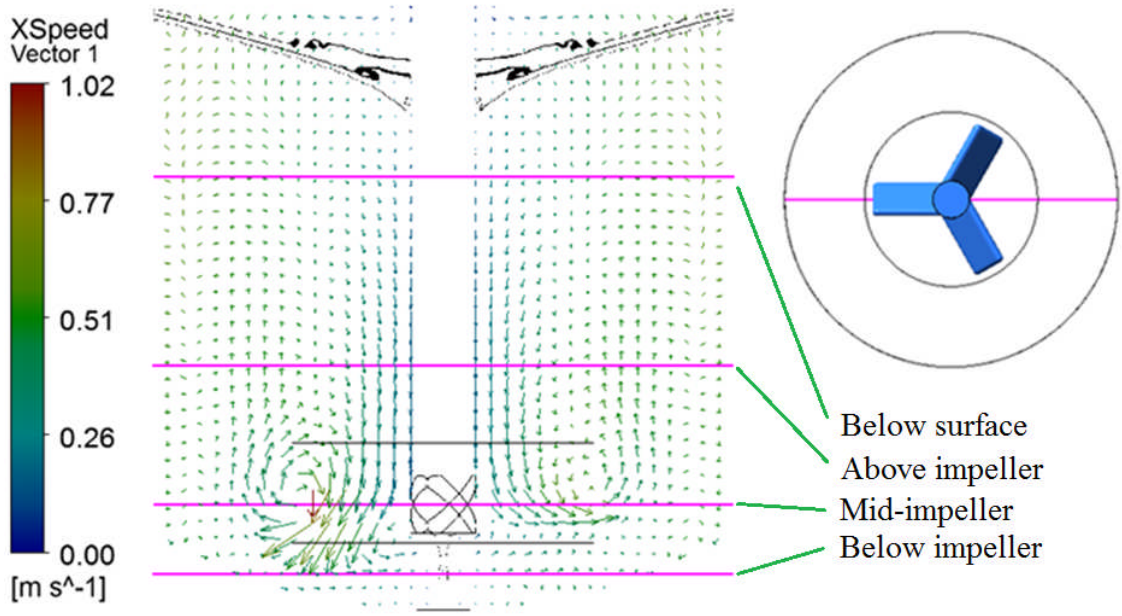

Figure 6.8 – Indication of height lines used in figures 6.5 and 6.6.

6.2.5 Vortex Geometry

The distribution of volume fractions of water and air in the tank is displayed in figure 6.9, which also reveals the shape of the vortex. As can be seen in the figure, the air-water interface is not very sharp, which could be due to numerical errors. The shape of the vortex (that is, free surface profile) in figure 6.5 and figure 6.8 is not well defined and varies significantly with the value of liquid volume fraction (LVF) used to capture the air-water interface.

A range of LVF values between 0.5 and 0.9 has been used in previous studies (for example Haque *et al.*, 2006 and 2011). In figures 6.5 and 6.8, three surface profiles are visible on the image as black lines at the surface, corresponding to LVFs of 0.1, 0.5 and 0.9, similar to the images in Zwart *et al.* (2003). The surface profiles for an LVF of 0.1 and 0.5 have a raised section, within which the profile seems to follow a “forced vortex” shape, and outside which it seems to follow a “free vortex” shape. It is interesting to note that this may be related to the point of transition between the “forced” and “free” vortices,

predicted by the simulation. The surface profile for an LVF of 0.9 displays a typical “free vortex” shape, only appearing “forced” right at the shaft.

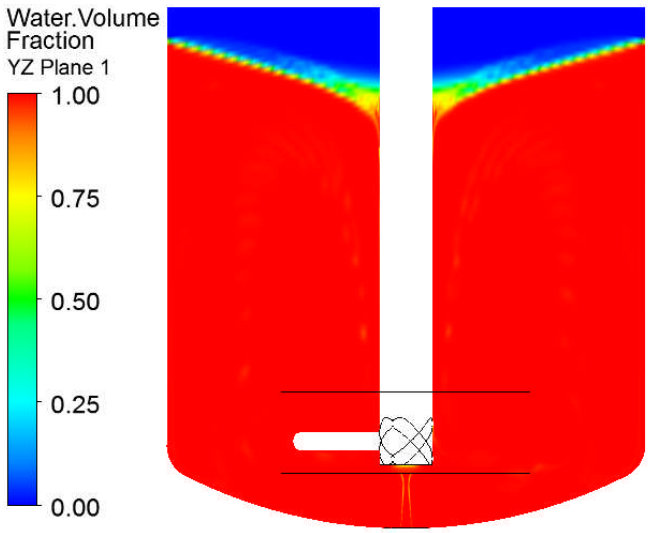

Figure 6.9 – Volume fraction contours obtained using the medium grid and the standard k-ε model, for the steady state process-only simulation.

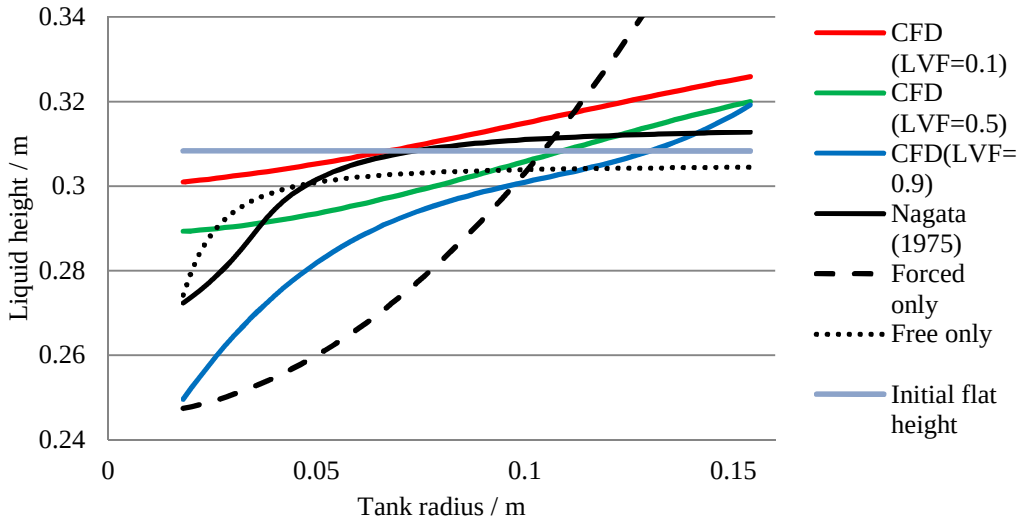

Figure 6.10 – Possible vortex profiles from the CFD (using a three-bladed pitched turbine) in comparison with Nagata's (1975) correlation (for a six-bladed Rushton turbine).

Figure 6.10 displays possible vortex profiles from the CFD simulations based on different values of LVF. Using an LVF of 0.1 (red line) or 0.9 (blue line) appears to deviate strongly from the expected surface position (that is, significantly far from the initial flat height), whereas the LVF of 0.5 (green line) lies in the expected area. However, the shape of the surface profile for an LVF of 0.5 is very different from that calculated using the Nagata (1975) correlation (black solid line), which uses a Rushton turbine rather than a pitched

blade impeller. The surface profiles for the free curve and the forced curve are also displayed in figure 6.10, to demonstrate the shape only. These profiles are derived from the equations given in Rieger *et al*. (1979) with the vortex depth and the tank wall depth (also calculated by equations in Rieger *et al*., 1979) as input parameters for the forced and free vortex, respectively, hence these profiles do not match up with the appropriate initial flat height displayed (all profiles ideally should cross the initial flat height line due to conservation of mass).

6.2.6 Heat Transfer

For the steady state semi-conjugate CFD simulation, figure 6.11 displays the temperature distribution inside the vessel and figure 6.12 displays the temperature distribution at the vessel wall (T_{ii}). In figures 6.11 and 6.12, the image is cut off just below the water surface in order to allow the distribution below the surface to be displayed with more contrast, because the wall temperature above this point is much higher than below the surface. A small temperature range of 0.4°C is used in figure 6.11 otherwise these small temperature variations would not be visible, as the mixing evens out the distribution quite effectively.

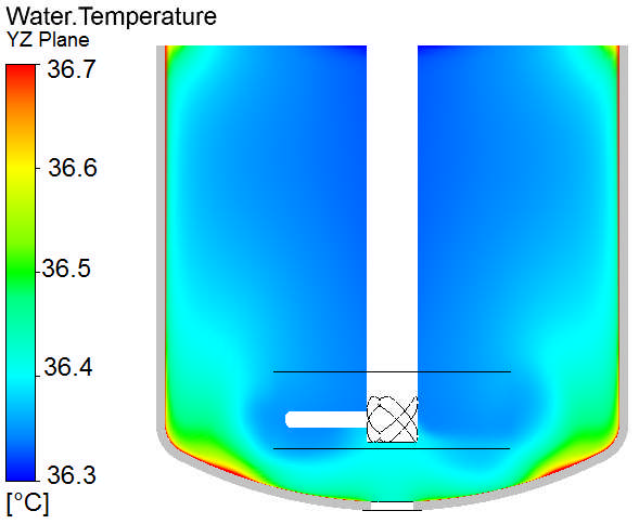

Figure 6.11 – Water temperature distribution in the bulk of the tank, for the steady state semi-conjugate simulation.

Higher temperatures occur at the toroidal section of the wall and above the liquid surface. The toroidal section is within the zone of secondary flow, described by Pedrosa and Nunhez (2003), and is where the greatest temperature spikes are expected. The higher temperature above the liquid surface is due to the low thermal conductivity of air, so the temperatures here are closer to the jacket temperature.

The lowest wall temperatures occur at the bottom of the jacket, because of the higher heat transfer coefficient (α_{ii}) in this region. As the water is forced downwards in these areas, the temperatures at the wall are closer to the temperature in the vessel. These higher values of heat transfer coefficient result from higher shear stress in these areas, as described in Mahmud *et al.*, (2015).

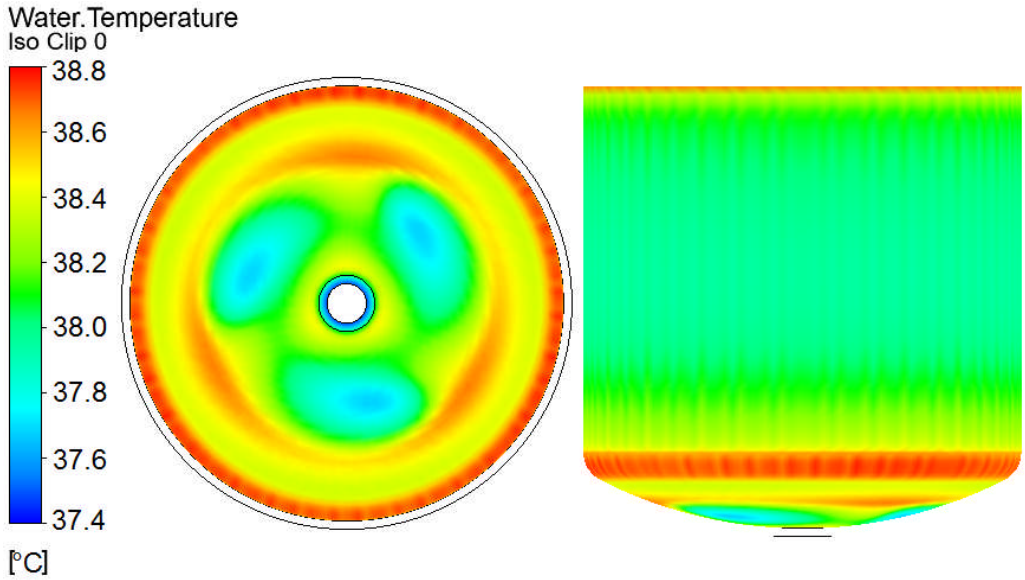

Figure 6.12 – Distribution of temperature at the vessel wall for the steady state semi-conjugate simulation.

As described in section 5.3.4, and in Bentham *et al.* (2015a), it was assessed that the flow pattern in plain jackets includes a major 'dead zone' (very low flow) at the bottom of the reactor, where natural convection dominates, and so the coldest jacket temperatures (T_{io}) tend to occur here, regardless of whether the overall process is of heating or cooling the vessel contents. As the bottom of the vessel has a higher heat transfer coefficient inside the vessel due to the impeller, the heat transfer is especially dominated by the jacket in these areas.

The distribution of heat transfer coefficient on the bottom and sides of the tank displayed in figure 6.13. The simulation uses the procedure outlined in section 5.5.1 to assess these values. This image is not cut off near the water surface, and displays the very low heat transfer coefficient resulting from the low conductivity of air. These results are visually similar to those found in Milewska and Molga (2010), which display three areas of high heat transfer coefficient below the pitched blades of the impeller. Figure 6.14 displays a similar pattern for the wall shear stress, as is expected considering the results of simulations in chapter 5.

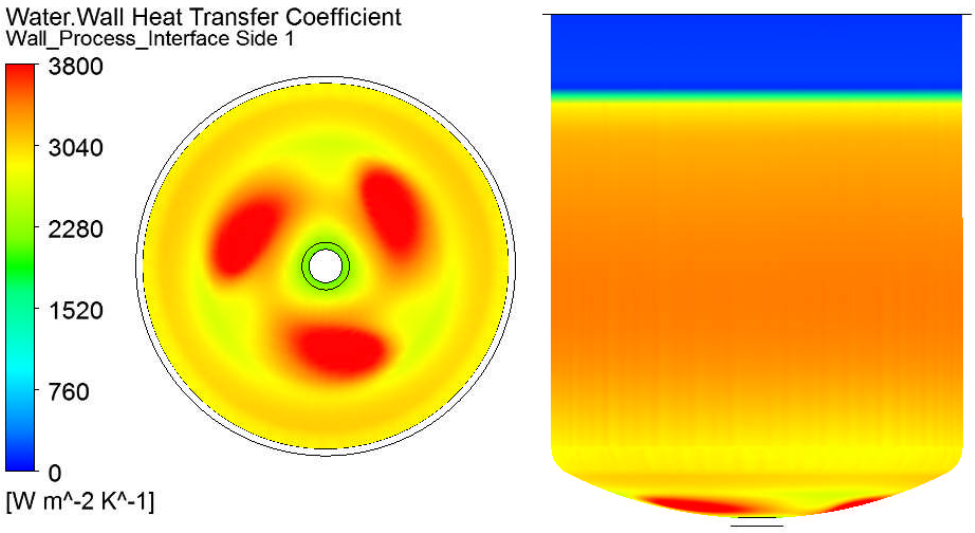

Figure 6.13 – Distribution of heat transfer coefficient at the vessel wall, for the steady state semi-conjugate simulation.

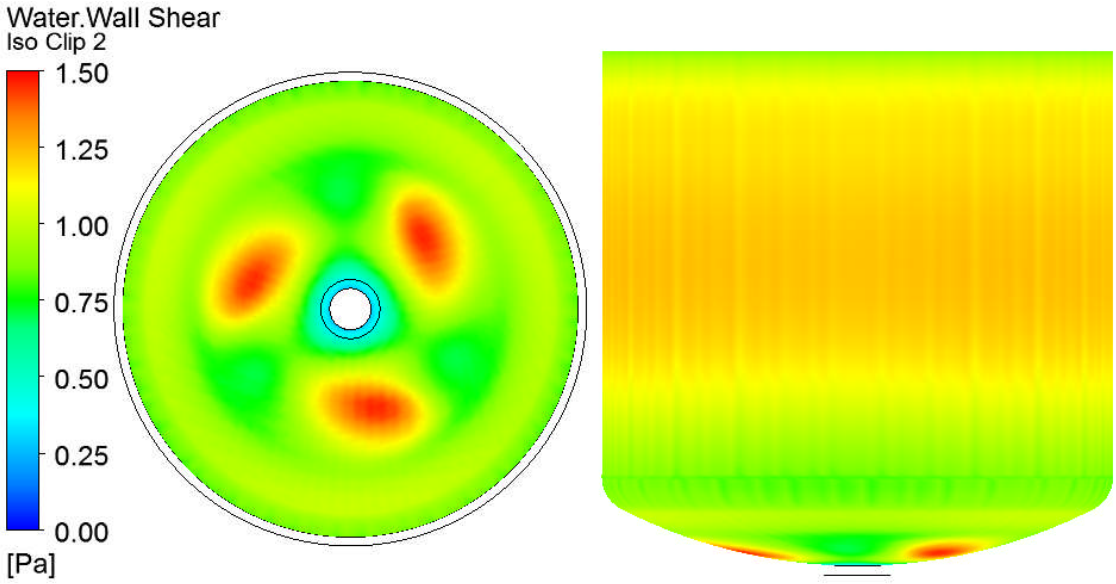

Figure 6.14 – Distribution of wall shear stress at the vessel wall, for the steady state semi-conjugate simulation.

The highest values of heat transfer coefficient and wall shear stress occur where the three pitched blades forced the liquid downwards. Below the blade tips, in this simulation, the heat transfer coefficient reaches a maximum of 3800 W m^{-2} K^{-1} and the wall shear a maximum of 1.46 Pa. At the walls, the average wall heat transfer coefficient (based on the procedure outlined in section 5.5.1) is predicted as 3280 W m^{-2} K^{-1} (corresponding to a U_j value of 101.5 W m^{-2} K^{-1}). This value of α_{ii} is somewhat higher than the prediction of 2663 W m^{-2} K^{-1} (corresponding to a U_j value of 100.8 W m^{-2} K^{-1}) from the correlation of Nagata *et al*. (1972), displayed in equation (6.2) (see section 6.1). However, both predictions are still high enough to mean that the dominant resistances to heat transfer are

those of the wall and jacket, which is why the U_j values are so similar. The average wall shear in this case is predicted as 1.08 Pa.

The definition of the inside film heat transfer coefficient depends on the temperature used (T_{def} in equation 6.11). This depends on the location of the temperature used as T_{def}. For example, using the inner temperature of the liquid (at the shaft), the average value of heat transfer coefficient in the simulation is 1142 W m^{-2} K^{-1} (corresponding to a U_j value of 96.0 W m^{-2} K^{-1}). This value of α_{ii} is significantly lower than the 2663 W m^{-2} K^{-1} predicted using the Nagata *et al*. (1972) correlation (again, the overall U_j is similar because the jacket and wall are the controlling resistances).

$$\dot{q}_w = \alpha_w\left(T_w - T_{def}\right) \tag{6.11}$$

In the ANSYS CFX software, the 'wall heat transfer coefficient' (α_w, which in this case is α_{ii}) is obtained using the procedure outlined in section 5.5.1. The definition of the temperature difference here is not recommended – although it often provides a reasonable estimate that falls within theoretical values, it is often a smaller temperature difference because the temperature is taken to be nearer to the wall rather than the average or bulk temperature. A lower temperature difference will mean a larger heat transfer coefficient is calculated. Using this procedure, the heat transfer coefficient on the process side in the CFD simulation was assessed as an average of 3213 W m^{-2} K^{-1}.

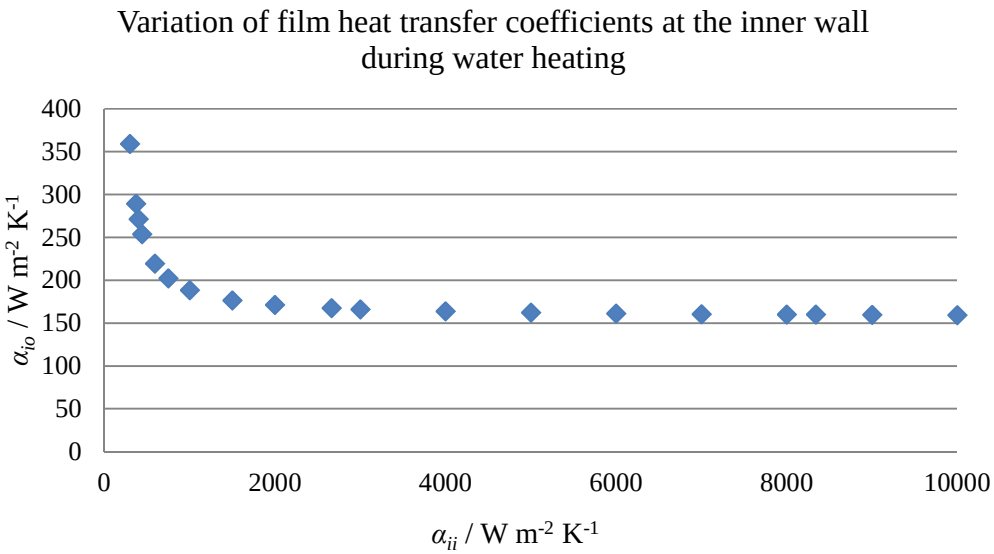

Figure 6.15 – Interdependence of inner and outer wall film heat transfer coefficients.

Figure 6.15 displays the jacket side film heat transfer coefficient (vertical axis) vs. the process side film heat transfer coefficient. The resistance to heat transfer in the 6 mm

glass wall provides a heat transfer coefficient of 200 W m^{-2} K^{-1}, so this is usually the main controlling resistance because of the relatively low thermal conductivity of glass (in this case, 1.2 W m^{-1} K^{-1}). If the jacket film heat transfer coefficient is between about 150 and 200 W m^{-2} K^{-1}, as predicted using the correlation of Bondy and Lippa (1983), and/or the process side film heat transfer coefficient is above about 800 W m^{-2} K^{-1}, as is predicted both by Nagata's (1972) correlation and the CFD simulations, the resistance to jacket side heat transfer becomes another controlling resistance and the process side heat transfer coefficient becomes less relevant overall.

6.2.7 Transient Semi-Conjugate Simulation

Results have been obtained for a transient simulation using the initial conditions as the steady state semi-conjugate simulation results obtained in sections 6.2.4 to 6.2.6 (*k-ε* model, medium grid). For this simulation, the settings and boundary conditions were the same as described in section 6.2.2, except that the 'transient' setting was active and the time setting were set to run for time steps of 0.0025 seconds for 100 seconds maximum. However, the maximum elapsed run-time of the simulation was set to 8 hours, which is not enough to simulate 100 seconds of operation. In the final results file, 11.09 seconds of operation had been simulated at the final time step. This was deemed to be a sufficient time (by the author), and the results obtained were indeed reasonable.

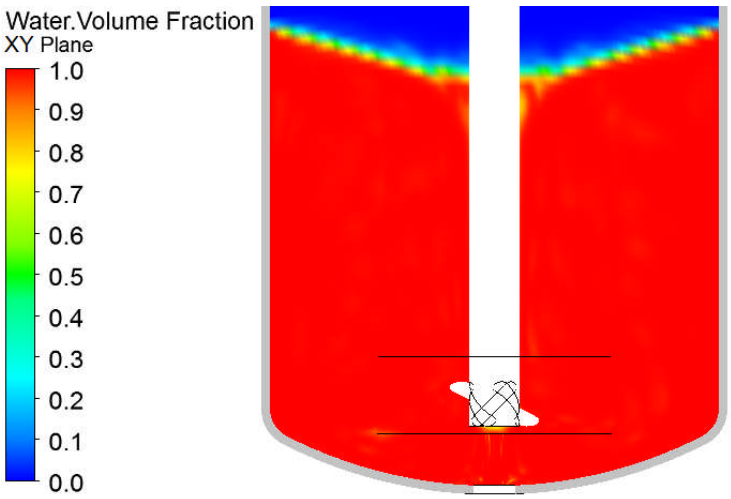

Figure 6.16 – Volume fraction contours for the transient semi-conjugate simulation.

The distribution of liquid volume fraction (LVF) is much better defined in the transient simulation, as is displayed in figure 6.16. Although the overall transition is a little smoother compared to the steady state simulation (figure 6.9, in section 6.2.5), the shape of the surface is more well defined. This is also visible in figure 6.17, which displays the streamlines and velocity vectors, in a similar fashion to figure 6.5 (in section 6.2.4). The

black wavy lines at the top of figure 6.17 indicate the positions of the LVF of 0.1, 0.5 and 0.9, from top to bottom.

The streamlines in figure 6.17 also present, as in the steady state simulation, zones of secondary flow near the walls (a slow-moving toroidal vortex that runs down the walls and up in the middle next to the primary flow zone).

Figure 6.18 displays the distribution of wall temperature in the transient semi-conjugate simulation. This is as would be expected – a large temperature drop through the wall, caused by the low thermal conductivity of the glass (1.2 W m^{-1} K^{-1}, about a tenth that of steel) and high resistance to heat transfer. The wall temperature above the surface, however, stays almost equal to the set jacket temperature of 78.2°C. This is due to the low thermal conductivity of air (0.03 W m^{-1} K^{-1}) compared to the water (0.62 W m^{-1} K^{-1}), as well as the comparatively low wall shear (lack of agitation) in the areas exposed to air.

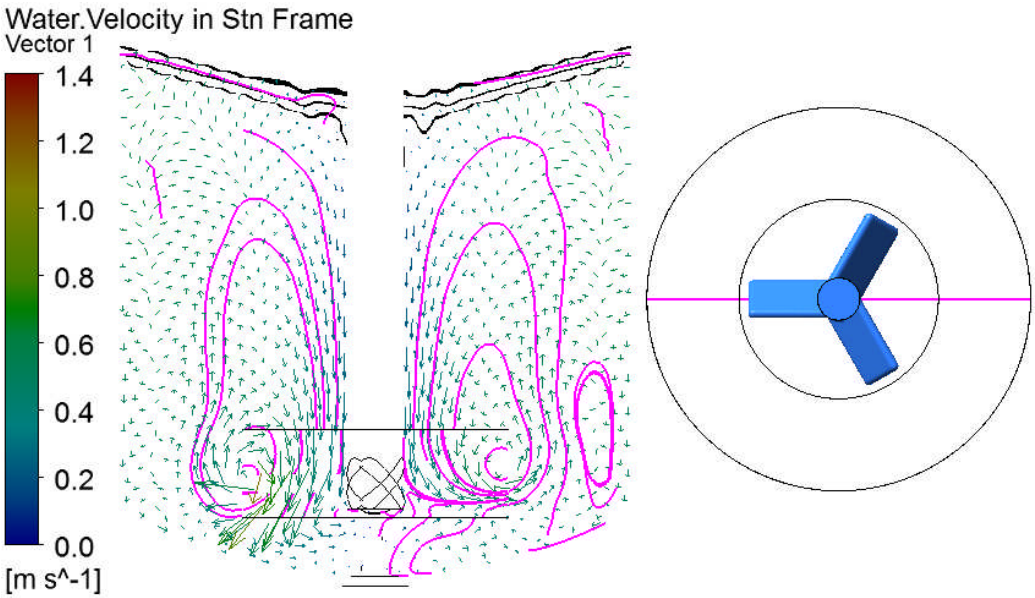

Figure 6.17 – Streamlines and velocity distributions for the transient semi-conjugate simulation.

Figure 6.19 displays the distribution of heat transfer coefficient and figure 6.20 displays the wall shear stress. The images display results only at an LVF above 0.5 (being defined as below the surface of the water in this case). Below the water surface, the average heat transfer coefficient is 3207 W m^{-2} K^{-1} (corresponding to a U_j value of 101.4 W m^{-2} K^{-1}) and the average wall shear stress is 1.07 Pa. The wall shear stress and heat transfer coefficient follow a very similar pattern to one another, as expected and similarly to the previous steady state simulations. The lower value of heat transfer coefficient (and lower shear stress) above the surface appears to be primarily due to the much lower density (and

hence much lower momentum) of the air. The highest value of heat transfer coefficient is located below the impeller blades, where the water is being forced downwards.

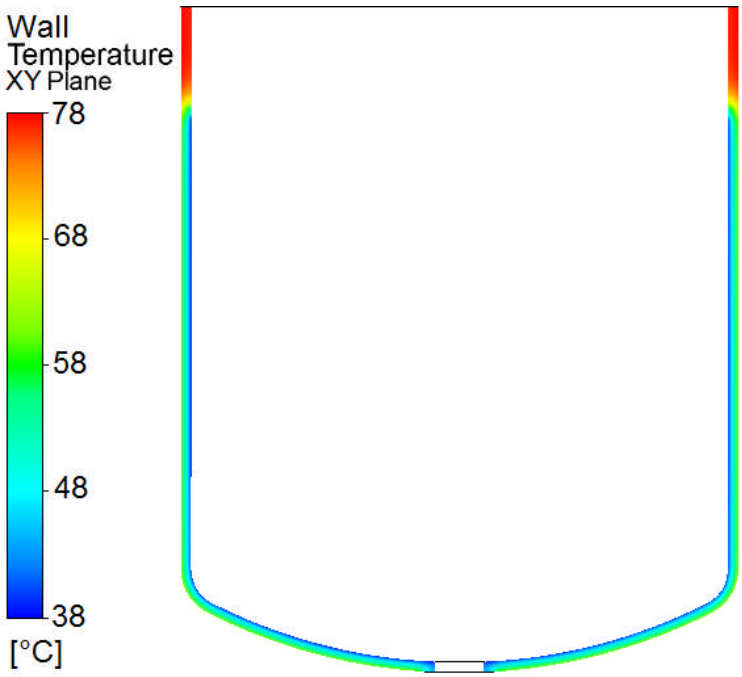

Figure 6.18 – Wall temperature distribution in the transient semi-conjugate simulation.

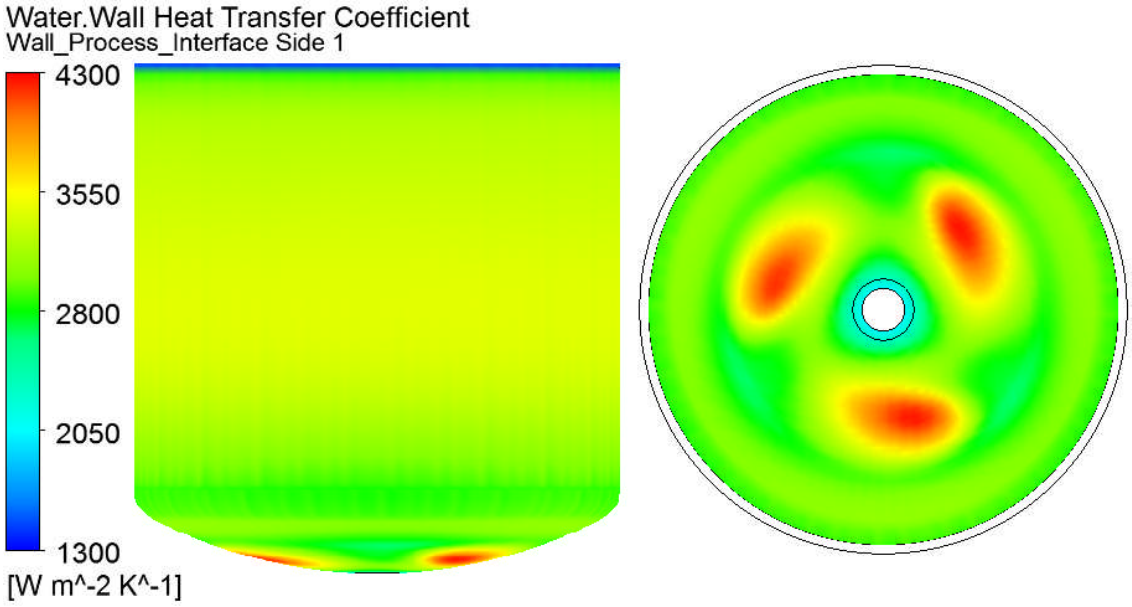

Figure 6.19 – Heat transfer coefficient distribution at the vessel wall, for the transient semi-conjugate simulation.

Figure 6.21 displays the wall temperature distribution. In this simulation, the average temperature at the wall, under the water surface, is 38.6°C. The temperature distribution appears to be almost the inverse of the heat transfer coefficient distribution, displaying high temperatures at the wall (due to the glass above the water surface heating up across the entire wall profile as explained previously) and low temperatures below the impeller

blades. These low temperatures in this case are entirely due to the impeller blades forcing the colder parts of the fluid onto the wall surface. This is because the jacket temperature distribution has not yet been combined as it would be in a full conjugate simulation.

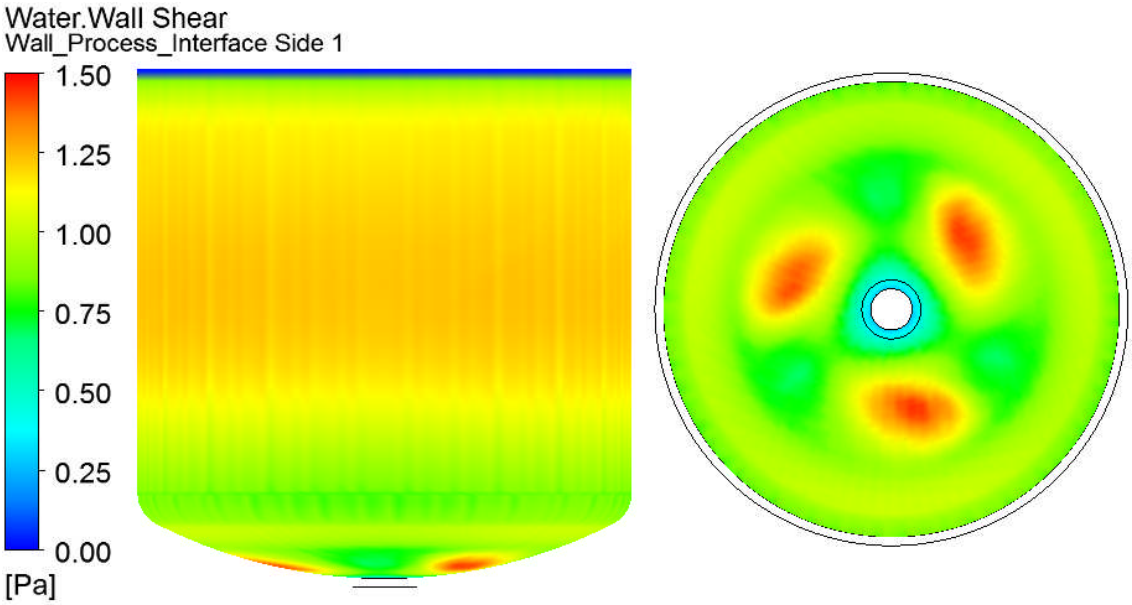

Figure 6.20 – Shear stress distribution at the vessel wall, for the transient semi-conjugate simulation.

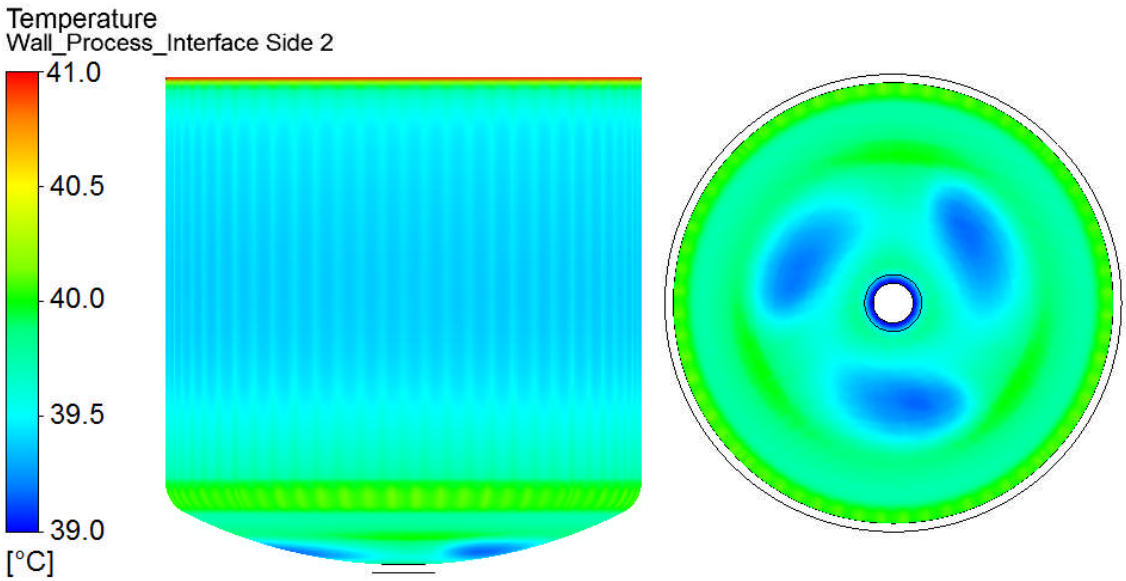

Figure 6.21 – Temperature distribution at the vessel wall, for the transient semi-conjugate simulation.

Figure 6.22 displays the temperature distribution inside the vessel, for the transient semi-conjugate simulation. This is similar to the steady state conjugate simulation displayed in figure 6.11 (in section 6.2.6). As in the steady state version, the temperature variation can only be seen if the range is narrowed (in this case to 0.5°C). This is due to the effectiveness of the mixing. In the water, again, higher temperatures are seen at the bottom of the vessel,

particularly near the toroidal section and in the zones of secondary flow, similar to section 6.2.6. Much higher temperature differences are seen in the air, again due to the lower thermal conductivity of the air. The air is heated up by the wall and rises out of the simulation space by natural convection. An equivalent volume of air at 30°C enters via the opening at the top. However, interfacial thermal conduction is not sufficient to affect the heat transfer and water temperature distribution compared to the effect of heating from the jacket.

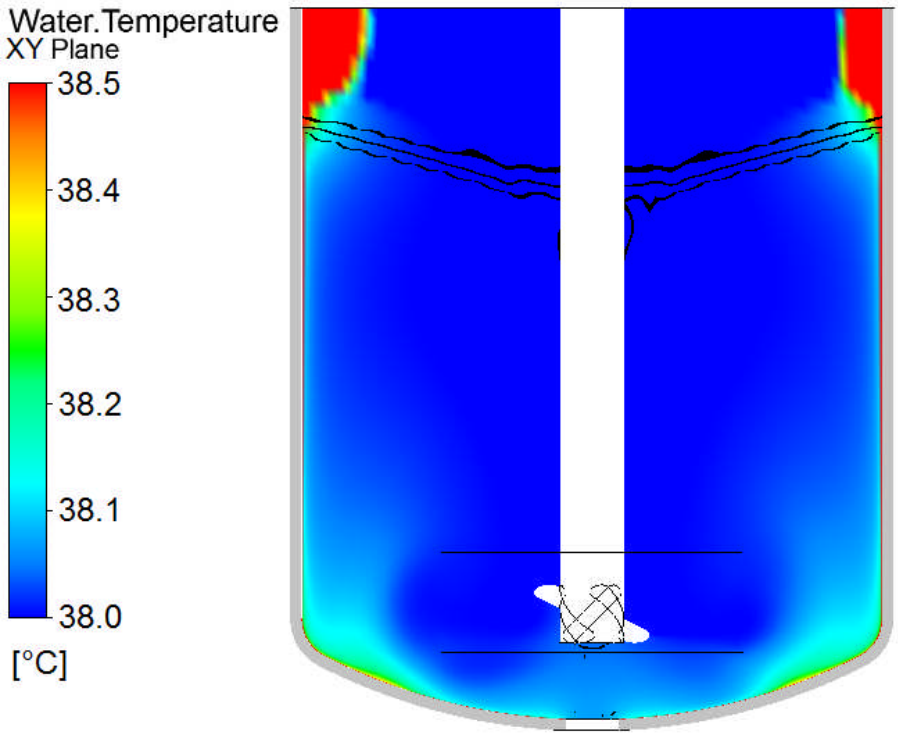

Figure 6.22 – Temperature distribution within the vessel, for the transient semi-conjugate simulation.

6.3 Summary of Modelling of the Process Side

Using CFD, the flow in the process side has been modelled using an isothermal model (with no wall mesh) and the flow and heat transfer have been modelled using a non-isothermal semi-conjugate model (with a wall mesh to add thermal inertia from the wall, but keeping the assumption of a constant jacket temperature). A steady state simulation and a transient simulation have been run for the semi-conjugate model.

The results obtained were similar to those predicted in similar CFD simulations in the literature (Milewska and Molga, 2010). Predicted vortex geometry is dissimilar to correlations found in the literature which assume a central forced vortex and outer free vortex, although this may be due to the different impeller type used. Additionally, the

vortex is difficult to define due to the gradual change in volume fraction as a result of numerical errors. In reality, the volume fraction has a step change and is very well defined.

Table 6.2 displays the average values obtained from the steady state and conjugate simulations. The steady-state and transient results are very similar, providing some support to the possibility that steady state simulations with pseudo time steps can be used in place of transient simulations. However, this is just one instance, so many more CFD simulations will have to be done to come to that conclusion.

Temperatures are not included in table 6.2 because the simulations were heated up for different amounts of time, thus they are not relevant for comparison between the two cases.

Table 6.2 – Average values obtained from the conjugate and semi-conjugate simulations.

Simulation	α_{ii} / W m^{-2} K^{-1}	Wall shear stress / Pa
Steady state semi-conjugate	3280	1.08
Transient semi-conjugate	3207	1.07

In the process side, hot spots are expected near the wall at the top and bottom of the reactor, particularly in zones of secondary flow where the mixing is lessened. As the water level is below the jacket, high temperature variations occur at the walls near the top because of insulation from the air.

7 CONJUGATE SIMULATION

7.1 Introduction to Conjugate Modelling

Through chapters 5 and 6, more of the assumptions laid out in section 4.2.1 have been relaxed. In this conjugate CFD simulation, the only assumptions still in place are that a steady state can apply and that there is a uniform constant ambient temperature and uniform constant heat transfer coefficient on the outer walls.

7.2 Steady State CFD Conjugate Simulation

7.2.1 Boundary and Setup Conditions

The conjugate simulation used the same settings and boundary conditions as the non-isothermal simulation with a wall mesh (see section 6.2.2 for the boundary values input), and combined these with the jacket mesh and boundary conditions from section 5.3.5, except for the differences outlined as follows. The main difference was that the jacket temperature was not constant – instead it was based on the originally measured jacket inlet temperature (T_{m1}) of 80.6°C. A general grid interface (GGI) was used on both sides of the wall. A visual representation of the thermal boundary conditions is displayed in figure 7.1.

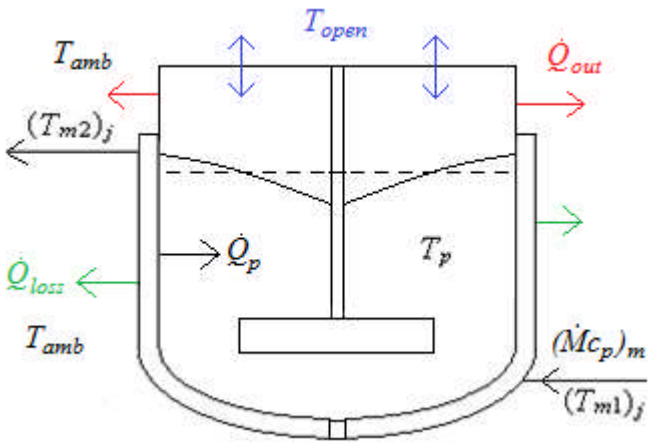

Figure 7.1 – Thermal boundary conditions and paths of heat in the conjugate simulation.

As in the non-isothermal simulation, the objective of this simulation was to assess the heat transfer to the water from the jacket at an instant in time when the jacket inlet temperature was 50°C higher than the process temperature, and the process temperature was not expected to be significantly higher than 30°C. The effect of heat transfer from the water outside the simulation boundary was therefore expected to be negligible in this simulation, so the

constant temperature ‘opening’ boundary condition at the top was deemed acceptable, despite being unphysical.

Grid independence tests were not performed on the full conjugate simulation, because they were already performed on all meshes in the separate jacket and process simulations.

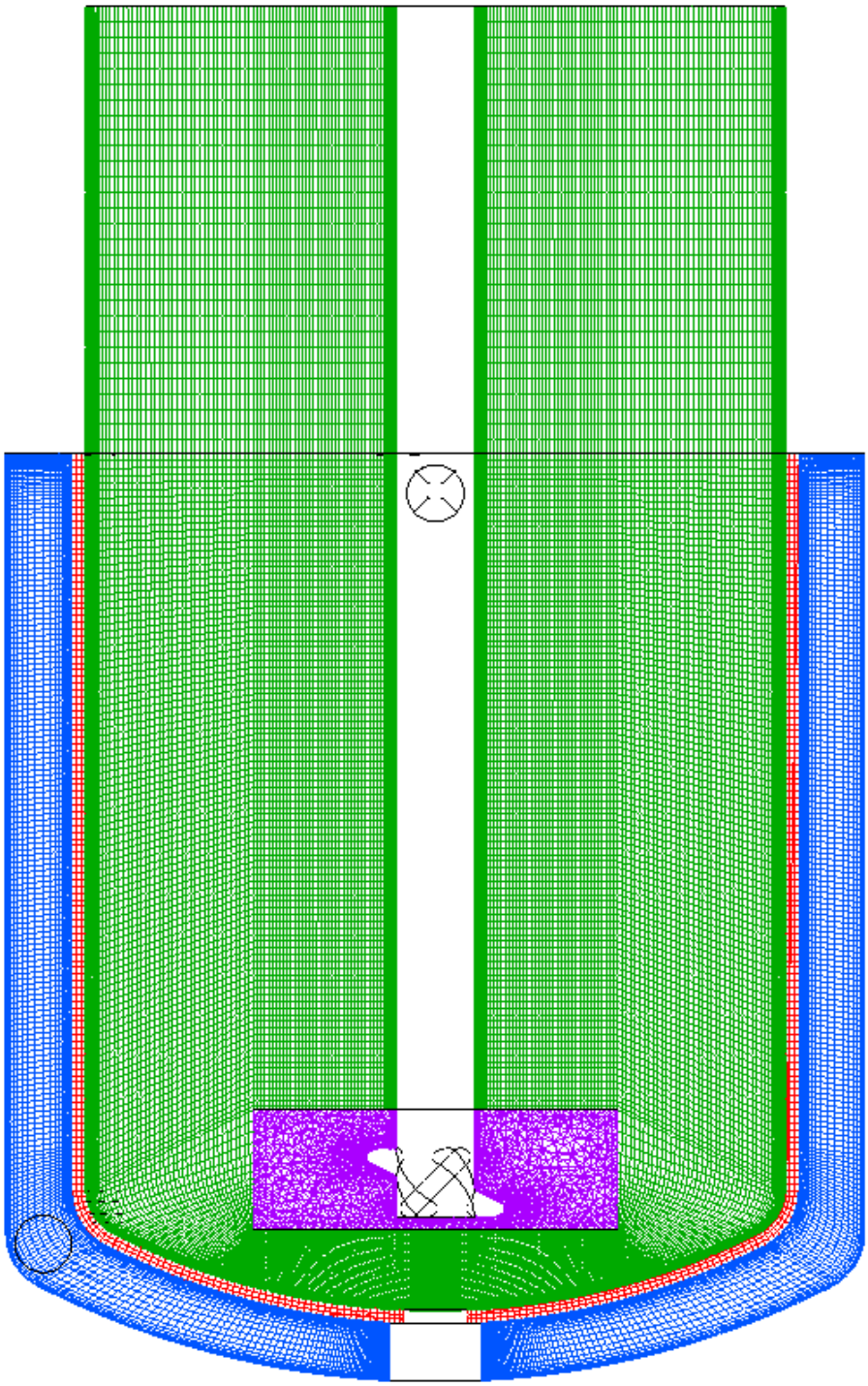

Figure 7.2 – Computational domains used in the conjugate simulation.

Figure 7.2 displays the full extent of the meshes (or ‘domains’) used in ANSYS CFX. In this image, the jacket mesh is in blue, the wall mesh is in red, the tank mesh in green and the impeller mesh in purple. This chapter deals with all four meshes simultaneously.

The model used in the only successful full conjugate run was the curvature corrected SST model, on the medium meshes for the tank and impeller and the coarse mesh for the jacket, and in steady state mode. In chapter 6, the SST model was concluded to need more refinement in the tank and impeller domains. Hence, the results are not entirely quantitatively realistic. However, much useful information can still be derived from this simulation.

7.2.2 Conjugate Heat Transfer Simulation

The results in this section will be presented in a similar fashion to section 5.5. However, the data are only displayed for the inner wall, as the general phenomena at the outer wall have already been investigated in section 5.5. Again, it must be emphasized that the variations taking the form of vertical lines visible in these results are a purely result of the polygonal structure of the mesh and not an intrinsic feature in reality.

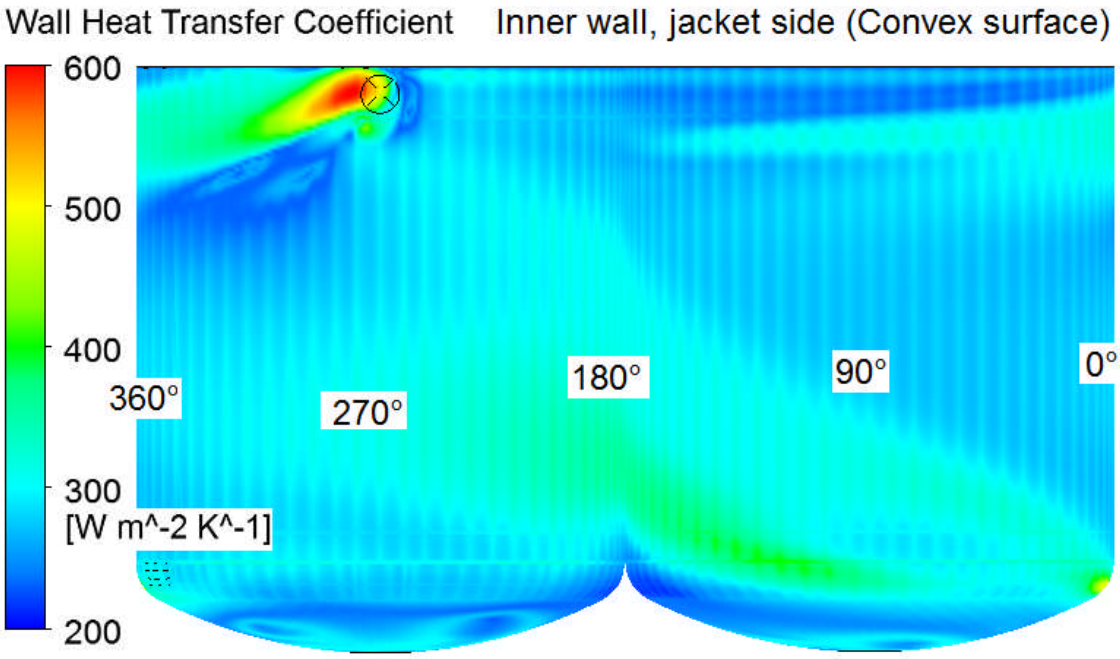

Figure 7.3 – Heat transfer coefficient on the jacket side of the inner wall, for the full conjugate simulation. View from the outside.

Figures 7.3 to 7.8 display results for the jacket s8ide. In figures 7.3 to 7.6, the heat transfer coefficient and wall shear stress again appear to follow similar distribution patterns. The average value of the jacket inner wall heat transfer coefficient is predicted to be 289

W m^{-2} K^{-1}, which is similar to that predicted by literature correlations and other CFD results (discussed in section 5.5).

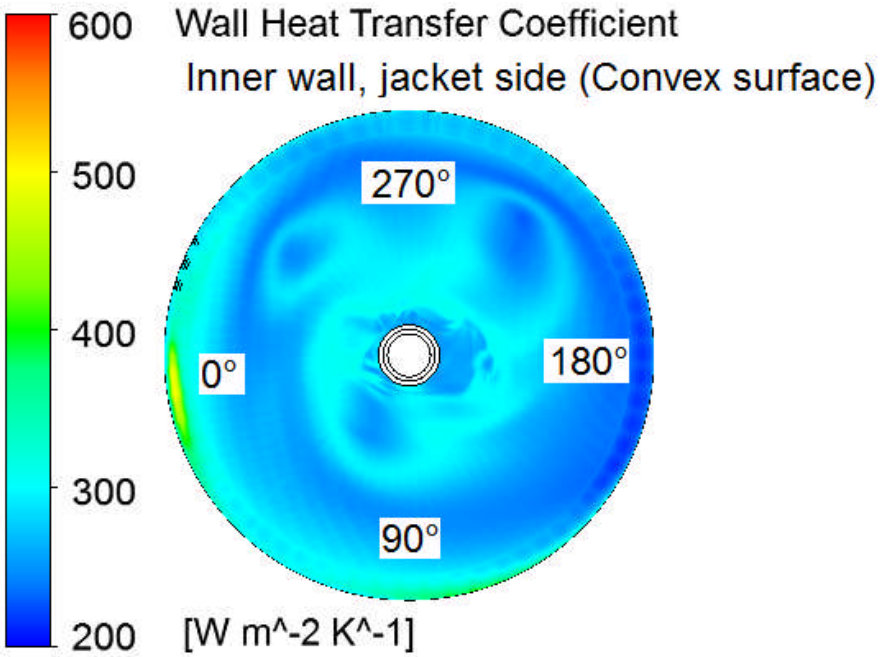

Figure 7.4 – Heat transfer coefficient on the jacket side of the inner wall, for the full conjugate simulation. View from the bottom.

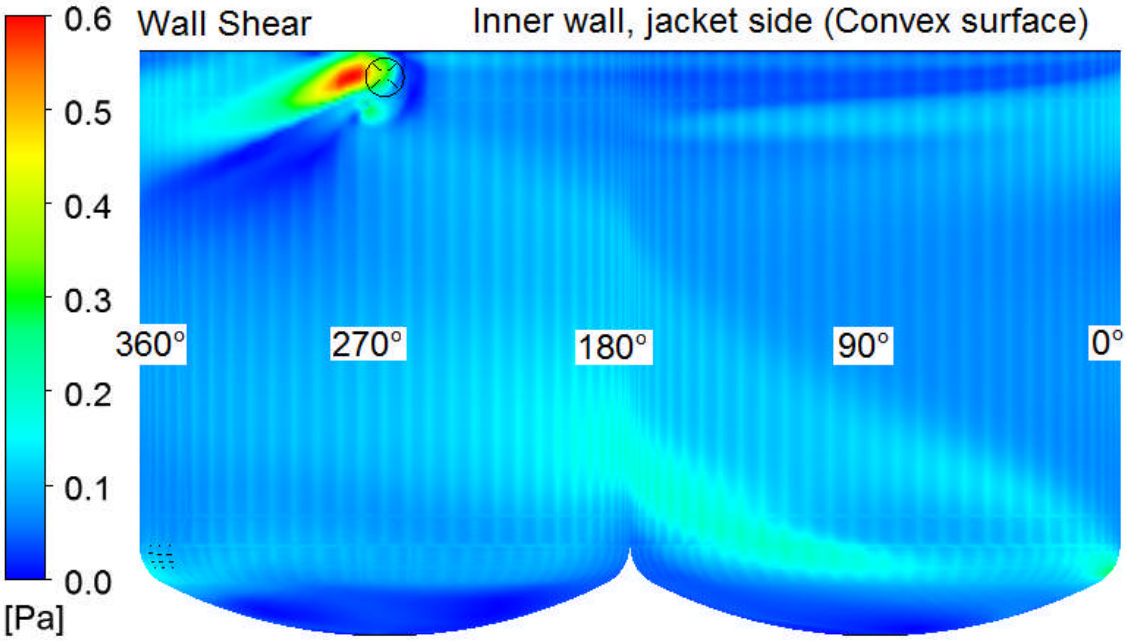

Figure 7.5 – Wall shear stress on the jacket side of the inner wall, for the full conjugate simulation. View from the outside.

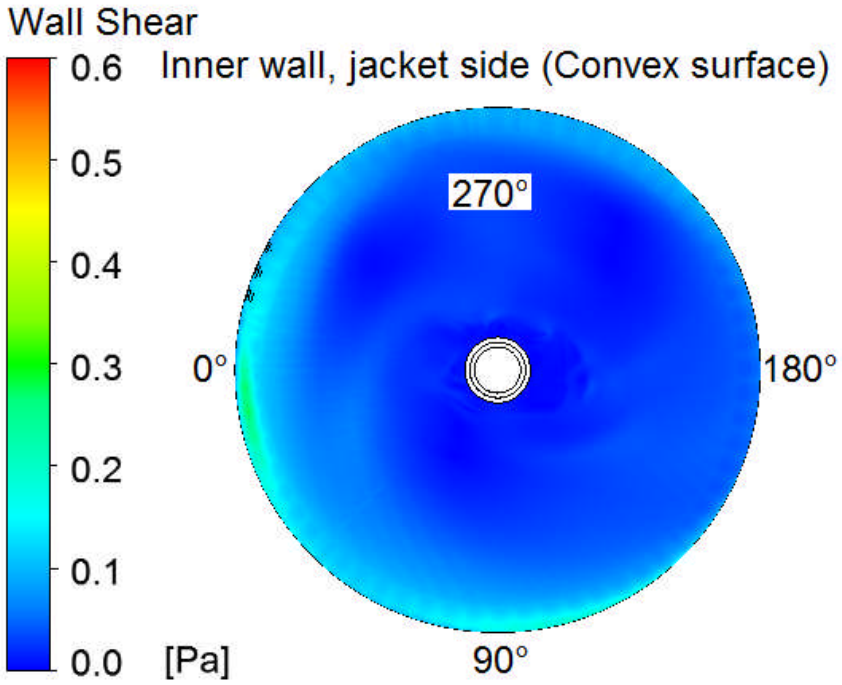

Figure 7.6 – Wall shear stress on the jacket side of the inner wall, for the full conjugate simulation. View from the bottom.

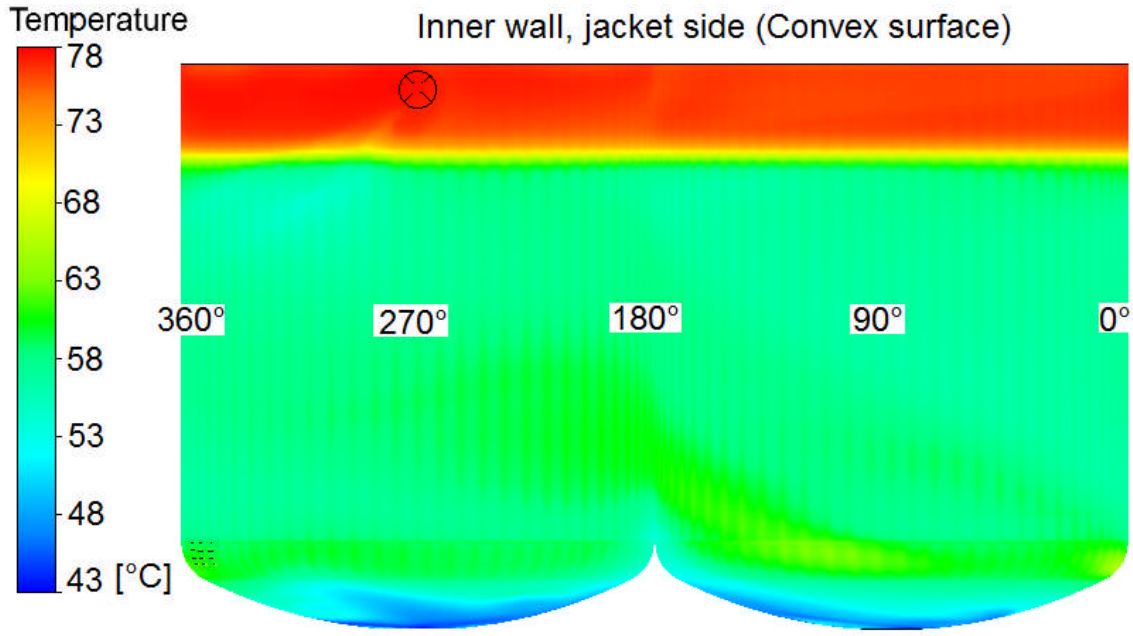

Figure 7.7 – Wall temperature on the jacket side of the inner wall, for the full conjugate simulation. View from the outside.

A pattern which appears to be the result of natural convection is visible at the bottom of the wall in figures 7.4, 7.6 and 7.8. The average wall shear stress on the jacket side is predicted to be 0.089 Pa. In general, the areas of higher wall shear and heat transfer coefficient on the jacket side also result in higher wall temperatures. This is because the jacket fluid is hotter than the process fluid (predicted average 59.2°C at the wall on the

jacket side), so a higher heat transfer coefficient will mean the temperature at the wall is closer to the jacket temperature, and hence hotter.

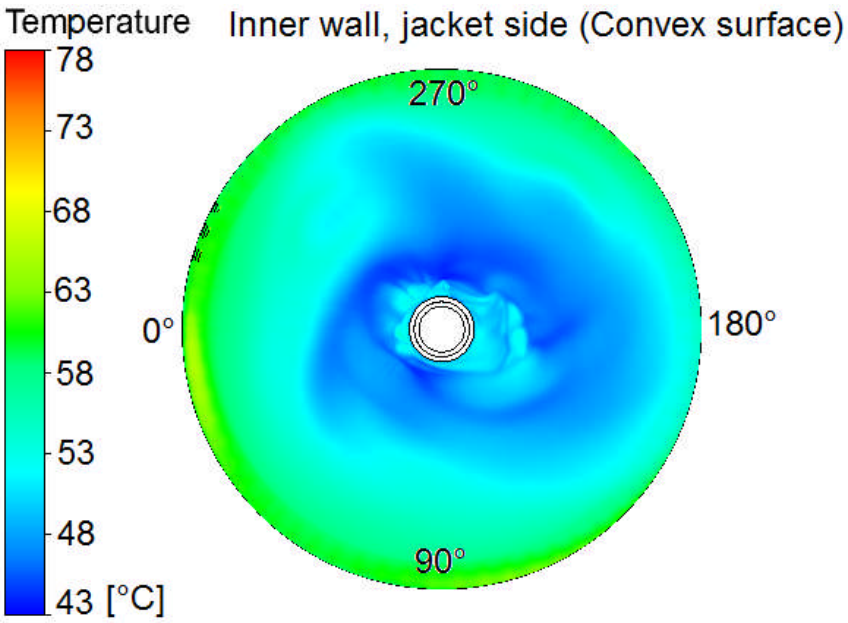

Figure 7.8 – Wall temperature on the jacket side of the inner wall, for the full conjugate simulation. View from the bottom.

Figures 7.9 to 7.14 display results for the process side. In these images, “wispy lines” are observed crossing the jacket almost horizontally (as well as the aforementioned vertical lines, which should be ignored). These rise as the angle around the jacket increases, and appear to be due to the effect of the jacket fluid.

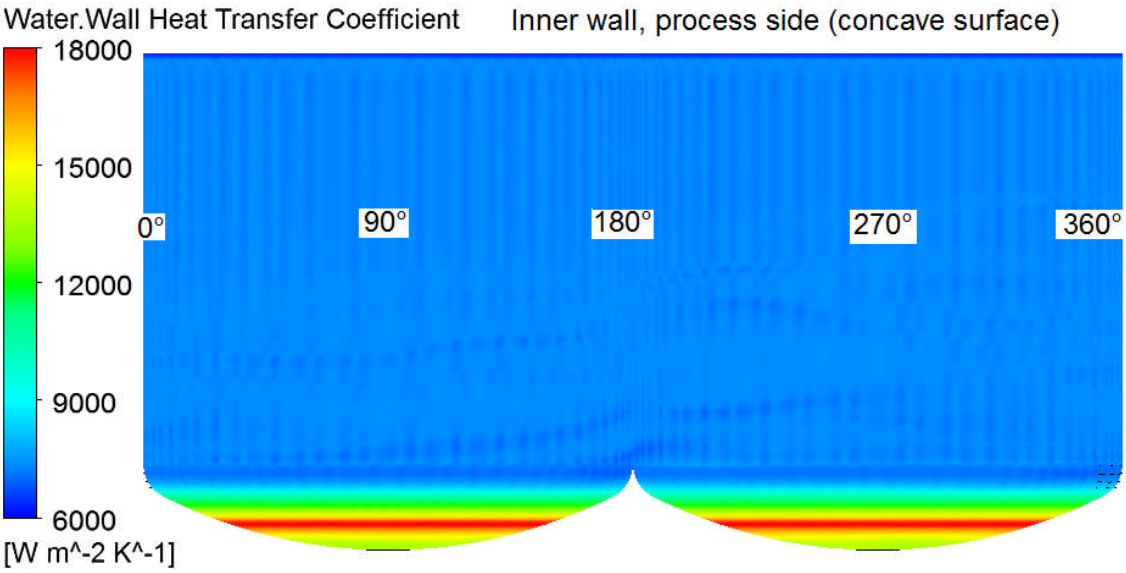

Figure 7.9 – Heat transfer coefficient on the process side of the inner wall, for the full conjugate simulation. View from the inside.

In the process side, the heat transfer coefficient now appears to be much higher than predicted by literature correlations or by the non-conjugate (or semi-conjugate) CFD simulations, with an average of 8765 W m^{-2} K^{-1} (corresponding to a combined U_j value of 116.6 W m^{-2} K^{-1}) below the water surface. It is not clear why the values of heat transfer coefficient are so much higher than expected in this simulation, or why their distribution follows a symmetrical ring shape rather than three individual areas corresponding to each impeller blade (as in figure 6.19 in section 6.2.7). It is speculated that this could be a result of a relatively low level of convergence (see appendix, section 10.5, for residuals). However, then it is unclear why there are three distinct areas of high wall shear stress in figure 7.12 or distinct areas of colder temperature in figure 7.14.

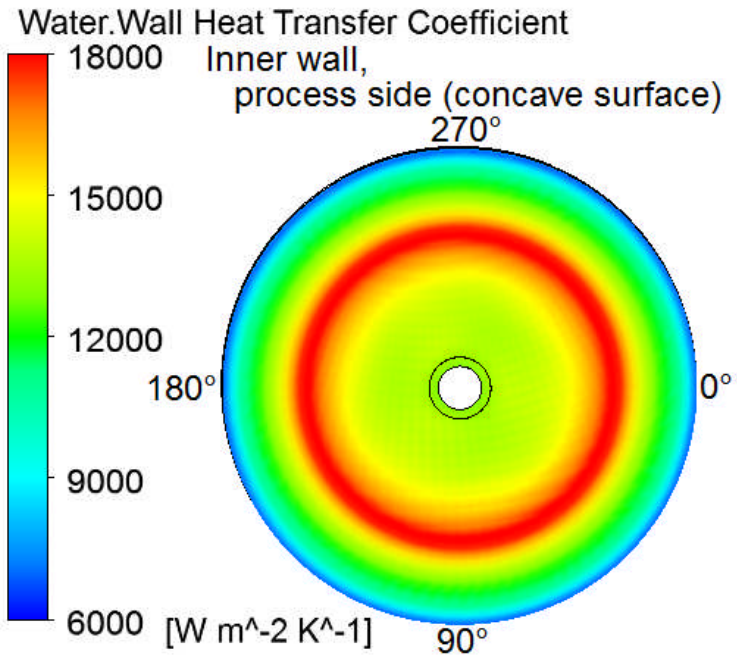

Figure 7.10 – Heat transfer coefficient on the process side of the inner wall, for the full conjugate simulation. View from the top.

The average wall shear stress on the process side, under the water surface, is predicted to be 0.664 Pa. Areas of higher shear stress caused by the impeller forcing the fluid downwards, displayed in figure 7.12, appear to be distributed differently to the more expected pattern observed in the semi-conjugate simulation (figure 6.20 in section 6.2.7) and also observed in the literature (Milewska and Molga, 2010). This difference may again be due to insufficient convergence, or, with further research, it may turn out to be the result of the jacket temperature distribution.

The average wall temperature on the process side, below the water surface, is predicted at 32.8°C. It appears that the temperature distribution in the jacket affects the wall

temperature on the process side (figures 7.13 and 7.14) which in turn affects the viscosity and hence the transfer of momentum on the process side (figures 7.11 and 7.12) is also influenced by the jacket, which in turn affects the heat transfer (figures 7.9 and 7.10). This phenomenon is more clearly seen at the sides of the jacket, that is, in figures 7.9, 7.11 and 7.13. However, the shape of the patterns of wall shear and temperature do not appear to match up well with the distribution of temperatures on the jacket inner wall (figure 7.7). Reasons for this discrepancy are unknown and will require further investigation.

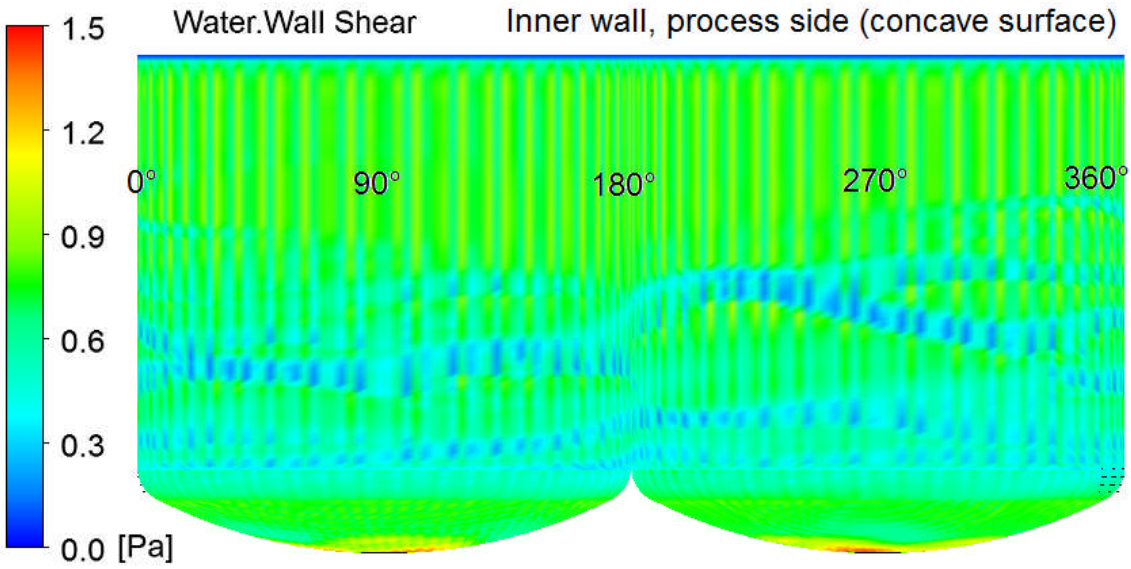

Figure 7.11 – Wall shear stress on the process side of the inner wall, for the full conjugate simulation. View from the inside.

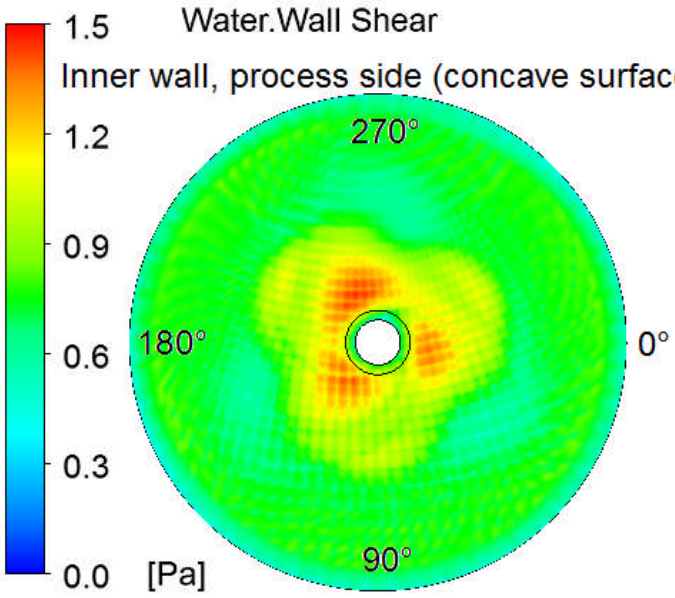

Figure 7.12 – Wall shear stress on the process side of the inner wall, for the full conjugate simulation. View from the top.

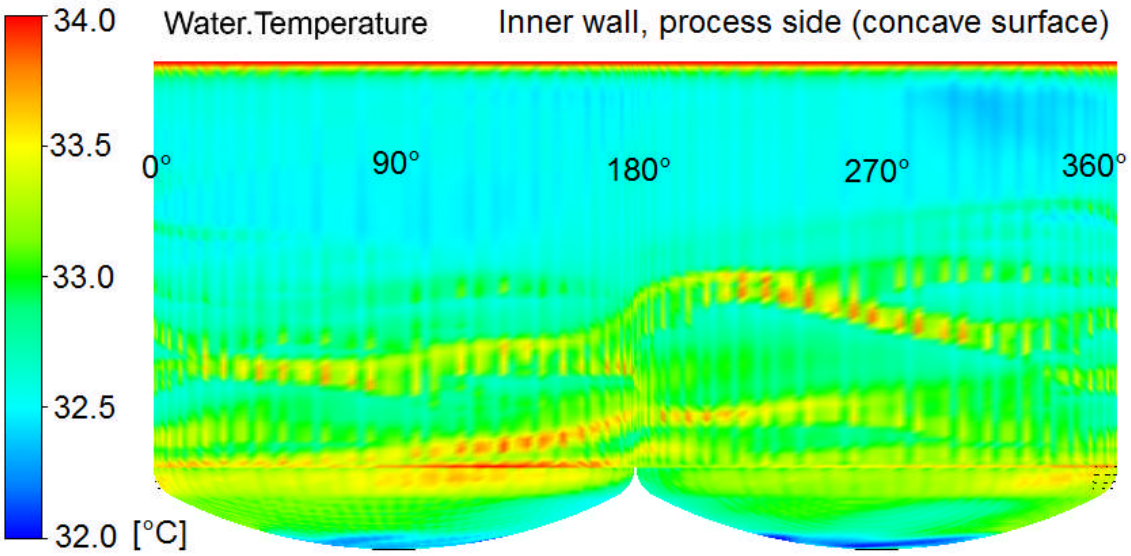

Figure 7.13 – Wall temperature on the process side of the inner wall, for the full conjugate simulation. View from the inside.

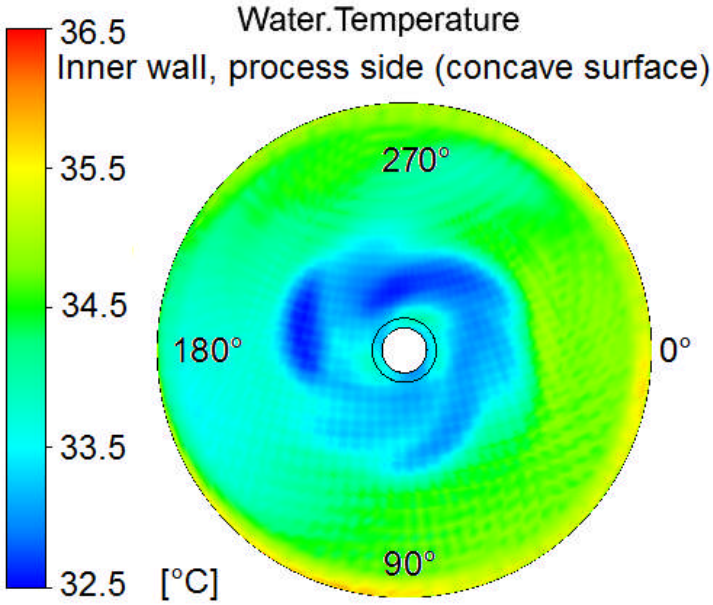

Figure 7.14 – Wall temperature on the process side of the inner wall, for the full conjugate simulation. View from the top.

The higher temperature areas in figure 7.13 display a similar pattern to the heat transfer coefficient and wall shear stress patterns on the jacket side (figures 7.3 and 7.5). Note that due to the position of the viewer looking at the relevant wall side, the view in figure 7.13 follows the jacket flow direction from left to right, while in figures 7.3 and 7.5 the jacket flow is followed from right to left. In this case, as was discussed in section 6.2.6, the wall and jacket film are the controlling resistances, and since the wall resistance is relatively constant, the distribution of heat transfer through the wall should be strongly influenced by the jacket flow, as in figure 7.13.

The temperature distribution in figure 7.14 appears to have some “cold spots” corresponding to the expected lower temperatures below the impeller blades (as the areas of higher heat transfer coefficient in the process side will mean the wall temperature here more closely matches that of the process side). However, these are not as smoothly distributed as the equivalent in the semi-conjugate version (figure 6.21 in section 6.2.7). This appears to be a factor of the influence of the jacket side temperature distribution (figure 7.8) which causes an unevenness of temperature conduction through the bottom of the wall.

The normalised imbalance summary is displayed in the appendix (table 10.8 in section 10.4). The errors in energy conservation both in the jacket (-1.6%) and in the water in the tank (3.4%) are above the acceptable error level of 1%. This may be due to insufficient convergence (see appendix, section 10.5.5) or the mesh quality or resolution may need to be improved.

7.3 Conclusions Drawn from the Conjugate Simulation

When the assumption of constant jacket temperature is relaxed, results for the conjugate simulation display significantly different patterns of wall heat transfer and shear stress (wall momentum). The conjugate simulation used the beta features of ANSYS CFX to have three domains (tank, wall and jacket) each with different domain physics and different materials (single-phase DW-Therm in the jacket, two-phase water and air in the tank).

The uneven flow in the jacket creates uneven distribution of heat transfer, which distorts the symmetrical patterns observed in the process side when a constant jacket temperature is assumed. However, the results for heat transfer coefficient are unexpectedly insensitive to the position of the impeller blades (whereas the temperature and wall shear distribution are sensitive to the impeller blade position) and the distributions of temperature, wall shear and wall heat transfer coefficient seem to vary based on flow attachment in the jacket inner wall, but these patterns do not match up well. These problems may be due to an insufficient level of convergence or mesh resolution in the simulation.

The simulation in chapter 7 (section 7.2) has been the only working fully conjugate simulation during the course of the PhD as there was not enough time to conduct further investigations before the deadline of submission of the thesis (and therefore the end of the funding from EPSRC). Further investigation into conjugate simulations, as well as

validation of the results, will be required, including the use of a better quality of impeller mesh, finer meshes in general, and different turbulence models. Nevertheless, these initial results prove a promising insight into the operation of plain jackets for stirred tank reactors.

No transient conjugate simulations could be set up, as all attempts so far to reach this "holy grail" have failed. Further learning of the workings of the programs of CFX may be required, as well as the time required to create new meshes that may be sufficient for investigating this problem. However, as chapter 6 has hinted, a steady-state conjugate simulation could still turn out to be sufficient.

Table 7.1 displays predicted overall heat transfer coefficients on the jacket-process side (U_j, which is equivalent to U_i) to compare with values investigated in the other chapters. The conjugate results are higher due to the insufficiently converged values (excessively high value of α_{ii}). However the difference is only about 15% because the jacket and wall resistances are the controlling resistances.

Table 7.1 – Comparison of inner wall overall heat transfer coefficients from different chapters in this thesis.

Model or correlation	**Chapter**	$\boldsymbol{U_j}$ / **W m^{-2} K^{-1}**
Steady state conjugate CFD	7	116.6
Transient semi-conjugate CFD	6	101.4
Steady state semi-conjugate CFD	6	101.5
Steady state semi-conjugate CFD with bulk T_p as T_{def} in the process side.	6	96.0
Steady state jacket-only CFD with Cooper (1984)	5	100.5
Bondy and Lippa (1983) with Cooper (1984)	5	93.8
Garvin (1999) with Cooper (1984)	5	112.1
Analytical model	4	80.6

The U_j values calculated using the analytical model in chapter 4 are significantly lower (by about 20%) than those predicted using CFD in chapters 5 and 6. The definition of temperature difference is not enough to account for this discrepancy. However, the definition of the area for heat transfer could explain the difference. Different areas used in the CFD models and experimental analyses are displayed in table 7.2. The heat transfer area used in the analytical model was the specified area of 0.422 m^2, while the under-water heat transfer area in the CFD simulations was 0.337 m^2. This is about 80% of the area

used in the analytical model, which explains why the overall U_j in the analytical model is about 80% of that of the semi-conjugate CFD models. Hence, the CFD models produce similar results for overall heat transfer coefficient when compared to the experiment.

Table 7.2 – Different areas used in the experimental and CFD simulations.

Area	**Used in experimental analysis (chapters 3 and4)**	**Used in CFD (chapters 5, 6 and 7)**	**With liquid level taken into account**
A_{ii} / m^2	0.4220	0.4018	0.3367
A_{io} / m^2	0.4555	0.4232	0.3603
A_{oi} / m^2	0.6356	0.5384	N/A
A_{oo} m^2	0.6766	N/A	N/A

8 CONCLUSIONS AND FUTURE RESEARCH

8.1 Overall conclusions

The CFD results appear to agree reasonably with the results in both a qualitative and quantitative sense, which is particularly useful when investigating phenomena in the use of a plain jacket with a stirred vessel. Despite significant errors and variation within different CFD models, much insight can still be derived.

Maldistribution of flow in plain jackets is a major problem associated with this type of equipment. The temperature distribution in plain jackets can vary by tens of degrees, and this can provide uneven heating. This can make necessary the use of strong and efficient mixing within the vessel, in particular during highly temperature-sensitive processes when the contents must be kept within a small temperature range. Heat transfer coefficients calculated using engineering correlations from the literature can be sufficiently accurate if the surface area for heat transfer and the average bulk temperature in the whole jacket are known accurately.

The swirl decays rapidly as the heat transfer fluid moves around the jacket. Although the tangential component of the velocity is greater than the axial velocity component, the pressure drop is much closer to a pure axial flow case (only about 10% higher). The average cross sectional area of flow in the jacket is therefore more likely to be closer to that of the pure uniform axial flow case than a concentrated, coil-like tangential flow case. The simulated amount of swirl generated in the plain jacket is much weaker than in jackets where a tangential flow is forced. It may be concluded that if no experimental data are available, calculating the jacket pressure drop using the axial flow assumption, adding the entry and exit head losses, and multiplying this total by a factor of 1.1 is recommended for plain jackets.

During heating, the average bulk temperature in the jacket is likely to be somewhat lower than the more commonly used average of the jacket inlet and outlet temperatures, due to natural convection effects in dead zones allowing significantly colder temperatures at the bottom of the jacket.

The vortex geometry using a pitched three-blade turbine is not well investigated experimentally in the literature and may differ from profiles generated by a paddle or Rushton turbine. Correlations for paddles in the literature produce a vortex shape that differs from the vortex shapes found in the CFD models in this thesis. Free surface vortex

geometry and vortex depth is hard to define using CFD because the liquid volume fraction changes gradually, whereas in reality there is a sudden step change and a well-defined surface. A free surface may need to be modelled for increased accuracy because it affects the shape of the flow volume and limits the total heat capacity of the contents of the vessel.

The film heat transfer coefficient on the process side is not likely to affect the overall heat transfer coefficient when a plain jacket is used with DW-Therm and a glass wall. In this setup, the resistance to heat transfer in the jacket film is likely to be a controlling resistance, which, when combined with the wall resistance, will limit the overall heat transfer coefficient. However, it should be noted that in pitched blade turbines, greater heat transfer will occur at the bottom of the vessel, and this is especially important in cooling, when the coldest jacket temperature is generally found in a “dead zone” at the bottom of the jacket.

The commonly used resistance model combined with engineering correlations can be reliable as an estimate to expected average temperatures in the jacket and vessel, for general use where the distribution of temperature and heat transfer may be less significant. Predicted values of heat transfer coefficient for the inner wall using the correlation of Bondy and Lippa (1983) are at most 5% different from the CFD values in the inner wall, at most 15% different in the outer wall. However, comparing the results of the resistance model, this translates into a temperature error only up to about 1.1°C in both the inner and outer wall. Other correlations would have higher errors in this case, but may be more suitable for other geometries such as guided flow or uniform annular flow.

The distributed parameter model laid out in chapter 4 demonstrates thermal inertia in the vessel wall and significantly adds to the overall heat capacity of the process. This added heat capacity effect must be considered to correctly and safely evaluate the effects of heating, which is very important in temperature-sensitive processes such as crystallisation or highly exothermic or endothermic reactions.

When all assumptions about heat transfer between the jacket and the process side are relaxed, the conjugate simulation demonstrates that uneven flow in the jacket creates uneven distribution of heat transfer, which can distort the patterns of heat transfer and momentum at the wall on the process side.

Improvements to the heat transfer process may include modification of the piping and connections, for example by keeping the reactor close to the heat exchanger or device that

controls the inlet temperature of the heat transfer fluid. Additionally, when designing a new reactor, the option should always be considered to choose a different and more efficient type of jacket, such as with guiding vanes, dimples or a half-pipe jacket.

8.2 Conclusions drawn from each chapter

As reviewed in chapter 2, mathematical models to simulate the conditions within stirred tank reactors have been developed in the literature and are becoming more sophisticated as research progresses. These models range from relatively simple analytical models, lumped parameter and distributed parameter models, to high level CFD models.

The data presented in chapter 3 are very useful for analysis and comparison with models of heat transfer, which is conducted in subsequent chapters. However, they do not describe the details of the flow or the distribution of temperature or pressure, as attempting to modify the equipment to provide this information would be difficult and expensive. CFD simulation (from chapter 5) is required to provide such detail to compare with the experimental analysis (from chapter 4).

In chapter 4, the data obtained in the experiments (from chapter 3) have been simulated using an analytical model to describe the jacket operation with time and to account for heat transfer between the jacket and the process, as well as heat loss to the surroundings. The lumped parameter model and analytical solutions used several important assumptions to simplify the mathematics behind the process. Heat transfer coefficients were predicted using the analytical model as well as industrially used engineering correlations found in the literature. The distributed parameter model has additionally accounts for the thermal inertia of the vessel wall.

Chapter 5 describes the expected pressure drops with the Bernoulli equation, and follows on to use CFD, which relaxes chapter 4's assumptions of perfect mixing, symmetry, uniform upward jacket flow and lack of longitudinal heat conduction in the vessel walls. The simulations appear to agree reasonably with the experimental results and analysis. Flow in the jacket is non-uniform and heat transfer is greater near the inlet and outlet ports of the jacket. Stagnation of flow occurs mostly at the bottom of the jacket and partly at the top. It is concluded that a mesh-intensive CFD simulation could reveal details such as temperature hotspots due to the maldistribution of flow.

In chapter 6, the flow in the process side has been modelled with CFD. The results obtained were similar to those predicted in similar CFD simulations in the literature.

Predicted vortex geometry is dissimilar to correlations found in the literature which assume a central forced vortex and outer free vortex, although this may be due to the different impeller type used. Additionally, the vortex is difficult to define due to the gradual change in volume fraction as a result of numerical errors. In the process side, hot spots are expected near the wall at the top and bottom of the reactor, particularly in zones of secondary flow where the mixing is lessened. As the water level is below the jacket, high temperature variations occur at the walls near the top because of insulation from the air.

In chapter 7, results for the conjugate simulation display significantly different patterns of wall heat transfer and shear stress (wall momentum) compared to modelling only the jacket side or only the process side. The uneven flow in the jacket creates uneven distribution of heat transfer, which distorts the symmetrical patterns observed in the process side when a constant jacket temperature is assumed. However, further investigation is required into this conjugate simulation.

8.3 Future Research

Further possible work will attempt to achieve as many of the following as possible:-

1. Further validation of data (more simulations, more experiments).
2. Simulations of cooling (only heating and boiling have been covered in this thesis).
3. More extensive comparison of results using different CFD models, such as Reynolds Stress models.
4. Performing transient conjugate CFD simulations of the process.
5. Obtaining further experimental data for model validation. Lower stirrer speeds, such as 180 rpm, are recommended to be within the acceptable range for CFD simulations.
6. Obtaining further results from laboratory scale reactors (between 0.5 litre and 5 litre capacity).
7. Finding the residence time distribution in the jacket.
8. The effect of scale-up on the heat transfer characteristics is to be investigated. These models will be scaled up to semi-tech and industrial sizes. As the reactor is scaled up, inhomogeneity increases and in an exothermic reaction it is more likely that there will be “hot spots” that produce much more heat per unit volume than the overall mixture.
9. The effects of agitation speed.
10. The responses to exothermic reactions.

11. Simulation of runaway reactions.
12. For accurate modelling of product distributions in these reactors, an appropriate micro-mixing model will be used to account for the effect of turbulent mixing on chemical reactions at molecular level.
13. Extension of the conjugate CFD model to include processes such as chemical reactions, runaway reactions, crystallisation, etc.
14. Control algorithms to be put in place to be able to set the heating or cooling system appropriately as would occur in industry.
15. Investigate the effects of wall changing the wall material. This should have a large impact as the wall is a controlling resistance to heat transfer in most cases.
16. Further development of the distributed parameter model (in MATLAB) to include chemical reactions, as well as more easily customisable jacket inlet temperature and flow profiles and variable physical properties of substances with temperature.
17. The distributed parameter models may also be developed further based on the CFD models to include separate, perfectly mixed “zones” in the reactor where the temperatures are different and where “hot spots” may occur – such as the zones of secondary flow. This is because the industry may not be able to practically use CFD in each case, due to high computational requirements and cost of licences, and may rely on simpler models instead.
18. More detailed error analysis.

9 REFERENCES

ALANE, A.; 2007; *The Experimental Study of Operating Characteristics, Stability and Performance of a Vertical Thermosyphon Reboiler Under Vacuum*. PhD Thesis, School of Chemical Engineering and Analytical Science, Faculty of Engineering and Physical Sciences University of Manchester.; 263 – 267. For formulae of physical properties, p. 355.

ALI, M; 2009; Safe Control of Exothermic Reactions in Jacketed Stirred Tank Reactors; MSc Dissertation for PEME5000M module; SPEME, University of Leeds.

ANSYS; 2012; *ANSYS Help 14.5*; ANSYS, Inc. Mechanical ADPL Theory Reference section 7.1 (Continuity. Momentum and energy equations), CFX Modeling Guide section 2.7.5 (Heat transfer), CFX Theory Guide section 2.8.1 (Mathematical formulation for heat transfer).

ANSYS; 2013; *ANSYS Help 15*; ANSYS, Inc. CFX Modeling Guide section 7.18 (Free Surface Flow), CFX Modeling Guide section 7.18.5.9 (Parallel), CFX Modeling Guide section 17.3.4 (Convergence Control Parameters), CFX Theory Guide section 2.2.2 (Two Equation Turbulence Models), CFX Theory Guide section 2.3.1 (ε-based Reynolds Stress Models), CFX Theory Guide section 2.3.2 (ω-based and BSL Reynolds stress models).

ARMENANTE, P. M.; LUO, C.; CHOU, C.; FORT, I.; MEDEK, J.; 1997; *Velocity profiles in a closed, unbaffled vessel: comparison between experimental LDV data and numerical predictions*; Chem. Eng. Sci. **52** (20); 3483 – 3492.

BENTHAM, E. J.; 2011; *Transient Operation of Stirred Tank Reactors: Exothermic Reactions*; MEng Dissertation for PEME5200 research project module; SPEME, University of Leeds.

BENTHAM, E. J.; HEGGS, P. J.; MAHMUD, T.; 2013; *Investigation of flow and pressure drop in a plain jacket of a stirred tank reactor*; Proc. 13th UK Heat Transfer Conference; Imperial College London. Paper 148.

BENTHAM, E. J.; HEGGS, P. J.; MAHMUD, T.; 2015a; *Heat Transfer in a Plain Jacket of a Pilot Scale Stirred Tank Reactor*; Proc. CHT-15, 6th International Symposium on Advances in Computational Heat Transfer, May 25-29, 2015, Rutgers University, New Brunswick, NJ, USA; International Centre for Heat and Mass Transfer Digital Library, Begell House.

BENTHAM, E. J.; HEGGS, P. J.; MAHMUD, T.; 2015b; *Run-around Coils for Energy Efficiency*; Proc. 14th UK Heat Transfer Conference; Heriot-Watt University, Edinburgh.

BIER, K.; SCHMADL, J.; GORENFLO, D.; 1983; *Influence of heat flux and saturation pressure on bool boiling heat transfer to binary mixtures*; Chem. Eng. Fundam. **1** (12), 79. As referenced by Hewitt *et al*. (1994).

BLASIUS, H.; 1913; *Das Ähnlichkeitsgesetz bei Reibungsvorgängen in Flüssigkeiten. Forsch*; Ver. deut. Ing, 131.

BONDY, F.; LIPPA, S.; 1983; *Heat transfer in agitated vessels*; Chemical Engineering, April 4th, 62 – 71.

BRAGINSKII, L. M.; 1967; *Theoretical Foundations of Chemical Engineering*; 560. As referenced by Brennan (1976).

BRENNAN, D. J.; 1976; *Vortex geometry in unbaffled vessels with impeller agitation*; Trans. Instn Chem. Engrs **54**, 209 – 217.

BROOKS, G.; SU, G. J.; Oct. 1959; *Heat Transfer in Agitated Vessels*; Chem. Eng. Prog. **55** (10), 54 – 57.

BROWN, R. W.; SCOTT, M. A.; TOYNE, C.; 1947; *An investigation of heat transfer in agitated cast iron vessels*; Ind. Eng. Chem. **25**, 181.

CHANDRA, A.; SINGH, H.; 2015; *Turbulent heat transfer in agitated vessel equipped with pitched blade turbine*; Proceedings of 6th International Symposium on Advances in Computational Heat Transfer (CHT-15), ICHMT; Begell House.

CHEN, C. Y.; HAWKINS, G. A.; SOLBERG, H. L.; 1946; Trans ASME **68**, 99. As referenced by Bondy and Lippa (1983).

CIOFALO, M; BRUCATO, A.; GRISAFI, F.; TORRACA, N.; *Turbulent Flow in Closed and Free-Surface Unbaffled Tanks Stirred by Radial Impellers*; 1996; Chem. Eng. Sci. **51** (14), 3557 – 3573.

COOPER, M. G.; 1984; Saturated Nucleate Boiling – A Simple Correlation. First UK National Conference on Heat Transfer, **2**, 785 – 793. As referenced by Alane (2007).

COULSON, J. M.; RICHARDSON, J. F.; 1999; *Coulson & Richardson's Chemical Engineering Volume 1, Sixth Edition*; Elsevier Butterworth-Heinemann, 66-67.

DISTELHOFF, M. F. W.; MARQUIS, A. J.; NOURI, J. M., WHITELAW, J. H.; 1997; *Scalar mizing measurements in batch operated stirred tanks*; Can. J. Chem. Eng. 75, 641 – 652. As referenced by Javed *et al*. (2006).

DITTUS, F. W.; BOELTER, L. M. K.; 1930; *Heat Transfer in Automobile Radiators of the Tubular Type*; University of California, Berkeley; Publications in Engineering **2**, 443. As referenced by Alane (2007).

DOUGLAS, J. F.; GASIOREK, J. M.; SWAFFIELD, J. A.; JACK, L. B; 2006; *Fluid Mechanics, 5th edition*; Pearson Prentice Hall; 355.

DREAM, R. F.; 1999; *Heat Transfer In Agitated Jacketed Vessels*; Chemical Engineering, January, 90 – 96.

ESDU 78031; 1971; *Internal Forced Convective Heat Transfer in Coiled Pipes*; ESDU.

ESDU 81045; 1981; *Forced convective heat transfer in concentric annuli with turbulent flow*; ESDU.

ESDU 92003; 1992; *Forced convection heat transfer in straight tubes. Part 1: turbulent flow*; ESDU.

ESDU 98003; 1998; *Design and performance evaluation of heat exchangers: The effectiveness – N_{TU} method, Part 1 – Introduction*; ESDU.

ESDU 98005; 1998; *Design and performance evaluation of heat exchangers: The effectiveness – N_{TU} method, Part 3 – Graphical and analytical data*; ESDU.

FENNEY, W.; TOLLEY, P.; ASPINALL, F.; 2011*; iPRD LSG 25 Litre Reaction Unit Piping & Instrument Diagram*; Drawing Numbers X48597-DRG-020 and X48597-DRG-021; Project for Leeds University; Boulting House, Firecrest Court, Centre Park, Warrington WA1 1RG.

PIPING & INSTRUMENT DIAGRAM

FORSTER, H. K.; ZUBER, N.; 1955; *Dynamics of vapour bubbles and boiling heat transfer*; AIChE J., **1**, 531. As referenced by Hewitt *et al*. (1994).

FRIED, E.; IDELCHIK, I. E.; 1989; *Flow Resistance: A Design Guide for Engineers*; Hemisphere Publishing Corporation, Taylor & Francis Group; 207 – 251.

GADDIS, E.; 2010; *Heat Transfer and Power Consumption in Stirred Vessels*; Section N3 of *VDI Heat Atlas, Second Edition*; Springer Books, 1465 – 1469.

GARVIN, J; 1999; *Understand the Thermal Design of Jacketed Vessels*; Chemical Engineering Progress, June, 61 – 65.

GIBBS, J. W.; 1902; *Elementary Principles in Statistical Mechanics, Developed with Especial Reference to the Rational Foundation of Thermodynamics*; New York: C. Scribner.

GNIELINSKI, V.; 2009; *Heat Transfer Coefficients for Turbulent Flow in Concentric Annular Ducts*; Heat Transfer Engineering **30** (6) 431 – 436.

GRAU, M. D.; NOUGUES, J. M.; PIUGJANER, L.; 2000; *Batch and semibatch reactor performance for an exothermic reaction*; Chemical Engineering and Processing **39**, 141 – 148.

GUNGOR, K. E.; WINTERTON, R. H. S.; 1986; *A General Correlation for Flow Boiling in Tubes and Annuli*; International Journal of Heat and Mass Transfer **29** (3), 351 – 358. As referenced by Alane (2007).

GUSTIN, J.; FILLION, J.; TRÉAND, G.; EL BIYAALI, K.;1993; *The phenol + formaldehyde runaway reaction. Vent sizing for reactor protection*; Journal of Loss Prevention in the Process Industries **6** (2), 103 – 113.

HAQUE, J. N.; MAHMUD, T.; ROBERTS, K. J.; 2006; *Modeling Turbulent Flows with Free-Surface in Unbaffled Reactors*; Ind. Chem. Eng. Res. **45**, 2881 – 2891.

HAQUE, J. N.; MAHMUD, T.; ROBERTS, K. J.; LIANG, J, K.; WHITE, G.; WILKINSON, D.; RHODES, D.; 2011; *Free–Surface Turbulent Flow Induced by a Rushton Turbine in an Unbaffled Dish–Bottom Stirred Tank Reactor: LDV Measurements and CFD Simulations*; The Canadian Journal of Chemical Engineering **89**, August issue, 745 – 753.

HEGGS, P. J.; HILLS, P. D.; 1994; *The Design of Heat Exchangers for Batch Reactors*; Foumeny, E. A.; Heggs, P. J. *Heat Exchange Engineering, Volume 4 – Advances in Design Operation*, Chapter 14; Honeysuckle International Publications, 219 – 235.

HEWITT, G. F.; SHIRES, G. L.; BOTT, T. R.; 1994; *Process Heat Transfer*; Begell House, inc., New York; 423 – 467 (Boiling Heat Transfer), 940 – 941 (Heat Transfer in the Jacket).

HUBER; 2010; *Operating Manual – Nuevo*. Accessed online 03/11/2014 with: http://www.huber-online.com/download/manuals/unistats_en.pdf

HUBER: High Precision Thermoregulation; *Huber Unistat 510w*; Accessed online 04/02/2014 with:-
http://www.huber-online.com/en/product_datasheet.aspx?no=1005.0001.05

JAVED, K. H.; MAHMUD, T.; ZHU, J. M.; 2006; *Numerical simulation of turbulent batch mixing in a vessel agitated by a Rushton turbine*; Chemical Engineering and Processing **45**, 99 – 112.

KAIYRZHANOVA, A; 2010; Control of Heat Release and Temperature Levels in Jacketed Stirred Tank Vessels; MSc Dissertation for PREN5300 module; SPEME, University of Leeds.

KAKAÇ, S.; SHAH, R. K.; AUNG, W.; 1987; *Handbook of Single-Phase Convective Heat Transfer*; Wiley Interscience, John Wiley and sons, 3·91 – 3·111.

KAYS, W. M.; LONDON, A. L.; 1964; *Compact Heat Exchangers* – Second Edition; 22 – 24.

LAUNDER, B. E.; 1989; *Second-moment closure: present… and future*; Int. J. Heat and Fluid Flow **10** (4), 282 – 300.

LAUNDER, B. E.; REECE, G. J.; RODI, W.; 1975; *Progress in the developments of a Reynolds-stress turbulence closure*; J. Fluid Mechanics **68**, 537 – 566.

LANDAU, R. N.; 1996; *Expanding the role of reaction calorimetry*; Thermochimica Acta **289**, 101 – 126.

LEHRER, I. H.; 1970; *Jacket-side Nusselt Number*; Ind. Eng. Chem. Process Des. Dev. **9** (4), 553 – 558.

LEHRER, I. H.; 1971; *Flow Model for a Jacket*; Ind. Eng. Chem. Process Des. Dev. **10** (3), 318 – 322.

LI, M.; WHITE, G.; WILKINSON, D.; ROBERTS, K.; 2004; *LDA Measurements and CFD Modeling of a Stirred Vessel with a Retreat Curve Impeller*; Ind. Eng. Chem. Res. **43**, 6534 – 6547.

MAHMUD, T.; HAQUE, J. N.; ROBERTS, K. J.; RHODES, D.; WILKINSON, D.; 2009; *Measurements and modelling of free-surface turbulent flows induced by a magnetic stirrer in an unbaffled stirred tank reactor*; Chem. Eng. Sci. **64**, 4197 – 4209.

MAHMUD, T.; BENTHAM, E. J.; HEGGS, P. J.; 2015; *Modelling the Free-Surface Turbulent Flow and Heat Transfer in an Unbaffled Vessel Agitated by a Pitched Three-Blade Turbine*; Proc. 14th UK Heat Transfer Conference; Heriot-Watt University, Edinburgh.

MARKOPOULOS, J.; KONTOGEORGAKI, E.; 1995; *Vortex depth in unbaffled single and multiple impeller agitated vessels*; Chem. Eng. Technol. **18**, 68 – 74.

MENTER, F. R.; 1994; *Two-equation eddy-viscosity turbulence models for engineering applications*; AIAA Journal **32** (8), 1598 – 1605.

MEZAKI, R.; MOCHIZUKI, M.; OGAWA, K.; 2000; *Engineering Data on Mixing*; Elsevier Science Ltd.; 249.

MILEWSKA, A; MOLGA, E. J.; 2007; *CFD simulation of accidents in industrial batch stirred tank reactors*; Chemical Engineering Science **62**, 4920 – 4925.

MILEWSKA, A; MOLGA, E.; 2010; *Safety aspects in modelling and operating of batch and semibatch stirred tank chemical reactors*; Chemical Engineering Research and Design **88**, 304 – 319.

MOODY, L. F.; 1944; *Friction factors for pipe flow*; Trans. Am. Soc. Mech. Engrs. **66**, 671.

MOSTINSKII, I. L.; 1963; *Calculation of heat transfer and critical heat fluxes in liquids*; Teploenergetika, **10** (4), 66. As referenced by Hewitt *et al*. (1994).

NAGATA, S.; YOSHIOKA, N.; YOKOYAMA, T.; 1955; *Studies on the power requirement of mixing impellers*; Memoirs of the Faculty of Engineering, Kyoto University **17**, 175 – 185.

NAGATA, S.; NISHIKAWA, M.; TAKIMOTO, T.; KIDA, F.; KAYAMA, T.; 1971; *Jacket Side Heat Transfer Coefficient in Mixing Vessel*; Kagaku Kogaku **35**, 924; Found in Mezaki, 2000, p. 249.

NAGATA, S. *et al*.; 1972; *Turbulent Heat Transfer from the Wall of a Jacketed Tank*; Heat Transfer Jpn. Res. **71**, 89 – 101. As referenced by Penney (1983).

NAGATA, S.; 1975; *Mixing: Principles and Applications*; Wiley, New York.

NOLAN, P. F.; BARTON, J. A.; 1987; *Some lessons from thermal-runaway incidents*; Journal of Hazardous Materials **14**, 233 – 239.

NOLAN, P. F.; 1993; *The runaway story*; Journal of Loss Prevention in the Process Industries **6** (2), 67 – 68.

PALEN, J. W.; YARDEN, A.; TABOREK, J.; 1972; *Characteristics of boiling outside large-scale horizontal multi-tube bundles*; AIChE Symp. Ser., **68** (118), 50. As referenced by Hewitt *et al*. (1994).

PEDROSA, S. M. C. P.; Nunhez, J. R.; 2003; *Improving heat transfer in stirred tanks cooled by helical coils*. Brazilian Journal of Chemical Engineering **20** (2).

PENNEY, W. R.; 1983; *Agitated Vessels*; Hewitt, G. F. *Heat Exchanger Design Handbook*, Chapter 3.14; Hemisphere Publishing Corporation.

PERRY, B.; GEDDES, W. R.; 2011; *A Localised Condensation Model for the Simulation of Kettle Evaporators*; The Twelfth UK National Heat Transfer Conference, paper 71.

PERRY, R. H; CHILTON, C. H.; 1973; *Chemical Engineers' Handbook*; McGraw-Hill, Inc. p. 10-17.

PETUKOV, B. S.; 1970; *Heat transfer and friction in turbulent pipe flow with variable physical properties*. Advances in Heat Transfer, Academic Press **6**, 503 – 564.

POINTWISE, INC; *Y+ Calculator – Compute Wall Spacing for CFD*; Accessed online 03/09/2014 with: http://www.pointwise.com/yplus/

RHIE, C. M.; CHOW, W. L.; 1983; *Numerical Study of the Turbulent Flow Past an Airfoil with Trailing Edge Separation*; AIAA J. **21** (11), 1525 – 1532.

RIEGER, F., DITLE, P., & NOVAK, V. 1979 *Vortex Depth in Mixed Unbaffled Vessels*. Chem. Eng. Sci. **34**, 397 – 403.

RUDNIAK, L.; MILEWSKA, A.; MOLGA, E.; 2011; *CFD Simulations for Safety of Chemical Reactors and Storage Tanks*; Chem. Eng. Technol. **34** (11), 1781 – 1789.

QVF; 2014; *Borosilicate glass: Physical properties of Borosilicate glass*; De Dietrich Process Systems GmbH; Accessed online 06/08/2014 by the following URL: http://www.qvf.com/glass-equipment/borosilicate-glass/physical-properties.html

SAW, J. L.; 2003; *Reaction Calorimetry and Heat Transfer*; PhD Thesis, University of Manchester Institute of Science and Technology (UMIST).

SCOPUS – Document Search; Accessed online 27/09/2015 with: http://www.scopus.com/; Search for "Flow Model for a Jacket" by Lehrer (1971) – no citations between 1996 (when Scopus records began) and 2015.

SEIDER , E. N.; TATE, G. E.; 1936; Ind. Eng. Chem. **28**, 1429. As referenced by Bondy & Lippa (1983).

SMIRNOV, P. E.; MENTER, F. R.; 2008; *Sensitization of the SST turbulence model to rotation and curvature by applying the Spalart-Shur correction term*; ASME Paper GT 2008-50480, Berlin, Germany. As referenced by ANSYS (2013).

SMIRNOV, P. E.; MENTER, F. R.; 2009; *Sensitization of the SST turbulence model to rotation and curvature by applying the Spalart-Shur correction term*; ASME Journal of Turbomachinery **131** (4), 04010.

SMIT, L.; DÜRING, J.; 1991; *Vortex geometry in stirred vessels*; Proceeds of the 7th European Conference on Mixing **2**, 633 – 639.

SNEE, T. J.; BASSANI, C.; LIGHTHART, J. A. M.; 1993; *Determination of the thermokinetic parameters of an exothermic reaction using isothermal, adiabatic and temperature-programmed calorimetry in conjunction with spectrophotometry*; Journal of Loss Prevention in the Process Industries **6** (2), 87 – 94.

SPALART, P. R.; SHUR, M.; 1997; *On the sensitization of turbulence models to rotation and curvature*; Aerospace Sci. Tech., **1** (5), 297 – 302.

SPEZIALE, C. G.; SARKAR, S.; GATSKI, T. B.; 1991; *Modelling the pressure-strain correlation of turbulence: an invariant dynamical systems approach*; J. Fluid Mechanics **277**, 245 – 272.

STEELE, C. H.; NOLAN, P. F.; LOWE, J. L.; HIRST, A.; STARKIE, A. J.; 1993; *Monitoring reaction exotherms in pilot scale batch reactors*; Journal of Loss Prevention in the Process Industries **6** (2), 115 – 124.

STEIN, W. A.; SCHMIDT, W,; 1983; *Wärmeübergang auf der Wärmeträgerseite eines Rührbehälters mit einem einfachen Mantel*; Forschung im Ingenieurwesen **59** (5), 73 – 90.

T.M. ELECTRONICS; 2004; *Data Sheet: Km03 Type 'K' General Purpose Probe*; Farnell element14; PDF document URL: http://www.farnell.com/datasheets/42675.pdf; Accessed online 23/09/2015.

VERSTEEG, H.; MALALASEKRA, W.; 2009; *An Introduction to Computational Fluid Dynamics – The Finite Volume Method – Second Edition*; Pearson.

WESTERTERP, K. R.; MOLGA, E. J.; 2006; *Safety and Runaway Prevention in Batch and Semibatch Reactors – A Review*; Chemical Engineering Research and Design **84** (7), 543 – 552.

WIKIPEDIA; *Tridiagonal matrix algorithm*; Page last modified 21/03/2011; Accessed online 13/04/2011 on http://en.wikipedia.org/wiki/Tridiagonal_matrix_algorithm
Note: this web page has since changed, but can be viewed by copying the original URL into the internet archive on http://archive.org/web/

WILCOX, D. C.; 1994; *Multiscale model for turbulent flows*; In AIAA 24th Aerospace Sciences Meeting. American Institute of Aeronautics and Astronautics.

WILCOX, D. C.; 2006; *Turbulence Modeling for CFD, 3rd Edition*; DCW Industries, Inc., La Canada CA.

WILCOX, D. C.; 2008; *Formulation of the k-omega turbulence model revisited*; AIAA Journal **46** (11), 2823 – 2838.

WOLFRAM MATHWORLD; *Law of Large Numbers*; Entries last updated 31/05/2012; Accessed online 07/06/2012 on the website:-
http://mathworld.wolfram.com/LawofLargeNumbers.html
WORLEY, N. G.; CHOJNOWESKI, B.; HARRISON, M.; POLLEY G. T.; SMITH, R. A.; WINTERTON, R. H. S.; 1985; *Boiling inside tubes: general aspects and saturated wet-wall heat transfer*; ESDU 85041. As referenced by Alane (2007).

ZLOKARNIK, M.; 1971; *Trombentiefe beim Ruhren in unbewehrten Behaltern*; Chem Ing. Tech. **43** (18), 1028 – 1030.

ZWART, P. J.; 2005; *Numerical Modelling of Free Surface and Cavitating Flows*; VKI Lecture Series, May 2005; ANSYS Canada Limited.

ZWART, P. J.; SCHEUERER, M.; BOGNER, M.; 2003; *Free Surface Flow Modelling of an Impinging Jet*; ASTAR International Workshop on Advanced Numerical Methods for Simulation of Two-Phase Flow; GRS Garching, Germany.

10 APPENDIX

10.1 DW-Therm Technical Data

Table 10.1 – Original DW-Therm data for density, heat capacity, conductivity and dynamic viscosity at temperatures ranging from -90°C to 200°C. Data provided by HUBER (2010).

T / °C	ρ / kg m^{-3}	c_P / J kg^{-1} K^{-1}	λ / W m^{-2} K^{-1} m	μ / kg m^{-1} s^{-1}
-90.0	969	1530	0.132	1.70E-01
-80.0	961	1550	0.131	8.78E-02
-70.0	952	1570	0.130	4.58E-02
-60.0	944	1600	0.128	2.44E-02
-50.0	935	1620	0.127	1.37E-02
-40.0	927	1640	0.126	8.06E-03
-30.0	918	1660	0.124	5.23E-03
-20.0	910	1680	0.123	3.82E-03
-10.0	902	1710	0.122	3.07E-03
0.0	893	1730	0.120	2.68E-03
10.0	885	1750	0.119	2.30E-03
20.0	876	1770	0.118	1.83E-03
30.0	868	1800	0.116	1.51E-03
40.0	859	1820	0.115	1.25E-03
50.0	851	1840	0.114	1.06E-03
60.0	842	1860	0.113	9.09E-04
70.0	834	1880	0.111	7.92E-04
80.0	826	1910	0.110	7.10E-04
90.0	817	1930	0.109	6.37E-04
100.0	809	1950	0.107	5.82E-04
110.0	800	1970	0.106	5.44E-04
120.0	792	2000	0.105	5.07E-04
130.0	783	2020	0.103	4.78E-04
140.0	775	2040	0.102	4.57E-04
150.0	767	2060	0.101	4.45E-04
160.0	758	2080	0.099	4.24E-04
170.0	750	2110	0.098	4.13E-04
180.0	741	2130	0.097	4.08E-04
190.0	733	2150	0.095	3.96E-04
200.0	724	2170	0.094	3.91E-04

10.2 Borosilicate Glass 3.3 Physical Properties

Table 10.2 – Borosilicate Glass 3.3 Physical Properties. Table adapted from QVF (2014).

Physical property	Temperatures / °C	Value
Mean linear thermal expansion coefficient (β)	20 to 300	$(3.3 \pm 0.1) \times 10^{-6}$ K^{-1}
Mean thermal conductivity (λ)	20 to 200	1.2 W m^{-1} K^{-1}
Mean specific heat capacity ($\tilde{c}_P$)	20 to 100	800 J kg^{-1} K^{-1}
Mean specific heat capacity ($\tilde{c}_P$)	20 to 200	900 J kg^{-1} K^{-1}
Density (ρ)	20	2230 kg m^{-3}

10.3 ICEM Mesh creation (for the jacket-only mesh)

The images in this section have been colour-inverted to conserve printing ink. That is, while the original curves were in green, red and blue, the curves in these images are rendered magenta, cyan and yellow respectively.

Using the 'Workbench Readers' option in ICEM, the geometry from ANSYS Design Modeller was imported. This is displayed in figure 10.1. The 'model' curves here are rendered magenta. The large gap in this image is because there were no vertical curves along the walls of the jacket.

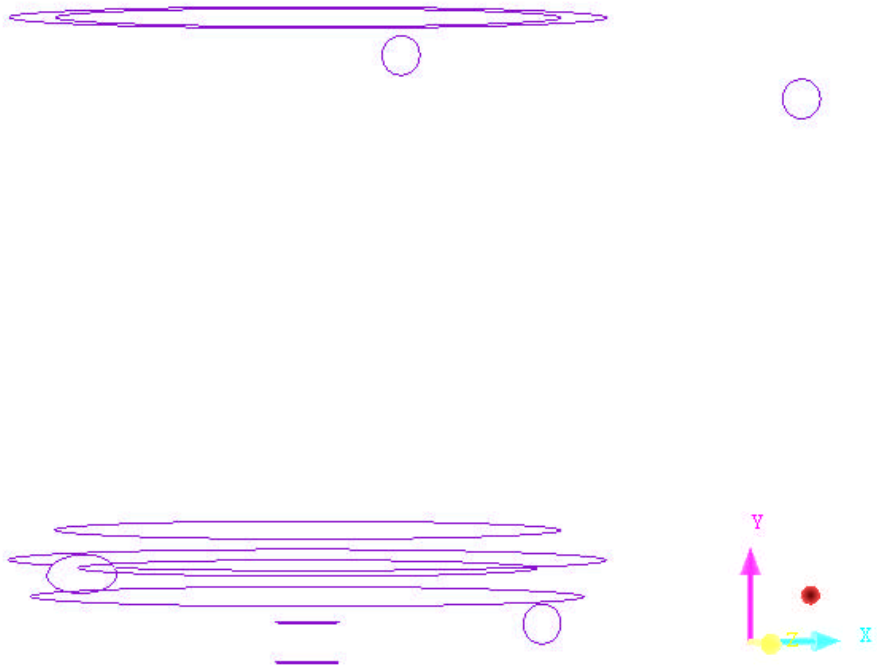

Figure 10.1 – Curves of the imported geometry.

Four attempts (or "strategies") were made to attempt to "block" the geometry. "Blocking" in this context means to divide the mesh into sub-sections (called "blocks") within which mesh elements can conform to the shape in a more well-defined way. Previous attempts were based on simpler geometries in which not every curve and point needs to be associated with a particular block. These attempts proved more difficult in later stages of meshing. The fourth strategy was to resort to creating all the individual curves and points that would all be associated to every block in the geometry.

A basic plan was made for which the blocks would be able to conform to. Each block is a hexahedral shape which is modified to conform to a part of the geometry, so curves must be added to the geometry in such a way as to separate it into hexahedron-like sections that connect perfectly to each other (that is, one face connecting to one face, in the internal structure).

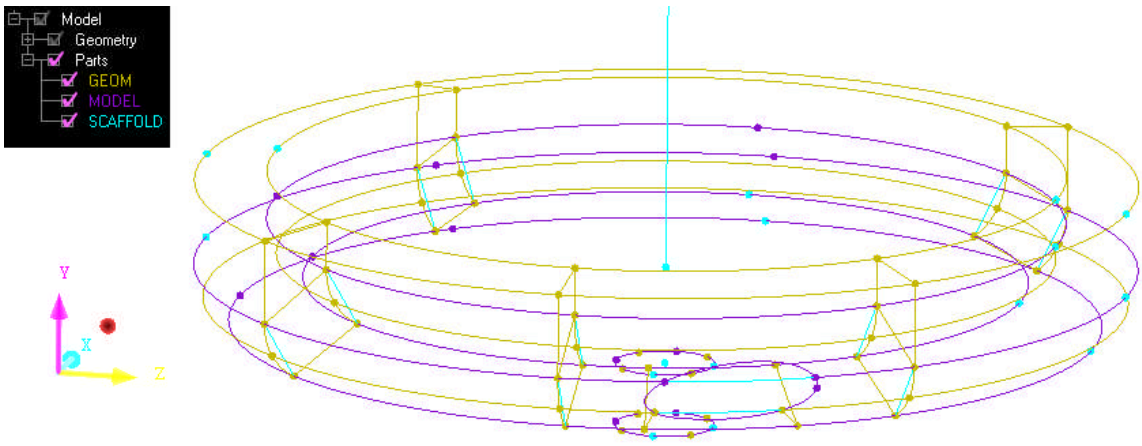

Figure 10.2 – Initial construction of extra curves required for blocking in the fourth strategy.

Initially, “scaffold” curves and vertices (rendered here in cyan) were created along the model curves to help to construct further ‘geometry’ curves (rendered here in yellow). The “scaffold” curves were straight, while the “geometry” curves were mapped to the surface of the model.

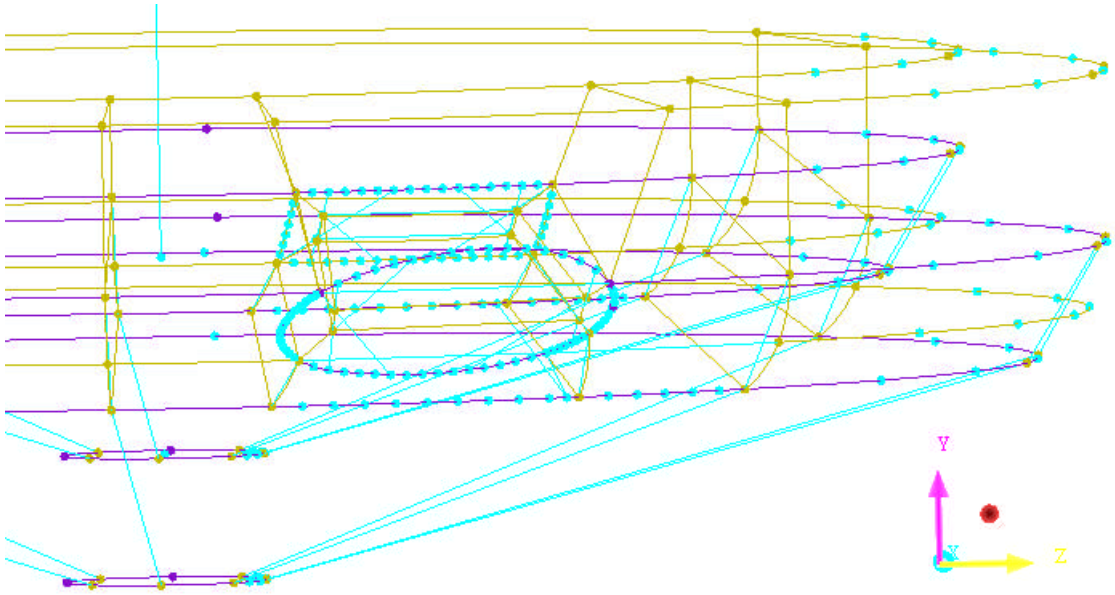

Figure 10.3 – Probing for points along the curves and connecting where each block is desired.

Figure 10.2 displays some of these curves at the bottom of the model and figure 10.3 displays further detail added, such as lines at the base and points around the inlet pipe connection to the jacket. Many points were generated so that it would be easier to probe for appropriate locations to create an o-grid around the inlet part without too much distortion in the block shapes. Figure 10.4 displays initial points at the top of the reactor. The cyan points here will be connected vertically to form the shapes of blocks on the top, including a smaller block where the outlet pipe will be.

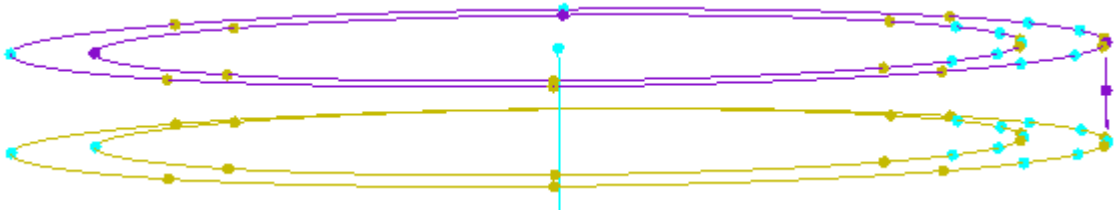

Figure 10.4 – Preparation for blocking the top pipe and top section of the jacket.

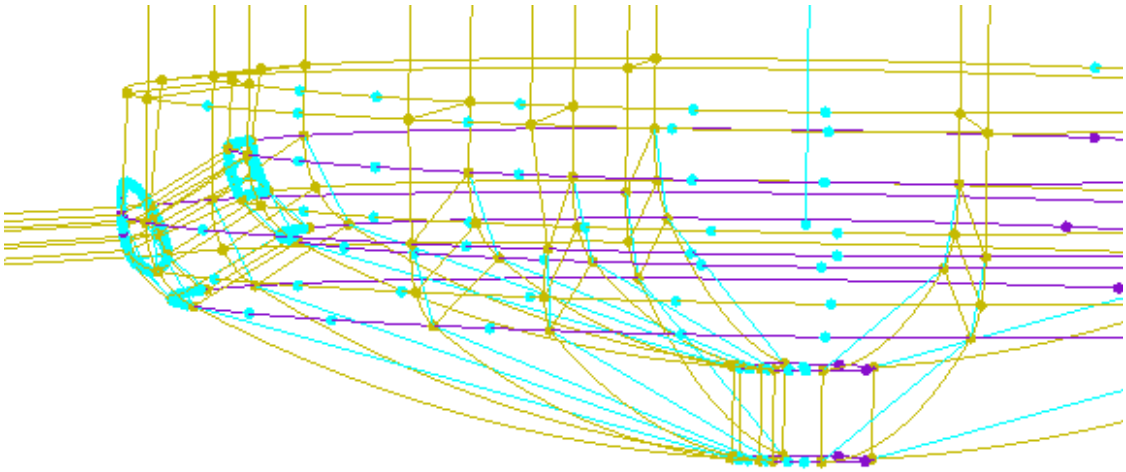

Figure 10.5 – Constructing all curves required for the blocking strategy (bottom view).

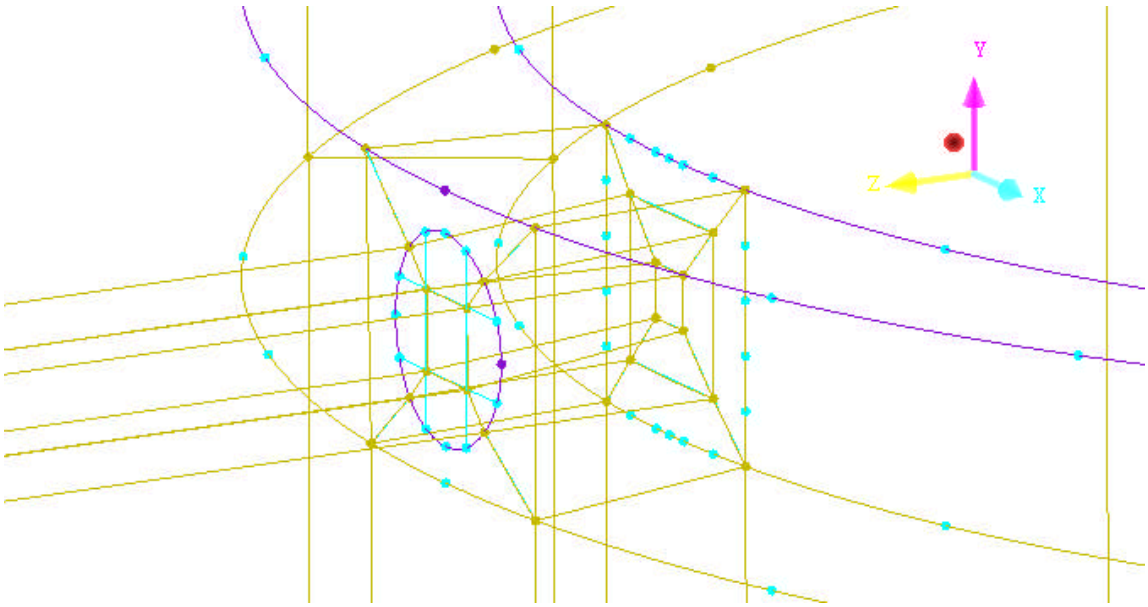

Figure 10.6 – Constructing all curves required for the blocking strategy (top view).

The “scaffold” (cyan) curves were then projected onto the surface of the model to form the “geometry” (yellow) curves. Details of this are displayed in figures 10.5 (bottom of the reactor) and 10.6 (top of the reactor). Notice in these figures how the yellow curves conform to the surface of the model, for example (in figure 10.5) the spherical part of the

base of the reactor, compared to the straight cyan curves. In figure 10.6 the shape of the o-grid running through the jacket to the outlet pipe is clearly visible as a series of concentric squares with connected corners.

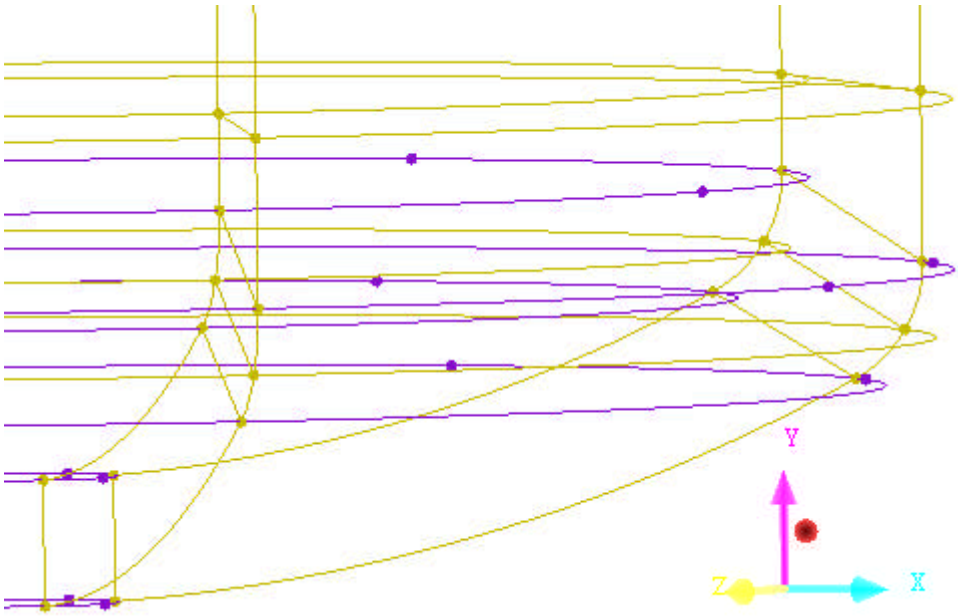

Figure 10.7 – Deselecting the “scaffold” curves.

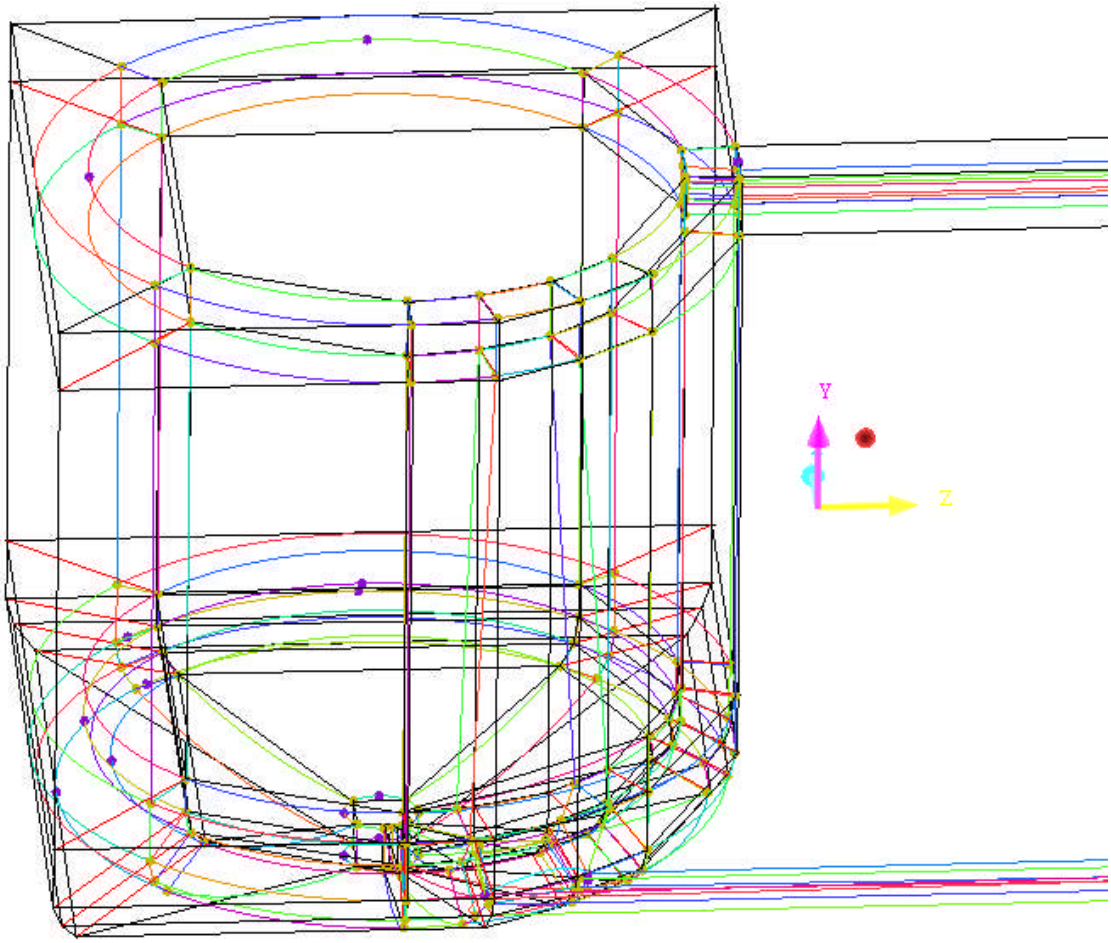

Figure 10.8 – Blocks in the ICEM jacket mesh, excluding the inlet pipe.

Once the “geometry” (yellow) curves were all created, the “scaffold” (cyan) curves could be deselected, revealing the geometry ready for blocking. This is displayed in figure 10.7.

Once the geometry was ready, the ‘create block’ option was selected and a large block was created to encompass the entire geometry. This was then split according to the block-like structure of the “geometry” (yellow) curves. The result is displayed in figure 10.8. However, due to the complexity of the structure, it was difficult to cut out an inlet pipe.

In ICEM, the central block structure is automatically surrounded by 26 hidden blocks (forming a 3-by-3-by-3 cube altogether). This extraneous structure is automatically labelled ‘VORFN’ by the program. From this ‘VORFN’ part, the extra block required for the inlet pipe could be selected and added to the blocks from the main geometry, thus un-hiding it. The result of this is displayed in figure 10.9. The vertices in this block were then adjusted to conform to the inlet pipe.

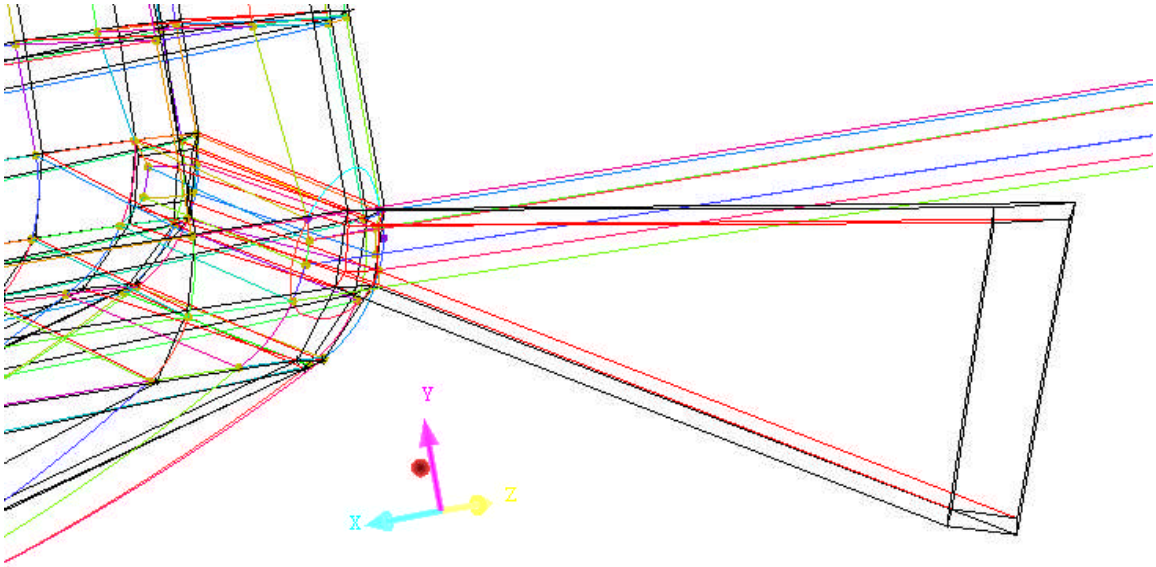

Figure 10.9 – The ‘VORFN’ block for the inlet pipe, added to the regular blocks.

For added clarity, figure 10.10 displays the final structure including the ‘VORFN’ blocks, which are rendered here in red. Notice that ICEM automatically splits the blocks in the ‘VORFN’ part when the regular geometry blocks are split. The somewhat chaotic structure in the middle of the figure is the result of the block splitting which was done for the inlet pipe without going through to the other side of the vessel. The advantage is that the main jacket blocking need not be more complicated than it already is. The disadvantage is that this would make it extremely difficult to model the interior vessel (process side) in the same mesh.

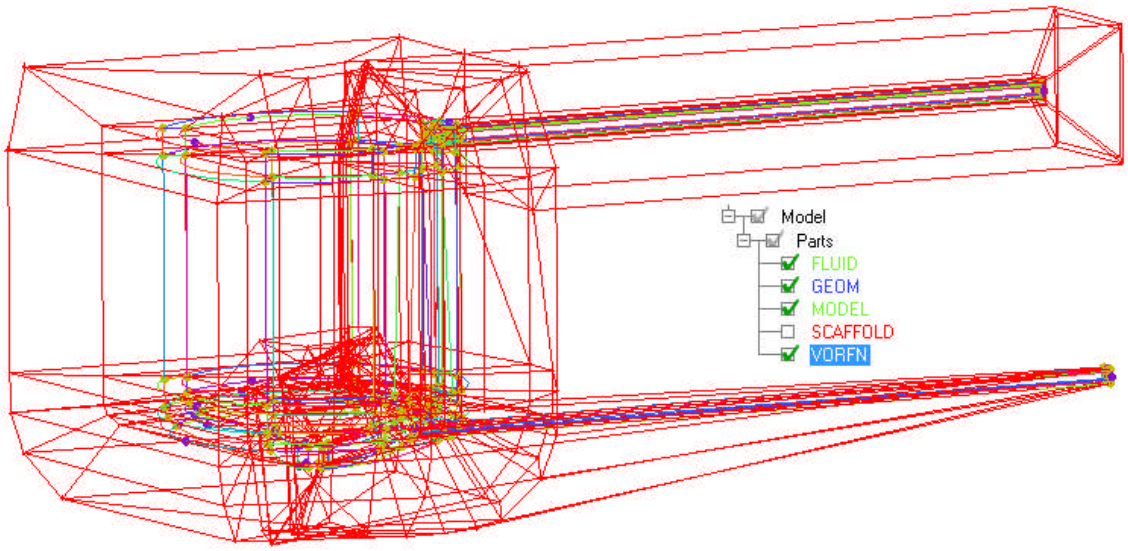

Figure 10.10 – The revealed ‘VORFN’ blocks in ICEM (rendered in red).

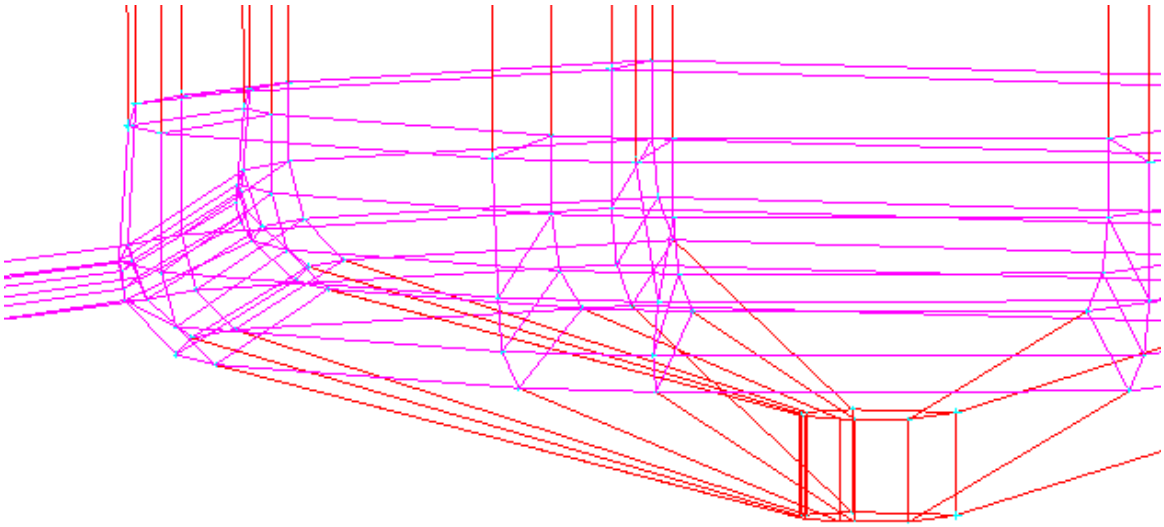

Figure 10.11 – Association process in progress.

Each vertex and edge of each block was then associated to a point and curve in the geometry and model. Figure 10.11 depicts this process under way. ICEM uses green (rendered magenta here due to the use of inverted colours to conserve printer ink) to indicate associated block edges and red (rendered cyan here) to indicate associated block vertices. Cyan edges (rendered red here) are used to indicate non-associated block edges.

Figure 10.12 displays the completed association for the whole structure. This is the shape of the connected blocks that will be part of the mesh.

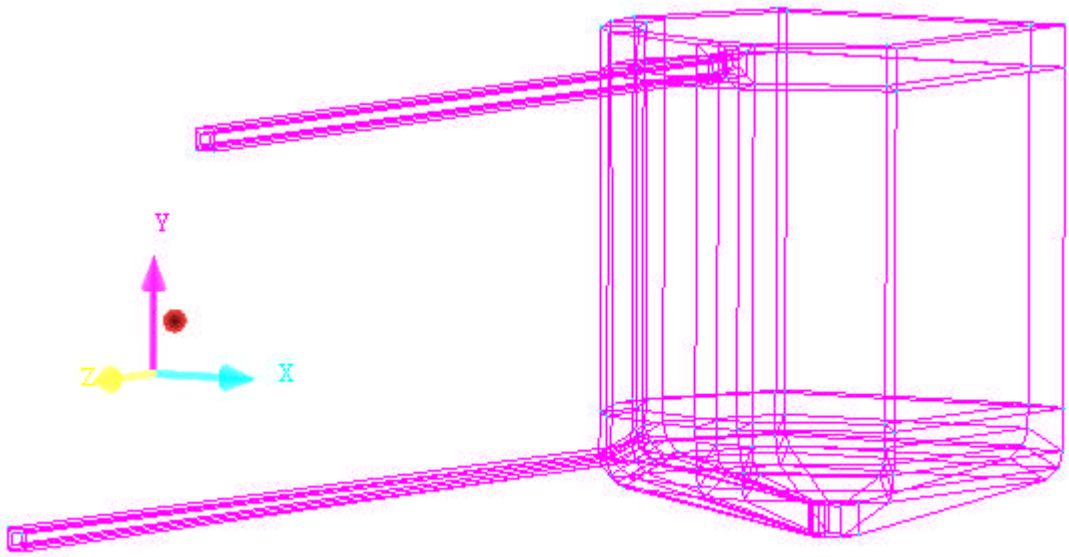

Figure 10.12 – Completed association of edges to curves and vertices to points.

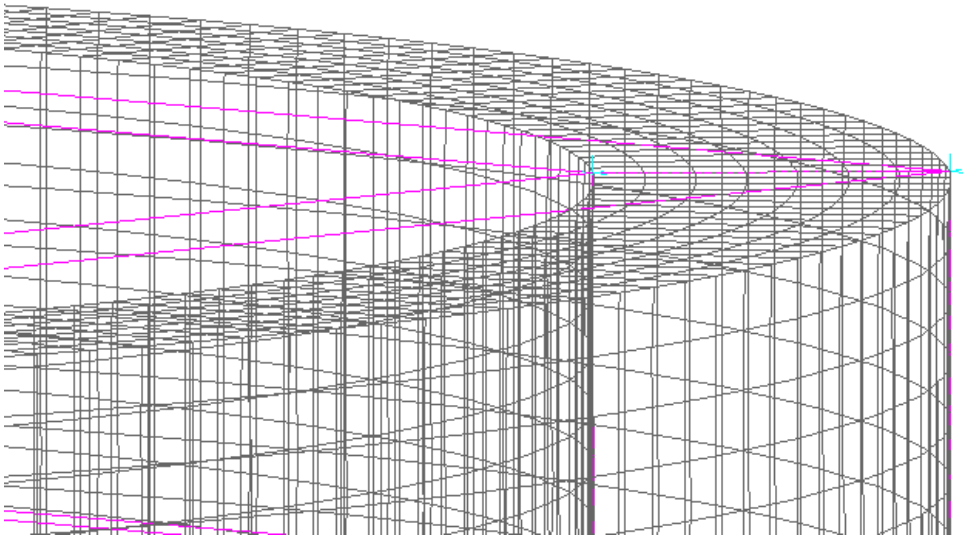

Figure 10.13 – Global element size set for the pre-mesh.

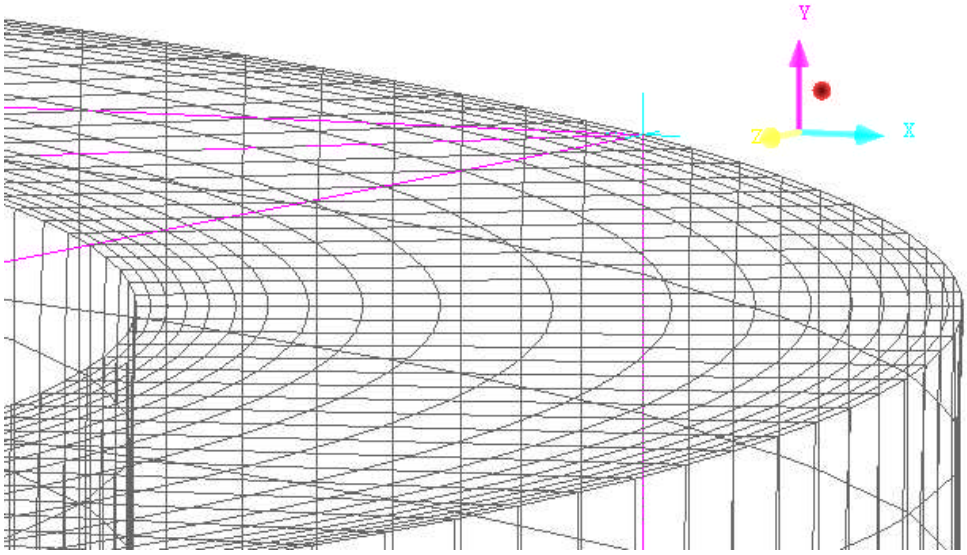

Figure 10.14 – Local refinement of the pre-mesh.

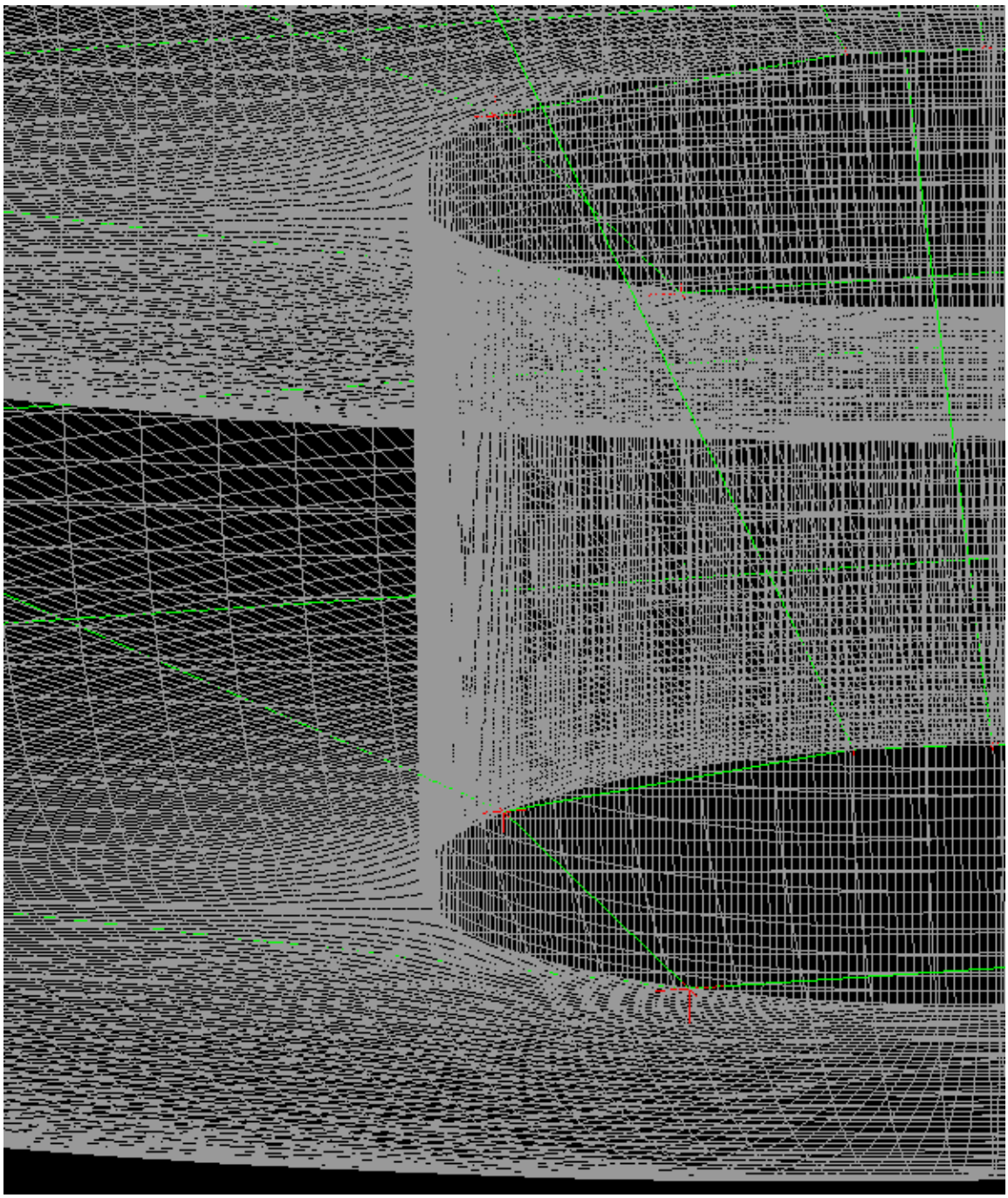

Figure 10.15 – A close-up of the coarse mesh at the bottom, without inverted colours (zooming out would render individual cells invisible).

The global element size was then set to 0.005 metres. Figure 10.13 depicts a close-up view of the top of the mesh at the back of the reactor when the pre-mesh is active. At this stage, the block edges all conformed to the geometry curves, but the block faces conformed to the geometry surfaces, which were not curved. This is the stage at which the cross section of the majority of the mesh structure becomes ‘polygonal’, causing the vertical distortions visible in the results in chapters 5 and 7. This problem arose with the original geometry but was only discovered at this stage and would necessitate complete re-meshing just to attempt to see if it could be rectified. It was found that neither

associating nor disassociating the faces helps, because associated faces are forced to conform to the polygonal cross section and disassociated faces cause problems with the meshing program).

Local refinement of the edges of the mesh involved making the cells at the wall smaller than the bulk. This had to be done using a manual ‘graph’ function, where a curve is drawn using manual inflection points on a graph of cell length vs. normalised edge length, and took several attempts to get to desired settings without causing problems. The result is displayed in figure 10.14. The local refinement parameters were copied to all parallel edges.

Figure 10.15 displays close-up detail of the final mesh, without inverted colours. The view is of the detail of the bottom of the jacket.

10.4 Mass, Momentum and Energy Balances

Table 10.3 – Domain imbalances for the jacket-only mesh.

Experiment		Domain Imbalance (%)				
Process Fluid	**Huber Set Point / °C**	**U-Mom**	**V-Mom**	**W-Mom**	**P-Mass**	**H-Energy**
Methanol	80	0.0000	0.0000	0.0000	0.0000	-0.0184
	85	0.0000	0.0000	0.0000	0.0000	-0.0151
	90	0.0000	0.0000	0.0000	0.0000	0.0588
	95	0.0000	0.0000	0.0000	0.0000	0.0005
	100	0.0000	0.0000	0.0000	0.0000	0.0110
Water	130	0.0000	0.0000	0.0000	0.0000	0.0418
	135	0.0000	0.0001	0.0000	0.0000	0.0844
	140	0.0000	0.0001	0.0000	0.0000	0.1315
	145	0.0000	0.0000	0.0000	0.0000	0.0722
	150	0.0000	0.0000	0.0000	0.0000	0.0341

Table 10.4 – Normalised imbalance summary for the jacket-only mesh using the Curvature Corrected SST model for boiling methanol in the process side, Huber set point 90°C. This type of summary is not available in the '.out' file for the normal SST model.

Normalised Imbalance Summary		
Equation	Maximum Flow	Imbalance (%)
U-Mom	4.6980E+01	0.0000
V-Mom	4.6980E+01	0.0000
W-Mom	4.6980E+01	0.0000
P-Mass	2.5690E-01	0.0000
H-Energy	3.5836E+04	-0.0652

Table 10.5 – Normalised imbalance summary for the jacket-only mesh using the BSL Reynolds Stress model for boiling water in the process side, Huber set point 135°C.

Normalised Imbalance Summary		
Equation	Maximum Flow	Imbalance (%)
U-Mom	4.4726E+01	0.0000
V-Mom	4.4726E+01	0.0000
W-Mom	4.4726E+01	0.0000
P-Mass	2.5330E-01	0.0000
H-Energy	5.2901E+04	-0.0133

Table 10.6 – Normalised imbalance summary for the steady state semi-conjugate simulation.

Normalised Imbalance Summary		
Equation	Maximum Flow	Imbalance (%)
U-Mom-Bulk-Impeller	2.0412E+02	0.0000
V-Mom-Bulk-Impeller	2.0412E+02	0.0000
W-Mom-Bulk-Impeller	2.0412E+02	0.0000
Mass-Water-Impeller	1.8082E+00	-0.0006
Mass-Air-Impeller	1.8082E+00	0.0000
U-Mom-Bulk-Tank	2.0412E+02	0.0000
V-Mom-Bulk-Tank	2.0412E+02	0.0000
W-Mom-Bulk-Tank	2.0412E+02	0.0000
Mass-Water-Tank	1.8082E+00	0.0006
Mass-Air-Tank	1.8082E+00	0.0000
H-Energy-Water-Impel	9.6844E+04	0.0704
H-Energy-Air-Impelle	9.6844E+04	0.0000
H-Energy-Water-Tank	9.6844E+04	1.4591
H-Energy-Air-Tank	9.6844E+04	0.0002
T-Energy-Wall	9.6844E+04	0.0000

Table 10.7 – Normalised imbalance summary for the transient semi-conjugate simulation.

Normalised Imbalance Summary		
Equation	Maximum Flow	Imbalance (%)
U-Mom-Bulk-Impeller	2.0367E+02	0.0002
V-Mom-Bulk-Impeller	2.0367E+02	-0.0003
W-Mom-Bulk-Impeller	2.0367E+02	0.0000
Mass-Water-Impeller	1.8166E+00	0.1242
Mass-Air-Impeller	1.8166E+00	-0.0001
U-Mom-Bulk-Tank	2.0367E+02	0.0030
V-Mom-Bulk-Tank	2.0367E+02	0.0003
W-Mom-Bulk-Tank	2.0367E+02	-0.0105
Mass-Water-Tank	1.8166E+00	-0.4651
Mass-Air-Tank	1.8166E+00	0.0006
H-Energy-Water-Impel	9.8744E+04	0.0693
H-Energy-Air-Impelle	9.8744E+04	0.0000
H-Energy-Water-Tank	9.8744E+04	1.4264
H-Energy-Air-Tank	9.8744E+04	0.0008
T-Energy-Wall	9.8744E+04	0.0001

Table 10.8 – Normalised imbalance summary for the steady state conjugate simulation.

Normalised Imbalance Summary		
Equation	Maximum Flow	Imbalance (%)
U-Mom-Bulk-Impeller	2.0356E+02	-0.0008
V-Mom-Bulk-Impeller	2.0356E+02	0.0007
W-Mom-Bulk-Impeller	2.0356E+02	0.0018
Mass-Water-Impeller	1.9135E+00	-0.0267
Mass-Air-Impeller	1.9135E+00	0.0000
U-Mom-Bulk-Tank	2.0356E+02	0.0009
V-Mom-Bulk-Tank	2.0356E+02	-0.0004
W-Mom-Bulk-Tank	2.0356E+02	-0.0009
Mass-Water-Tank	1.9135E+00	0.0264
Mass-Air-Tank	1.9135E+00	0.0000
U-Mom-Jacket	5.2341E+01	-0.0008
V-Mom-Jacket	5.2341E+01	-0.0002
W-Mom-Jacket	5.2341E+01	0.0004
P-Mass-Jacket	2.7610E-01	-0.0002
H-Energy-Water-Impel	4.6464E+04	0.1623
H-Energy-Air-Impelle	4.6464E+04	0.0000
H-Energy-Water-Tank	4.6464E+04	3.4460
H-Energy-Air-Tank	4.6464E+04	0.0013
T-Energy-Wall	4.6464E+04	-0.0001
H-Energy-Jacket	4.6464E+04	-1.6329

10.5 Graphs of Residuals and Monitor Points for Main Simulations

10.5.1 Methanol Batch Distillation Experiment

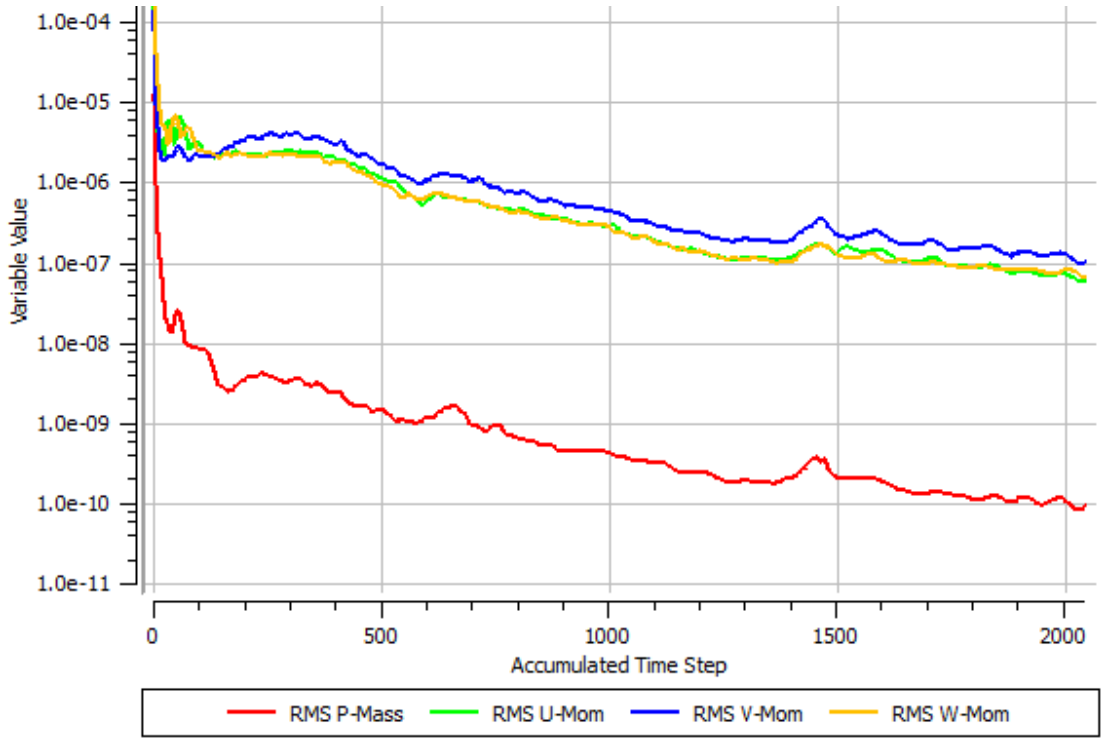

Figure 10.16 – Mass and momentum residuals for the curvature corrected SST model in the jacket for the methanol batch distillation experiment when the Huber set point temperature is 90°C.

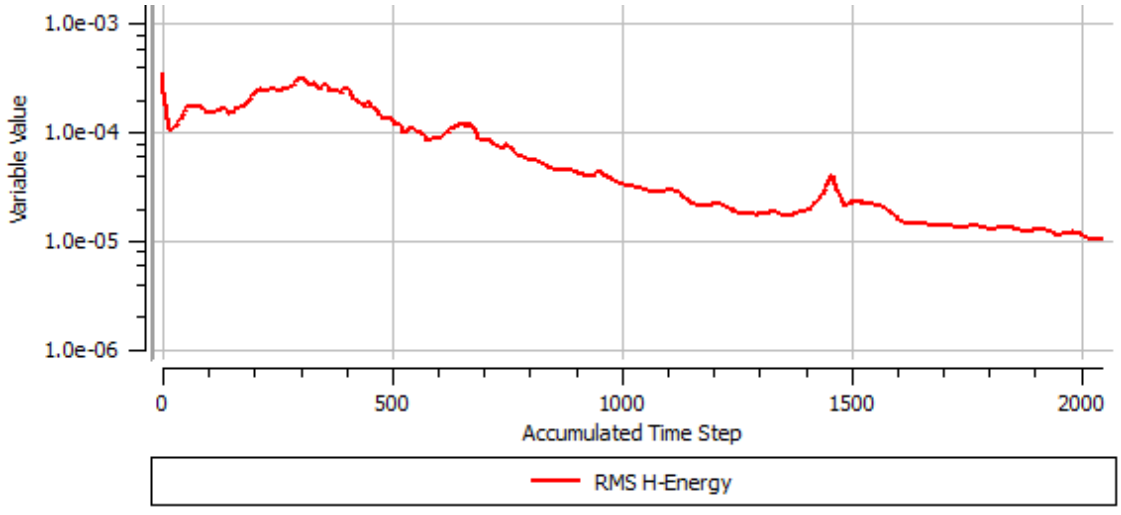

Figure 10.17 – Heat transfer residuals for the curvature corrected SST model in the jacket for the methanol batch distillation experiment when the Huber set point temperature is 90°C.

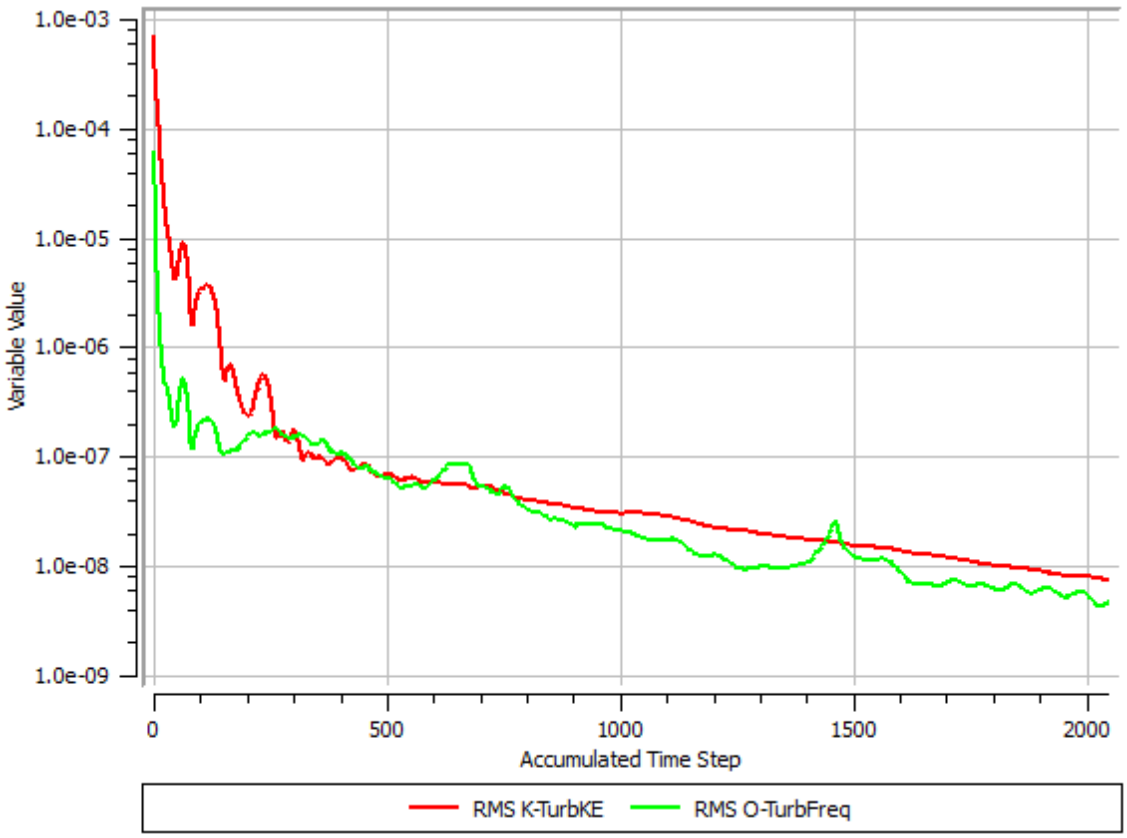

Figure 10.18 – ***k*** and ***ω*** residuals for the curvature corrected SST model in the jacket for the methanol batch distillation experiment when the Huber set point temperature is 90°C.

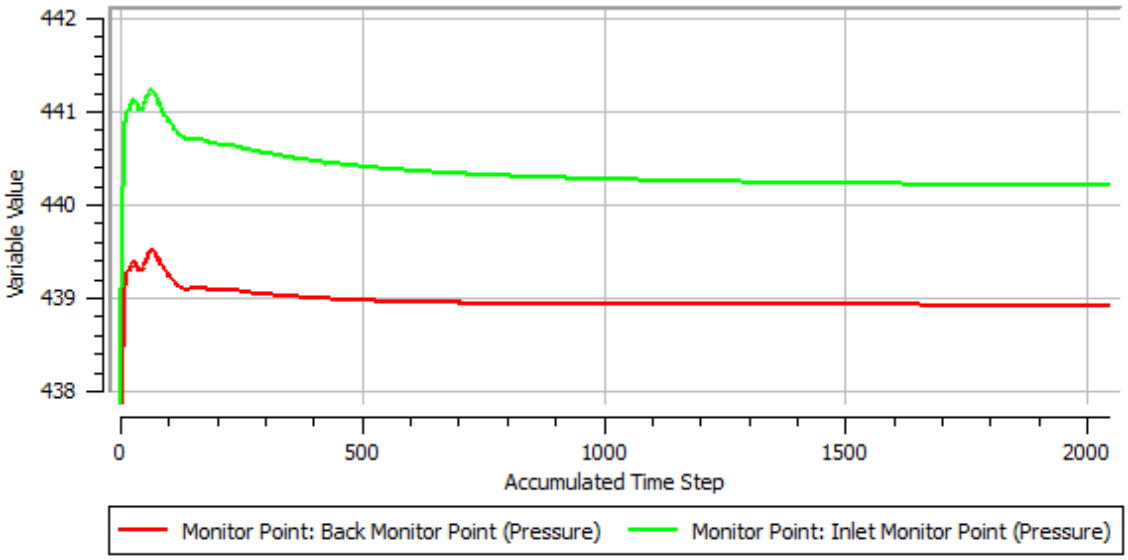

Figure 10.19 – Monitor points for the curvature corrected SST model in the jacket for the methanol batch distillation experiment when the Huber set point temperature is 90°C.

10.5.2 Water Batch Distillation Experiment

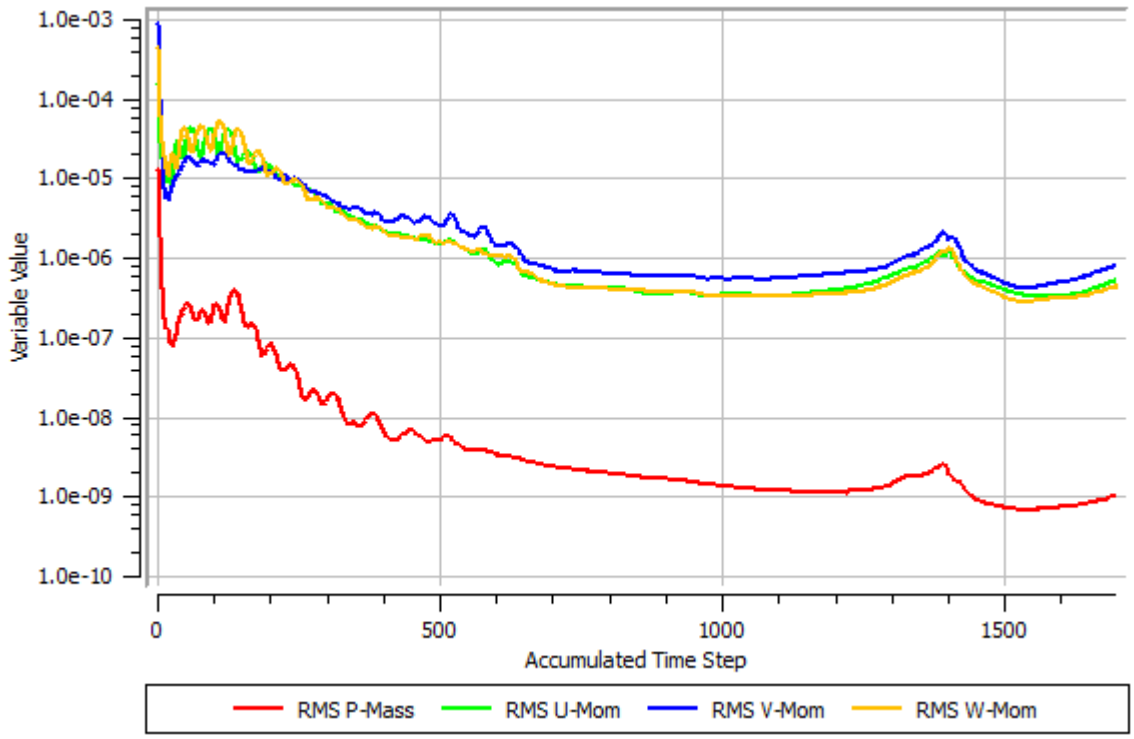

Figure 10.20 – Mass and momentum residuals for the curvature corrected SST model in the jacket for the water batch distillation experiment when the Huber set point temperature is 135°C.

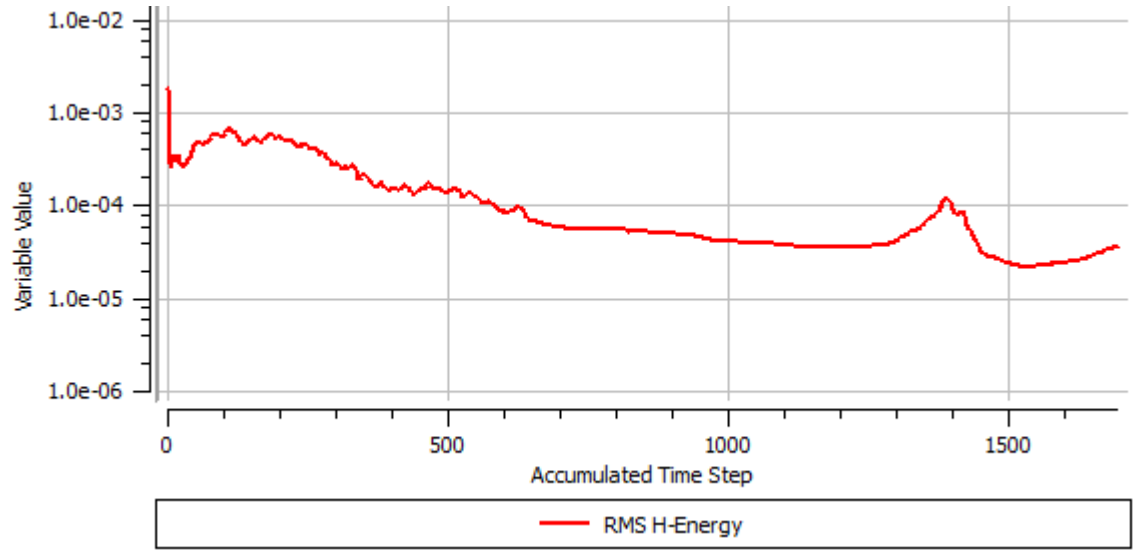

Figure 10.21 – Heat transfer residuals for the curvature corrected SST model in the jacket for the water batch distillation experiment when the Huber set point temperature is 135°C.

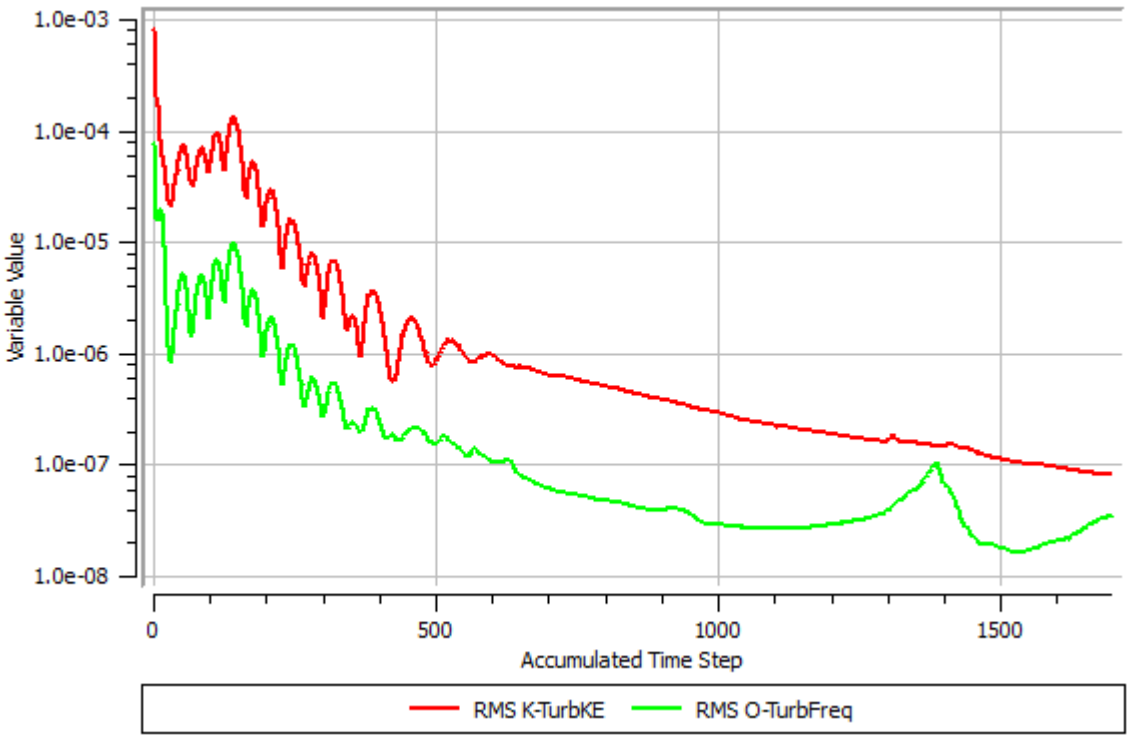

Figure 10.22 – ***k*** and ***ω*** residuals for the curvature corrected SST model in the jacket for the water batch distillation experiment when the Huber set point temperature is 135°C.

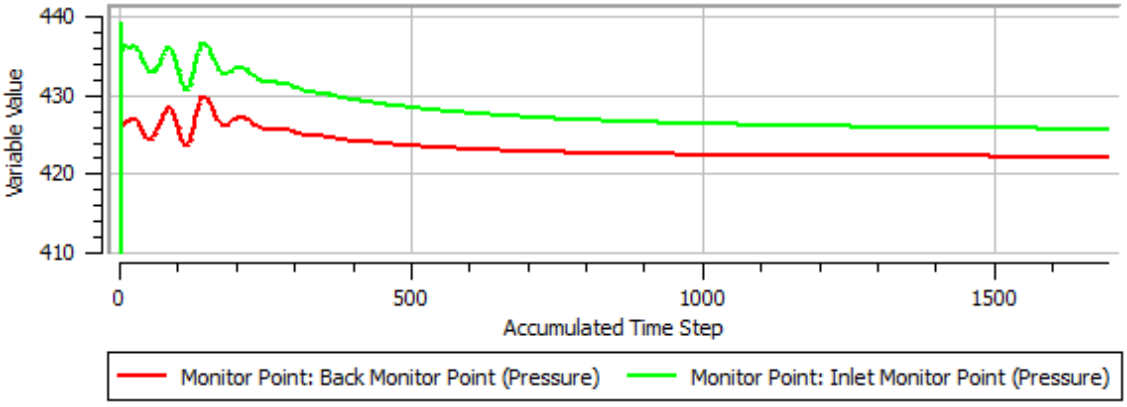

Figure 10.23 – Monitor points for the curvature corrected SST model in the jacket for the water batch distillation experiment when the Huber set point temperature is 135°C.

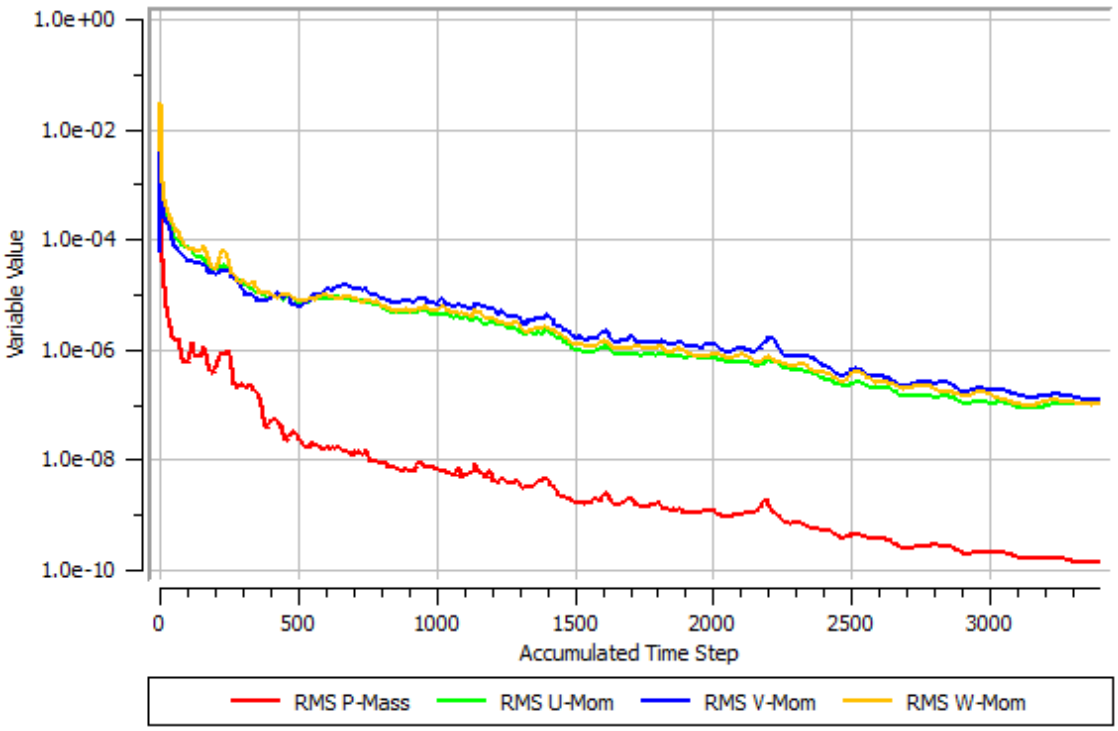

Figure 10.24 – Mass and momentum residuals for the BSL Reynolds Stress model in the jacket for the water batch distillation experiment when the Huber set point temperature is 135°C.

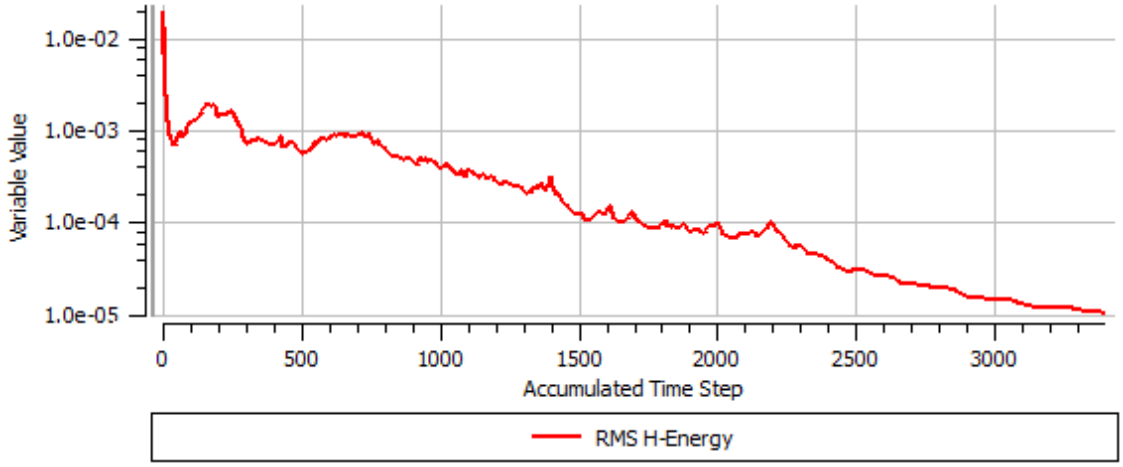

Figure 10.25 – Heat transfer residuals for the BSL Reynolds Stress model in the jacket for the water batch distillation experiment when the Huber set point temperature is 135°C.

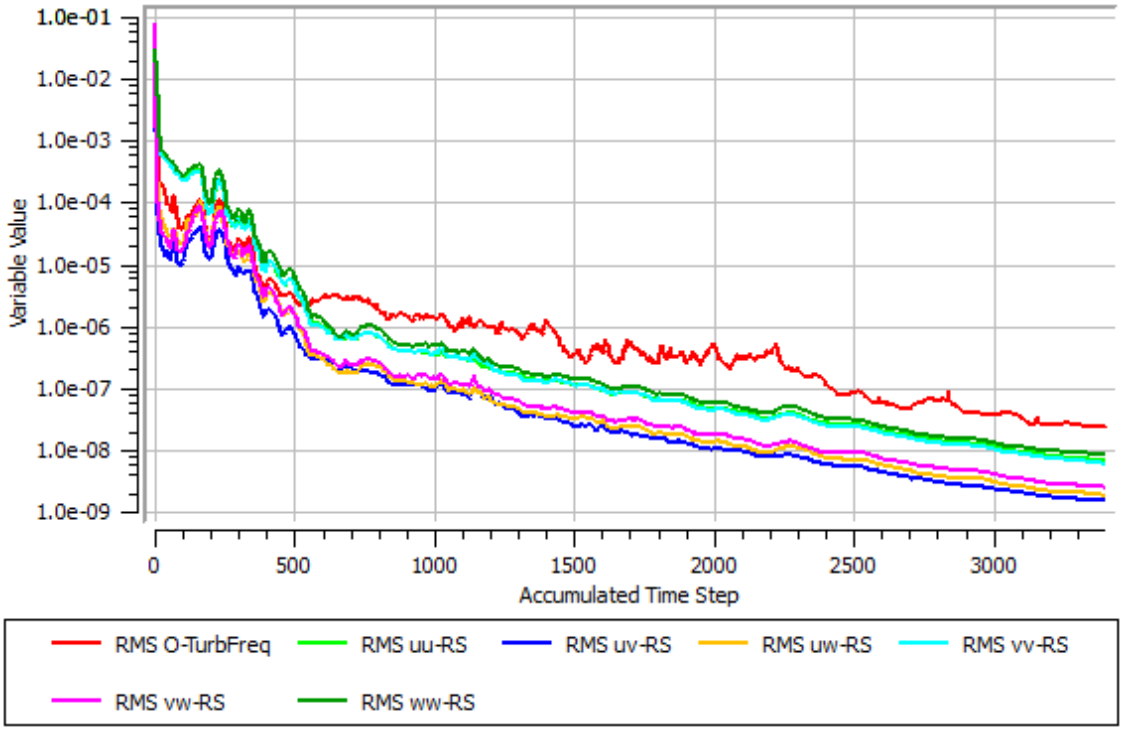

Figure 10.26 – Reynolds Stress residuals for the BSL Reynolds Stress model in the jacket for the water batch distillation experiment when the Huber set point temperature is 135°C.

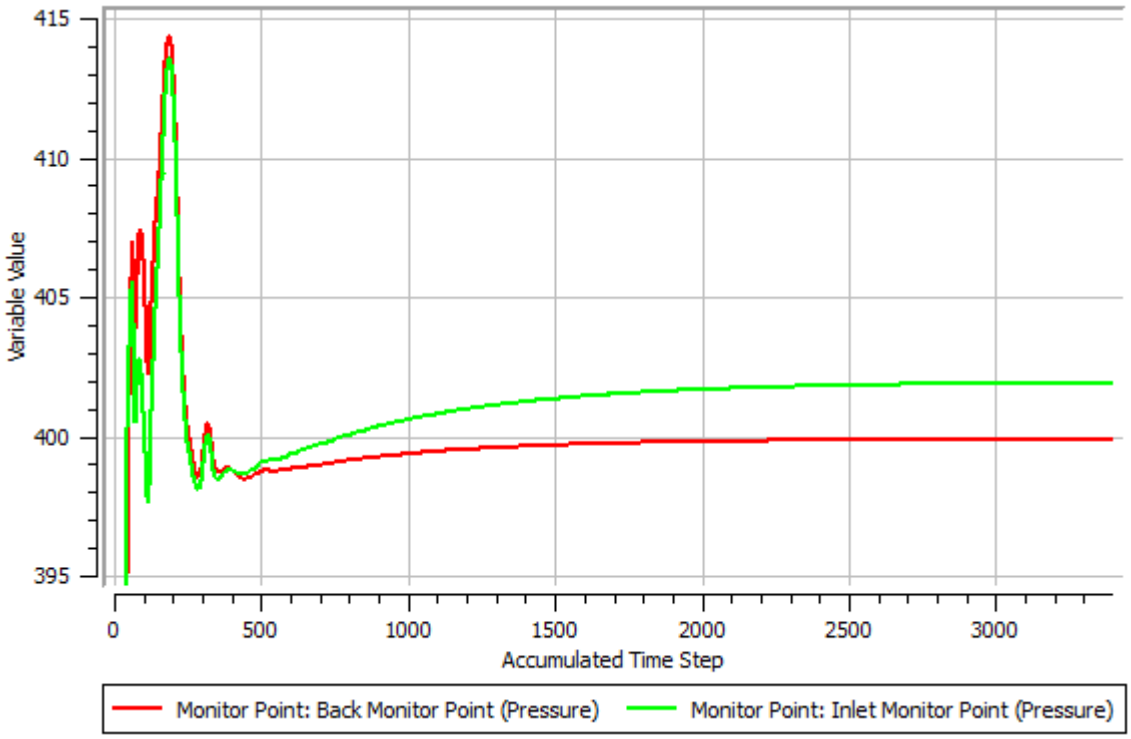

Figure 10.27 – Monitor points for the BSL Reynolds Stress model in the jacket for the water batch distillation experiment when the Huber set point temperature is 135°C.

10.5.3 Steady State Semi-Conjugate Model

The settings and results for this simulation are displayed in section 6.2.6.

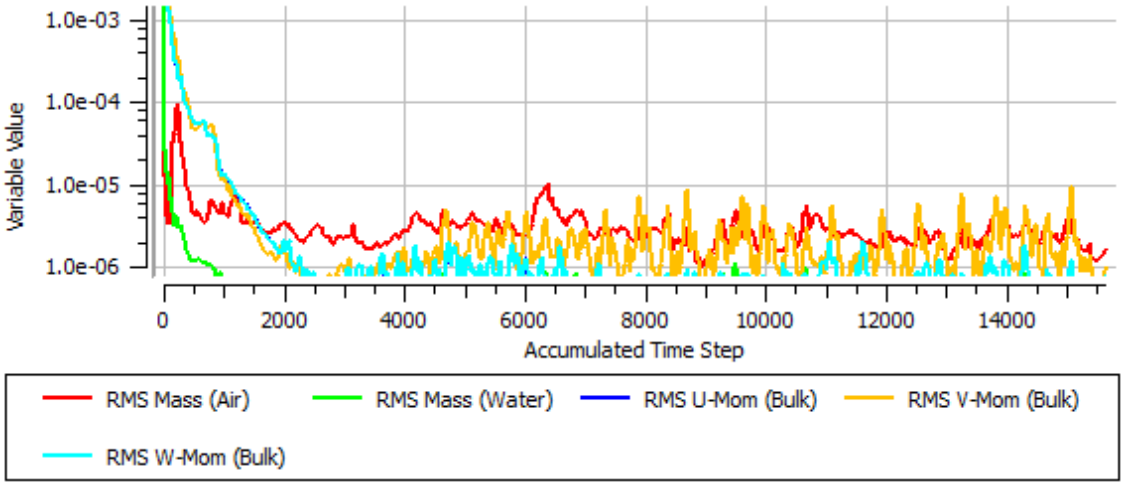

Figure 10.28 – Mass and momentum residuals for the steady state semi-conjugate model.

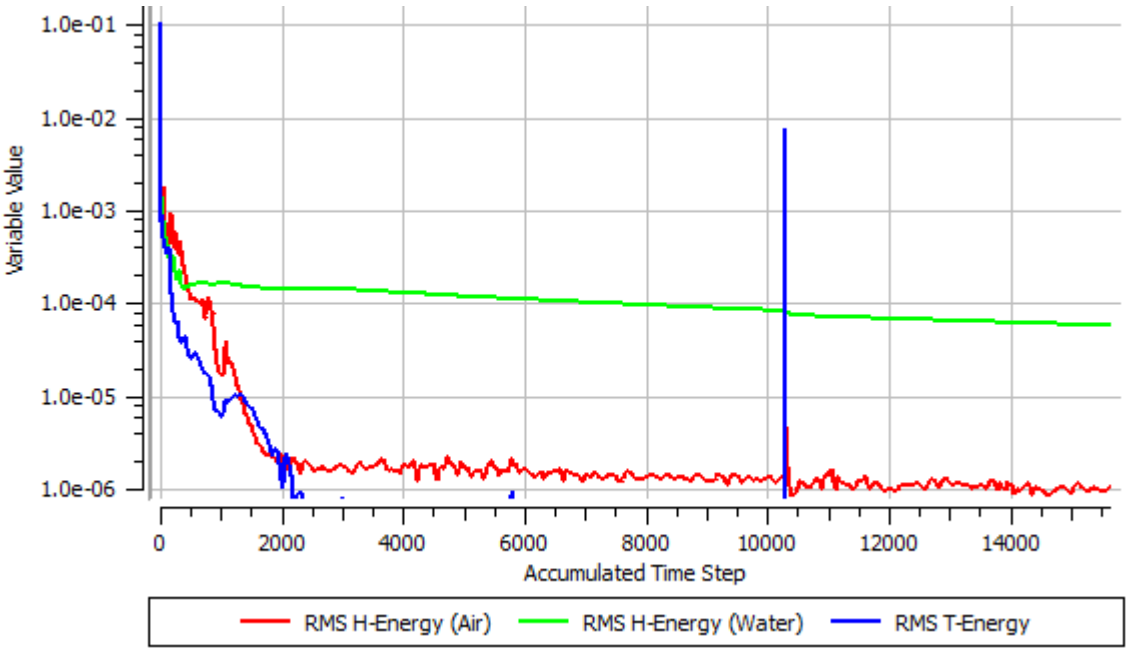

Figure 10.29 – Heat transfer residuals for the steady state semi-conjugate model.

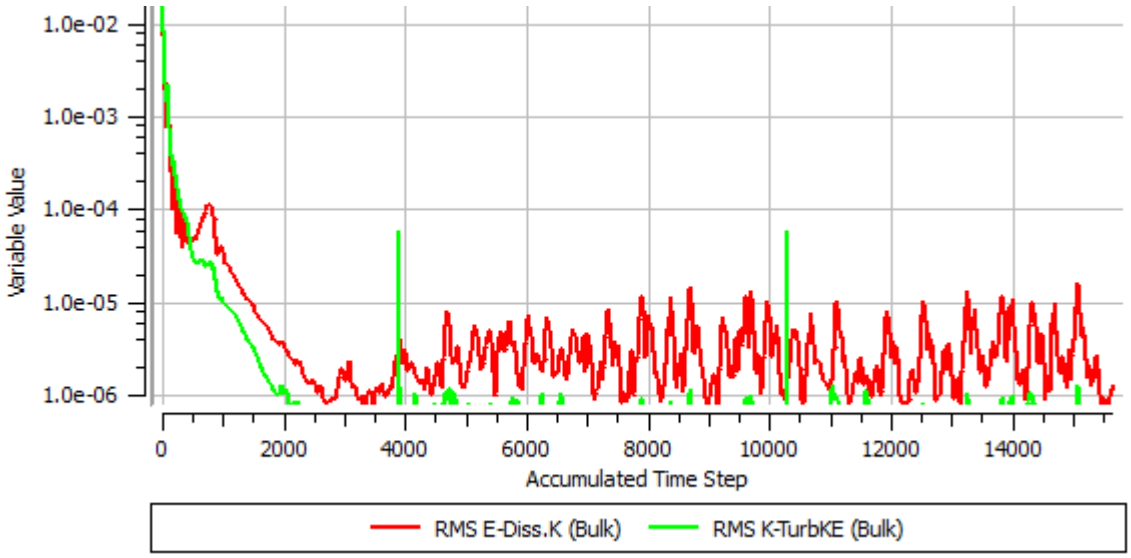

Figure 10.30 – ***k*** and ***ε*** residuals for the steady state semi-conjugate model.

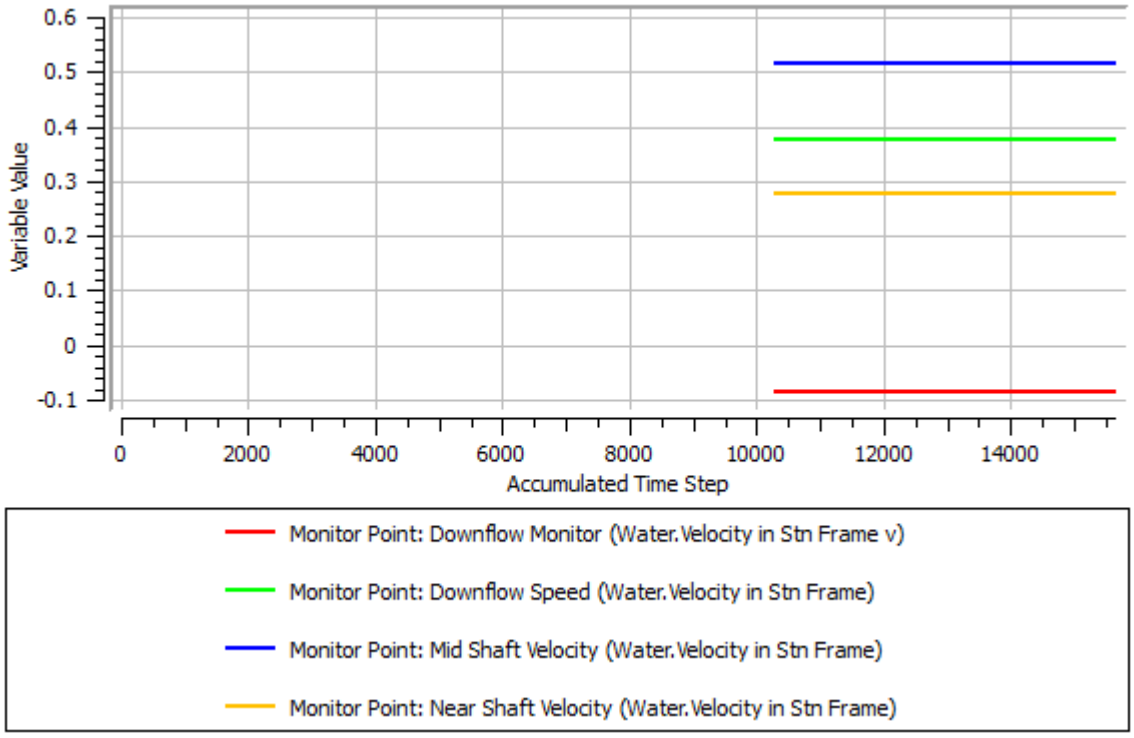

Figure 10.31 – Monitor points for the steady state semi-conjugate model.

10.5.4 Transient Semi-Conjugate Model

The settings and results for this simulation are displayed in section 6.2.7.

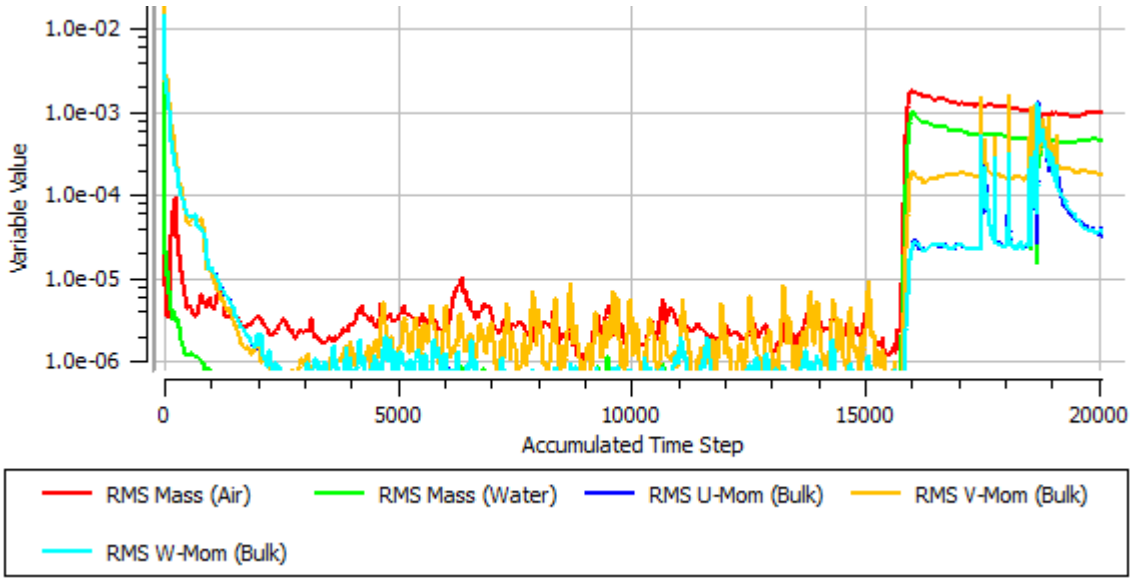

Figure 10.32 – Mass and momentum residuals for the transient semi-conjugate model.

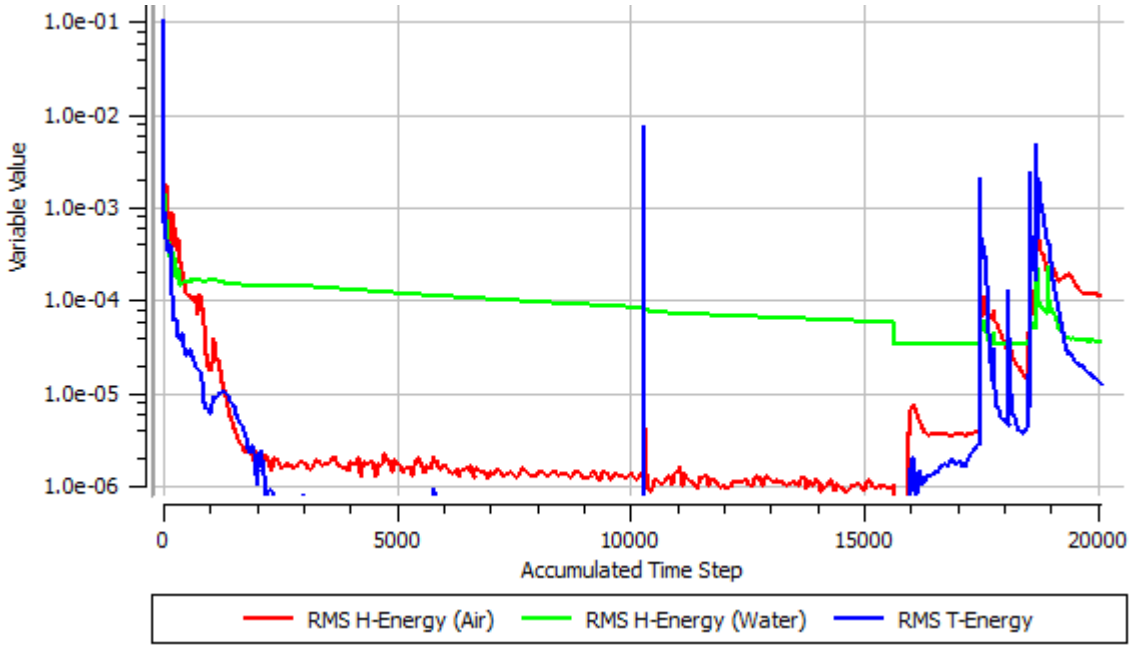

Figure 10.33 – Heat transfer residuals for the transient semi-conjugate model.

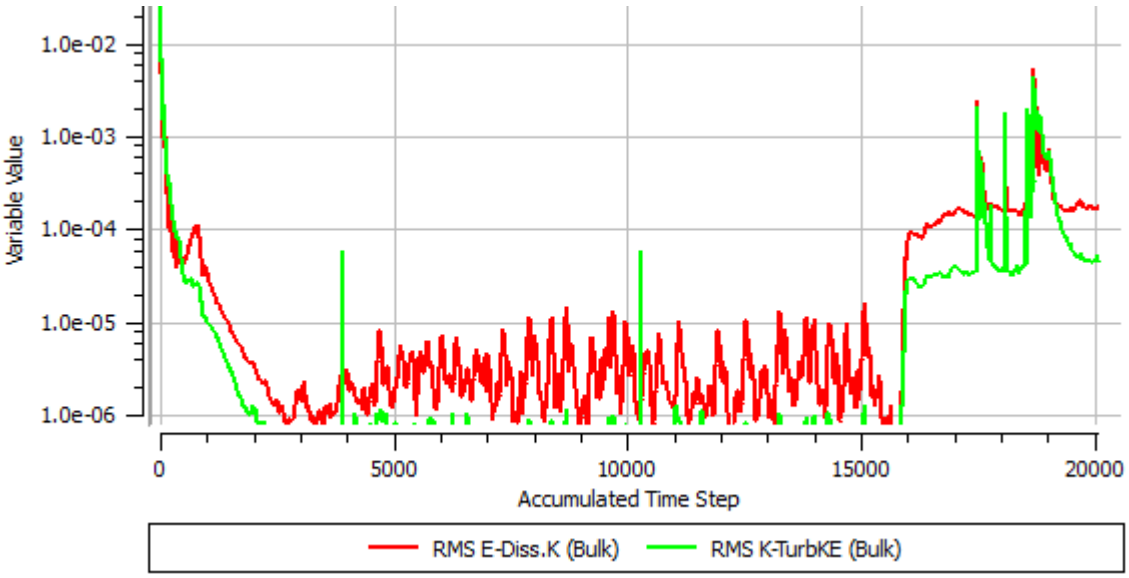

Figure 10.34 – ***k*** and ***ε*** residuals for the transient semi-conjugate model.

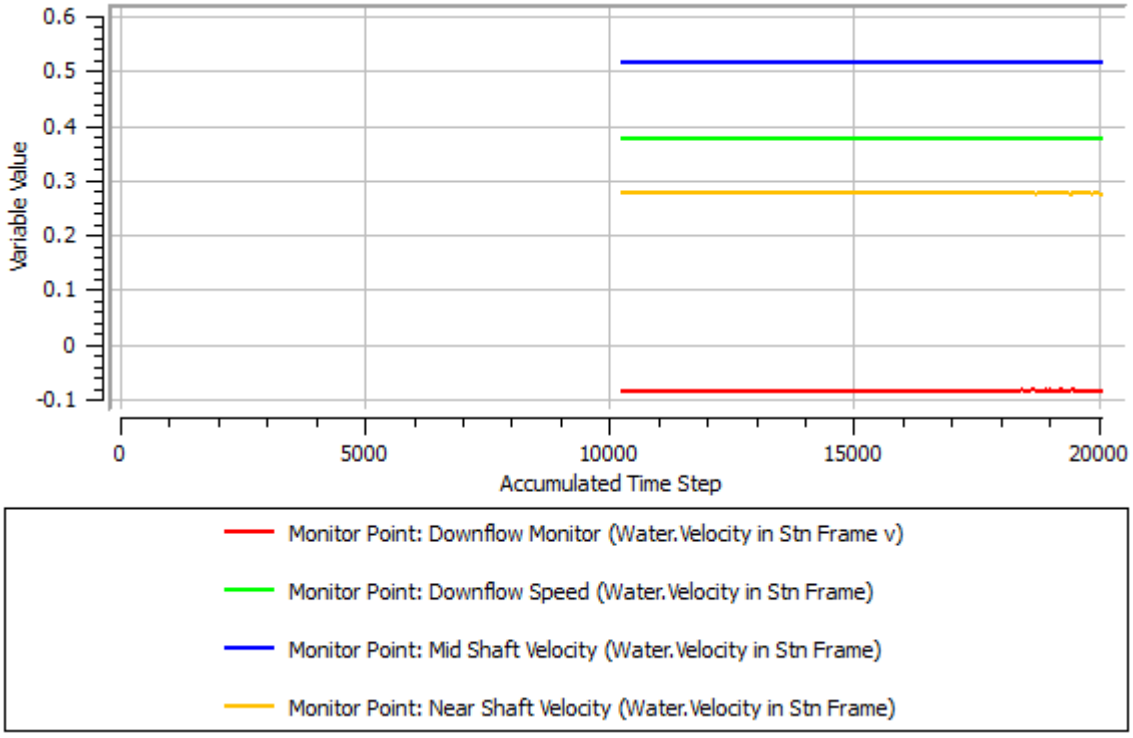

Figure 10.35– Monitor points for the transient semi-conjugate model.

10.5.5 Steady State Conjugate Model

The settings and results for this simulation are displayed in section 7.1.2.

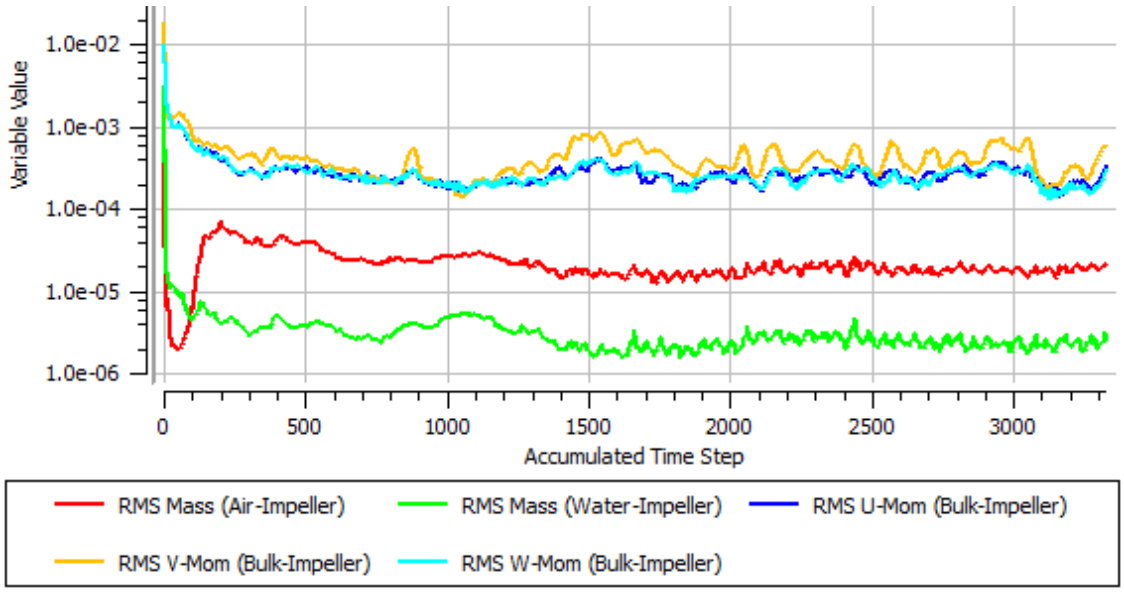

Figure 10.36 – Process mass and momentum residuals for the steady state conjugate model.

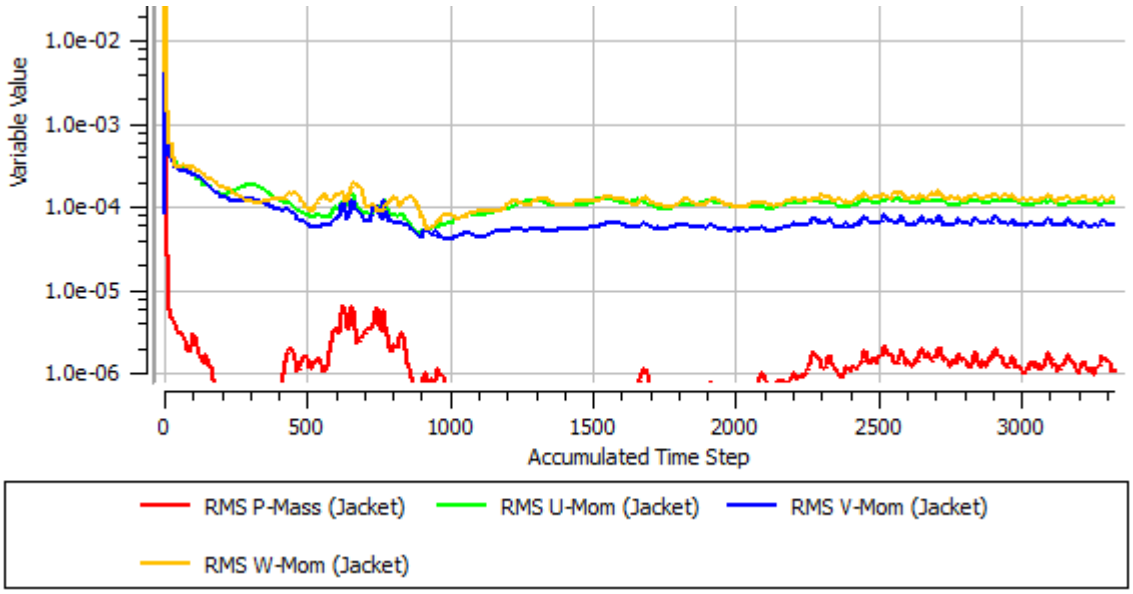

Figure 10.37 – Jacket mass and momentum residuals for the steady state conjugate model.

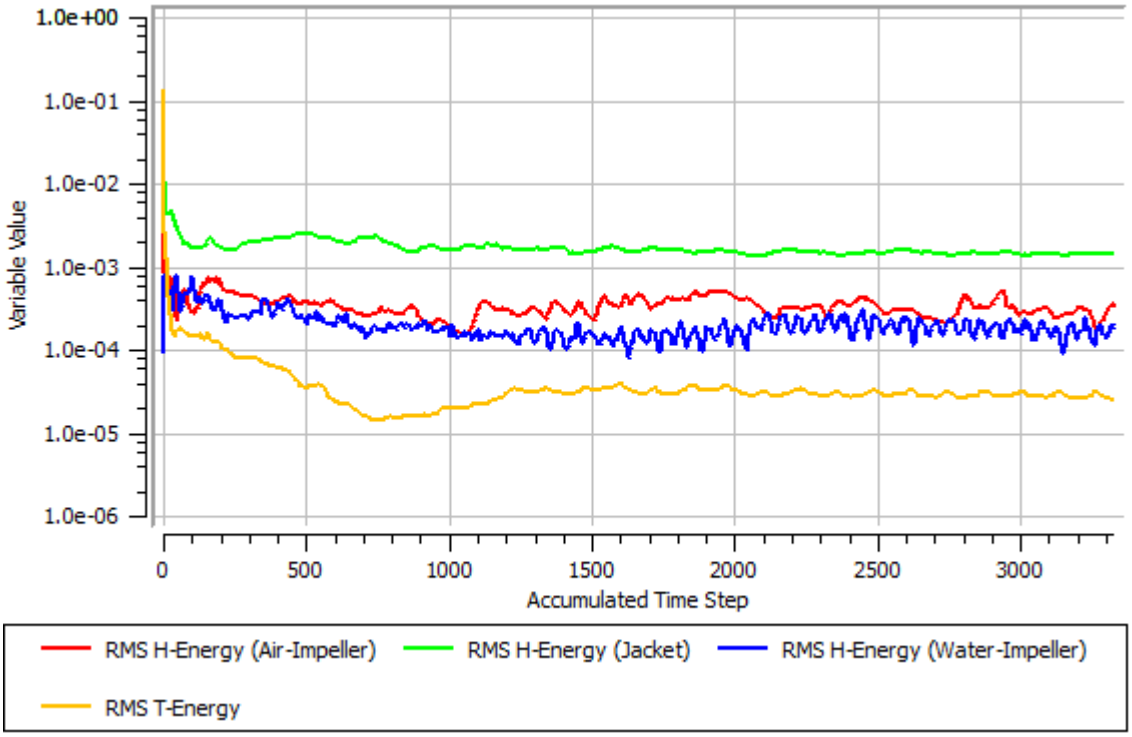

Figure 10.38 – Heat transfer residuals for the steady state conjugate model.

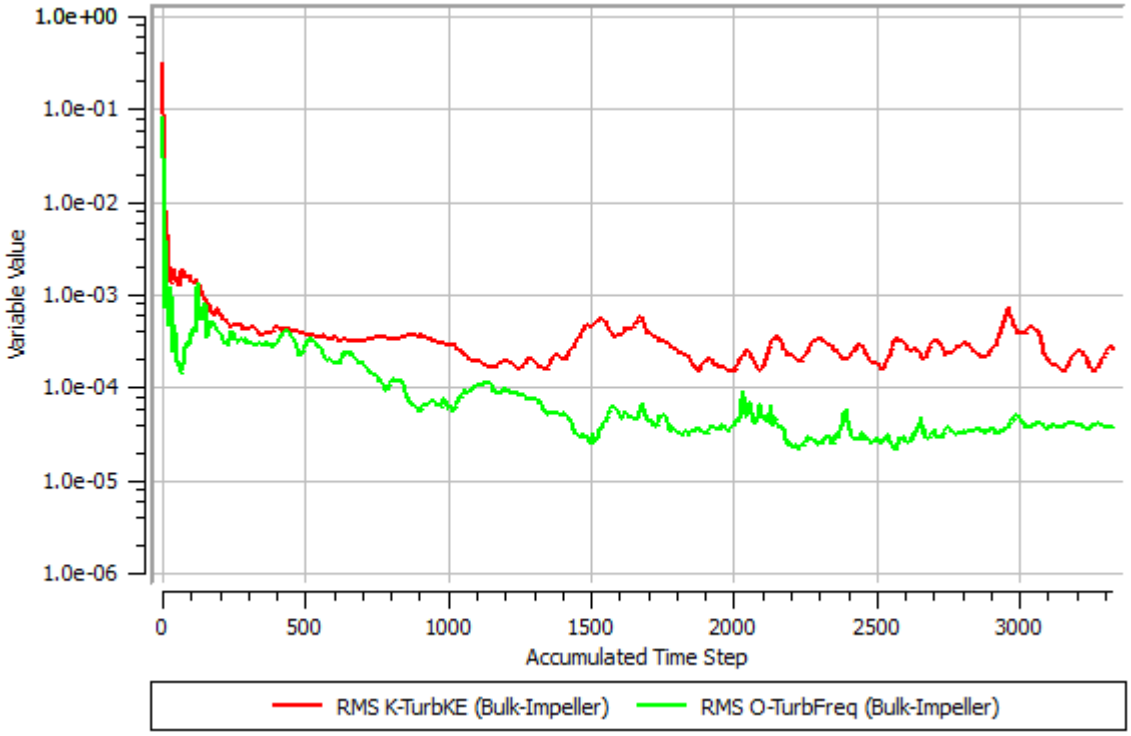

Figure 10.39 – Process ***k*** and ***ω*** residuals for the steady state conjugate model.

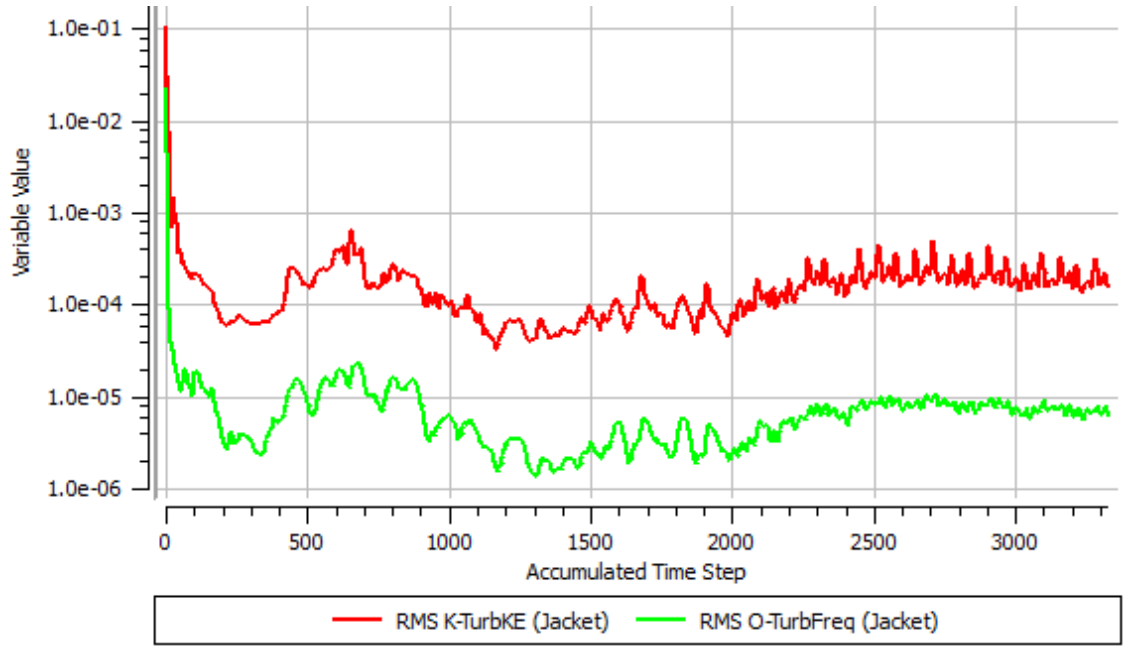

Figure 10.40 – Jacket ***k*** and ***ω*** residuals for the steady state conjugate model.

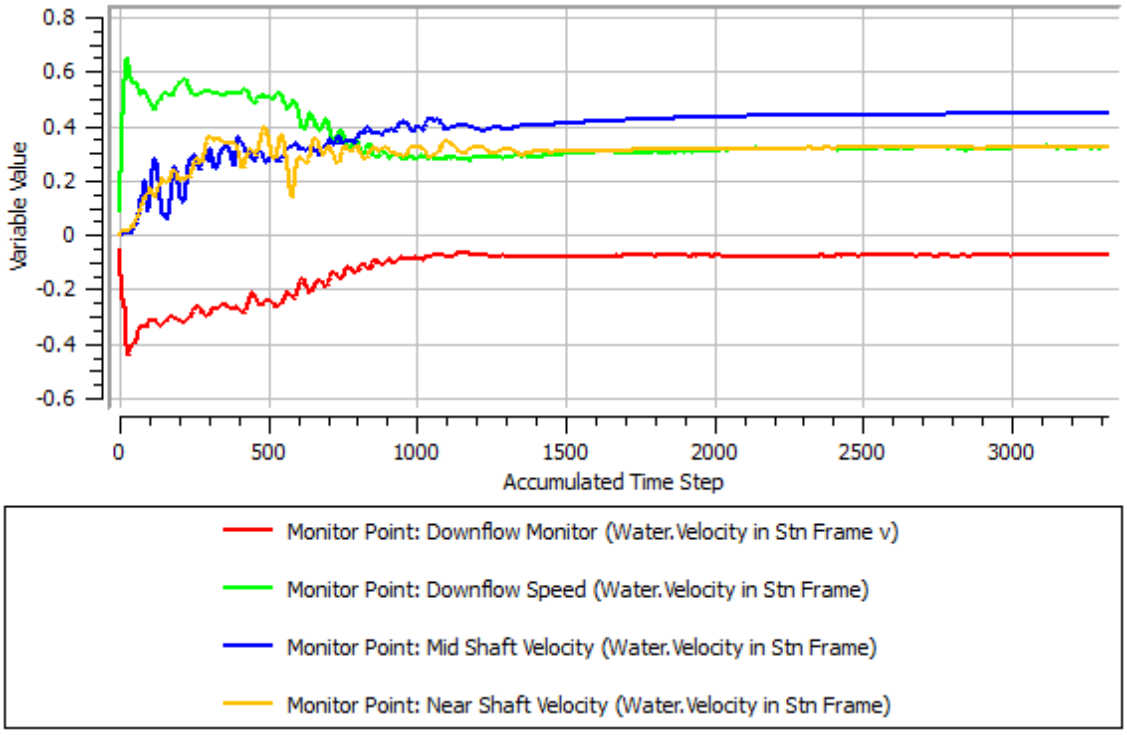

Figure 10.41 – Monitor points for the steady state conjugate model.

10.6 Detail of the Distributed Parameter Model

10.6.1 Numerical Solution

As derived in section 4.5.1, the equations to solve numerically are:-

$$\left.\frac{\partial T_w}{\partial t'}\right|_z = K_w\left(\left.\frac{\partial^2 T_w}{\partial r^2}\right|_z + \frac{1}{r}\left.\frac{\partial T_w}{\partial r}\right|_z\right) \tag{10.1}$$

where:-

$$K_w = \lambda_w/(\rho c_P)_w \tag{10.2}$$

In the jacket:-

$$\left.\frac{\partial T_m}{\partial z}\right|_{t'} = -K_m\left(T_m - T_w|_{r=r_o}\right) \tag{10.3}$$

where:-

$$K_m = \alpha_o A_o'/\left(\dot{M}c_P\right)_m \tag{10.4}$$

In the vessel:-

$$\frac{\mathrm{d}T_p}{\mathrm{d}t'} = K_p\left(\tilde{T}_w\big|_{r=r_i} - T_p\right) \tag{10.5}$$

where:-

$$K_p = \alpha_i A_i/(Mc_P)_p \text{ and } \tilde{T}_w\big|_{r=r_i} \text{is the average inner wall temperature.} \tag{10.6}$$

The temperature dependence on dimensional variables is as follows:-

$$T_w = \mathrm{fn}(r,t,z), \qquad T_m = \mathrm{fn}(t,z), \qquad T_p = \mathrm{fn}(t) \tag{10.7}$$

When $t < 0$:-

$$T_w = \mathrm{fn}(r,z), \qquad T_m = \mathrm{fn}(z), \qquad 0 \le z \le Z, \qquad r_i \le r \le r_o, \qquad T_p = T_{p1} \tag{10.8}$$

Boundary conditions are:-

$$\text{at } r = r_i, \qquad -\lambda_w\frac{\partial T_w}{\partial r} = \alpha_i\left(T_p - T_w\right) \tag{10.9}$$

$$\text{at } r = r_o, \qquad -\lambda_w \frac{\partial T_w}{\partial r} = \alpha_o (T_w - T_m) \tag{10.10}$$

$$\text{and at } z = 0, \qquad T_m = T_{m1} \tag{10.11}$$

These first have to be discretised. Let the time interval $0 \leq t \leq N$ be split into intervals of equal time Δt. Let $t_{(\mathrm{n})}$ equal nΔt where n is an integer ranging from 0 to N. Therefore $t_{(N)}$ is the time at which the simulation is chosen to be ended, for example when steady state is approximated.

Similarly, let the distance interval $r_i \leq r \leq r_o$ be split into intervals of equal length Δr where $r_{(\mathrm{i})}$ equals iΔr and i is an integer from 0 to W. Note the use of brackets to differentiate between these different subscripts. The boundary values of r are therefore:-

$$r_{(0)} = r_i \text{ and } r_{(W)} = r_o = r_i + W\Delta r \tag{10.12}$$

Also, let the height interval $0 \leq z \leq Z$ be split into equal intervals Δz where $z_{(\mathrm{j})}$ equals jΔz and z is an integer from 0 to Z. The boundary values of z are therefore:-

$$z_{(0)} = 0 \text{ and } z_{(Z)} = Z\Delta z = z_j \tag{10.13}$$

Note that in equation (10.13), z_j (using an italic subscript) is the full height of the jacket, while $z_{(\mathrm{j})}$ (using a bracketed, non-italic subscript) denotes a particular jacket height.

There are two options for solution – the explicit method and the fully implicit backward method.

The explicit method is first-order accurate. It is useful for very small time steps, although this severely restricts the size of the distance steps and the result becomes unstable if larger distance or time steps are used. Instability in the solution, if it occurs, should be obvious – for example with rapidly oscillating or diverging values, indicating that either the steps must be shortened or an implicit method should be used.

The fully implicit backward method is unconditionally stable, that is, the values will not diverge. It can therefore be used at larger time or distance steps to reduce computing time. However, at small enough time steps, this is less accurate than the explicit method. Approximating the differential terms with numerical equivalents, using the central difference method for the wall profiles and forward difference for the change in process fluid temperature with time:-

$$\frac{T_{w(\mathrm{n+1,i,j})} - T_{w(\mathrm{n,i,j})}}{\Delta t'}$$
$$= K_w \left(\frac{T_{w(\mathrm{n+1,i+1,j})} - 2T_{w(\mathrm{n+1,i,j})} + T_{w(\mathrm{n+1,i-1,j})}}{\Delta r^2} + \frac{1}{r} \frac{T_{w(\mathrm{n+1,i+1,j})} - T_{w(\mathrm{n+1,i-1,j})}}{2\Delta r} \right) \quad (10.14)$$

$$\frac{T_{p(\mathrm{n+1})} - T_{p(\mathrm{n})}}{\Delta t'} = K_p \left(\tilde{T}_{w(\mathrm{n,0,j})} - T_{p(\mathrm{n})} \right) \quad (10.15)$$

where $\tilde{T}_{w(\mathrm{n,0,j})}$ is the average of all the $T_{w(\mathrm{n,0,j})}$ values.

Applying the modified central difference at $\mathrm{n} + 1$ and $\mathrm{j} - 0.5$ on the height profile:-

$$\frac{T_{m(\mathrm{n+1,j})} - T_{m(\mathrm{n+1,j-1})}}{\Delta z} = \frac{1}{2} \left(\left. \frac{\partial T_m}{\partial z} \right|_{\mathrm{n+1,j}} + \left. \frac{\partial T_m}{\partial z} \right|_{\mathrm{n+1,j-1}} \right)$$
$$= -\frac{K_m}{2} \left(T_{m(\mathrm{n+1,j})} - T_{w(\mathrm{n+1},W,\mathrm{j})} + T_{m(\mathrm{n+1,j-1})} - T_{w(\mathrm{n+1},W,\mathrm{j-1})} \right) \quad (10.16)$$

Equation (10.14) is re-arranged into equation (10.18) via equation (10.17) as follows:-

$$T_{w(\mathrm{n,i,j})} = \left(1 + \frac{2K_w \Delta t'}{\Delta r^2} \right) T_{w(\mathrm{n+1,i,j})} - K_w \Delta t' \left[\frac{T_{w(i+1,n+1,j)} + T_{w(\mathrm{n+1,i-1,j})}}{\Delta r^2} + \frac{T_{w(\mathrm{n+1,i+1,j})} - T_{w(\mathrm{n+1,i-1,j})}}{2r\Delta r} \right] \quad (10.17)$$

$$\therefore T_{w(\mathrm{n,i,j})} = \left(1 + \frac{2K_w \Delta t'}{\Delta r^2} \right) T_{w(\mathrm{n+1,i,j})} - \left(\frac{K_w \Delta t'}{\Delta r^2} + \frac{K_w \Delta t'}{2r\Delta r} \right) T_{w(\mathrm{n+1,i+1,j})} - \left(\frac{K_w \Delta t'}{\Delta r^2} - \frac{K_w \Delta t'}{2r\Delta r} \right) T_{w(\mathrm{n+1,i-1,j})} \quad (10.18)$$

and equations (10.15) and (10.16) respectively become equations (10.19) and (10.20).

$$T_{p(\mathrm{n+1})} = \left(K_p \Delta t' \right) \tilde{T}_{w(\mathrm{n,0,j})} + \left(1 - K_p \Delta t' \right) T_{p(\mathrm{n})} \quad (10.19)$$

$$\left(1 + \frac{K_m \Delta z}{2} \right) T_{m(\mathrm{n+1,j})} - \frac{K_m \Delta z}{2} T_{w(\mathrm{n+1},W,\mathrm{j})} = \left(1 - \frac{K_m \Delta z}{2} \right) T_{m(\mathrm{n+1,j-1})} + \frac{K_m \Delta z}{2} T_{w(\mathrm{n+1},W,\mathrm{j-1})} \quad (10.20)$$

Note that the perfect mixing assumption implies that for every time step, in equation (10.15), the total heat flux at the inner wall temperature $\tilde{T}_{w(\mathrm{n,i=0,j})}$ is taken, becoming $T_{w(\mathrm{n,i=0})}$ before re-use in equation (10.19) to find the values at the next time step.

The discrete forms of the boundary conditions in equations (10.9) to (10.11) respectively are:-

$$-\lambda_w \frac{T_{w(\mathrm{n},1,\mathrm{j})} - T_{w(\mathrm{n},-1,\mathrm{j})}}{2\Delta r} = \alpha_i \left(T_{p(\mathrm{n})} - T_{w(\mathrm{n},0,\mathrm{j})}\right) \tag{10.21}$$

$$-\lambda_w \frac{T_{w(\mathrm{n},W+1,\mathrm{j})} - T_{w(\mathrm{n},W-1,\mathrm{j})}}{2\Delta r} = \alpha_o \left(T_{w(\mathrm{n},W,\mathrm{j})} - T_{m(\mathrm{n},\mathrm{j})}\right) \tag{10.22}$$

$$\text{and } T_{m(\mathrm{n},0,0)} = T_{m1} \tag{10.23}$$

Equations (10.21) and (10.22) are re-arranged to the following for time n + 1:-

$$T_{w(\mathrm{n}+1,-1,\mathrm{j})} = T_{w(\mathrm{n}+1,1,\mathrm{j})} + \left(\frac{2\alpha_i \Delta r}{\lambda_w}\right) T_{p(\mathrm{n}+1)} - \left(\frac{2\alpha_i \Delta r}{\lambda_w}\right) T_{w(\mathrm{n}+1,0,\mathrm{j})} \tag{10.24}$$

$$T_{w(\mathrm{n}+1,W+1,\mathrm{j})} = T_{w(\mathrm{n}+1,W-1,\mathrm{j})} + \left(\frac{2\alpha_o \Delta r}{\lambda_w}\right) T_{m(\mathrm{n}+1,\mathrm{j})} - \left(\frac{2\alpha_o \Delta r}{\lambda_w}\right) T_{w(\mathrm{n}+1,W,\mathrm{j})} \tag{10.25}$$

The value of $T_{p(\mathrm{n}+1)}$ is needed in equation (10.24), and this is known using equation (10.19) (by the forward difference method). Note that the central difference method will not be used here because it would require iteration, as the fully implicit backward method is used and $\tilde{T}_{w(\mathrm{n}+1,0,\mathrm{j})}$ would be required, which is not found until the whole jacket profile has already been evaluated at the next time step. At the inside wall, equation (10.18) becomes:-

$$\begin{aligned} T_{w(\mathrm{n},0,\mathrm{j})} = {} & \left(1 + \frac{2K_w \Delta t'}{\Delta r^2}\right) T_{w(\mathrm{n}+1,0,\mathrm{j})} - \left(\frac{K_w \Delta t'}{\Delta r^2} + \frac{K_w \Delta t'}{2r_i \Delta r}\right) T_{w(\mathrm{n}+1,1,\mathrm{j})} \\ & - \left(\frac{K_w \Delta t'}{\Delta r^2} - \frac{K_w \Delta t'}{2r_i \Delta r}\right) T_{w(\mathrm{n}+1,-1,\mathrm{j})} \end{aligned} \tag{10.26}$$

Equations (10.24) and (10.26) are combined to eliminate the fictitious value of $T_{w(\mathrm{n}+1,-1,\mathrm{j})}$ and re-arranged to form equation (10.27):-

$$\begin{aligned} & T_{w(\mathrm{n},0,\mathrm{j})} + \left(\frac{K_w \Delta t'}{\Delta r^2} - \frac{K_w \Delta t'}{2r_i \Delta r}\right)\left(\frac{2\alpha_i \Delta r}{\lambda_w}\right) T_{p(\mathrm{n}+1)} \\ & \qquad = \left[1 + \frac{2K_w \Delta t'}{\Delta r^2} + \left(\frac{K_w \Delta t'}{\Delta r^2} - \frac{K_w \Delta t'}{2r_i \Delta r}\right)\left(\frac{2\alpha_i \Delta r}{\lambda_w}\right)\right] T_{w(\mathrm{n}+1,0,\mathrm{j})} \\ & \qquad - \frac{2K_w \Delta t'}{\Delta r^2} T_{w(\mathrm{n}+1,1,\mathrm{j})} \end{aligned} \tag{10.27}$$

At the outside wall, equation (10.18) becomes:-

$$T_{w(\mathrm{n},W,\mathrm{j})} = \left(1 + \frac{2K_w\Delta t'}{\Delta r^2}\right)T_{w(\mathrm{n}+1,W,\mathrm{j})} - \left(\frac{K_w\Delta t'}{\Delta r^2} + \frac{K_w\Delta t'}{2r_o\Delta r}\right)T_{w(\mathrm{n}+1,W+1,\mathrm{j})} - \left(\frac{K_w\Delta t'}{\Delta r^2} - \frac{K_w\Delta t'}{2r_o\Delta r}\right)T_{w(\mathrm{n}+1,W-1,\mathrm{j})} \quad (10.28)$$

Equations (10.25) and (10.28) are combined to eliminate the fictitious value of $T_{w(\mathrm{n}+1,W+1,\mathrm{j})}$ and re-arranged to form equation (10.29):-

$$T_{w(\mathrm{n},W,\mathrm{j})} = \left[1 + \frac{2K_w\Delta t'}{\Delta r^2} + \left(\frac{K_w\Delta t'}{\Delta r^2} + \frac{K_w\Delta t'}{2r_o\Delta r}\right)\left(\frac{2\alpha_o\Delta r}{\lambda_w}\right)\right]T_{w(\mathrm{n}+1,W,\mathrm{j})} - \left(\frac{2K_w\Delta t'}{\Delta r^2}\right)T_{w(\mathrm{n}+1,W-1,\mathrm{j})} - \left(\frac{K_w\Delta t'}{\Delta r^2} + \frac{K_w\Delta t'}{2r_o\Delta r}\right)\left(\frac{2\alpha_o\Delta r}{\lambda_w}\right)T_{m(\mathrm{n}+1,\mathrm{j})} \quad (10.29)$$

The constant terms in equations (10.18), (10.20), (10.27) and (10.29) will be shortened as follows:-

$$\frac{K_w\Delta t'}{\Delta r^2} = \mathrm{b}_1 \quad (10.30)$$

$$\frac{K_m\Delta z}{2} = \mathrm{b}_2 \quad (10.31)$$

$$\frac{\alpha_i\Delta r}{\lambda_w} = \mathrm{b}_3 \quad (10.32)$$

$$\frac{\alpha_o\Delta r}{\lambda_w} = \mathrm{b}_4 \quad (10.33)$$

$$K_p\Delta t' = \mathrm{b}_5 \quad (10.34)$$

$$1 + 2\mathrm{b}_1[1 + \mathrm{b}_3(1 - \mathrm{p}_i)] = \mathrm{b}_6 \quad (10.35)$$

$$1 + 2\mathrm{b}_1[1 + \mathrm{b}_4(1 + \mathrm{p}_o)] = \mathrm{b}_7 \quad (10.36)$$

Thus equations (10.18), (10.20), (10.27) and (10.29) respectively become:-

$$T_{w(\mathrm{n},\mathrm{i},\mathrm{j})} = (1 + 2\mathrm{b}_1)T_{w(\mathrm{n}+1,\mathrm{i},\mathrm{j})} - \mathrm{b}_1(1 + \mathrm{p})T_{w(\mathrm{n}+1,\mathrm{i}+1,\mathrm{j})} - \mathrm{b}_1(1 - \mathrm{p})T_{w(\mathrm{n}+1,\mathrm{i}-1,\mathrm{j})} \quad (10.37)$$

$$(1 - \mathrm{b}_2)T_{m(\mathrm{n}+1,\mathrm{j}-1)} + \mathrm{b}_2T_{w(\mathrm{n}+1,W,\mathrm{j}-1)} = (1 + \mathrm{b}_2)T_{m(\mathrm{n}+1,\mathrm{j})} - \mathrm{b}_2T_{w(\mathrm{n}+1,W,\mathrm{j})} \quad (10.38)$$

$$T_{w(\mathrm{n},0,\mathrm{j})} + 2\mathrm{b}_1\mathrm{b}_3(1 - \mathrm{p}_i)T_{p(\mathrm{n}+1)} = \mathrm{b}_6T_{w(\mathrm{n}+1,0,\mathrm{j})} - 2\mathrm{b}_1T_{w(\mathrm{n}+1,1,\mathrm{j})} \quad (10.39)$$

$$T_{w(\mathrm{n},W,\mathrm{j})} = \mathrm{b}_7T_{w(\mathrm{n}+1,W,\mathrm{j})} - 2\mathrm{b}_1T_{w(\mathrm{n}+1,W-1,\mathrm{j})} - 2\mathrm{b}_1\mathrm{b}_4(1 + \mathrm{p}_o)T_{m(\mathrm{n}+1,\mathrm{j})} \quad (10.40)$$

$$\text{where } \mathrm{p} = \frac{\Delta r}{2r}, \qquad \mathrm{p}_i = \frac{\Delta r}{2r_i}, \qquad \mathrm{p}_o = \frac{\Delta r}{2r_o} \quad (10.41)$$

Equations (10.37) to (10.40) form a tridiagonal system of equations, which can be represented in the form:-

$$\boldsymbol{D}(\mathrm{n},\mathrm{j}) = \boldsymbol{S}(\mathrm{j})\boldsymbol{T}(\mathrm{n}+1,\mathrm{j}) \tag{10.42}$$

$$\text{where } \boldsymbol{D}(\mathrm{n},\mathrm{j}) = \begin{bmatrix} (1-\mathrm{b}_2)T_{m(\mathrm{n}+1,\mathrm{j}-1)} + \mathrm{b}_2 T_{w(\mathrm{n}+1,W,\mathrm{j}-1)} \\ T_{w(\mathrm{n},W,\mathrm{j})} \\ T_{w(\mathrm{n},W-1,\mathrm{j})} \\ \vdots \\ T_{w(\mathrm{n},1,\mathrm{j})} \\ T_{w(\mathrm{n},0,\mathrm{j})} + 2\mathrm{b}_1\mathrm{b}_3(1-\mathrm{p}_i)T_{p(\mathrm{n}+1)} \end{bmatrix}, \tag{10.43}$$

$$\boldsymbol{T}(\mathrm{n}+1,\mathrm{j}) = \begin{bmatrix} T_{m(\mathrm{n}+1,\mathrm{j})} \\ T_{w(\mathrm{n}+1,W,\mathrm{j})} \\ T_{w(\mathrm{n}+1,W-1,\mathrm{j})} \\ \vdots \\ T_{w(\mathrm{n}+1,1,\mathrm{j})} \\ T_{w(\mathrm{n}+1,0,\mathrm{j})} \end{bmatrix} \tag{10.44}$$

$$\text{and } \boldsymbol{S}(\mathrm{j}) = \begin{bmatrix} 1+\mathrm{b}_2 & -\mathrm{b}_2 & 0 & 0 & \dots \\ -2\mathrm{b}_1\mathrm{b}_4(1+\mathrm{p}_o) & \mathrm{b}_7 & -2\mathrm{b}_1 & 0 & \dots \\ 0 & -\mathrm{b}_1(1+\mathrm{p}) & 1+2\mathrm{b}_1 & -\mathrm{b}_1(1-\mathrm{p}) & \ddots \\ 0 & 0 & \ddots & \ddots & \ddots \\ \vdots & \vdots & \ddots & \ddots & \ddots \\ 0 & \cdots & \dots & -2\mathrm{b}_1 & \mathrm{b}_6 \end{bmatrix} \tag{10.45}$$

Initially, the vessel and contents are all at an initial temperature T_s, when the jacket heating fluid inlet temperature T_{m1} is increased with a step change for pre-heating. The thermal response to heating can now be studied. For $\mathrm{j} = 0$ at any time step, the top values in the vectors of $\boldsymbol{D}(\mathrm{n},0)$ and $\boldsymbol{T}(\mathrm{n}+1,0)$ are set both equal to T_{m1} and the top row of $\boldsymbol{S}$ is changed so that:-

$$\boldsymbol{S}(0) = \lceil 1 \quad 0 \quad 0 \quad 0 \quad \dots \rceil \tag{10.46}$$

Initially, and at zero height, equation (10.43) is set to:-

$$\boldsymbol{D}(0,0) = \begin{bmatrix} T_{m1} \\ T_s \\ \vdots \\ T_s \\ T_s + 2\mathrm{b}_1\mathrm{b}_3(1-\mathrm{p}_i)T_{p(1)} \end{bmatrix} \tag{10.47}$$

For the first time step, at any other height, equation (10.43) becomes:-

$$\boldsymbol{D}(0,\mathrm{j}) = \begin{bmatrix} (1-b_2)T_{m(\mathrm{n}+1,\mathrm{j}-1)} + b_2 T_{w(\mathrm{n}+1,W,\mathrm{j}-1)} \\ T_s \\ \vdots \\ T_s \\ T_s + 2\mathrm{b}_1\mathrm{b}_3(1-\mathrm{p}_i)T_{p(1)} \end{bmatrix} \tag{10.48}$$

This means that for every time step, the distance profile can only be found once $T_{w(\mathrm{n}+1,W,\mathrm{j}-1)}$ has been found, from the next time step. This poses no significant problem as it has been assumed, as previously stated, that each temperature profile along the length is independent from the temperature profile in the wall at any time step.

To perform Thomas' Algorithm to find the temperature distribution at the next time step, the known matrices $\boldsymbol{S}(0)$ and $\boldsymbol{S}(\mathrm{j})$ must be broken down into known vectors $\boldsymbol{A}(0)$, $\boldsymbol{B}(0)$, $\boldsymbol{C}(0)$, $\boldsymbol{A}(\mathrm{j})$, $\boldsymbol{B}(\mathrm{j})$ and $\boldsymbol{C}(\mathrm{j})$, where $\boldsymbol{A}(\mathrm{j})$ is the right diagonal, $\boldsymbol{B}(\mathrm{j})$ is the middle diagonal and $\boldsymbol{C}(\mathrm{j})$ is the left diagonal. For every term in each vector, the row number is the same as for the matrix, therefore the top term in vector $\boldsymbol{A}(\mathrm{j})$ and the bottom term in vector $\boldsymbol{C}(\mathrm{j})$ must always be zero. Wikipedia (2011) had a pre-written MATLAB function named "TDMAsolver.m", displayed in figure 10.42. This has been used to solve the tridiagonal system at each time step. Once the average value of $\tilde{T}_{w(\mathrm{n}+1,0,\mathrm{j})}$ has been found, $T_{p(\mathrm{n}+2)}$, is found using equation (10.19) for the next time step.

```
function x = TDMAsolver(a,b,c,d)
% a, b, c are the column vectors for the compressed tridiagonal matrix, d
% is the right vector
n = length(b); % n is the number of rows
% Modify the first-row coefficients
c(1) = c(1) / b(1);       % Division by zero risk.
d(1) = d(1) / b(1);       % Division by zero would imply a singular matrix.
for i = 2:n
    id = 1 / (b(i) - c(i-1) * a(i));  % Division by zero risk.
    c(i) = c(i)* id;                  % Last value calculated is redundant.
    d(i) = (d(i) - d(i-1) * a(i)) * id;
end
% Now back substitute.
x(n) = d(n);
for i = n-1:-1:1
    x(i) = d(i) - c(i) * x(i + 1);
end
end
```

Figure 10.42 – Implementation of Thomas' algorithm with "TDMAsolver.m" in MATLAB. Based on code in Wikipedia (2011).

An example of the main program script for the distributed parameter model in MATLAB is presented in the next section (10.6.2). Temperatures in this code are currently in K rather than °C. The profiles for heat transfer rates at the outer wall ($\dot{Q}_m$) and the inner

wall ($\dot{Q}_p$) are worked out via equations (10.49) and (10.50). Central difference is not needed here as the rates are found independently for each time step.

$$\dot{Q}_{m(\mathrm{n})} = -\left(\dot{M}c_P\right)_m\left(T_{m2(\mathrm{n})} - T_{m1}\right) = -\left(\dot{M}c_P\right)_m\left(T_{m(\mathrm{n},Z)} - T_{m1}\right) \tag{10.49}$$

$$\dot{Q}_{p(n)} = \frac{(Mc_P)_p\left(T_{p(\mathrm{n})} - T_{p(\mathrm{n}-1)}\right)}{\Delta t} \tag{10.50}$$

10.6.2 MATLAB Code

```
% Distributed Parameter Model for steady initial temperature
clear
clf

% Ending time
tf = 10000;      % s

% Jacket height
Z = 0.33;        % m

% Process mass
Mp = 20;         % kg

% Process specific heat capacity
cPp = 4184;      % J kg^-1 K^-1

% Process fluid initial temperature
Tp1 = 293.15;    % K

% Initial temperature of system
Ts = Tp1;

% Jacket fluid mass flow
Mm = 0.2631;     % kg s^-1

% Jacket fluid specific heat capacity
cPm = 1950.9;    % J kg^-1 K^-1

% Wall radii
ro = 0.16;       % m
ri = 0.154;      % m

% Wall thickness
deltaw = ro-ri; % m

% Wall conductivity
lambdaw = 1.2; % W m^-1 K^-1

% Wall density
rhow = 2230;     % kg m^-3

% Wall specific heat capacity
```

```
cPw = 800;    % J kg^-1 K^-1

% Outside area
Apro = 2*pi*ro; % m
Ao = Apro*Z;    % m^2

% Inside area
Apri = 2*pi*ri; % m
Ai = Apri*Z;    % m^2

% Resistances
alphao = 293;   % W m^-2 K^-1
alphai = 2633;   % W m^-2 K^-1

% Finite differences
dr = deltaw/10; % m
dz = 0.01;       % m
dt = 10;        % s

% Number of steps
W = deltaw/dr;
J = Z/dz;
N = tf/dt;

% Jacket fluid inlet temperature function
Tm1 = zeros(N+1,1);
for n = 1:N/5
   Tm1(n) = 293.15 + (373.15 - 293.15)*n/(N/5); % K
end
for n = (N/5)+1:N+1
   Tm1(n) = 373.15; % K
end


% Compressed constants 1
Kw = lambdaw/(rhow*cPw);
Km = alphao*Apro/(Mm*cPm);
Kp = alphai*Ai/(Mp*cPp);

% Compressed constants 2
pin = dr/(2*ri);
pout = dr/(2*ro);
b1 = Kw*dt/(dr^2);
b2 = Km*dz/2;
b3 = alphai*dr/lambdaw;
b4 = alphao*dr/lambdaw;
b5 = Kp*dt;
b6 = 1 + 2*b1*(1 + b3*(1-pin));
b7 = 1 + 2*b1*(1 + b4*(1+pout));

% Pre-allocation of vector sizes
vecA = zeros(W+2,1);
```

```
vecB = zeros(W+2,1);
vecC = zeros(W+2,1);
vecD = zeros(W+2,1);

% Components of known matrix at time n and height 0

% Diagonal A
vecAn0 = vecA;
vecAn0(2) = -2*b1*b4*(1+pout);
for i = 3:W+1
   r = ri + (i-2)*dr;
   p = dr/(2*r);
   vecAn0(i) = -b1*(1+p);
end
vecAn0(W+2) = -2*b1;

% Diagonal B
vecBn0 = vecB;
vecBn0(1) = 1;
vecBn0(2) = b7;
for i = 3:W+1
   vecBn0(i) = 1 + 2*b1;
end
vecBn0(W+2) = b6;

% Diagonal C
vecCn0 = vecC;
vecCn0(2) = -2*b1;
for i = 3:W+1
   r = ri + (i-2)*dr;
   p = dr/(2*r);
   vecCn0(i) = -b1*(1-p);
end

% Components of known matrix at any time and nonzero height
vecAnj = vecAn0;
vecBnj = vecBn0;
vecBnj(1) = 1+b2;
vecCnj = vecCn0;
vecCnj(1) = -b2;

% Pre-allocation of mean Tw(0,n) profile
Tw0n = zeros(N+1,1);
Tw0n(1) = Ts;

% Pre-allocation of Tp profile
Tpn = zeros(N+1,1);
Tpn(1) = Tp1;
Tpn(2) = b5*Tw0n(1) + (1-b5)*Tpn(1);

% Pre-allocation of Qm and Qp profiles
Qm = zeros(N+1,1);
```

```
Qp = zeros(N+1,1);

% Components of known vector at time 0 and height 0
vecD00 = vecD;
vecD00(1) = Tm1(1);
for i = 2:W+1
   vecD00(i) = Ts;
end
vecD00(W+2) = Ts + (2*b1*b3*(1-pin))*Tpn(2);

% Initial outer and inner Tw profiles
TwW0j = zeros(J+1,1);
for j = 1:J+1
   TwW0j(j) = Ts;
end
Tw00j = zeros(J+1,1);
for j = 1:J+1
   Tw00j(j) = Ts;
end

% Initial Tm profile
Tm0j = zeros(J+1,1);
Tm0j(1) = Tm1(1);
for j = 2:J+1
   Tm0j(j) = (b2/(1+b2))*TwW0j(j)...
      + ((1-b2)/(1+b2))*Tm0j(j-1)...
      +(b2/(1+b2))*TwW0j(j-1);
end

% Jacket exit temperature
Tm2 = zeros(N+1,1);
Tm2(1) = Tm0j(J+1);

% Wall profile at time 1 and height 0
vecT10 = TDMAsolver(vecAn0, vecBn0, vecCn0, vecD00);

% Height profile vectors at time 1
Tm1j = Tm0j;           % vector for Tm(j) at n=1
Tm1j(1) = vecT10(1);    % = Tm1 in this case
TwW1j = TwW0j;         % vector for Tw(j) outer at n=1
TwW1j(1) = vecT10(2);   % value from previous TDMA solution
Tw01j = Tw00j;         % vector for Tw(j) inner at n=1
Tw01j(1) = vecT10(W+2); % value from previous TDMA solution

% Initialising for height profile
vecD0j = vecD00;

% Calculation of height profile at n=1
for j = 2:J+1

% Components of known vector at time 1 and height j
vecD0j(1) = (1-b2)*Tm1j(j-1) + b2*TwW1j(j-1);
```

```
vecT1j = TDMAsolver(vecAnj, vecBnj, vecCnj, vecD0j);
Tm1j(j) = vecT1j(1);
TwW1j(j) = vecT1j(2);
Tw01j(j) = vecT1j(W+2);
end

% New exit temperature
Tm2(2) = Tm1j(J+1);

% Mean inner wall temperature at n=1
Tw0n(2) = mean(Tw01j);

% Procedure applied for all further time levels

% Ready for time steps
vecDn0 = vecT10;
Tmnj = zeros(J+1,1);
TwWnj = TwW1j;
Tw0nj = Tw01j;

for n = 2:N % time steps

% Forward difference to find Tp at n+1
Tpn(n+1) = b5*Tw0n(n) + (1-b5)*Tpn(n);

% at zero height
vecDn0(1) = Tm1(n);
vecDn0(W+2) = Tw0nj(1) + (2*b1*b3*(1-pin))*Tpn(n+1);

% Wall profile at time n+1 and height 0
vecTn0 = TDMAsolver(vecAn0, vecBn0, vecCn0, vecDn0);

% Ready for height steps
Tmnj(1) = vecTn0(1);    % = Tm1 in this case
TwWnj(1) = vecTn0(2);   % value from previous TDMA solution
Tw0nj(1) = vecTn0(W+2); % value from previous TDMA solution

% Initialising for height profile
vecDnj = vecDn0;

% Calculation of height profile
for j = 2:J+1

% Components of known vector at height j
vecDnj(1) = (1-b2)*Tmnj(j-1) + b2*TwWnj(j-1);
vecTnj = TDMAsolver(vecAnj, vecBnj, vecCnj, vecDnj);
Tmnj(j) = vecTnj(1);
TwWnj(j) = vecTnj(2);
Tw0nj(j) = vecTnj(W+2);
end

% New exit temperature
```

```
Tm2(n+1) = Tmnj(J+1);

% Mean inner wall temperature
Tw0n(n+1) = mean(Tw0nj);

% Ready for the next time step
vecDn0 = vecTn0;

end % time steps

% Time axis
time = zeros(N+1,1);
for n = 0:N
time(n+1) = n*dt;
end

% Qm profile
for n = 0:N
   Qm(n+1) = -Mm*cPm*(Tm2(n+1) - Tm1(n+1));
end

% Qp profile
Qp(1) = 0;
for n = 1:N
   Qp(n+1) = (1/dt)*Mp*cPp*(Tpn(n+1) - Tpn(n));
end

% Plotting curves
plot(time,Tpn,'k')
hold on
plot(time,Tm1,'b')
plot(time,Tm2,'r')
legend('Tp','Tm1','Tm2')
xlabel('Time / s')
ylabel('Temperature / K')
hold off

figure(2)
plot(time,Qm,'b')
hold on
plot(time,Qp,'r')
legend('Qm rate','Qp rate')
xlabel('Time / s')
ylabel('Heat transfer rate / W')
hold off
```

10.7 Detail of the Experimental and Safety Procedures

10.7.1 Standard operating procedure

Here, only the standard operating procedure for the methanol distillation experiment will be presented. The standard operating procedure for the water distillation experiment was the same but without the recommended safety procedures for handling methanol.

Process summary

This distillation procedure has been designed to test the heat losses associated with the large scale system.

- Hazards:-

  Methanol is colourless liquid. It is highly flammable. Its boiling point is 65°C. It may cause eye irritation and may have a degreasing effect on the skin.

  In the event of contact with either skin or eyes, wash immediately with plenty of water – for eyes continue for at least 15 minutes – and obtain medical help as soon as possible.

  In the event of inhalation, remove from exposure and obtain immediate medical help.

  In the event of spillage, use the spill kit to soak up the liquid and place in a drum for disposal.

- Personal Protective Equipment Required:-

  Safety Glasses

  Antistatic Lab Coat

  Antistatic Steel Toe Capped Shoes

  Industrial Marigold Gloves

Special Considerations for Safe Operation of the Large Scale Glassware when using Flammable Solvents

Always:-

- Wear antistatic safety shoes.
- Earth metal drums, funnels and scoops.
- Blanket vessel contents with nitrogen.

- Break vacuum with nitrogen.
- Transfer solvents using residual vacuum (<1m/s line velocity) to prevent static build up in transfer lines.
- Clean up spillages immediately.

Never:-

- Charge solids to vessels from plastic bags. The static build up may discharge and ignite the solvent.
- Place electrical items in the fume cupboard which are not ATEX rated when flammable solvents are in use.
- Use non conducting plastics, beakers, funnels, scoops, filter funnels.
- Transfer 2-phase systems.
- Use the Large Scale Glassware Laboratory to store flammables.

Stage 1. Pre Batch Checks

Step No.	Operation	Comment	Operator Initials
1.1	Confirm that the fume cupboard air flow is greater than 0.4m/s and air flow failure alarm is functioning.	Acceptable: Y/N	
1.2	Confirm that the agitator failure alarms are functioning.	Acceptable: Y/N	
1.3	Confirm that the high temperature alarms on the Hubers are set to 180^{o}C. (Temperature Class 3 solvents: Max jacket temp 180^{o}C, max process temp 156^{o}C)	Acceptable: Y/N	
1.4	Confirm the earth testing to the fume cupboard, scaffolding and floor mat is in date.	Acceptable: Y/N	
1.5	Inspect the silicon seal in the fume cupboard base and confirm it is complete and intact.	Acceptable: Y/N	
1.6	Confirm there are only ATEX rated electrical appliances are inside the fume cupboard.	Acceptable: Y/N	
1.7	Confirm all vessels are empty and all lines have been drained.	Acceptable: Y/N	

1.8	Confirm all valves are in the closed position and manhole covers are closed.	Acceptable: Y/N
1.9	Confirm the nitrogen supply is adequate for the daily use.	Acceptable: Y/N
1.10	Confirm the condenser water is switched on and flowing.	Acceptable: Y/N
1.11	Confirm that all hosing is attached to the condensers and Huber units and that it is in good repair with no leaks.	Acceptable: Y/N
1.12	Confirm that hosing connects the scrubber unit to the reaction units via the condenser vents and it is good repair.	Acceptable: Y/N
1.13	Confirm the scrubber vent is inserted into the fume cupboard ducting.	Acceptable: Y/N
1.14	Confirm all raw materials to be used are in the Large Scale Glassware solvent storage area.	Acceptable: Y/N
1.15	Confirm all Personal Protective Equipment is available for use.	Acceptable: Y/N

Stage 2. Set up the scrubber

Step No.	Operation	Comment	Operator Initials
2.1	Charge 15 litres Deionised Water to the scrubber via the manhole.		
2.2	Open the valves, on the scrubber column and reactors, to the 25 and 50 litre vessels.	Vent is open Y/N?	
2.3	Turn on the scrubber pump.		

Stage 3. Distillation of Methanol Mixture

Step No.	Operation	Comment	Operator Initials
3.1	Ensure the vent valves are open to the scrubber.		
3.2	Flush the 25 litre vessel with 40 litres of nitrogen/min for 15 minutes.		

3.3 Reduce the nitrogen flow to 5 litres/minute to ensure that nitrogen is flowing through the vessel.

3.4 Earth the 25 l drum.

3.5 Using the residual vacuum charge the vessel with 5 litres of methanol straight from the metal drum.

3.6 When the charge is complete, isolate the charge line and release the vacuum.

3.7 Open the valve and allow the contents of the measure vessel to enter the 25 litre vessel.

3.8 Repeat steps 3.5 to 3.7 until 20 litres of methanol have been charged.

3.9 Start the agitator and the Huber.

3.10 Ensure data logging of readings produced by temperature reading/Huber at set intervals.

3.11 Record the water temperature and enter it as the set point of into the Huber controller using “process mode”, then allow the contents of the 25 litre vessel to reach equilibrium.

3.12 Enter a set point of 60^{o}C into the Huber controller and heat the contents of the 25 litre vessel while monitoring using Labview. Ensure the vessel is configured for distillation to the receiver.

3.13 When the Huber internal temperature rise begins to slow down, change the Huber control to “internal mode” and enter a set point of 75^{o}C. Take care not to overload the condenser.

3.14 Hold this setting for 10 minutes, pumping the distillate back into the reactor when it is collected. Take a sample of the distillates.

3.15 Enter a set point of 80^{o}C into the Huber controller and heat the contents of the 25 litre vessel while monitoring using Labview.

3.16 Repeat Step Nos. 3.14 – 3.15 with the set points of 85^{o}C, 90^{o}C, 95^{o}C, 100^{o}C and 105^{o}C.

3.17 Set the temperature to 20^{o}C using the Huber controller, cooling the contents of the 25 litre vessel while monitoring using Labview.

3.18	Change the Huber control to “process mode”.		
3.19	At this point set Huber temp to ambient and allow process to cool.		

Stage 4. Discharge and Drying of the 25 Litre Unit

Step No.	Operation	Comment	Operator Initials
4.1	Discharge 25 litre vessel and receiver via the bottom outlet valves straight into the drums and allow the equipment to drain by leaving the valves open.		

10.7.2 Safety and risk assessment

A single risk assessment document covered both the water and methanol distillation experiments, as well as acetone (acetone was used in a training run before the main experiments as well as to clean out the reactors after use). It was signed by the author, the primary supervisor and the laboratory manager.

The first section of the risk assessment document was entitled “Hazardous area classification and basis of safety”. The basis of safety was the elimination of ignition sources. This section had the following three questions:-

Q: “Are you using or making any chemicals which during processing are capable of detonation, deflagration, high rate decomposition or have a pyrophoric nature?” A: “No.”

Q: “Do any of the chemicals or processing activities require a Basis of Safety of an Inert Blanket rather than a Basis of Safety of Elimination of Ignition Sources?” A: “No. Inert blanket will be used as a secondary safety measure.”

Q: “Do any chemicals fall outwith the scope of the electrical ATEX standard of Temperature Class 4 and or Gas Type 2C?” A: “No.”

The second section of the document was entitled “Reaction scheme & brief summary of reaction principles (Show or describe all processes, reagents, intermediates, products, by-products, off-gases and summary conditions)”. In this section was written: “Measurement of heat flow across the reactor during various distillation rates of water, methanol and acetone. There is no reaction.” No further information was required because there was no reaction.

The third section was entitled “COSHH – intrinsic chemical hazards (List all materials in scheme, including isolated intermediates, off-gases, scrubber liquors, clean-out solvents and waste)”. The information displayed in table 10.9 was below it:-

Table 10.9 – COSHH details (part of the risk assessment).

Material	**Quantity / kg**	**Significant Intrinsic Hazards and Risk Phrases**	**Special Precautions or Personal Protective Equipment**
Deionised water	60	Methanol & Acetone: Highly flammable Methanol: Toxic – danger of very serious irreversible effects through inhalation, in contact with skin and if swallowed. Acetone: Irritating to eyes, repeated exposure may cause skin dryness or cracking, vapours may cause drowsiness and dizziness.	Safety glasses, antistatic lab coat, antistatic steel toe capped boots, industrial marigold gloves. Especially with methanol, avoid skin contact or splashes, and take care not to inhale vapours.
Methanol	20		
Acetone	60		

The fourth section was entitled “Reactive chemical hazards of each material (List sensitivities, incompatibilities (including interactions with condenser coolant, Huber oil and scrubber liquors), thermochemical threats, flash points etc)”. The information displayed in table 10.10 was below it:-

Table 10.10 – Reactive hazards and control measures (part of the risk assessment).

Material	**Reactive Hazards**	**Control Measures Required**
Methanol, acetone	Flammable (reaction with oxygen in air)	Elimination of ignition sources within the fume cupboard. Constant air flow to remove flammable vapours. Nitrogen blanket

The fifth section was entitled “Energy hazards of the process (List energies present, sources)”. It had two parts: “What is the Stability of the Raw Materials, Intermediates, Products and Distillation Residues etc especially if elevated temperatures are required?” and “What Reaction Energy is Present?”

The second question (“What Reaction Energy is Present?”) was not applicable, so this section was about the boiling points of the substances (water 100°C, methanol 65°C, acetone 56°C). The possible dangers were pressure rise due to possible excessive boiling of the substances and overloading of the condenser. The substances greatly expand when boiled and correspondingly greatly contract when condensed. The control measures were to firstly keep the vent valves open to the scrubber to equalise the pressure, and secondly to watch the condenser for signs of overload and cool the reactor if this were to occur. The last line of safety was the bursting disk, set to release if the pressure difference between the system and surroundings was 0.4 bars or more.

The sixth section was entitled “Other physical hazards (List any other significant hazards that could conceivably arise, including spillage and clean-up)”. The natures of the hazards listed were spillage of the liquids and the flammability of the vapour. The hazards could arise from charging or discharging the vessel, not collecting all the contents after the experiment, and accidentally leaving the run-off valves open (this would be checked in the standard operating procedure).

The control measures for spillage were firstly to use suitable gloves when cleaning. If a small spillage were to occur, it would be soaked up with tissues (which would be left in the fume cupboard until any flammable liquid had evaporated). If a larger spillage were to occur, the fume cupboard would be purged, all windows would be closed, and any flammable liquid would be left to evaporate. If a very large spillage occurred, the spill kit would be used, as well as closing all windows, purging the fume cupboard and leaving it to evaporate.

The control measures for flammable vapour during these operations were to ensure that all the drums (which were made of metal) were earthed during charging, and the substances were charged using residual vacuum only (not pumped). Flammable solvents would be discharged into glass bottles. Waste disposal bins would be placed into the fume cupboard during filling, so any vapours would stay in the fume cupboard.

The seventh section was entitled “Potential hazards arising from mal-operation (List process deviations that could give rise to a hazard)”. The potential deviations listed here were if the run-off valves were open (causing large spillage), or the vent valves were closed (causing pressure build-up), or if there was a large enough temperature difference (causing thermal shock to the vessel wall). The control measures for spillage were discussed in the previous section. The control measures for pressure build-up were to

check the vent valves were open (as part of the standard operating procedure) and to have the bursting disk in place. The control measures for temperature difference were to monitor the difference between the jacket inlet temperature and the process temperature and to make sure this difference does not exceed 50°C. The Huber control system would do this automatically if set to “process mode”.

The eighth section was entitled “Emergency shutdown procedures”. The emergency situations identified were temperature spikes (from Huber malfunction or mal-operation), the possibility of the fire alarm activating during an experiment and the possibility of fume cupboard failure.

The control measures for temperature spikes were three temperature trips and alarms set in the Huber unit. Firstly if there was a 50°C difference between jacket inlet temperature and process temperature this would be controlled the system was in “process mode” and monitored if the system was in “internal mode”. Secondly an alarm would activate if the Huber temperature reached the set maximum temperature of 156°C. And lastly the Huber would automatically shut down if the temperature of the DW-Therm reached 180°C as it is too close to its boiling point of 200°C. Additionally, monitoring and observation of the process was essential.

If the fire alarm were to go off, the emergency action was to use the radio to contact the fire wardens and alert them to the situation. Then it was to be established whether it was a drill or a real fire. If it was a real fire, the Huber control would be set to 20°C and all personnel would evacuate (with the radio, so fire wardens could still be contacted). If it was a drill, operators would keep working because the process required monitoring.

If the fume cupboard air flow failed, the Huber system would be set to 20°C immediately upon discovery. If it was thought that significant flammable gases could escape (if there was boiling methanol or acetone), a major threat of fire or explosion would be present. In this case, the fire alarm would then be activated and all personnel would evacuate. Fire wardens would be informed of the situation.

The ninth section was entitled “Hazards arising from service or equipment failures (List services required and consequence of failure)”. Possible hazards identified were insufficient fume cupboard air flow, loss of nitrogen blanket on the contents of the system, condenser overload, and high pressure in the reactor if the valves were closed. The control / action measures from failures of the fume cupboard or temperature control (condenser

overload) and pressure build-up were discussed in previous sections of the risk assessment document. For the nitrogen blanket, part of the standard operating procedure is to ensure sufficient nitrogen is present before and during the experiment.

The tenth section was entitled “Special detoxification of waste (List any special measures required to safely detoxify waste)”. This section was not applicable to these experiments.

The eleventh section was entitled “Cleanout of equipment (List equipment to be cleaned and solvents required to clean out the equipment)”. The reactor was to be cleaned out at the end with acetone, a flammable and irritant substance. Control measures for acetone were the use of ATEX-rated equipment in the fume cupboard, the fume cupboard air flow, and the presence of a nitrogen blanket when flammable substances were in the system. This cleaning would be done by the lab manager after the experiment was finished.

The twelfth section was entitled “Disposal of waste (List types of waste expected and disposal method)”. For the deionised water, no hazards were present and the waste route would be normal drainage. For methanol (flammable and toxic) and acetone (flammable and irritant), disposal would be taken care of by the Chemistry Stores personnel.

The thirteenth section was entitled “Who is at risk from this experiment? (Address the risk to all those who may come in contact with this experiment)”. All operators and visitors were considered “at risk” and the risks were from coming into contact with the solvents (liquid or vapour) and from entering the hazardous area (fume cupboard) which was required at times such as when discharging the vessel. To alleviate these risks, primarily, care was to be taken to avoid skin contact and splashes, and to avoid inhalation of the vapours. Personal protective equipment was also to be used – lab coats and safety glasses were to be worn at all times in the lab, and additionally, in the hazardous area and when handling solvents, industrial marigold gloves and anti-static steel toe capped boots were to be worn.

10.7.3 Risk Assessment Form

1.0 Process to be Operated

1.1 Stage 1 – Materials Usage / Batch

Material/Chemical	Quantity
Water	60 L – 20 L for 25 L vessel, 40 L in 50 L vessel
Methanol	30 L – used in 25 L vessel only
Acetone	60 L – 20 L for 20 L vessel, 40 L for 50 L vessel
Product generated / batch	Total 20 L each for 25 L vessel, 40 L each for 50 L vessel

1.2 Stage 1 – Number of Batches Required: 4 for 25 L vessel, 2 for 50L vessel

1.3 Stage 1 – Estimated Cycle Time / Batch: 1 day

1.4 Stage 1 – Estimated Clean-out Time: N/A (acetone will be used last in both vessels)

1.5 Stage 1 – Estimated Manufacturing Time: N/A

1.6 Stage 1 – Brief Process Outline

Process Operation	Volume in Vessel
1. Heating to reflux	Full capacity (80% of total volume)
2. Distilling at different rates (increasing jacket temperatures in steps)	Full capacity (80% of total volume)
3. Cooling to ambient temperature	Full capacity (80% of total volume)

2.0 Stage 1 – Hazard & Operability Study

2.1 Consider all aspects of the chemical process and how they will be operationally carried out. (Include: Movement and storage of chemicals, manual handling issues, weighing, splitting bulk chemicals into manageable size packages, charging of chemicals and potential interactions in charging lines, reaction, discharging from vessels, discharging from vac filter, drying, type of product and waste drums, etc.)

No reactions present

Process Operation or Activity	Action Required or Control Measure
1. Manual handling	Trolley for main drums, maximum carrying weight 10kg

2.2 Stage 1 – Additional Questions (if not covered in the above study)

Activity	Action Required or Control Measure
Is the equipment of a suitable size for the reaction? Is the agitator covered throughout the processing?	Yes Yes
Is there any risk of serious frothing?	No

Are there any anticipated viscosity or physical form changes?	Boiling during distillation
Do any raw materials require melting before use?	No
Is there enough cooling capacity around the vessel jacket available to control exotherms?	N/A
Is there a static hazard from charging any dry powder? Is there a dust cloud hazard?	N/A N/A
What high temperature alarm set point is required for operation of the Hubers?	OT = 180ºC T Max = 156ºC (Temperature classification T3)
Is the vent size (19mm) adequate to release gas and avoid the reaction pressurising the equipment?	Yes
Is any gas or vapour used or formed in the reaction? Is the scrubber required? What scrubber liquor will be used and what strength is required?	Yes, due to evaporation and boiling Yes (for acetone and methanol experiments) Deionised water (for acetone and methanol experiments)
Is any out of hours working required to cover the work? If so, how will this be managed?	Strict working hours 8am – 4pm, possibly up to 5pm. James may agree to supervise 4pm to 5pm.
Is all electrical equipment to be placed inside the fume cupboard of the standard required to enable the use of flammable solvents and flammable dusts?	A check is required on the thermometers to be used on the outside of the jackets – see action 1.
Are all operators of the Large Scale Glassware fully trained?	Erik Bentham and Nick Fitch are trained. Scott Shaw is not trained and is only allowed in the presence of either Erik or Nick.
Are all heating and cooling activities designed to prevent thermal shock to the vessels?	Yes

2.3 Stage 1 – Materials of Construction Review

	Reactor		Charge/Discharge/Transfer Hosing				
Chemical / Intermediate / Product	Borosilicate Glass	PTFE	Viton	Rubber	Silicone	Neoprene	Other Required - Marprene
Deionised water	√	√	√	√	-	-	√
Methanol	√	√	x	√	-	-	√
Acetone	√	√	x	√	-	-	√

Repeat Hazard & Operability Study for each Stage of the Process.

N/A – the above risk assessment covers all stages.

3.0 Action List – (List all actions which arise from the above risk assessment. All actions must be completed before commencing manufacture)

Action	Responsible Person	Completion Date
1. A static hazard risk assessment is required for the thermometer probes to be attached to the jackets. If a static hazard is potentially present, the written justification must be supplied before staring work.	S Pollard to check static risk. F. Muller to supply written justification.	Before startup can commence.

4.0 Process Instruction Sheet

Have Process Instructions for operating the process in the Large Scale Glassware been completed? Yes.
Process Instruction Document References: 1. iPRD/KgLab/PISheet – Erik/25 litre/water/heating profile 2. iPRD/KgLab/PISheet – Erik/25 litre/methanol/distillation 3. iPRD/KgLab/PISheet – Erik/25 litre/methanol-water/distillation 4. iPRD/KgLab/PISheet – Erik/25 litre/acetone/distillation 5. iPRD/KgLab/PISheet – Erik/50 litre/water/heating profile 6. iPRD/KgLab/PISheet – Erik/50 litre/acetone/distillation